Adsorption at Treated Steel-Paint Interfaces

Poon, Chun Yin Jeffrey

This thesis is submitted for the degree of
Doctor of Philosophy

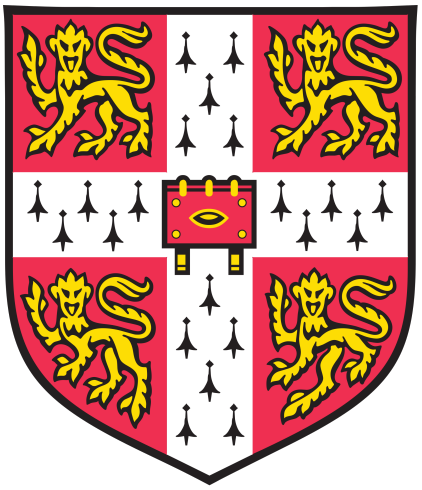

St. Edmund's College
Department of Chemistry
University of Cambridge
United Kingdom
July 2019

ūmišam šukun ḫidūtam
urrī u mūšī sūr u mēlil
lū ubbubū ṣubātūka
qaqqadka lū mesi mê lū ramkāta
ṣubbi ṣeḫram ṣābitu qātīka
marḫītum liḫtaddâm ina sūnīka
annāma šī[mti awīlūtim?]

Make merry each day,
dance and play day and night!
Let your clothes be clean,
let your head be washed, may you bathe in water!
Gaze on the little one who holds your hand,
let a woman enjoy your repeated embrace!
For such is the destiny of [mortal men].

-At the End of the Word, *The Epic of Gilgamesh*

CONTENTS

Declaration

This thesis is the result of my own work and includes nothing which is the outcome of work done in collaboration except as declared in the Preface and specified in the text. It is not substantially the same as any that I have submitted, or, is being concurrently submitted for a degree or diploma or other qualification at the University of Cambridge or any other University or similar institution except as declared in the Preface and specified in the text. I further state that no substantial part of my thesis has already been submitted, or, is being concurrently submitted for any such degree, diploma or other qualification at the University of Cambridge or any other University or similar institution except as declared in the Preface and specified in the text. It does not exceed the prescribed word limit for the relevant Degree Committee.

Work included in this thesis contributed towards the publication of a paper titled 'Characterizing Surfaces of Garnet and Steel, and Adsorption of Organic Additives' (*Langmuir*, 2018, 34, 26, 7726-7737, from Chapters 5, 6, 8, 9). Work from Chapter 10 has been published in a paper under the title of 'Characterisation of Short Time Marine Corroded Surfaces' (*J. Electrochem. Soc.*, 2019, 166, 14, C509-C519). Work from Chapters 6 and 11 are under review at the Journal of Physical Chemistry C (16th October 2019), titled 'The Surface Chemistry of Almandine Garnet'.

1. ACKNOWLEDGEMENTS

I would like to thank my inspirational and supportive supervisor, Prof. Stuart Clarke, for his enthusiasm and energy. It has been a great pleasure working under his supervision. I would like to thank all those who worked in the Shell project team: Dr. Mary Wood, Ms. Fahmida Khan, Ms. Anke Krautsieder, and most importantly Dr. David Madden. I have learned much from his careful approach. His meticulous attention-to-detail is something that I shall continue aspiring to.

I would like to thank Dr. Mike Casford for his help in all things infrared- and SFG-related. His good humour and patience is always appreciated. I thank Ms. Laura Healy and Dr. Chris Rolfe for their help with ICP analysis. I thank all those at the NEXUS XPS Serivce and Harwell XPS Service for all their XPS help and sharing their insights in spectra analysis. I thank Mr. Simon Griggs and Dr. Sean Collins for their support and help at the Department of Materials and Metallurgy at Cambridge concerning the FIB and EELS data analysis. A special thank-you to Dr. Giulio Lampronti from the Department of Earth Sciences for his infinite patience and humour while we worked at the electron microscope.

It has been a wonderful time working at the BP Institute, and I thank all of my colleagues there for making it possible. Special thanks go to those working in the Clarke group and those I shared an office with: Dr. Mary Wood, Dr. Tim Beeson-Jones, Dr. Alex Evans, Ms. Surabhi Agrawal, and Mr. Edward Hinton. I shall miss the banter.

I thank Shell for providing the financial support for this project. I especially thank Dr. Ron van Tol, Dr. Lene Haviid, Dr. Hans Sonke, and Dr. Damodaran Raghu for their helpful suggestions and enthusiasm.

Last, and most importantly, I thank my family. They have given me helpful suggestions when I am in doubt, encouragement when I am down. I cannot be more grateful for their support throughout my thirteen years in the UK. I owe you all a great debt of gratitude.

2. ABSTRACT

In this thesis, a wide range of surface sensitive techniques have been used to characterise surfaces relevant to offshore steel structures, to provide fundamental understanding of steel-paint binding that prolongs coating lifespans and corrosion inhibition.

Particular steel surfaces are characterised before and after almandine garnet abrasive blasting. Significant build-up and coverage of abrasive residue (almandine and calcium carbonate) is identified on the post-treatment steel, covering up to a third of the steel surface. Given the importance of the blasting materials on the surface, almandine garnet is also characterised for its surface chemistry and behaviour. By characterising both bare steel and almandine garnet, adsorption on 'real' garnet-blasted steel substrates can be modelled.

A dry ice-garnet mixed stream is also investigated to see whether abrasive residue could be reduced. It is found that a quarter of the steel surface is covered with blasting residue. However, cooling and moisture-condensation leads to corrosion spots formation.

The adsorption of potential paint additives and components on S355 steel and garnet are determined using solution depletion isotherms. Quantitative data such as equilibrium adsorption constants, and estimation of monolayer molecular geometries are collected. The latter is further investigated through novel surface spectroscopy. In brief, most organics are found to have higher affinity to steel than garnet.

The steel surface is shown to be likely to corrode in offshore conditions with corrosion marine aerosols in a matter of a few hours. It is these corrosion products which will be substrates for coating/paint molecules. A 'salt drop' corrosion study simulates relatively short timescale aerosol exposure (mins to hours). Surface chemical-environments are characterised. The corrosion products are found to be porous, inhomogeneous in chemical environment, and evolve through time, with adsorbed/occluded marine ions.

Finally, as steel corrosion products are likely to adsorb marine salts, ion adsorption on almandine garnet is investigated. Cations of sodium, magnesium, and calcium are found to specifically adsorb. Numerical model co-fitting of data from different techniques successfully obtains the adsorption equilibria and constant, and the surface site density of almandine garnet. The study highlights a general need for more complete studies, using multiple adsorption experiments, for aqueous phase adsorption investigations on minerals in the future.

3. INTRODUCTION

3.1 Purposes and Aims

The purpose of this project is to prolong the longevity and improve the performance of coating systems on steels which are exposed to offshore environments. As painting is essentially the application of organic molecules onto a steel surface, chemically-rationalised solutions are essential to its improvement. In this project, abrasive blasted steel surfaces are characterised. The adsorption of different chemical functionalities are assessed by providing quantitative adsorption data, as coating adhesion promotors and/or corrosion inhibitors.

Simulated marine corrosion of steel surfaces, a proxy to offshore environment, in repainting-relevant timescales is conducted to observe any significant surface chemical changes that may affect paint adsorption. Inorganic ion adsorption at the paint-steel interface is to be characterised, in case of its influence in the rate of water ingress at the interface.

The potential root causes of the onset of marine corrosion underneath painted layers in an offshore environment are to be investigated in this project, to discover potential improvements in chemical anti-corrosion solutions.

3.2 Surfaces

This section outlines differences between surface and bulk atoms of the same material. This has implications for adsorption and chemical functionalities used to promote coatings adhesion and corrosion inhibition. Initially a metal crystalline surface is considered as a relatively simple system to introduce surface chemistry.

Significant property differences exist between surface layers and the bulk material, including electronic,[1] crystallographical,[2] and chemical[3,4]. Newly created surfaces expose many atoms in their original bulk crystallographic

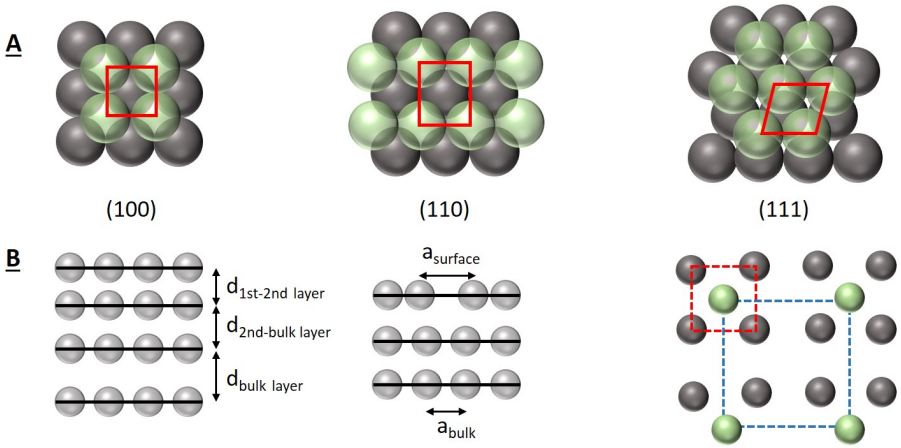

Fig. 3.1: Example cartoons of a selected sample of face-centred cubic (FCC) crystal structures and surface stabilisation effects. Surface atoms are in green, bulk atoms in grey. A: Selected range of crystal structures of different Miller indices. B: Mechanisms of surface energy minimisation. Left to right: Relaxation, Reconstruction, and reconstructed surface with fewer interfacial atoms exposed.

arrangements,[5] but with fewer bonding neighbours (coordination number). With fewer neighbours to bond with, these surface atoms have a higher energy when compared with their bulk counterparts. In Figure 3.1A, a range of common face-centred cubic (FCC) crystal faces common in iron oxides are displayed.[6,7] The green surface atoms demonstrate the fall of coordination numbers compared to those in the bulk in black, from 12 to 8 in (100), from 12 to 7 in (110), and from 12 to 9 in (111). The energetic difference due to this coordination number change, as well as material number density, is reflected in the surface energy, γ. The higher the coordination number change between the surface and bulk atoms in a crystal structure, the higher the surface energy.

A variety of behaviour is observed to minimise the higher surface energy illustrated in Figure 3.1B. These include the strengthening of existing coordination bonds leading to surface layer structural 'relaxations' distortions, resulting in the propagation of some atoms into the bulk. The surface/near-surface atomic layers are drawn towards the bulk, with the reduction of near-surface layers distances to each other. 'Reconstruction' rearrangements are also observed involving the changing of the local crystal structure, of surface atoms. The decrease in the number of atoms exposed at the interface thus lowers the surface energy.[8] High energy uncoordinated sites can also lead to

the reaction of interfacial atoms with external species. Many metal surfaces readily form surface oxide and/or hydroxide layers when exposed to atmospheric oxygen and water.[9] Native surface layer of iron oxides is found to form on a new S355 steel surface,[10,11] a carbon steel used in offshore strucutres. The detailed characterisation of surface chemistry is therefore important to improving adsorption of coating molecules.

3.3 The Solid-Liquid Interface

The interaction of such surfaces with other matter such as the solid-liquid interface, can greatly influence chemical behaviour. Sometimes single molecular adsorbed layers can dominate the surface chemistry. Many modifications are done through 'dosing' the surface with a liquid solution,[12] forming monolayer or multilayer coverage on the surface. These layers have minute chemical signatures in comparison to the bulk, making for difficult analysis. Therefore techniques sensitive to the surface chemical environments are needed. This thesis employs a wide range of state-of-the-art techniques to determine surface behaviour.

3.3.1 Surface Charge and the Double Layer

This work includes the exposure of steel and minerals to aqueous solution, the surface double layer and ion adsorption/complexation that occurs is now outlined.

When a solid surface is exposed to a liquid, a number of reactions can occur. They include proton exchange (acid-base reactions depending on the surface chemical group), cations and anions can bind, sometimes through ligand exchange or complexation at surface sites. These processes sometimes lead to proton loss/gain. A net surface charge develops leading to the formation of an electrical double layer (EDL), as shown in Figure 3.2.[13] The layer closest to the solid substrate is known as the Inner Helmholtz Plane (IHP) and is considered to comprise charged groups chemically bonded on the surface including unsolvated ions. The second layer is the Outer Helmholtz Plane (OHP) and is often considered as a plane of solvated ions. The combination of the two planes forms the Stern layer.

Random thermal diffusional motion of ions in solution is introduced forming a diffuse layer (Gouy-Chapman model). This layer lengthscale is set by the Debye length, dependent upon solution properties such as ionic strength (Equation 3.1). The shortcoming of this model assumes ions to be point

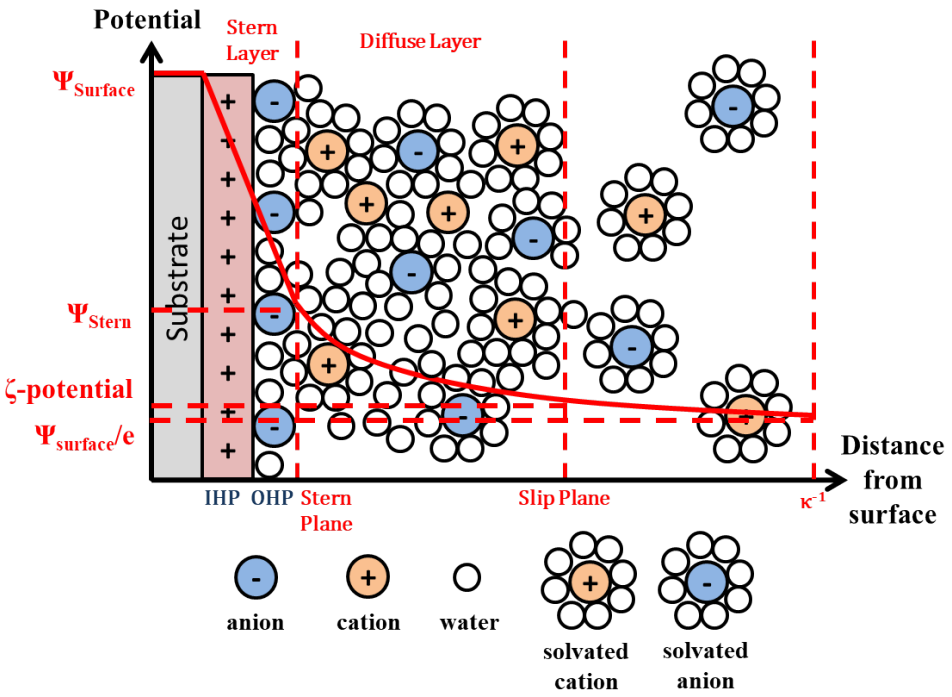

Fig. 3.2: Schematic diagram of the Stern model of the electrical double layer, of a positively charged surface.

charges where charge density on the solid surface becomes unfeasibly high. Hence Stern combined the compact Helmholtz ion packing with the diffuse model. While these bound ion planes take into account the physical dimensions of the ions, they are insufficient for the neutralisation of net surface charge. Hence the remainder of this coulombic charge is counterbalanced by a diffuse layer extending into the solution (Gouy layer).[14] This charging generates a potential, ψ_0, at the interface.

$$\kappa^{-1} = \sqrt{\frac{kT\epsilon_r\epsilon_0}{2e^2I}} \tag{3.1}$$

$$I = \frac{1}{2}\sum a_i z_i^2 \tag{3.2}$$

$$\sigma = \sqrt{8c_0\epsilon_r\epsilon_0 RT}\sinh(\frac{z\psi_0 F}{2RT}) \tag{3.3}$$

$$\sigma = \frac{\epsilon_r\epsilon_0\psi_0}{\kappa^{-1}} \tag{3.4}$$

Eqation 3.1 contains k as the Boltzmann constant, T the absolute temperature in Kelvin. ϵ_r the dielectric constant of the liquid medium and ϵ_0 the permittivity of free space. I is the ionic strength of the solution expressed in Equation 3.2 where a_i and z_i are respectively the activity and valency of species i in solution. The thermodynamic aspects of electrolyte non-ideality are addressed most notably by Debye-Hückel theory.[15] At low ionic concentrations, the solution behaviour tends towards ideality and activity can be approximated by concentration, c_i. Potential at the surface, ψ_0 falls linearly within the Stern plane then decreases exponentially in the diffuse layer beyond.[16] The boundary between the fluid attached to the surface from the mobile fluid is known as the 'slip plane'. The potential at this plane is called the ζ-potential. The lengthscale of this potential is the Debye length κ^{-1}.

Equation 3.1 demonstrates Debye length as inversely proportional to the ionic strength of the solution, and represents the decrease of surface potential with respect to distance from surface. In high ionic strength systems, charged species may approach the surface without significant electrostatic attraction/repulsion. The relationship between the surface charge density, σ, and surface potential is expressed in the Grahame equation, for a symmetrical electrolyte with valency z in Eq.3.3,[17] c_0 the electrolyte number density/solution concentration (in mol m^{-3} or mol dm^{-3}), R the molar gas constant, and F the Faraday constant. At low surface potentials, Equation 3.3 is linearised into Eq.3.4. The surface charge density is therefore linked to the ionic strength of the solution, which impacts on ion adsorption through electrostatic attraction/repulsion.

3.3.2 Adsorption

A variety of different surface complexation models have been proposed to explain ion adsorption:[18–20] including standard EDL theory, the constant-capacitance model,[21] and other complex models involving further interfacial ion layers.[22–24] All surface complexation models are based in four fundamental concepts. First, all adsorption on oxides happen at specific coordination sites of particular surface groups. Second, mass action law equations describe chemical dynamic equilibrium quantitatively explain the adsorption reactions on these sites, with total mass conserved. Third, adsorption reactions lead to surface charges. Fourth, surface charge effects on adsorption can be included by the applying a surface potential-dependent coulombic correction factor, derived from EDL theory and applied in addition to mass law equilibrium constants. From these conditions spring a large selection of numerical simulation techniques for complexation reactions at the steel iron oxide-water

interface.

Surface Protonation

$$\equiv \mathrm{XOH_2}^+ \rightleftharpoons \equiv \mathrm{XOH}^0 + \mathrm{H}^+ \qquad K_{a1}^{app} = \frac{[\equiv \mathrm{XOH}^0][\mathrm{H}^+]}{[\equiv \mathrm{XOH_2}^+]} \tag{3.5}$$

$$\equiv \mathrm{XOH}^0 \rightleftharpoons \equiv \mathrm{XO}^- + \mathrm{H}^+ \qquad K_{a2}^{app} = \frac{[\equiv \mathrm{XO}^-][\mathrm{H}^+]}{[\equiv \mathrm{XOH}^0]} \tag{3.6}$$

$$\Delta G_{tot}^0 = \Delta G_{int}^0 + \Delta G_{coul}^0 = \Delta G_{int}^0 + \Delta z F \psi_0 \tag{3.7}$$

$$K^{int} = K^{app} \exp(\Delta z F \psi_0 / RT) \tag{3.8}$$

Solid-water interfaces are often charged due to the amphoteric nature of many oxide surfaces. Equations 3.5 and 3.6 describe 'protonation/deprotonation steps' of a surface site, signified by $\equiv \mathrm{XOH_n}^{n-1}$. [≡...] and [...] respectively represent the surface concentrations and solution activities of a species. K_{a1}^{app} and K_{a2}^{app} are the *apparent* equilibrium constants of reactions influenced by the coulombic factor. This can be better understood thermodynamically in terms of total free energy of adsorption, ΔG_{tot}^0 described by Equation 3.7. The adsorption free energy comprises two components, the *'intrinsic'* term (ΔG_{int}^0) and coulombic term (ΔG_{coul}^0). Δz is the surface species charge change in the adsorption reaction. The free energy terms can be re-expressed into intrinsic equilibrium constants (Equation 3.8), without coulombic charge effects. The exponent is referred to as an coulombic correction factor, an activity coefficient for the long-range electrostatic effects of charged surface species.

Figure 3.3 shows iron oxide surface charge responses under different pH and ionic strength conditions. The x-intercept pH, which there is no net surface charge, is called the Point of Zero Charge (PZC). Above it the surface is negatively charged and below the surface is positively charged. Qualitatively a negatively charged oxide surface electrostatically attracts cations, hence its adsorption more favourable at high pH.[25] The coulombic correction factor allows quantitative reflection of this charge-influenced adsorption in complexation calculations.

Ion Binding

$$\equiv \mathrm{XOH}^0 + \mathrm{A}^{2-} + \mathrm{H}^+ \rightleftharpoons \equiv \mathrm{XA}^- + \mathrm{H_2O} \tag{3.9}$$

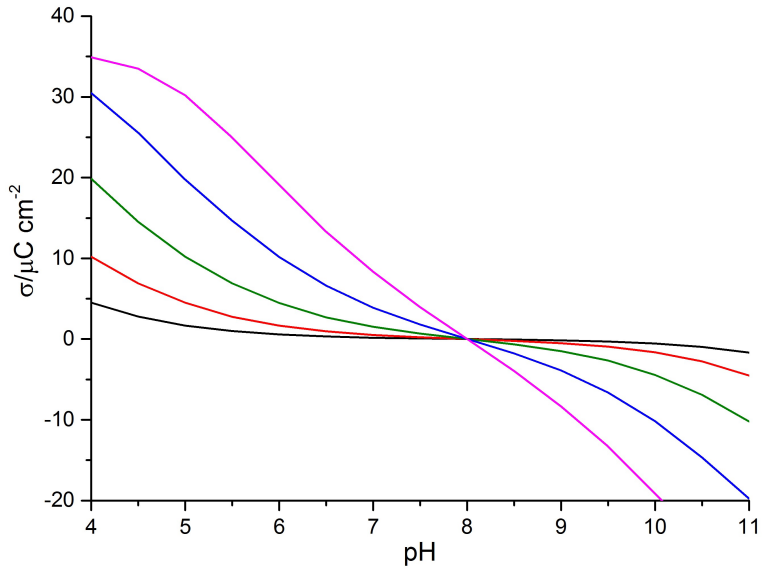

Fig. 3.3: Relationship between pH and surface charge under various ionic strengths of a 1:1 electrolyte for an hydrous ferric oxide, derived numerically using Eq. 3.3 and 3.13. Black: 0.1 mM, Red: 1 mM, Green: 10 mM, Blue: 100mM, Magenta: 1000 mM ionic strength.

$$K_{1\mathrm{A}}^{app} = \frac{[\equiv \mathrm{XA}^{2-}]}{[\equiv \mathrm{XOH}^{0}][\mathrm{A}^{2-}][\mathrm{H}^{+}]} \tag{3.10}$$

$$\equiv \mathrm{XOH}^{0} + \mathrm{M}^{2+} \rightleftharpoons \equiv \mathrm{XOM}^{+} + \mathrm{H}^{+} \tag{3.11}$$

$$K_{\mathrm{M}}^{app} = \frac{[\equiv \mathrm{XOM}^{+}][\mathrm{H}^{+}]}{[\equiv \mathrm{XOH}^{0}][\mathrm{M}^{2+}]} \tag{3.12}$$

$$\sigma = \frac{F}{AS}[[\equiv \mathrm{XOH_2}^{+}] - [\equiv \mathrm{XO}^{-}] + [\equiv \mathrm{XOM}^{+}] - 2\,[\equiv \mathrm{XA}^{2-}] + [...] \tag{3.13}$$

Adsorption of various anions and cations onto surface sites are considered similarly as surface acidity, example reactions are shown in Equations 3.9 and 3.11, with respective apparent adsorption constants. Multivalent ions often have multiple modes of interaction and equilibrium constants. The resultant site charge form part of the surface charge and EDL. The contributions to the surface charge, σ, is outlined by Equation 3.13, where A is the specific area and S mass concentration of the sorbent. Adsorbate-to-adsorbant ratios can

particularly influence surface complexation behaviour to be outlined in a later Chapter 10. Combination of mass law, mass conservation and surface charge equations allow for adsorption calculations. Save for very simple systems, the large number of chemical species often require numerical calculations, through software like Visual MINTEQ used in this work.

4. THEORETICAL BASES OF EXPERIMENTAL TECHNIQUES

4.1 Surface Titration

Surface titrations identify surface group chemistry, site density, and point of zero charge (PZC) on sparingly soluble mineral oxides,[26] nanoparticles,[27] and bacteria.[28] Acid-base titrations operate by adding/removing protons from surface groups by respectively adding acid/base/electrolytes into an aqueous suspension containing the surface, often in powdered form to maximise the surface-to-volume ratio. Aqueous proton/hydroxyl ion are considered to be 'potential determining ions' (PDIs) The method characterises the 'acidity' (pK_a, equilibrium acid constants) and charge on the surface, with or without the influence of other PDIs and organic adsorbates.

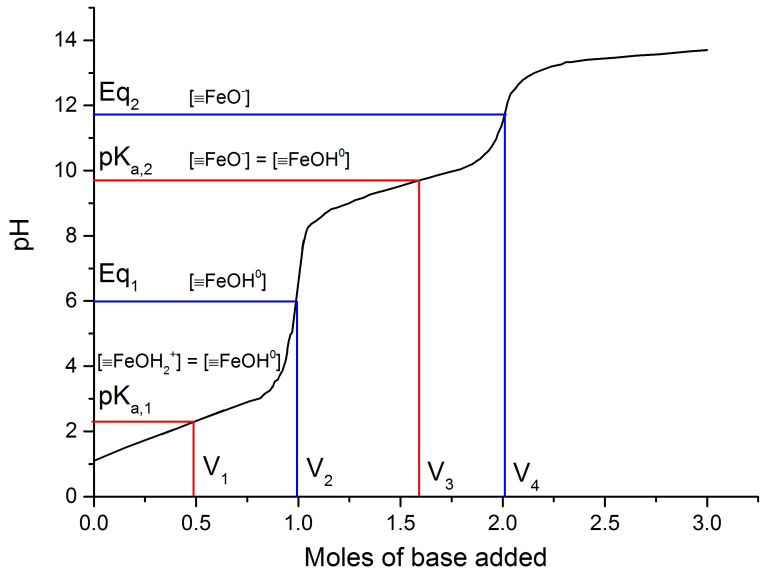

Fig. 4.1: Example curve of an acid-base titrated iron oxide surface, as a 'diprotic acid', with notable features labelled.

The analytical process of titration can be separated into four discrete steps.[29]

First the pH measurement of the suspension aqueous solution. Second is the surface titration that determines the titration kinetics. This can be probed through different titration speeds, with or without background electrolyte.[30] Third, from the pH values and known volume of titrant, the proton concentration are calculated. Fourth is the conversion of proton consumption/response into surface charge. In most cases, a non-adsorbing indifferent electrolytes are used to keep the ionic strength of the solution practically constant as it affects surface charge responses (Figure 3.3).

$$pH = pK_a + \log\frac{[\equiv \mathrm{XOH_n}^{n-1}]}{[\mathrm{XOH_{n+1}}^{n}]} \tag{4.1}$$

Surface hydroxyl groups are often considered as 'diprotic acids', functionalities that can be deprotonated, as well as protonated, as previously shown in Equations 3.5 and 3.6. The two equilibrium acid constants (K_{a1}, K_{a2}) can be calculated. An example of a titration is shown in Figure 4.1, of an iron oxide. Inflection points in the figure at base titrant volumes V_1 and V_3 are where the protonated and deprotonated surface groups are of equal concentration. One can rearrange acid constants equations into Equation 4.1. Concentrations of the two surface species at the inflection points cancel, with pH equivalent to the acid constant pK_a.

$$V = V_4 - V_2 \tag{4.2}$$

$$n_S = \frac{VC_t}{SA} \tag{4.3}$$

For a single surface group, the group density can be estimated using equivalence points (e.g. base titrant volumes V_2 and V_4 in Figure 4.1), the amount of titrant added that is sufficient to completely neutralise one particular species on the surface.[31] The titrant volume difference at equivalence points (Equation 4.2) of known concentration C_t, solid specific surface area A, suspension solid concentration S can be used to calculate the surface site density, n_S, of a particular group using Equation 4.3.

Surface titrations allow for the calculation of surface charge. In an indifferent electrolyte aqueous solution, only the deprotonated ($\equiv \mathrm{XOH_2}^{+}$) and protonated groups ($\equiv \mathrm{XO}^{-}$) determine the surface charge. Calculations are listed in Equations 4.4 to 4.10. In the formulae, c_A and c_B are the molar concentrations of titrant acid or base. F, A, S, and σ are all defined above

in Chapter 3. [Y] represents the concentration of unknown constituents that can react with protons and hydroxyl ions. This comparison between sample and blank titrations ensures impurities or any unknown surface moieties on the experimental apparatusare taken into account.[32]

$$(c_A - c_B)_{susp} = \mathrm{TOTH}_{susp} \tag{4.4}$$
$$= [\mathrm{H^+}] - [\mathrm{OH^-}] + [\equiv \mathrm{XOH_2^+}] - [\equiv \mathrm{XO^-}] + [\mathrm{Y}] \tag{4.5}$$

$$(c_A - c_B)_{blank} = \mathrm{TOTH}_{blank} \tag{4.6}$$
$$= [\mathrm{H^+}] - [\mathrm{OH^-}] + [\mathrm{Y}] \tag{4.7}$$

$$\Delta(c_A - c_B) = \mathrm{TOTH}_{susp} - \mathrm{TOTH}_{blank} \tag{4.8}$$
$$= [\equiv \mathrm{XOH_2^+}] - [\equiv \mathrm{XO^-}] \tag{4.9}$$

$$\sigma = (\frac{F}{AS})\Delta(c_A - c_B) \tag{4.10}$$

For titrations in an indifferent electrolyte, the pH of null surface charge corresponds to the 'pristine' point of zero charge (PZC), the point of common intersection between surface charge titration curves, under different ionic strengths.[33] It should also correspond to the average between the two surface intrinsic equilibrium acid constants (assuming both originate from the same functionalities and reacts in equal measure for both pK_a) seen in Equation 4.11. 'Intrinsic' constants are previously defined in Equation 3.8.

$$pH_{PZC} = \frac{1}{2}[pK_{a1}^{int} + pK_{a2}^{int}] \tag{4.11}$$

4.1.1 Experimental

All surface titrations pH measurements in this thesis were measured using a Unitrode Pt100 probe attached to a Metrohm 809 Titrando. All titrants (salt, acid, base) were 0.1 M in concentration and were dosed at a rate of 0.6 mL $\mathrm{min^{-1}}$. Acid/base or salts solutions were supplied by Sigma Aldrich. The suspension was titrated under stirring through a magnetic bean stirrer. All titration were done at the BP Institute, University of Cambridge.

4.2 Zeta-Potential Measurements

Zeta-potential, or ζ-potential, is the electrical potential at the slip plane of a surface of a particle/interface. The experimental determination is through electrophoresis, the motion of dispersed particles relative to the suspending medium under a spatially uniform electric field.[34]

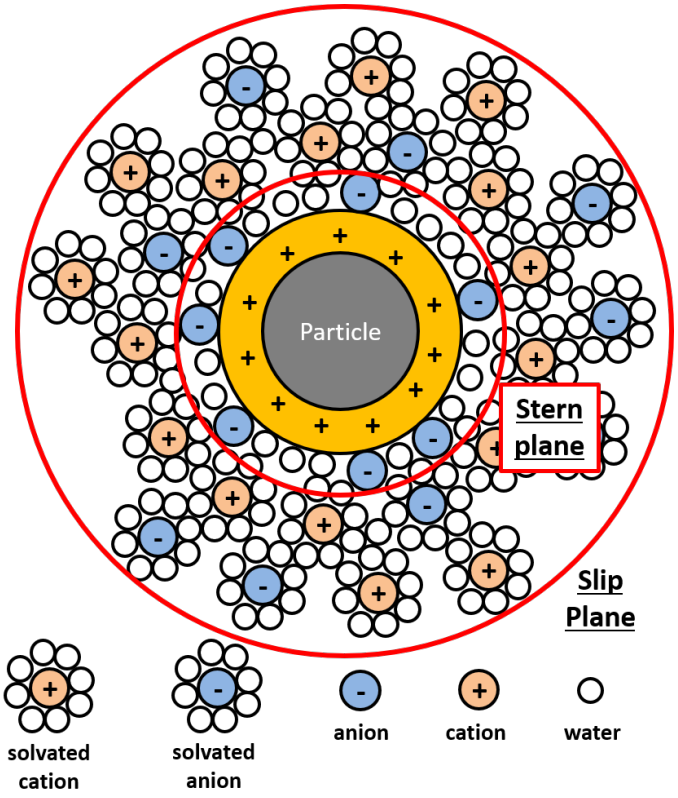

Fig. 4.2: Cartoon showing the double layer structure of a positively charged surface, with the locations of the Stern plane (encapsulating the Stern layer) and the slip plane (encapsulating both Stern and Diffuse layers) relative to the particle surface.

$$\zeta = \frac{\eta \mu_E}{\epsilon_0 \epsilon_r} \tag{4.12}$$

$$\mu_E = \frac{v_d}{E} \tag{4.13}$$

This electrokinetic experiment is governed by the Smoluchowski equation shown in Equation 4.12.[35] The ζ-potential is determined by the fluid viscosity

η, the particle electrophoretic mobility μ_E, the vacuum permittivity ϵ_0, and the dielectric constant of the liquid medium ϵ_r. The mobility is defined by the drift velocity v_d (particle rate of migration), divided by the electric field E, in Equation 4.13.

Mobility of the particles under an electric field is monitored through dynamic light scattering (DLS). The method measures differences of incoming light scattering by the particles under the uniform electric field. Changes in the measured intensity over time are analysed through an auto-correlation function (ACF). In the time domain, the ACF exponential decay (decorrelation) speed is dependent on the diffusion rate. Smaller particles have faster mobility, leading to faster ACF exponential decay, whereas it is vice versa for larger particles.[36] ACF analysis leads to determination of particle size distribution.

4.2.1 Experimental

All zeta/ζ-potential measurements were obtained using a Brookhaven Instrument ZetaPlus Zeta Potential Analyser. Suspension concentrations of 1 mg mL^{-1} or lower were used. Solution were contained in a plastic cuvette with 10 mm optical pathlength. The pH of the suspensions were tracked using high precision pH indicator paper with 0.2 or 0.3 pH value measurement increments, made by either Fluka or Waterman.

4.3 Solution Depletion Isotherms

Solution depletion isotherms are useful to determine important kinetic and thermodynamic properties of an adsorbate-adsorbant system. Interpreting isotherm data is useful in extracting physical quantities, to explain the interactions within such systems.

4.3.1 Henry Isotherm

The Henry isotherm assumes a linear relationship between adsorption surface coverage, θ, and equilibrium concentration of adsorbate in solution, c. They are correlated by an equilibrium constant, K_H, as shown in Equation 4.14. Surface coverage θ is the fraction of occupied sites/adsorption from the total number of surface sites or maximum adsorption, where q is amount adsorbed and Q the maximum amount adsorbed. The adsorption equilibrium constant, K in general, is the ratio between rate constants of adsorption against desorption in a kinetic-derivation, where k_{ads} and k_{des} are respectively rate constants for adsorption and desorption in Equation 4.16.

$$\theta = K_H c \tag{4.14}$$

$$\theta = q/Q \tag{4.15}$$

$$K = \frac{k_{ads}}{k_{des}} \tag{4.16}$$

Henry isotherm behaviour is typical of many adsorption isotherms in the low surface coverage regime. Sparse distribution makes lateral interactions between adsorbates unlikely or negligible.[37]

4.3.2 Langmuir Isotherm

Langmuir isotherm is underpinned by a number of assumptions. Firstly adsorption on an adsorbant is limited to a single monolayer ($0 \leq \theta \leq 1$). Secondly all adsorbant surface sites are energetically equivalent (i.e. no defects, terraces etc.) Thirdly, the enthalpy of adsorption remains constant irrespective of the amount adsorbed. In other words, there are no lateral interactions between adsorbates and other sites in close proximity.[38]

In the low concentration regime, there is initial fast increase of adsorption q with adsorbate concentration, c, following a Henry isotherm. With further concentration increase, adsorption reaches a plateau and achieves 'complete' monolayer adsorption Q. The behaviour is related through an equilibrium adsorption constant of K_L, as expressed in Equation 4.17.

$$q = \frac{QK_{ads}c}{1 + K_{ads}c} \tag{4.17}$$

$$\frac{c}{q} = \frac{1}{K_L Q} + \frac{c}{Q} \tag{4.18}$$

To effectively extract the adsorption constant and monolayer adsorption, one can linearise Equation 4.17 into Equation 4.18. Adsorbate equilibrium concentration in solution, c, is plotted against ratio between solution concentration and adsorption, $\frac{c}{q}$. With the appropriate data-point weighting, the line gradient gives us $\frac{1}{Q}$ and the y-intercept $\frac{1}{K_L Q}$.

4.3.3 Freundlich Isotherm

The Freundlich isotherm empirically relates the adsorption and equilibrium concentration. Adsorption behaviour is described by Equation 4.19, like the Henry isotherm with an extra interaction parameter of n, encapsulating the lateral interactions between adsorbates.

$$q = QK_F c^{\frac{1}{n}} \tag{4.19}$$

Non-linear empirical data fitting has to be employed. This isotherm is commonly used for heterogenous surfaces.[39]

4.3.4 Brunauer-Emmett-Teller (BET) Isotherm

The Brunauer-Emmett-Turner (BET) isotherm has similar characteristics to a Langmuir isotherm, differing in that it allows for the formation of multilayers of adsorbate.[40]

There are a few assumptions: firstly adsorbate can physically adsorb infinitely. Secondly interactions between each adsorbed layer is permitted. Thirdly the adsorption for each layer is Langmuirian. Adsorption occur at surface sites, one site adsorbs one molecule. The only adsorbate interaction is inter-layer. One lower-layer molecule acts as a one adsorption site for another in the upper-layer. The uppermost adsorbate layer is in dynamic equilibrium with the gas/liquid phase. Desorption is a kinetically-controlled process, with the enthalpy of adsorption same across the uppermost layer and inner-layers treated as a condensed phase. At saturation pressure/concentrations, P_0, the number of layers tends to infinity.[41]

BET adsorption isotherms of gas molecules are used to assess the surface area of powdered samples, including in this work for adsorbant powders. Nitrogen gas is often used as an adsorbate due to its well-defined molecular surface area of 16.2 $Å^2$.[42,43] For such a gas-solid system, the adsorption behaviour is described in Equation 4.20. P and P_0 are respecitvely the adsorbate equilibrium and saturation pressures. v and v_m are the adsorbate equilibrium and monolayer volume. K_B is the BET equilibrium adsorption constant.

$$\frac{P}{vP_0 - P} = \frac{1}{v_m K_B} + \frac{K_B - 1}{QK_B}\frac{P}{P_0} \tag{4.20}$$

BET-type isotherm can also used in rationalising liquid-solid phase adsorp-

tions but it is not employed in this work.

4.3.5 Other Models & The Liquid Phase

The list of models above is by no means exhaustive. Many modifications have been done, especially to the Langmuir isotherm due to its simplicity, to better rationalise adsorption data: Temkin,[44] Frumkin isotherms[45], are examples of including lateral interactions in their models. In this work, the Langmuir-type model often suffices and any further theoretical interpretations are outlined in detail. Note that these models describe adsorption by a singular species in gaseous phase. For solid-liquid systems seen in this work, factors such as possible competitive adsorption (vs. solvent, other components) may need to be considered for adequate rationalisation of adsorption data.

4.3.6 Experimental Procuedures

The basic procedure of the isotherm experiment is shown in Figure 4.3. High surface area-to-volume powders are exposed to an adequate, but preferably minimal volume of solution with different adsorbate concentrations. Low liquid volume lowers the experimental error in the amount adsorbed. The samples are then tumbled to allow equilibration. The adsorbent powder is then separated, often through centrifugation, from the liquid supernatant. Adsorbate equilibrium concentration is then measured through different analytical methods (UV-Visible, Infrared, NMR spectroscopies in this work), depending on the chemical nature of the species.

The change in adsorbate concentration in solution is attributed to amount adsorbed, and can be calculated through Equation 4.21. c_i and c_f are respectively the input and final analyte concentration. V is the total volume of the liquid during equilibration. A is the specific area of the solid substrate (i.e. S355 powder) and S is the equilibrated suspension solid concentration. q is the adsorption of the adsorbate per unit area.

$$q = \frac{(c_i - c_f)V}{AS} \tag{4.21}$$

For solution isotherms adsorption measurements are always expressed as the amount of adsorbate adsorbed relative to that of the solvent or any other components in the solution. Competitive adsorption of solvents and other species is possible, leading to seemingly 'negative' adsorption results.[46] In

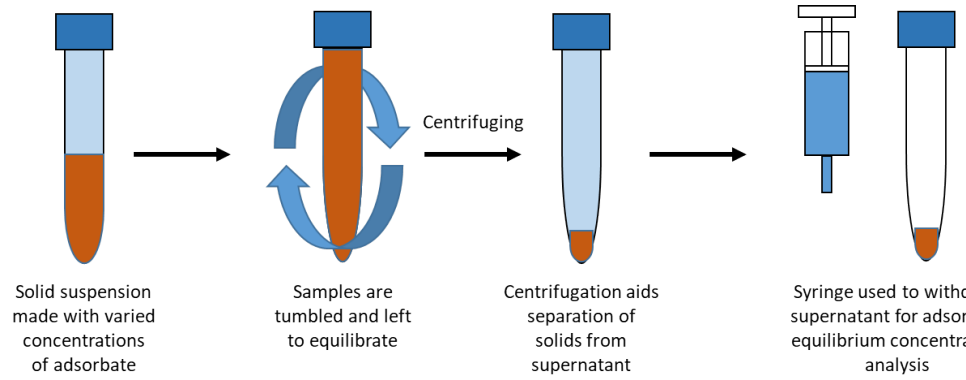

Fig. 4.3: Schematic outlining the experimental procedures of a solution depletion isotherm.

this work, solvents with weak interactions with the surface are used so no such complications are expected.

Fourier Transform-Infrared Spectrscopy (FT-IR)

Transmission infrared spectroscopy was conducted with a Perkin Elmer Spectrum 100 FTIR Spectrometer. Samples were analysed using a liquid cell, through caesium chloride windows with a 2 mm polytetrafluoroethylene spacer.

Quantitative Nuclear Magnetic Resonance Spectrometry (qNMR)

Quantitative Nuclear Magnetic Resonance Spectrometry (qNMR) was conducted with a Bruker Avance III HD 500 MHz Smart Probe Spectrometer, at the Department of Chemistry, University of Cambridge. ^{1}H NMR spectra was taken and dodecane solvent supression processing was undertaken before further quantitative analysis of the analyte of interest.

4.4 Scanning Electron Microscopy and Energy Dispersive X-Ray Spectroscopy (SEM-EDX)

The topography and surface features of steel and its corrosion products, should there be any, are often not visible to the naked eye. This is especially true for corrosion features that are generated at short corrosion timescales.[47]

In scanning electron microscopy (SEM), the sampled surface is exposed to a focused beam of high energy primary electrons produced by a set-up illustrated in Figure 4.4.[48] The beam is used to scan across the sample surface

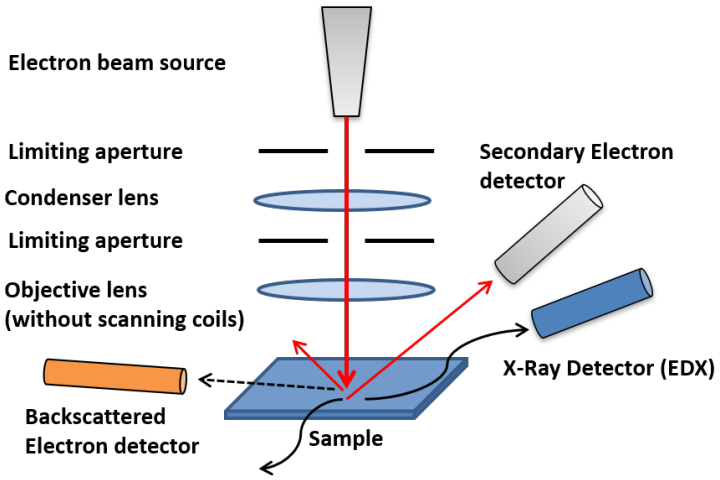

Fig. 4.4: Schematic diagram of a scanning electron microscopy/backscattered electron-energy dispersive X-ray spectroscopy (SEM/BSE-EDX) set-up.

to produce a two-dimensional image of the substrate by detecting the resultant electrons from sample. The variation of number of secondary electrons (SE), emitted from the surface generated by primary beam ionisation of sampled atom electrons, reflects the topography. Ionisation of electrons through secondary electron emission leads to radiation of characteristic X-rays and is diagnostic of each element, leading to elemental identification through energy dispersive x-ray spectroscopy (EDX).

Figure 4.5 shows the interaction between the sample substrate with the incident primary electron beam, demonstrating the different 'interaction volume' each emitted-type of electron has. Figure 4.5 shows characteristic X-rays for EDX have significant interaction volumes in the sample, limiting the technique's 'surface sensitivity'. While EDX serves as a readily available elemental-analysis tool, more stringent requirements for surface sensitivity would usually need other techniques.

Backscattered electrons (BSE) are reflected or backscattered out from the sample through elastic interactions with sample atoms. Higher atomic number elements backscatter electrons more than lighter elements owing to their higher number of atomic electrons. Therefore sample areas with heavier elements would appear brighter on the image. This behaviour makes BSE ideal for providing better elemental contrast, while SE is good for topographical surveying.

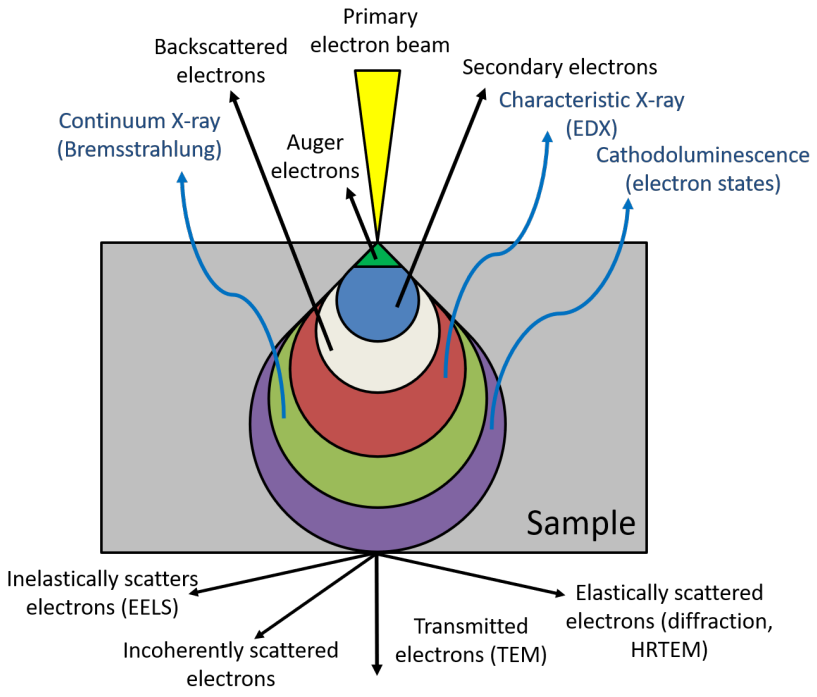

Fig. 4.5: Schematic diagram of the interaction between a primary electron beam with a sample substrate. Radiation emitted is labelled in blue curly arrows and emitted electrons are in black straight arrows.

4.4.1 Experimental

Untreated steel surfaces were analysed with a JEOL Model JSM 6360LV electron microscope at the Department of Chemistry, University of Cambridge. The acceleration voltage used was typically 20 kV with a working distance of 20 mm unless stated otherwise. The accompanying EDX spectra were taken using an Oxford Inca EDS. Polished and abrasive blasted steels data was collected using a QEMSCAN 650F microscope made by FEI, USA, at the Department of Earth Sciences, University of Cambridge. EDX spectra were collected using a QUANTAX EDS by Bruker.

4.5 Electron Backscatter Diffraction (EBSD)

Backscattered electron diffraction (EBSD), now often coupled with SEM-EDX systems, uses the elastically backscattered electrons that pass through the surface crystals. The crystals are used as diffraction gratings. The resul-

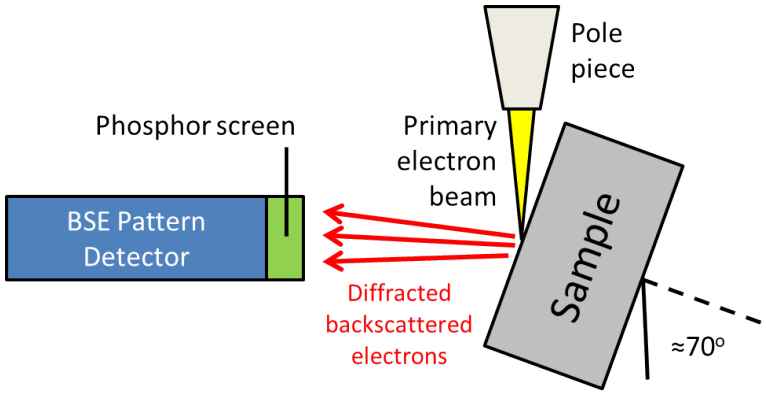

Fig. 4.6: Schematic diagram of a simplified EBSD set-up.

tant interference lines (Kikuchi lines) can be attributed to particular crystallographic Miller indices, and the collection of these lines can be assigned to a particular surface crystal of known elemental composition.[49,50] These backscattered electron diffraction patterns are collected through a phosphr screen, as shown in Figure 4.6. An example spectrum of magnetite shown in Figure 4.7.

The primary use of EBSD is to determine surface microstructural information of a material down to nanometre resolution.[49] In this work, the reactivity of metallic steel prevents the use of other 'direct' chemical surface group characterisation, such as surface titration. Surface crystal identification of iron oxides native to the steel through EBSD can be referenced to well-known surface data from the literature, allowing the inferring of steel surface chemistry.

4.5.1 Experimental

All EBSD analyses were conducted though the QEMSCAN 650F, through a QUANTAX EBSD detector by Bruker at the Department of Earth Sciences, University of Cambridge.

4.6 Transmission Electron Miscrospy (TEM) and Electron Energy Loss Spectroscopy (EELS)

Transmission electron microscopy (TEM) uses electrons transmitted *through* the sample to obtain structural, chemical, crystallographic information. The use of electrons allows formation of high resolution images. The lengthscale of

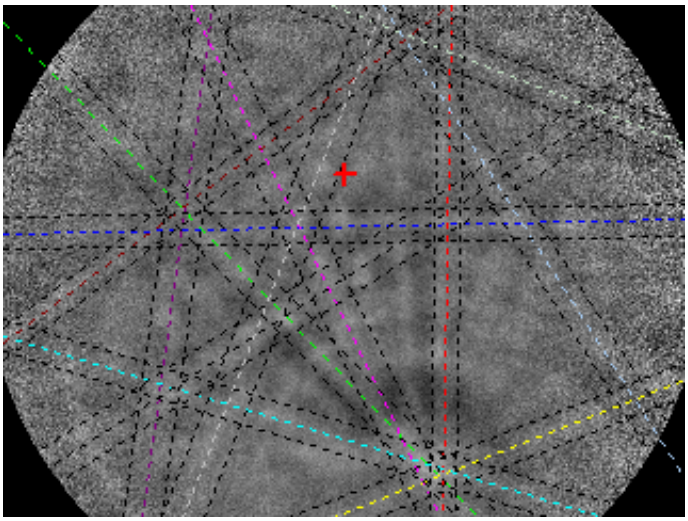

Fig. 4.7: Kikuchi lines of magnetite, with database indexed lines for the mineral superimposed on top.

spatial resolution can be approximated as the same as de Broglie wavelength of the electron expressed in Equation. 4.22. λ is the de Broglie wavelength of the electron. e and m_0 are respectively the electron charge and mass. V is the acceleration voltage by the microscope. h is the Planck constant. The operator can vary the acceleration voltage to achieve different electron wavelengths for better resolution.[51]

$$\lambda = \frac{h}{(2m_e eV)^{1/2}} \tag{4.22}$$

The interaction between the sample and the primary electrons is demonstrated in Figure 4.5. The transmitted/scattered electrons co-linear to the primary beam allows for the imaging of the specimen. Elastically scattered electrons, after interaction with the sample atoms and 'deflected' at a scattering angle, are detected to give diffraction patterns and high-resolution TEM (HRTEM). The elastically scattered electrons can be simplified by thinking them as displaying wave-like behaviour when they constructively and destructively interfere with each other after interacting with the specimen atoms, having respectively in-phase and out-of-phase relationships scattered at different angles. This interference pattern is described by Braggs' law (Equation 4.23) and essentially uses the crystal lattice of the sample as diffraction gratings.[52] λ is the 'wavelength' of the incident electron. n is a positive integer. d is the interplanar spacing. θ_B is the scattering angle. An example diffraction

pattern can be seen in Figure 4.8 of a corroded steel surface. The centre is the transmitted beam, with circular diffraction patterns of crystalline (dots) steel and amorphous (broad rings) iron oxide phases surrounding it.

$$n\lambda = 2d \sin \theta_B \tag{4.23}$$

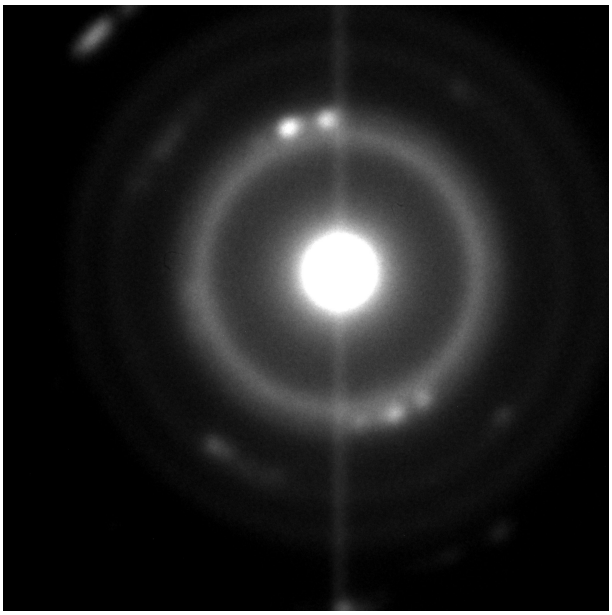

Fig. 4.8: A diffraction pattern generated at the steel-corrosion product interface, where both crystalline ferrite (dots) and amorphous (circular rings) iron oxide phases are both characterised by the electron beam, with the bright 'transmitted' beam at the centre.

Some incident-beam electrons lose energy interacting with the sample, called inelastic scattering. The process can be summarised into three components: X-ray, secondary electron generation, and energy-loss electron scattering through the sample. The generation of characteristic, Bremsstrahlung, and cathodoluminescence X-rays provide chemical information of the specimen atoms. Characteristic X-rays are useful for EDX spectroscopy.[53]

Secondary electrons (SE) are from specimens ionised by primary beam electrons. They are ejected from the conduction or valence band of the sample. If electrons are ejected from core shells by the energy released from an ionised atom returning to its ground state, no X-rays are to be seen and these electrons are called Auger electrons. SEs are of relatively low energy and can

barely escape the sample surface. Hence they are relatively 'surface sensitive' and provide good contrast for specimen topography.

Auger electrons are even more so. Despite difficult interpretation of data, they are sensitive to surface chemical environments especially in lighter elements. Accurate analyses require ultra-high vacuum system which are not common in electron microscopes. Therefore it is infrequently used.

The inelastically scattered primary electron is transmitted through the sample (energy-loss electron). It contains local chemical environment information from its interaction with sampled atoms. This forms the basis of Electron Energy Loss Spectroscopy (EELS) for (scanning-)TEM.

The user may control the beam energy to achieve better resolved images. However with higher primary beam energy comes with increased probability of beam damage and sample heating. Therefore a balance must be struck between beam energy and sample integrity.

4.6.1 Experimental

A sample must be sufficiently thin for TEM analysis so the primary beam electrons can transmit through, at a given primary electron energy and average atomic number of the specimen. Typically a sample of around 100 nm thickness is ideal for imaging alone, while electron spectroscopy and HRTEM require yet thinner samples ($\leq$ 50 nm). Obtaining thin, yet representative samples is a challenge. In some cases a thin slice can be 'thinned' further to become viable for TEM.

The thinning of samples in this work were done *in situ* through a focused ion beam (FIB) of gallium ions (Ga^+) to mill samples. Sample surfaces were commonly coated first with an electron-beam deposited platinum, then a thicker ion-beam deposited platinum layer was used to minimise sample beam damage. A simplified schematic of a FIB set-up is shown in Figure 4.9 Sample electron transparency assessment was done through a JEOL 200 CX microscope, using a tungsten filament with bright- and dark-field imaging, and a diffractor to determine the crystallinity of interfacial corrosion products.

Electron transparent samples were further analysed using a FEI Tecnai Osiris microscope with FEI Super-X for EDX analysis and Gatan Enfinium ER 977 spectrometer for electron energy loss spectroscopy (EELS) at 200 kV

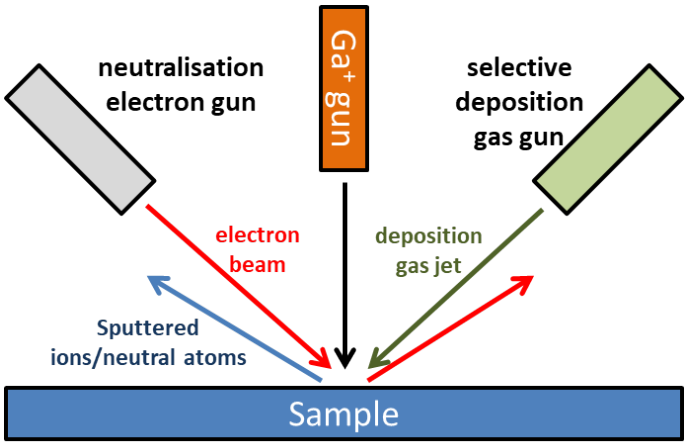

Fig. 4.9: Schematic showing the set-up of a focused ion beam ion-milling and deposition set-up.

acceleration voltage. The beam convergence semi-angle was set to 11.0 mrad and for EELS the collection semi-angle was 15.4 mrad. All TEM work was done at the Department of Materials Science and Metallurgy, University of Cambridge.

The EELS data was analysed through Hyperspy software. Iron (II) and Iron (III) reference spectra were respectively from siderite ($FeCO_3$) and hematite collected within the EELS Data Base.[54,55] These reference spectra were reprocessed to obtain only their lineshape. The spectra backgrounds preceding the iron L_{23} ionisation edge were subtracted and intensities normalised. A single set of universal energy offset and energy scale parameters for both reference line-shapes were fixed, allowing for the relative intensities to be determined by fitting. Therefore the relative energies of the spectra were retained in the experimental raw data fitting and the reference line-shapes was used for iron oxidation state independent component analysis (ICA) to qualitatively disentangle EELS spectrum images for iron (II) and iron (III) oxidation state signals and their spatial distribution.[56] Oxidation state ratio-maps were made through FIJI software, from the National Institute of Health, Bathesda, USA.

4.7 X-ray Photoelectron Spectroscopy (XPS)

X-ray photoelectron spectroscopy (XPS) is used as a surface sensitive technique to extract atomic composition and chemical environment information

from a material. It utilises the photoelectric effect by exciting electrons from the surface material using X-ray radiation, typically from an aluminium (1486.6 eV) or magnesium (1253.6 eV) source. The process is displayed in Figure 4.10. The kinetic energy of photoelectrons is detected. Using Equation 4.24, the binding energy characteristic of the originating environment can be determined, with E_{BE} and E_{KE} being the respective electron binding and kinetic energies, E_{ph} the incident X-ray photon energy, and Φ the 'work function', generally understood to be the energy required for a photoelectron to leave the specimen surface.

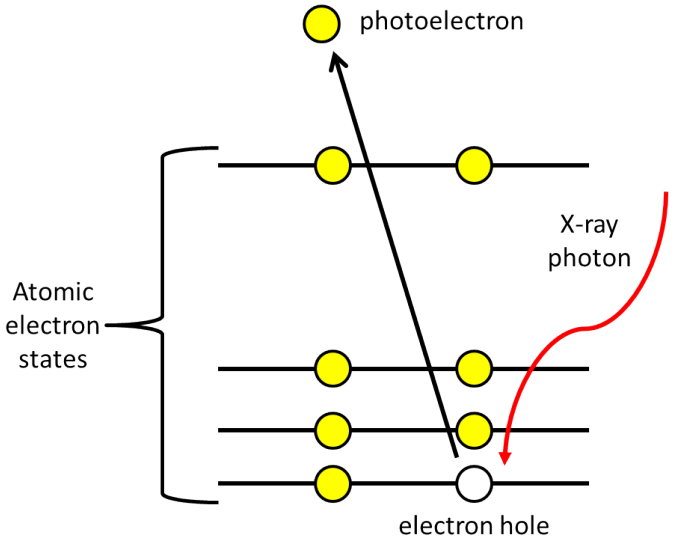

Fig. 4.10: Cartoon demonstrating the photoelectron emission process.

$$E_{BE} = E_{ph} - (E_{KE} + \Phi) \tag{4.24}$$

The binding energy of a photoelectron is dependent on a number of factors. First the element from which the electron is emitted. Second is the orbital from which the electron is ejected. Third is the chemical environment from which the electron is released. Quantitative analysis is accessible due to the photoelectron emission cross-section being independent to chemical environment. The photoemission rate is assumed to be far greater than the rate of electron reorganisation within atoms according to Koopmans' theorem. Therefore the binding energies measured are reflective of the initial state of the surveyed atoms.[57]

The origin (0 eV) of the binding energy scale is referenced with respect to the spectrometer Fermi level for ease of comparison. Different orbitals of the same element have different binding energy levels, resulting in multiple peaks in a spectrum from one single element. At each energy level, multiple peaks may arise corresponding to chemical environments the element possesses. Therefore XPS allows for atomic percentage (peak intensity normalised with respect to total photoelectron intensity) analysis of different elements through taking into account of their relative sensitivity factors (RSF) to incident X-rays,[58] in addition to detailed chemical information upon peak deconvolution.[59]

The inelastic mean free path (IMFP), of the electron is typically limited to around 15 Å($\approx 3\lambda$, λ being the electron wavelength), which is virtually universal across materials.[60,61] Photoelectrons originating from the bulk are generally lost due to this short mean free path. The resultant spectrum is considered to arise only from the surface layers

To further enhance surface sensitivity of XPS, angle resolved XPS (ARXPS) can be used. The set-up is shown in Figure 4.11. Where conventional XPS surveying angle is the surface normal, ARXPS allows the sample stage to be tilted therefore varying the surveying angle, θ. In Figure 4.12, greater tilt angle θ collects photoelectrons from 'shallower' regions of the specimen, enhancing surface contribution to the spectrum. ARXPS detects firstly the surface chemical composition, like XPS. Second it enables relatively simple determination of composition variation for topmost surface layers. Adsorption geometry elucidation is possible when coupled with Density Functional Theory calculations.[62] XPS can be coupled with depth profiling (using sputtering guns) by removing the topmost layers, surveying deeper into the sample.

XPS spectra often have a sloping blackground that increases at higher binding energies relative to the spectrometer, a result of photoelectron energy loss from inelastic collisions as they travel through the sample. Hence they are detected to have lower kinetic energies and calculated to have supposedly higher binding energies. Many background fittings exist.[63] The most commonly seen is the Shirley method that requires the user to estimate a background at the low and higher binding energy ends of the spectrum. This 'step' in intensity difference is smoothened through an iterative approach to form the background.[64,65] Another popular method is the Tougaard approach that considers background from inelastic scattering.[66] In this work the Shirley method is considered suitable. Peaks for which low binding energy

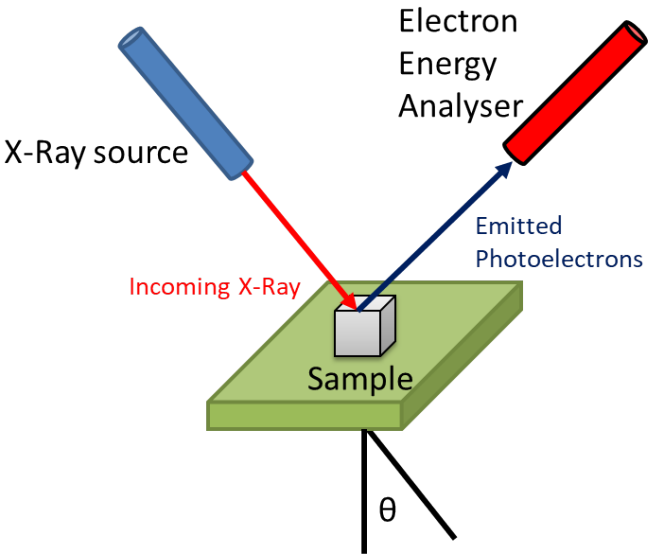

Fig. 4.11: Simplified schematic showing the essential set-up of an XPS experiment.

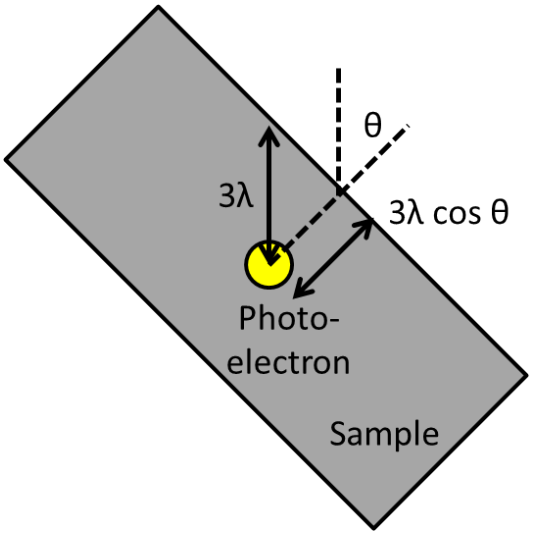

Fig. 4.12: Schematic showing the shallower escape depth for the photoelectron in an ARXPS set-up, increasing the XPS sensitivity.

signals are of higher intensity than that of higher binding energy, a linear background is used.

Photoelectrons excitation from the sample surface may lead to surface potential changes depending on the sample conductivity, particularly for insulating

materials. This effect can lead to changes in peak binding energies. Hence a common reference peak is used by setting the alkyl carbon sub-peak (C−C) in the carbon 1s peak to be 284.8 eV.

In this work, peak fittings have been performed using Gaussian-Lorentzian (70%:30%, also known as a Voigt function) peaks shapes. Peak widths are affected by a variety of factors. First the intrinsic peak width can be affected by spin-orbit coupling and lifetimes of electron holes made by the departure of photoelectrons. Second are effects from the final state, including satellite peak formation and lattice vibrations due to photoelectron excitations. Third are effects of instrument from the quality of the monochromatic X-ray source and the resolution of electron detectors. For metallic samples, an asymmetrical peak is often observed due to excitation of 'free' conduction electrons above the Fermi energy.[67]

Spin-orbit coupling leads to multiplet peak structure.[68] Each chemical environment exhibited by the surveyed element would have such interactions. The intensities of these peaks follow the degeneracy of the overall angular momentum: $2J+1$. J is the overall angular momentum from spin-orbit coupling defined in the series: $J = (L+S), (L+S-1), ..., |L-S|$. L and S are the respective orbital and electronic contributions. The typical value for S is $1/2$ due to XPS exciting only one electron at a time. For example, for an iron 2p orbital there will be spin-orbital splitting giving states of $2p_{3/2}$ and $2p_{1/2}$. Following the degeneracy of these orbitals, the two peaks have a respective intensity ratio of 2:1. This is shown in Figure 4.13, where after background correction the $2p_{3/2}$ peak is twice the size of $2p_{1/2}$. This is likewise true for their respective component peaks labelled with the same colour.

Other features include satellites, low intensity peaks at slightly higher binding energies than the main peak, from a non-purely monochromatic radiation source, and 'shake-up' features due to photoelectron interaction with the ion it is leaving, exciting the electron further. These features include surface plasmon resonance for conductive materials. Multiplet splittings are also known to occur due to unpaired core electrons after photoexcitation interacting with unpaired valence electrons. Therefore multiple final electronic states are possible, represented as a broad peak with multiplet structure.

4.7.1 Experimental

Steel XPS surface analysis was done using a Thermo Scientific K-Alpha X-Ray Photoelectron Spectrometer at the NEXUS XPS service at the Univer-

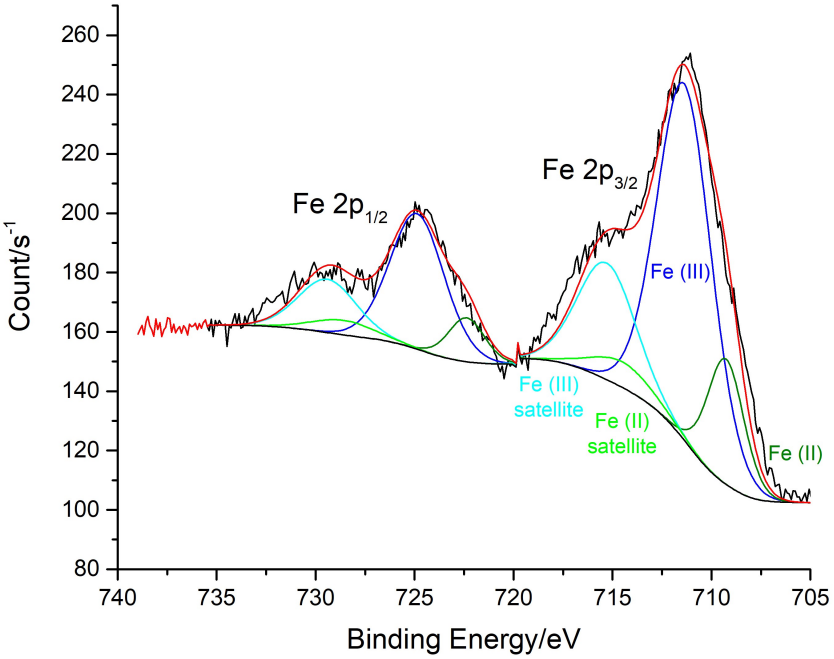

Fig. 4.13: Example spectrum of an iron 2p peak surveyed at 22.5°, of iron $2p_{3/2}$ and $2p_{1/2}$ spin-orbit-coupling splitted peaks on a polished almandine garnet mineral surface.

sity of Newcastle, with a pass energy of 200 eV and energy steps of 0.4 eV. X-ray spot size of 400 μm^2 was used for maximum sample intensity. Any XPS depth profiling was done through a 4 kV monoatomic argon beam, with a rastering size of 1 mm × 2 mm.

Almandine garnet XPS spectra and Angle Resolved XPS (ARXPS) experiments were collected using a Thermo Fisher Scientific ESCALAB 250Xi instrument. A monochromated Al K Alpha 1486.68 eV source was used. Depth profiling etching was done with a 1 kV argon monoatomic ion beam unless stated otherwise. This work was done at the Cavendish Laboratory, University of Cambridge. Spectra collected with surveying angle above 50° were done using a Thermo Theta Probe Mk III spectrometer, using a monochromatic aluminium 1486.68 eV photon source at the Harwell XPS Service, University College London.Charge compensation was provided by a dual mode (argon cation and electron) flood gun. The analysis area was defined by the incident X-ray beam which was micro-focused to 400 μm diameter spot on the sample surface. High resolution core line spectra were collected as follows. An energy step size of 0.1 eV was used. Angle resolved data was

collected in parallel in the range 22.5° to 77.5° from normal, in bin sizes of 5 deg. The analyser was operated in constant analyser energy (CAE) mode with a pass energy of 50 eV. The total acquisition time for each core line was approximately 50 minutes. Survey spectra were collected as above, except that the pass energy was 200 eV and parallel angle resolved data was not collected. The total time to collect a survey spectrum was approximately 5 minutes.

All surveying angles were measured with respect to the surface normal. All spectral data was analysed through CasaXPS software. Binding energy shifts were calibrated by referencing the C−C 1s peak to 284.8 eV.

4.8 Sum Frequency Generation Spectroscopy

Sum frequency generation spectroscopy (SFG) exploits the surface spectroscopic selection rules for coincidental, co-propagating infrared (IR) and visible lasers over the same region at the same time to give surface specificity. The output radiation from the surface is the frequency-sum of the two lasers as depicted in Figure 4.14. SFG spectra are capable of providing information on molecular orientation by analysing peak shapes, and spectral differences under polarisation variations of input and output beams.[69–72] A brief outline is given below.

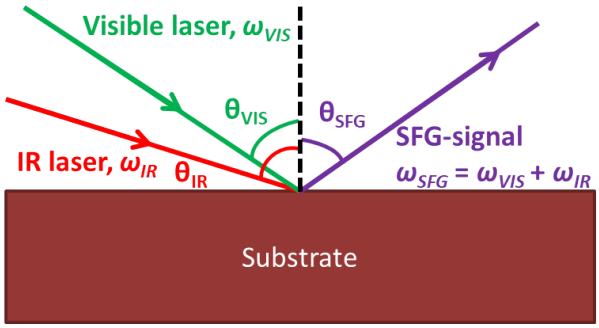

Fig. 4.14: Schematic outlining the SFG technique.

When a light beam travels through a medium, its electric field **E** generates a bulk polarisation **P** that is related by Equation 4.25. $\chi^{(1)}$ is the first-order susceptibility that is the macroscopic average of electron polarisability (α) in bulk. ϵ_0 is the vacuum permittivity. For non-coherent light sources, emitted light frequencies are linearly-dependent on that of incident laser. When the

magnitude of the electric field is high, non-linear effects become significant as shown in Equation 4.26. $\chi^{(n)}$ and $\mathbf{E}^n$ are respectively the susceptibility and laser electric field of the nth-order.

$$\mathbf{P} = \epsilon_0 \chi^{(1)} \mathbf{E} \tag{4.25}$$

$$\mathbf{P} = \epsilon_0 (\chi^{(1)} \mathbf{E} + \chi^{(2)} \mathbf{E}^2 + \chi^{(3)} \mathbf{E}^3 + ...) \tag{4.26}$$

With multiple incident lasers as in SFG are used, multiple surface electric fields are generated. The resultant electron oscillations occur as a combination of the different electric field frequencies as in Equation 4.27, where ω_i is the frequency of the incident beam i, oscillating in time t. Most importantly the non-linear effects for SFG arise from the second-order polarisation term $\mathbf{P}^{(2)}$ shown in Equation 4.28.

$$\mathbf{E} = \mathbf{E}_1 \cos(\omega_1 t) + \mathbf{E}_2 \cos(\omega_2 t) \tag{4.27}$$

$$\begin{aligned}
\mathbf{P}^{(2)} =& \epsilon_0 \chi^{(2)} (\mathbf{E}_1 \cos(\omega_1 t) + \mathbf{E}_2 \cos(\omega_2 t))^2 && (4.28)\\
=& \epsilon_0 \chi^{(2)} (\mathbf{E}_1^2 \cos^2(\omega_1 t) + \mathbf{E}_2^2 \cos^2(\omega_2 t) + 2\mathbf{E}_1 \mathbf{E}_2 \cos(\omega_1 t) \cos(\omega_2 t)) && (4.29)\\
=& \epsilon_0 \chi^{(2)} (... + \mathbf{E}_1 \mathbf{E}_2 \cos((\omega_1 + \omega_2) t) + \mathbf{E}_1 \mathbf{E}_2 \cos((\omega_1 - \omega_2) t)) && (4.30)
\end{aligned}$$

The expansion of Equation 4.28 yield a number of terms relating the fields generated by the two incident lasers. Different techniques exploit these features.[73] The field term relevant to SFG is $\frac{1}{2}\mathbf{E}_1 \mathbf{E}_2 \cos((\omega_1 + \omega_2)t)$. In Figure 4.14, the SFG emitted beam is the sum-frequency of the IR and Visible laser frequencies (ω_i).

Ignoring the time-dependency of the SFG electric field leads to Equation 4.31 where the second-order polarisation is the product of the second-order susceptibility constant $\chi^{(2)}$ and the electric fields from both IR and Visible lasers ($\mathbf{E}_{\mathrm{VIS}}$, $\mathbf{E}_{\mathrm{IR}}$).

$$\mathbf{P}^{(2)}_{\mathrm{SF}} = \epsilon_0 \chi^{(2)} \mathbf{E}_{\mathrm{VIS}} \mathbf{E}_{\mathrm{IR}} \tag{4.31}$$

The second-order susceptibility is very important in providing the selection rules of SFG, leading to its surface specificity. It is a third-rank tensor, a

matrix with 27 components (3^3). It relates the polarisation to the electric field vectors of IR and Visible radiation through Equation 4.32 where i, j, and k refer to the sum-frequency, visible, and IR terms respectively.

$$\mathbf{P}^{(2)}_{\mathrm{SF}} = \epsilon_0 \sum_{i}^{x,y,z} \sum_{j}^{x,y,z} \sum_{k}^{x,y,z} \chi^{(2)}_{ijk} \mathbf{E}_{j,\mathrm{VIS}} \mathbf{E}_{k,\mathrm{IR}} \tag{4.32}$$

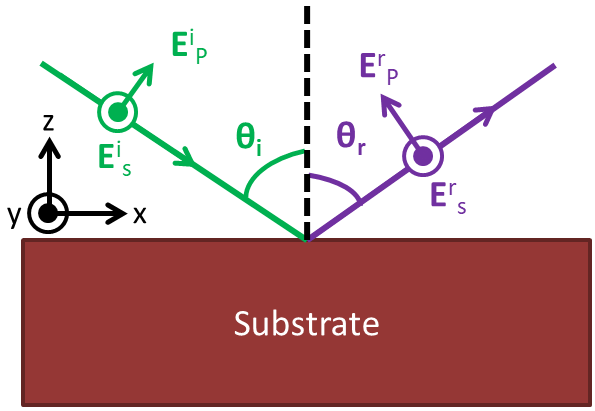

Fig. 4.15: S and P components of incident (i) and reflected (r) light, as viewed in the xz plane. $\mathbf{E}$ is the electric field of each component.

A propagating electromagnetic light ray typically oscillates in more than one direction. It is therefore useful to resolve the electric field vectors in two components perpendicular to each other, particularly for incident light onto a surface. At non-surface normal angles, there is varying extent of how each component is transmitted or reflected. The two orthogonal components are 'S' and 'P' to denote light that are polarised either perpendicular or parallel to the incident plane (i.e. xz plane, with surface normal direction being z), as shown in Figure 4.15. The surface electric field vectors ($\mathbf{E}_x$, $\mathbf{E}_y$, and $\mathbf{E}_z$) can then be related to the incident P and S electric fields ($\mathbf{E}_P$, $\mathbf{E}_S$) by 'linear Fresnel factors' (K_x, K_y, K_z) giving Equation 4.33 (expressed for just one component for clarity). The intensities of the two sum-frequency light polarisation terms are sums of the squared absolute values of the component sum-frequency electric fields. They are related to the polarisations using non-linear Fresnel factors (or 'L-factors').[74]

$$\mathbf{P}^{(2)}_{i,\mathrm{SF}} = \epsilon_0 \chi^{(2)}_{ijk} K_j \mathbf{E}_{P/S,\mathrm{VIS}} K_k \mathbf{E}_{P/S,\mathrm{IR}} \tag{4.33}$$

Centro-symmetric environments, e.g. bulk crystal, are isotropic. Therefore

the second-order electric field susceptibility is given by Equations 4.34 and 4.35. Equations 4.34 and 4.35 can only simultaneously be true if $\chi^{(2)}_{ijk} = 0$. Therefore from Equation 4.33 one can conclude that there is no SFG signal from a centro-symmetrical environments. SFG is a surface-specific technique as this symmetry is broken at the interface and a signal is expected.

$$\chi^{(2)}_{ijk} = \chi^{(2)}_{-i-j-k} \tag{4.34}$$

$$-\chi^{(2)}_{ijk} = \chi^{(2)}_{-i-j-k} \tag{4.35}$$

$$\chi^{(2)}_{ijk} = \frac{N}{\epsilon_0} < \beta_{ijk} > \tag{4.36}$$

$$\beta_{\alpha\beta\gamma} = \frac{1}{2\hbar} \frac{M_{\alpha\beta} A_{\gamma}}{\omega_v - \omega_{\mathrm{IR}} - i\Gamma_v} \tag{4.37}$$

Second-order susceptibility is the macroscopic average of electron polarisability, called 'hyperpolarisability' β_{ijk}. The relationship between second-order electric field susceptibility and averaged hyperpolarisability (over all orientations) is shown in Equation 4.36, where N is the number of molecules per unit surface area. The hyperpolarisability is given in Equation 4.37. $\beta_{\alpha\beta\gamma}$ is the hyperpolarisability in a molecular coordinate system (α, β, γ, not directly related to surface coordination system). $\hbar$ is the reduced Plank constant. $M_{\alpha\beta}$ and A_{γ} are respectively Raman and IR transition moments. ω_v is the frequency at a given molecular vibration and Γ_v its damping constant. $i = \sqrt{-1}$.[69] From this equation one can conclude the second selection rule: a mode must be both IR- and Raman- active for it to appear in SFG spectra.

Although second-order electric field susceptibility, $\chi^{(2)}_{ijk}$, is a tensor with 27 components, only a few terms have non-zero values depending on the symmetry at the surface. If the surface is of C_∞ point group symmetry, $x = -x$, $y = -y$, but $z \neq -z$, there are only *four* non-zero components: $\chi^{(2)}_{zxx} \equiv \chi^{(2)}_{zyy}$, $\chi^{(2)}_{xzx} \equiv \chi^{(2)}_{yzy}$, $\chi^{(2)}_{xxz} \equiv \chi^{(2)}_{yyz}$, and $\chi^{(2)}_{zzz}$.[75] These elements can be sampled by selecting different polarisation combiations of the incident and emitted lasers, summarised in Table 4.1. The polarisation combinations are presented with the convention from the highest frequency to the lowest: Sum-Frequency, Visible, Infrared. For metal surfaces, which virtually reflects all the intensity of the IR laser, one gets large electric fields in the z-direction and essentially no fields in the x- or y- directions. As a result, only susceptibility elements containing z-components give significant signal. This contributes to the par-

ticular use of PPP and SSP polarisation combinations for this work.

Tab. 4.1: Second-order electric field susceptibility components probed by polarisation combinations.

Polarisation Combination	**Elements Sampled**
PSS	$\chi^{(2)}_{zyy}$
SPS	$\chi^{(2)}_{yzy}$
SSP	$\chi^{(2)}_{yyz}$
PPP	$\chi^{(2)}_{zzz}$, $\chi^{(2)}_{zxx}$, $\chi^{(2)}_{xzx}$, $\chi^{(2)}_{xxz}$

In this work, the alkyl region (2800 to 3750 cm^{-1}) is of most interest. The symmetrical, antisymmetrical, and Fermi resonance vibrational stretches of methyl ($-CH_3$) and methylene ($-CH_2-$) groups can give information on molecular orientation and tilt angle,[76] particularly for linear-alkyl chained surfactants using the intensity ratio between methyl symmetric (r^+) and antisymmetrical stretches (r^-).[77–79]

4.8.1 Experimental

Sum Frequency Generation (SFG) spectra were sampled using an EKSPLA Narrowband Picosecond Spectrometer sending 30 ps pulses at 20 Hz frequency, under a MdLTAG laser with a wavelength of 1064 nm. A copropagating geometry was used for the sampling, with angles 53° and 60 ° to the surface normal for the infrared and visible laser (532 nm) respectively. Spectra intensities were normalised by dividing the SFG signal intensity with the product of the infrared and visible laser intensities. PPP and SSP polarisation measurements were collected. Spectra were recorded in the alkyl region over 2800 to 3750 cm^{-1}, and phosphate and carboxyl groups over 1000 to 1300 cm^{-1} and 1400 to 1800 cm^{-1} regions respectively.

4.9 Time of Flight - Secondary Ion Mass Spectrometry (TOF-SIMS)

Secondary ion mass spectrometry (SIMS) is a surface sensitive method that sputters the sample surface using a high-energy ion gun, typically of bismuth (Bi^+) or oxygen ($O_2{}^+$) ions. The ion gun excites the surface atoms and generates secondary ions. The emitted ions have kinetic energies which are dependent on the mass-to-charge ratio (m/z). The detector can therefore

determine the mass of the ions and form a mass spectrum at each sputtering increment and build a depth-profile of elements as the surface is etched over time as shown in Figure 4.16.

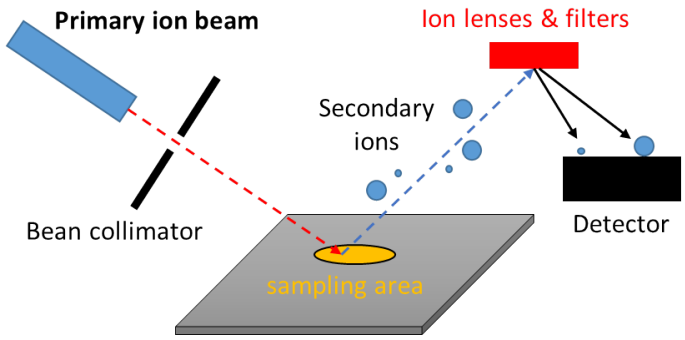

Fig. 4.16: Simplified schematic of a TOF-SIMS set-up.

SIMS performance follows Equation 4.38. $I_{s,m}$ is the secondary ion beam current of species m. I_p is the primary ion beam current. y_m is the yield of sputtered ions for species m. $\alpha^{\pm}$ is the probability of ionisation for positive/negative ions. θ_m is the surface layer fraction of species m and η the analysis transmission, the ion collection efficiency of the detector. With these multiple factors, it is clear that reliable quantitative analysis is complex. Not all ions are produced in equal ease for the same element in different chemical environments. Therefore the precise depth sputtered often need verification from either atomic force microscopy (AFM), or from rigorous sputtering comparison to a similar, well-defined reference material. Additional difficulties can arise from surface charging should the specimen be an electrical insulator, leading to interactions with the secondary ions generated.

$$I_{s,m} = I_p y_m \alpha^{\pm} \theta_m \eta \tag{4.38}$$

Much work has been done to improve the quantitative analysis power of this technique including the use of relative sensitivity factors (RSFs).[80] In this project, only a qualitative depth distribution of elements are needed to detect the penetration/builiding up abrasive material on a abrasive-blasted surface.

4.9.1 Experimental

TOF-SIMS measurements were conducted using an IONTOF TOF-SIMS 5, with a 25 keV bismuth/oxygen ion beam in high-current bunched mode

rastering over a 100 mm^2 area, at the Royal School of Mines, Imperial College London.

4.10 Inductively Coupled Plasma (ICP)

Inductively coupled plasma (ICP) techniques use an argon plasma source reacting in very high temperatures between 6000 to 10,000 K.[81,82] An aerosolised aqueous liquid sample is introduced to the plasma. The inelastic collisions between the sample atoms with the argon ions and electrons lead to ionisation, electron excitations, and any molecules broken down into their constituent atoms then ions. The atoms lose and regain electrons repeatedly within the plasma, excited electrons return to the ground states and lead to the emission of elemental characteristic wavelengths of radiation. The emission is subsequently analysed in a spectrometer and the elements identified schematically illustrated in Figure 4.17.

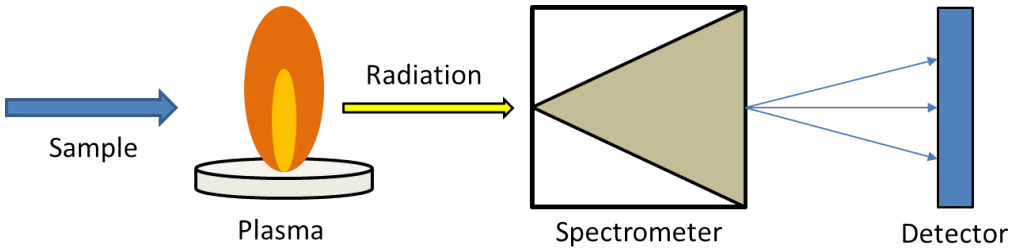

Fig. 4.17: A simplified outline of the ICP-OES analysis of a sample.

The emission from the plasma can be analysed by a variety of methods, the most common being atomic emission spectroscopy (AES),[83,84] optical emission spectroscopy (OES),[85,86] mass spectrometry (MS). All the methods are commonly used to detect atomic concentrations within a sample, with varying lower detection limits, with MS being the most sensitive.[87] The sample spectrum intensities for various analyte elements are then compared to calibration samples of known elemental concentrations. Hence quantitative sample concentration data is determined. In this work, ICP-OES is the primary method of analysis.

4.10.1 Experimental

Inductively Coupled Plasma coupled with Optical Emmission Spectroscopy (ICP-OES) were conducted using a PerkinElmer Optima 8000 ICP-OES

Spectrometer for the detection of ions of interest. The instrument has a lower-detection limit of 0.05 μg L^{-1} for calcium ions, 0.04 μg L^{-1} for magensium ions, 1 μg L^{-1} for aluminium and 10 μg L^{-1} for sulfur/sulphate ions. All ICP experiments were conducted in the Department of Geography, University of Cambridge.

4.11 Ultraviolet-Visible Spectroscopy

Ultraviolet-visible (UV-Vis) spectroscopy utilises electronic transitions (from ground to excited state) within atoms and molecules, to detect species with electronic structures that would absorb UV and visible radiation. The electronic excitations are between the highest occupied molecular orbitals (HOMOs) and lowest unoccupied molecular orbitals (LUMOs). The HOMO-LUMO energy gaps determine the absorbance frequency of a chemical species: the higher the energy difference, the lower the absorbance wavelength. Aromatic compounds have delocalised π-electron systems that are excitable within the UV-Visible range, making them ideal analytes.[88]

The correlation between absorbance and concentration is outlined by the Beer-Lambert Law, shown in Equation 4.40. A is the absorbance, the logarithmic ratio between outgoing radiation intensity I and incident intensity I_0. ϵ is the molar extinction coefficient, a reflection of the probability of electronic transitions. c is the analyte concentration, and l the pathlength the radiation has to travel through the sample.

$$A = \log \frac{I}{I_0} \tag{4.39}$$

$$A = \epsilon c l \tag{4.40}$$

4.11.1 Experimental

All ultraviolet-Visible (UV-Vis) spectroscopy was done using an Agilent 8453 UV-Visible Spectrometer. Hellma absrotpion cuvette of 3 mL volume with a pathlength of 10 mm, made of Suprasil quartz, were used to contain liquid samples during measurement.

5. CHARACTERISATION OF SURFACE TREATED ENGINEERED STEEL AND RELATED SURFACES

5.1 Background

5.1.1 Steel Corrosion

Metals are used in everyday life. Corrosion is an electrochemical reaction which consumes material, caused by the environment that the metal is exposed to.[89] Save for a few inert metals such as gold,[90] corrosion presents a great challenge that starts at the surface of the metal and then propagates into the bulk.[91] Corrosion undermines and contaminates materials, leading to significant departure from designed properties.[92] The cost of corrosion in the United Kingdom is 4 to 5% of the gross national product and around 3% of gross domestic product in the United States.[93,94]

Corrosion can be thought of as an electrochemical reaction, with half electrode reactions occurring across the substrate surface. These cell reactions occur mainly in three types:

1. Dissimilar electrode cells: electrodes containing electrically-conducting impurities as a separate phase. As a result each of the two materials form a half-cell and react once kinetically-viable conditions are met.

2. Concentration cells: two identical electrodes each in contact with solutions of different reactant concentrations.

3. Differential temperature cells: two identical electrodes but with different temperatures.

Over 25% of steel produced annually is used for construction purposes.[95]. Steel corrosion in air is a result of concentration cell reactions due to spatial oxygen concentration differences shown in Figure 5.1, as differential aeration cells.

Reactions of these cells can be considered as the sum of two half-cells, anodic and cathodic reactions respectively shown in Equations 5.1 and 5.2, with re-

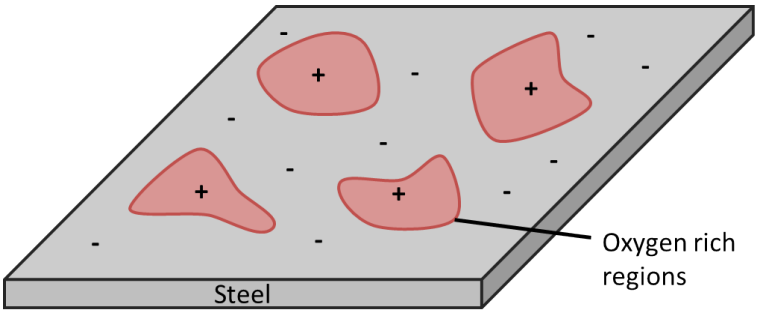

Fig. 5.1: Schematic showing local-action cells on a corroding steel surface. Regions in red are cathodic sites sites with cathodic reaction, that have a higher dissolved oxygen concentration than surrounding areas. Grey areas a less oxygen-rich in comparison.

spective standard electrode potentials (E°) of -0.44 V and +0.401 V.[96] The overall Equation 5.3 has a cell potential of +0.841 V. These equations denote a reaction in equilibrium, described by a Nernst equation seen in Equation 5.4, where [...] denotes species concentration (ideal approximation for activities), p_{O_2} is the fugacity/partial pressure of oxygen, E° the standard cell potential, E the cell potential at temperature T. The solid state of iron and overwhelming concentration of water (55.5 M) remains virtually unchanged during the cell reaction, both [Fe] and H_2O equal to unity. A simplified Equation 5.5 is used. The cell potential is dependent on the concentration of dissolved iron (II) ions, hydroxyl irons, and the partial pressure of oxygen in solution.

$$Fe^{2+}(aq) + 2e^- \rightleftharpoons Fe(s) \qquad \text{anode} \tag{5.1}$$

$$O_2(g) + 2H_2O + 4e^- \rightleftharpoons 4OH^-(aq) \qquad \text{cathode} \tag{5.2}$$

$$2Fe(s) + O_2(g) + 2H_2O \rightleftharpoons 2Fe^{2+}(aq) + 4OH^-(aq) \tag{5.3}$$

$$E = E^\circ - \frac{RT}{4F} \ln \frac{[Fe^{2+}]^2[OH^-]^4}{[Fe]^2 p_{O_2}[H_2O]^2} \tag{5.4}$$

$$E = 0.841\text{V} - \frac{RT}{4F} \ln \frac{[Fe^{2+}]^2[OH^-]^4}{p_{O_2}} \tag{5.5}$$

The standard cell potential allows for determination of other thermodynamic

properties such as the standard Gibbs energy change, ΔG° through Equation 5.6, in turn allowing calculation of the equilibrium constant, K of the corrosion reaction. n is the number of electrons involved in the cell reaction. The kinetic theory of electrochemical reactions cells is addressed by using Butler-Volmer kinetics (empirical) and/or Marcus theory (theoretical). They are probed experimentally through polarimetry and electrochemical impedance spectroscopy.[93,97,98] Corrosion kinetics is not the focus of this thesis and will not be detailed further.

$$\Delta G^\circ = -nFE^\circ = -RT \ln K \tag{5.6}$$

Corrosion on steels is often addressed through organic coatings on surfaces. They are reported to work by retarding/precluding the diffusion of corrosive species onto the reactive metal substrate, through adsorbing inorganic/organic additives to arrest the anodic, cathodic, or both half-electrode reactions.[99–101] However coatings are often prone to failure upon prolonged contact with corroding solutions/species. Hydrophilic channels may begin traversing through the paint. Eventually these channels reach the protected substrate and corrosion occurs underneath the coating. Corrosion reactions lead to blisters and cavities formation, propagating laterally along the steel-paint interface leading to coating failure.[102]

To have a rationalised approach towards future coatings formulation, basic surface chemistry on the substrate needs to be understood (e.g. finding suitable species to bind strongly onto the surface). Therefore this chapter focuses on the surface chemical characterisation of carbon steel S355, often used for offshore structures due to its strong strength.[103,104] '355' denotes the yield strength of the steel to be 355 MPa before plastic deformation occurs. Stress above this value deforms the metal permanently.

The steel is often cleaned by and repainted after abrasive blasting treatment, a fast way of removing old paint and corrosion products in often dangerous offshore environments.[105] Hence the post-blasting treatment steel surfaces will be characterised to determine possible competitive adsorption of paint components on the post-treatment steel.

5.1.2 Native Surface Oxide on Steel

Native oxide layers on steel and their cohesiveness is influential to the corrosion resistivity of a material. One method to index this property is the

Pilling-Bedworth ratio (PBR) calculated using Equation 5.7, where M and D are respectively the molecular weight and density of corrosion products. m and d are the molecular weight and density respectively for the metal. n is the number of metal atoms in the molecular formula of the surface oxide. (e.g. Fe_2O_3, n= 2)

$$\text{PBR} = \frac{Md}{nmD} \tag{5.7}$$

If PBR $\ll 1$ the volume of the corrosion product is much smaller than the reactant metal, leading to cracks and pores in the native metal oxide layer. Should PBR ≥ 1, the volume of the corrosion product is greater than that of reactive metal substrate, the scale is said to be under compression, and is cohesive and protective. However, if PBR $\gg 1$, corrosion scale formations may buckle and detach from the surface due to excessive internal stress. It is well-established that aluminium metal is well-protected by its surface aluminium oxide and has a PBR of 1.3. For magnesium, whose metallic oxide is not protective, has a PBR of 0.8.

For stainless steels, a layer of protective chromium oxide (Cr_2O_3) oxide forms on the surface resisting corrosion.[106–108] The native iron oxide(s) on carbon steel is less clear. Postulations of magnetite (Fe_3O_4) and hematite (Fe_2O_3) formations on the surface estimated from XPS are reported, with little verification from other techniques,[109–111] or are obtained from thick corrosion scales that are hardly relevant to repainting conditions.[112] However both stainless steels and carbon steels have PBR values of 2.1, but carbon steel readily corrodes upon contact with water. Therefore PBR has significant deficiencies but provides a simple estimation of surface oxide cohesiveness. This work looks at the native surface oxides of the S355 carbon steel with multiple techniques, to clearly establish the surface chemical environment(s) and crystallinity.

5.1.3 Surface Treatment in Offshore Environments

The often hazardous conditions in offshore environments requires a fast surface cleaning method to remove old coatings and corrosion products prior to repainting, for better coating surface adhesion.[113] Abrasive blasting fits such criteria. This is a versatile technique where many parameters can be used to achieve varied surface effects. The literature concerning blasting performance are overwhelmingly empirical.[114] In general an abrasive material with high hardness compared to the material-to-be-removed is preferable, making al-

mandine garnet abrasive (Mohs hardness 7, *cf.* 4 for steel) suitable. It is also effective in surface salt removal. Some salts are known to be detrimental to coating adhesion and promote corrosion.[115–117] Offshore marine environments contain significant amount of marine aerosols that could trigger immediate corrosion should 'wet' blasting techniques be used.[118] Therefore dry abrasive blasting constitutes a suitable method.

The removal of old paints, often made of polymers, varies with the speed and angle of collision by the abrasive particles. At glancing-angle blasting, the particles undergo abrasion where most of the kinetic energy is dissipated through friction due to the large cutting cross-section with the polymer film. The particles impregnate into the polymer and scratches off superficial layers of coating. At higher blasting angles, low speed particles collide onto the polymer layer but its kinetic energy is too low, and only leads to fatiguing of the coating later. At medium collision speeds, plastic deformation of the film is seen. Deeper polymer penetration and material removal becomes common.[114] High speed particle-coating collision leads to contact-melting and removal of the polymer. Depending on the physical properties of the coating, there will be different optimal blasting parameters.[119]

Upon completion of old polymer-coating removal, the abrasive particles would collide onto corrosion products and possibly mill-scale on the steel surface. This is illustrated in Figure 5.2. Upon impact onto this brittle layer, the immediate, topmost area undergoes plastic deformation/indentation. Lateral cracks below plastic deformation pit form while radial cracks propagate along the surface. Lateral cracks would form at the outer-inner scale interface while at the same interface ring cracks form directly below the impact zone. The vertical cross-section of the brittle-layer failure adopts a cone shape, propagating from the top of the scale to the softer steel substrate.[120]

The effects of almandine garnet abrasive blasting have on the S355 steel surface are investigated in this work, with subsequent exploration of organics- and inorganic ion-adsorption on the post-treatment steel.

5.2 Experimental

5.2.1 Materials

The S355 steel sheets for this project were cut into 1 cm x 1 cm x 1 cm 'coupons' (Parker Steel, UK). The alloying composition of the steel were listed in Table 5.1. For polished samples, the steel coupons were first ground

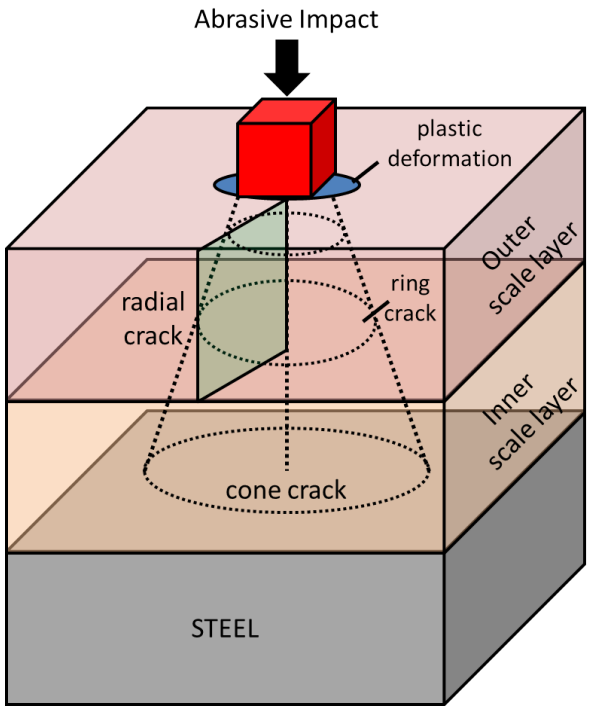

Fig. 5.2: Schematic showing propagation of cracks upon abrasive particle impact on a brittle corrosion-/mill-scale.

down with 320 grit silicon carbide paper. The samples were then subsequently polished using successively finer grades of diamond paste made by Kemet, UK. Samples were polished in 25 μm grit diamond paste for 30 min, then 14, 6, and 1 μm diamond pastes for 10 min each. The substrates were then immersed in 2% neutracon solution (Decon Laboratories Ltd, UK), under sonication in a Bioblock Scientific 750 W Sonicator for 1 min to remove any diamond paste residues. The coupons were then rinsed with 50 mL ultrapure water (18.2 MΩ cm^{-1} resistivity) for 10 times, and placed in 50 mL of ultrapure water to sonicate for 1 min, and rinsed 10 time more. The surfaces were blow-dried with a jet of dry nitrogen then stored in vacuum to prevent any possible corrosion.

Abrasive blasted samples were blasted using the almandine garnet, a natural mineral. All almandine garnet abrasive was sourced from GMA Garnet in Australia. The abrasive particles were 80 mesh (177 mum) in size. The composition of this naturally-sourced mineral was quoted in Table 5.2. The S355 steel surfaces were blasted using a F1200 Bench-Top Blast Cleaning System, with a Model F21 Dust Collection Unit, and a 80 psi-capable blast

gun from Guyson International Ltd., UK. The default blasting conditions was under 40 psi at 10 cm distance. A Model 400 blasting gun with a 6.4 mm diameter ceramic nozzle with an 2.8 mm diameter air control jet was used.

Tab. 5.1: S355 steel alloying elements composition, iron to balance

C/%	**Si/%**	**Mn/%**	**P/%**	**S/%**	**Cr /%**	**Mo/%**
0.20	0.50	0.90-1.65	0.035	0.030	0.30	0.10
Ni/%	**Al/%**	**Cu/%**	**N/%**	**Nb/%**	**Ti /%**	**V/%**
0.50	0.020	0.35	0.015	0.060	0.030	0.12

Tab. 5.2: Quoted composition of almandine garnet abrasive

Chemical Name	**Formula**	**Percentage Composition**
Almandine Garnet	$Fe_2Al_3(SiO_4)_3$	$> 97\%$
Ilmenite	$FeTiO_3$	$< 1.5\%$
Calcium Carbonate	$CaCO_3$	$< 1.5\%$
Zircon	$ZrSiO_4$	$< 0.2\%$
Quartz	SiO_2	$< 0.5\%$

5.2.2 Equipment

All experimental instruments were detailed in Chapter 4 unless specifically stated otherwise.

5.3 Untreated Steel

The S355 steel samples are analysed as received here. There is visible mill-scale on the surface.

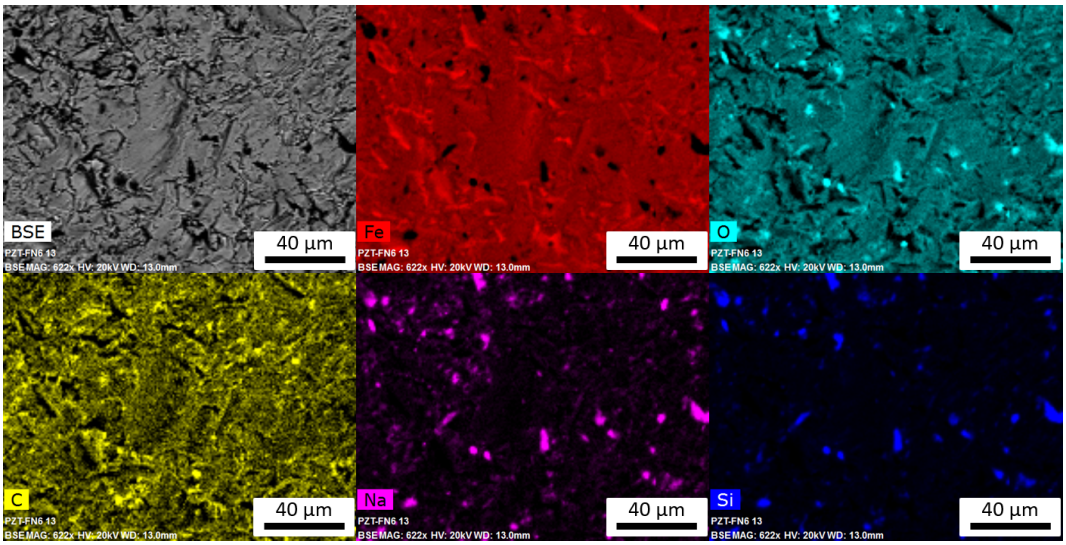

Fig. 5.3: BSE-EDS surface elemental maps of untreated S355 sample. Each individual colour denotes a different element. (Black/white: backscattered electron micrograph, red: iron, cyan: oxygen, yellow: carbon, purple: sodium, navy: silicon)

5.3.1 SEM-EDX

Electron micrographs were collected to capture an outline of the topography of untreated S355 steel surface. The backscattered electron (BSE) map in Figure 5.3 shows significant roughness. The oxygen map shows oxygen content is widespread on the surface, with bright spots of higher intensity that are closely associated with those seen in carbon, sodium, and silicon maps. The carbon, sodium, and silicon signatures are common in surface contamination by dust (carbon, silicon) and salts (sodium) that may be introduced during the hot-rolling of S355 steel. Salt contamination is often influential to future steel corrosion.[93] The pervasiveness of oxygen content supports mill-scale being a thick layer of native surface oxide.

EDX data of untreated S355 steel surface is shown in Figure 5.4. The penetrative analysis, due to its high sampling volume into the steel bulk, has iron being the predominant element (approximately 90%) as expected of steel and all the surface associated elements including contaminants seen in elemental mapping. Oxygen content (3.5%) remains significantly higher than other minor elements (maximum 2.6%), including the major alloying element manganese. EDX experiment supports the mill-scale being a layer of iron oxide.

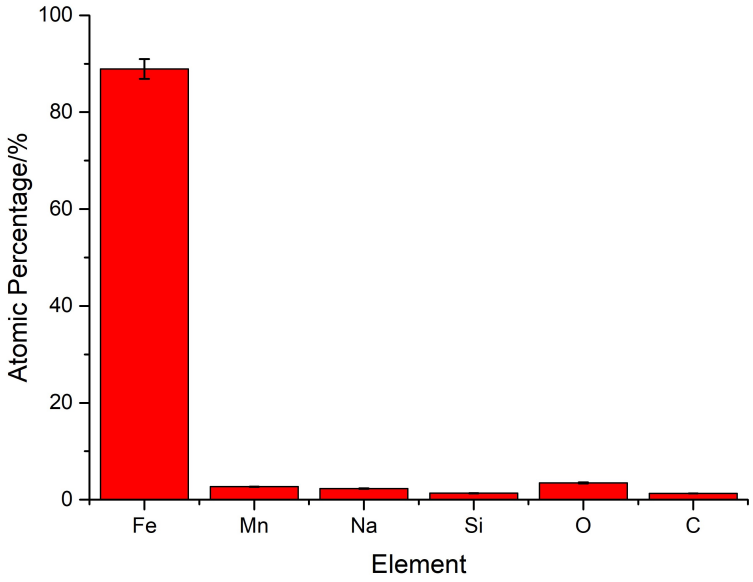

Fig. 5.4: EDX surface elemental composition of untreated S355 steel.

5.3.2 XPS

XPS surface and depth profiling analyses were performed on the untreated S355 steel. Figure 5.5A shows the depth profiling spectra. It is clear that with further etching (from bottom to top), the iron 2p signal from 705 to 740 eV becomes progressively stronger, indicative of the increased contribution of bulk steel. Figure 5.5B shows the elemental analyses of the different etching stages. Iron content increases, while the oxygen content remains steady. In the deepest etching of 180 s, the iron to oxygen ratio is approximately two to three, supportive of a thick iron oxide layer similar to hematite, Fe_2O_3 on the untreated steel surface.

Carbon content decreases with respect to increased etching, indicative of surface contamination by adventitious carbon instead of alloying. Calcium, silicon, aluminium content, with trace sodium and chlorine are persistent despite deeper etching. A possible cause is the rough topography of the untreated steel surface. So the etched depth is much shorter (nanometres) than the surface roughness (microns). This in-depth occlusion leads to continued surveying of contaminant elements despite increased etching as illustrated in Figure 5.6.

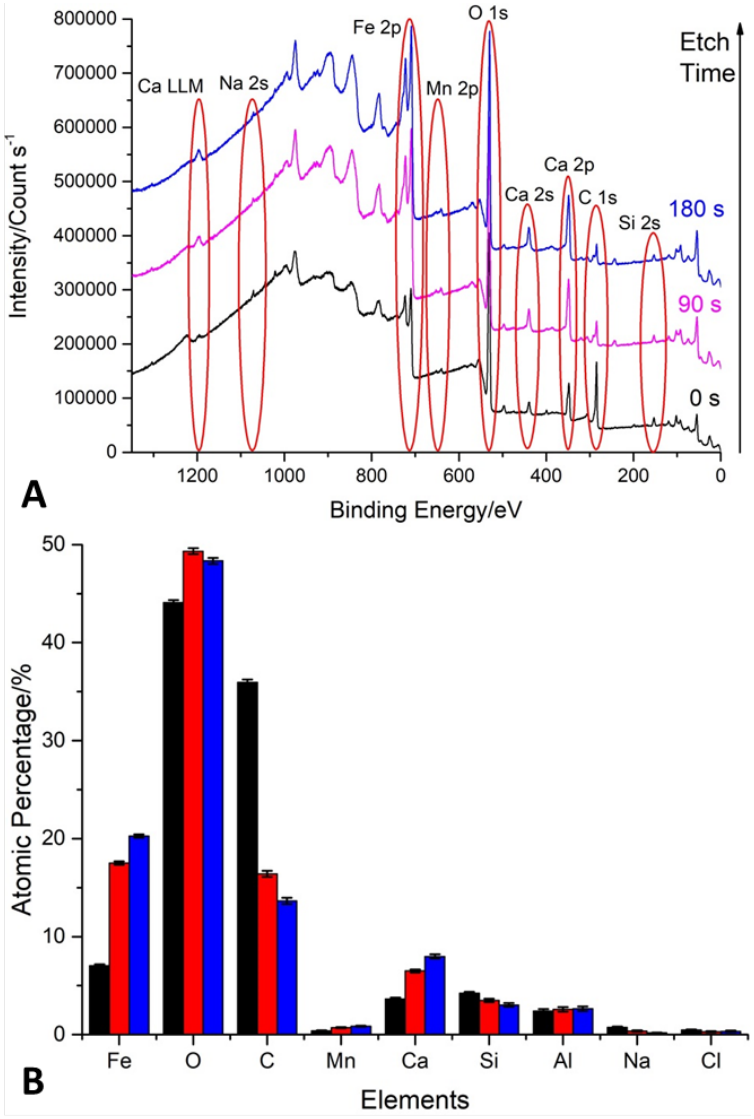

Fig. 5.5: A) XPS surface and depth profiling of elemental composition of untreated S355 sample. Sample intensity has been vertically offset for clarity of comparison. B) XPS depth-profiling elemental analysis through 0 (black), 90 (red) and 180 s (blue) etching.

5.3.3 TOF-SIMS

TOF-SIMS was used to provide depth-profile elemental analysis. Oxygen characterisation was not available due to the use of oxygen ion-etching. In Figure 5.7 the initial 750 s of sputtering, all elemental signals are diminishing, typical of surface charging. This is indicative of an insulating native layer

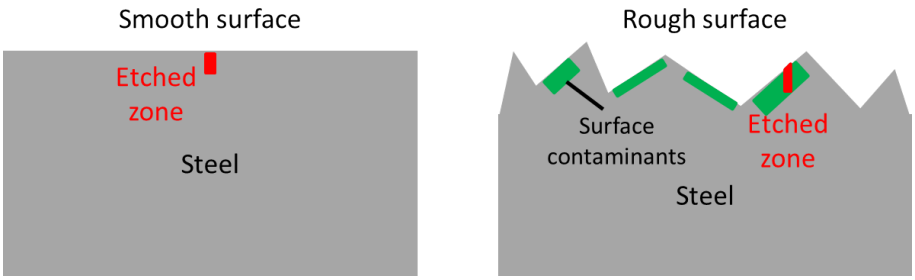

Fig. 5.6: Cartoon illustrating the difference in etching responses between smooth, flat surfaces against roughened, contaminated surfaces.

present on the untreated S355 surface, consistent with a proposed layer of iron oxide.

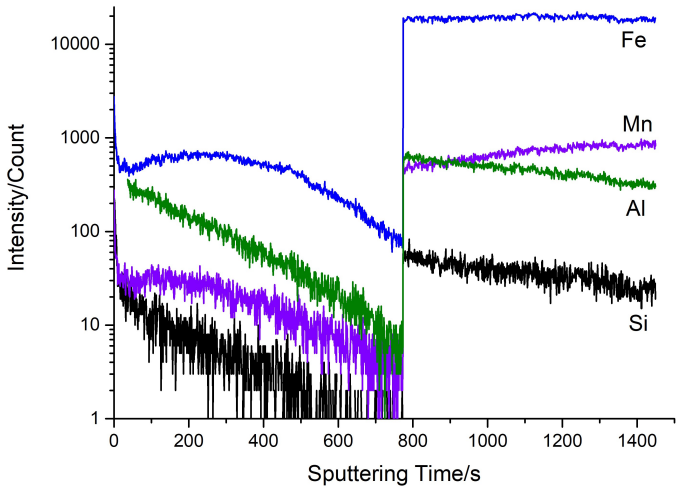

Fig. 5.7: TOF-SIMS depth profiling of elements of untreated S355 sample. Settings were modified from 750s onwards to compensate for charging effects from insulating surface.

Further etching and compensated charging effects are seen from 750 s of sputtering. The expected bulk steel alloying composition, as shown in Table 5.1 is observed in Figure 5.7, with iron being the dominant species along with major alloying element of manganese. The bulk composition result agrees with EDX and XPS findings, and the initial charging effects imply the existence of a top oxide layer.

5.3.4 Summary of Results

The combination of the three techniques provides qualitative (TOF-SIMS, EDX) and surface sensitive quantitative (XPS) results. Bulk metal has been successfully detected, dominated by iron with alloying element manganese. All experimental techniques identify surface contamination by elements such as aluminium, calcium, silicon, sodium, and chlorine on the mill-scale. The mill-scale is characterised as a thick layer of insulating iron oxide native to the steel surface. TOF-SIMS and XPS agree with the steel composition listed on Table 5.1, with no trace elements exceeding 10% in atomic percentage.

5.4 Polished Steel

S355 steel coupons were polished to sub-micron roughness to provide a reproducible, controlled generation of a steel surface for analysis. Polishing procedures were described in detail in Materials in the Experimental section.

5.4.1 SEM-EDX

SEM-EDX was used to survey for elements on the surface of the S355 steel. In Figure 5.8A, after polishing, the millscale of the untreated steel coupon is visibly removed to give a mirror finish of bare steel.

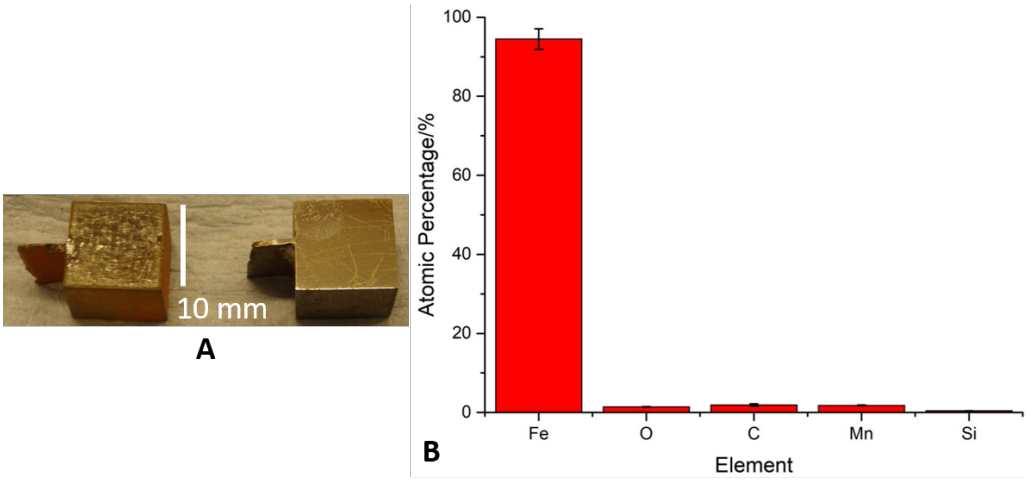

Fig. 5.8: A) Visual comparison between the surface of untreated (left) and polished (right) S355 steel. B) EDX determined elemental composition of polished steel surface.

The accompanying EDX analysis of the polished surface is shown in Figure

5.8B. EDX analysis, due to the larger sampling volume into the bulk, shows the polished steel to be mainly iron. The oxygen content of the polished steel is lower than that of millscale-covered untreated steel surface, supporting the idea that millscale consists of iron oxide. Minor alloying elements of carbon, manganese, and silicon are also observable by EDX. Sodium seen on untreated steel samples is absent on the polished steel, confirming the element as a surface contaminant.

5.4.2 TOF-SIMS

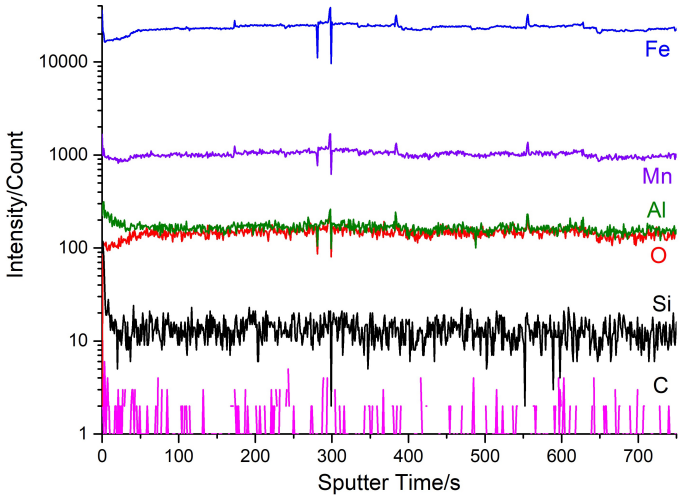

Fig. 5.9: TOF-SIMS depth profiling of elements of polished S355 sample.

Identical TOF-SIMS detection settings used to untreated steel were repeated for the polished steel, though a primary beam of 25 kV bismuth cations instead of oxygen molecule anions is used. Hence surface oxygen secondary ions can be detected.

In Figure 5.9, elemental levels appear to be constant with respect to sputtering time. The elements with the highest intensities are iron and major alloying element manganese. Traces of aluminium, oxygen, silicon are detected whilst the carbon content appears to be low. This quick plateauing of signals is indicative of the bulk steel appearing *via* minimal sputtering. Unlike the untreated samples, where much signal variation is seen due to the thick mill scale oxide layer present, one can conclude the native oxide layer on the polished steel to be very thin.

The TOF-SIMS results agree with EDX findings, confirming the bulk com-

position of S355. The technique is not a quantitative technique without carefully-controlled reference materials. For a complex material such as alloyed steel it is difficult to obtain. Hence the thin surface oxide is to be characterised using the more surface-sensitive quantitative approach such as XPS.

5.4.3 XPS

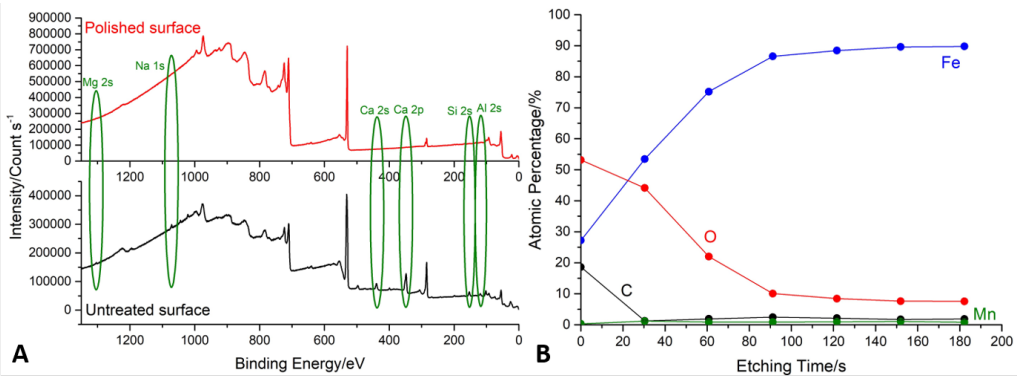

Fig. 5.10: A: Surface XPS comparison between the surface of untreated (bottom) and polished (top) S355 steel spectra. With locations of elements of interest highlighted. B: Element depth profiling of major detected elements for a polished S355 steel sample.

Table 5.3 shows the elemental composition of the polished S355 surface identified by XPS. The major elements are shown to be mainly iron and oxygen. The rich oxygen environment supports the presence of a thin native surface oxide layer. Manganese is seen as an alloying element with a significant but low atomic percentage. The surface spectra has a high carbon content compared to bulk steel composition listed in Table 5.1 and is likely to be adventitious carbon. In Figure 5.10A, elements which are present at the untreated surface (bottom) is shown to be removed when steel was polished (top); namely magnesium, sodium, calcium, aluminium, and a significant amount of silicon, revealing these elements to be surface contaminants.

Depth profiling analysis are shown in Figure 5.10B. The results show that at the surface, there is a very significant oxygen presence in comparison to the iron, at 53% to 27%. A significant carbon presence is detected at around 20%. Deeper etching leads to iron content increase and plateaus at approximately 90% whereas oxygen and carbon content decreases, albeit the oxygen decrease is at a much slower rate and plateaus at approximately 7%.

Tab. 5.3: XPS-identified surface elements on polished S355 steel

Element	Atomic Percentage/%
Fe	27.2 ± 0.2
O	53.2 ± 0.2
C	18.6 ± 0.3
Mn	0.31 ± 0.1
Si	0.71 ± 0.2

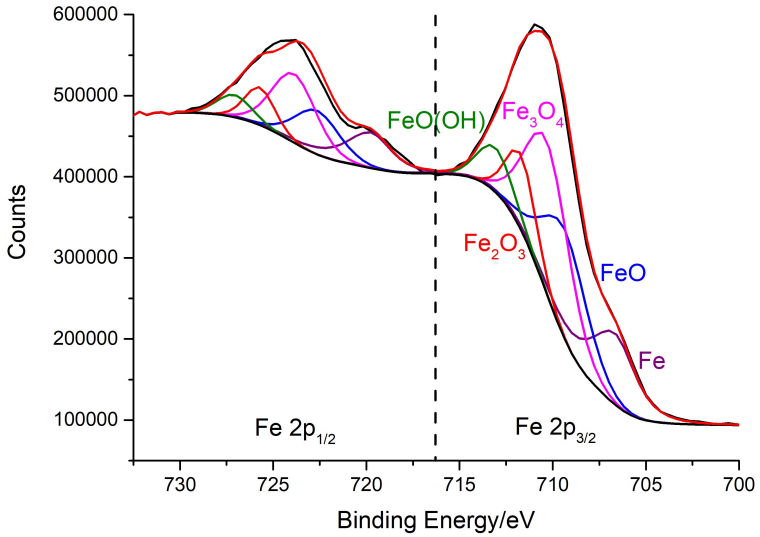

Fig. 5.11: An example XPS spectrum only of the Fe $2p_{3/2}$ region for clarity, with component peaks identified.

The results in Figure 5.10B show that the rapidly decreasing carbon is concentrated only at the surface. Therefore it is likely adventitious carbon. The steady manganese atomic percentage confirms its role as an alloying element. The slow decrease in oxygen content with respect to etching, compared to carbon, suggests the existence of a native iron oxide layer on the surface despite millscale-removal by polishing. The rapid increase iron content through etching confirms that while a native iron oxides layer exists, it is most likely to be thin.

XPS allows component peak fitting for chemical environments for particular elements. To estimate the surface chemistry of the steel, it is necessary to determine the surface speciation and surface site density of S355 steel. 'Dry'

techniques like XPS, and EBSD, are particularly attractive as they do not expose the steel to water, minimising the risk of corrosion changing the steel surface during characterisation.

Figure 5.11 shows an example component peak fitting of various iron oxides on the surface. The fitting parameters (peak position, width) are constrained using a XPS database of known iron oxides.[121] The peak-fitting results are shown in Table 5.4.

Tab. 5.4: XPS peak fitting parameters and results of polished S355 steel surface at the Fe $2p_{3/2}$ region

Species	**Position/eV**	**Full-Wdith-Half-Maximum (FWHM)/eV**	**Percentage Area/%**
Fe	706.72	2.23	13.08
FeO	709.40	2.81	24.09
Fe_3O_4	710.55	3.09	42.03
Fe_2O_3	711.80	1.87	11.49
FeO(OH)	712.77	2.20	9.32

The Fe $2p_{3/2}$ regional analysis results show that the steel surface oxide is composed of a variety of iron oxides; wustite (FeO), magnetite (Fe_3O_4), hematite (Fe_2O_3), goethite (FeO(OH)) and lepidocrocite (FeO(OH)).[122] Each species has its own chemical environment with different peak shapes. Metallic iron (Fe) remains detectable. Since the photoelectron escape path is very short ($\approx$ 15 Å),[60] this is indicative of a very thin layer of native iron oxides on the S355 steel for metallic iron photoelectrons to be surveyed. Table 5.4 shows the prominent oxide species to be magnetite, followed by wustite, and hematite. Different oxides have varying crystal structures and densities,[123] leading to an incohesive surface oxide layer subject to easy corrosion onset at the crystal grain-boundaries.[124] Corrosive species can easily penetrate at the boundaries and corrode the S355 bulk iron beneath.

5.4.4 EBSD

EBSD was used to characterise the surface crystals on the S355 steel and was very surface sensitive. Figure 5.12A shows results from a typical EBSD

experiment on the S355 steel surface. SEM identifies the location on the specimen to be analysed. The site area is divided into pixels, in this case 367×73 pixels. Surface diffraction lines (e.g. Figure 5.12B for wustite) at each pixel is analysed and the contributing surface crystal identified by referencing the lines observed to a database. In Figure 5.12A, one can see no particular distribution cluster for a particular type of surface iron oxide, forming a polycrystalline surface oxide layer.

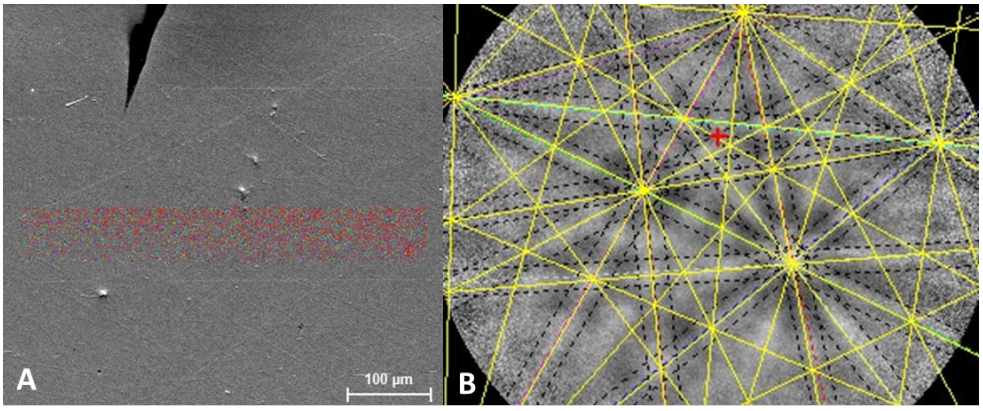

Fig. 5.12: Example EBSD experiment showing A) sampling of the polished steel surface, with each individual coloured pixel indicating the surface iron oxide species identified at that location: magnetite (red), wustite (green), hematite (blue), goethtite (yellow), and lepidocrocite (magenta). B) Example Kikuchi lines associated with wustite, FeO.

Figure 5.13 shows the identified crystal phases distribution on the S355 surface. The majority of the surface iron oxides present are magnetite. This agrees with literature.[125] The surface is also populated with a mixture of iron (II) and iron (III) species (wustite, hematite, goethite, and lepidocrocite), each respective oxidation state crystals contribute approximately a quarter of the surface crystal population.

A comparison of results for identified surface iron oxides on S355 steel is shown in Figure 5.14. XPS and EBSD results show good agreement, allowing for a more confident assessment of the S355 steel surface chemistry. The surface site on iron oxides are hypothesised to be iron hydroxyl groups, and each type of oxide have their own site density and adsorption behaviour.[126] The average surface oxidation state of iron and the average site density can

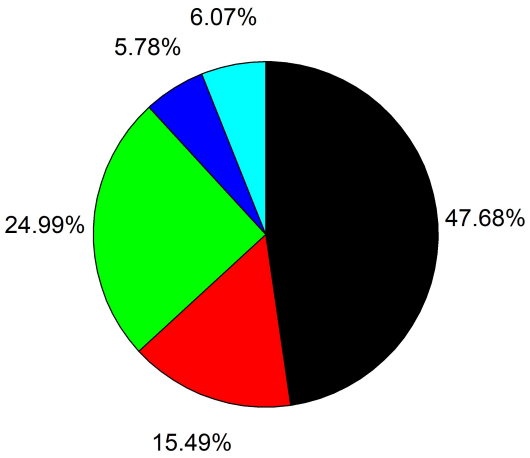

Fig. 5.13: The distribution of surface iron oxides identified on the polished S355 steel coupon. The list of iron oxides include: magnetite (black), hematite (red), wustite (green), goethite (blue), and lepidocrocite (cyan).

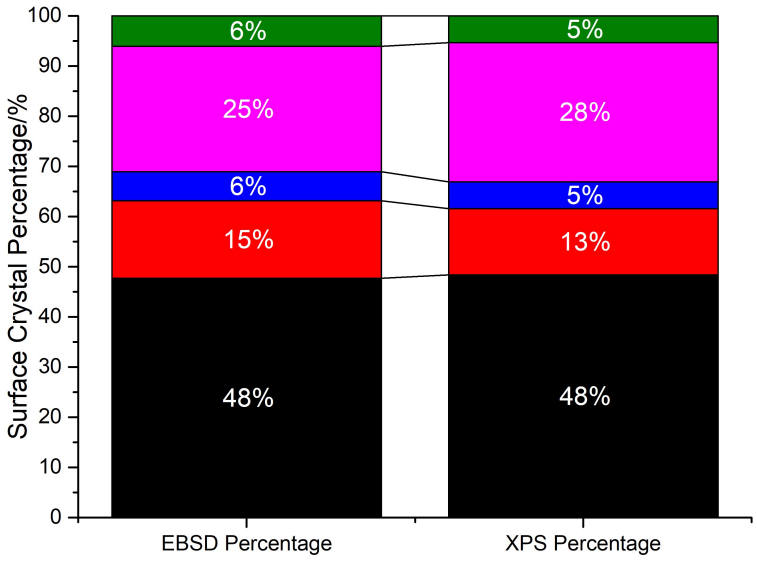

Fig. 5.14: Comparison between EBSD and XPS techniques, the species listed are : magnetite (black), hematite (red), goethite (blue), wustite (magenta), and lepidocrocite (green).

be inferred from literature data of each iron oxide crystal.[127] The values are respectively determined to be 2.59 ± 0.01 and 5.24 ± 0.1 sites nm^{-1}.

Tab. 5.5: Surface chemistry estimation from agreeing XPS, EBSD data of polished S355 steel surface.

Species	**Percentage Surface/ %**	**Average −OH group of crystal/ nm^{-1}**	**Average −OH group contribution/ nm^{-1}**	**Average Fe Oxidation State contribution**
Magnetite	47.7	5.2	2.48	1.27
Hematite	15.5	4.4	0.682	0.47
Goethite	5.8	6.0	0.34	0.17
Lepidocrocite	6.1	8.0	0.49	0.18
Wustite	25.0	5.0	1.25	0.50
Sum	**100.0**		**5.24**	**2.59**

5.4.5 Summary of Results

A variety of surface sensitive techniques was employed and the results were consistent with each other. The low surface oxygen percentage from penetrative EDX, and TOF-SIMS quick etching into the bulk of the steel, have identified the presence of a very thin film of native iron oxide layer on the polished S355 steel surface.

XPS results highlight that polishing is an effective and controlled method for removing surface contaminants on the S355 steel. The technique also simultaneously provides chemical environment information for each element, gaining insights into the speciation of the surface iron oxide layer.

The species identified by XPS peak fitting agrees with EBSD data, independently verifying the findings of both techniques that multiple iron oxide species are present at the surface. The EBSD does not identify discrete preferred zones of iron oxide crystals, confirming the oxide layer on S355 steel to be prone to corrosion in aqueous environments. Corrosive species can penetrate at the crystal boundaries and access the reactive S355 bulk iron beneath.

The average site density on S355 steel is estimated to be 5.24 ± 0.1 sites nm^{-1} and its average surface iron oxidation state 2.59 ± 0.01, respectively. Through a combination of 'dry' surface sensitive techniques, the interfacial chemistry

can still be determined when 'wet' techniques such as surface titration are not viable options due to the reactivity of the substrate-of-interest in water.

5.5 Abrasive Blasted Steel

A suite of state-of-the-art techniques were used to characterise abrasive-blasted steel surfaces, as well as investigating the effects of different blasting times and pressures had on the surface coverage of abrasive residues on blasted-steel.

5.5.1 SEM-EDX

The effectiveness of abrasive blasting in removing tough millscale is demonstrated in Figure 5.15. The dark mill scale seen in zone A is quickly removed within 5 seconds of blasting, into a grey metallic surface seen in zone B that is visibly roughened.

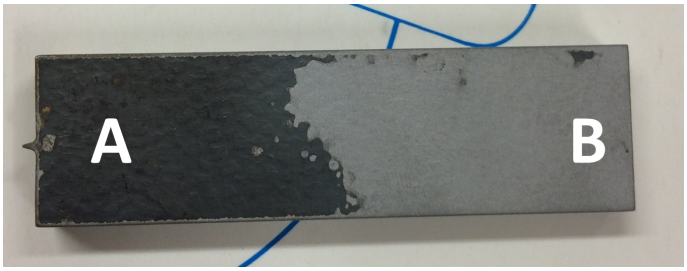

Fig. 5.15: Visible effects of almandine garnet abrasive blasting on a untreated steel surface. Zone A: untreated, mill scale-covered steel. Zone B: steel surface after 5 seconds of blasting.

SEM-EDX was used as a robust sampling technique to characterise a surface. Multiple points on the blasted steel were surveyed to ensure a consistent elemental analysis.

To see the effects of the abrasive-blasting treatment, EDX spectra of an untreated millscale-covered S355 steel sample is compared to an untreated steel sample after 30 seconds of almandine garnet blasting. The different spectra are shown in Figure 5.16. The untreated sample surface has elements carbon, oxygen, trace silicon, manganese, and iron.

For the abrasive blasted sample, the oxygen profile has significantly diminished in comparison to non-blasted steel due to visible millscale removal.

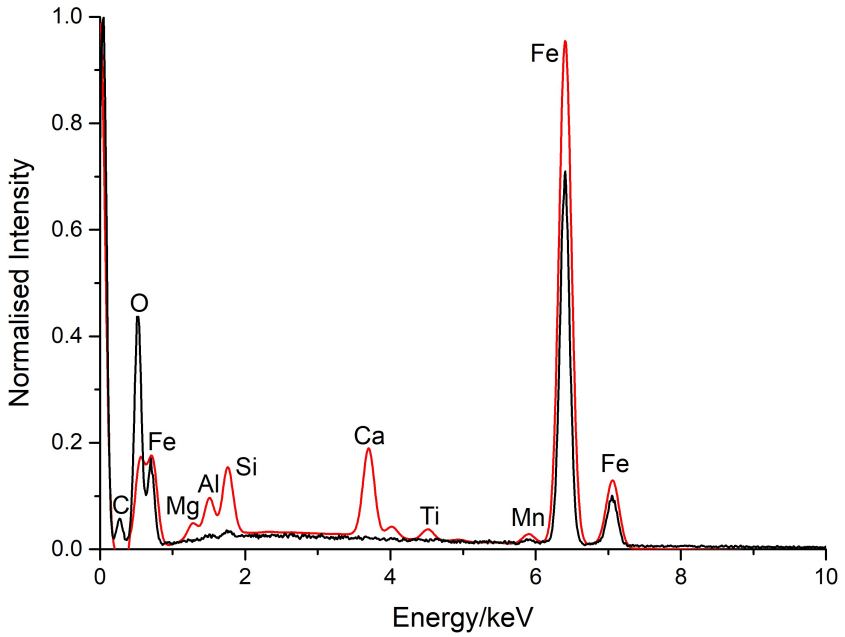

Fig. 5.16: Example EDX spectra collected on differently treated S355 steel surfaces, each peak with elemental labels attached. Black: untreated steel; red: steel surface abrasive blasted for 30 s.

Significant increase of magnesium, aluminium, silicon, calcium, titanium signatures is seen in addition to the steel alloying elements. The intensified signals of these elements can be rationalised by considering the abrasive composition listed in Table 5.2. The aluminium and silicon content can be attributed to the almandine garnet mineral. Strong calcium signature comes from the calcium carbonate and the titanium peak stems from the ilmenite impurities within the blasting mixture. Magnesium content may be from possible mineral contamination, or magnesium content inside the almandine garnet itself in the form of pyrope, common in garnet mineral-deposits.[128]

Atomic percentages of the abrasive-blasted surface are compared to untreated, and polished S355 steel surfaces, shown in Figure 5.17. The iron and oxygen atomic percentages are relatively similar between untreated samples and abrasive-blasted samples due to the blasting process removing the millscale iron oxide, but adds a number of other oxides to the steel surface. In comparison to the polished S355 steel, abrasive-blasting has introduced many new elements to the surface; with abrasive associated elements (Ca, Si, Al, Mg, Ti) of sizeable atomic percentage contributions ranging from 2% to 8%. The results offer first evidence of significant amount of abrasive residue

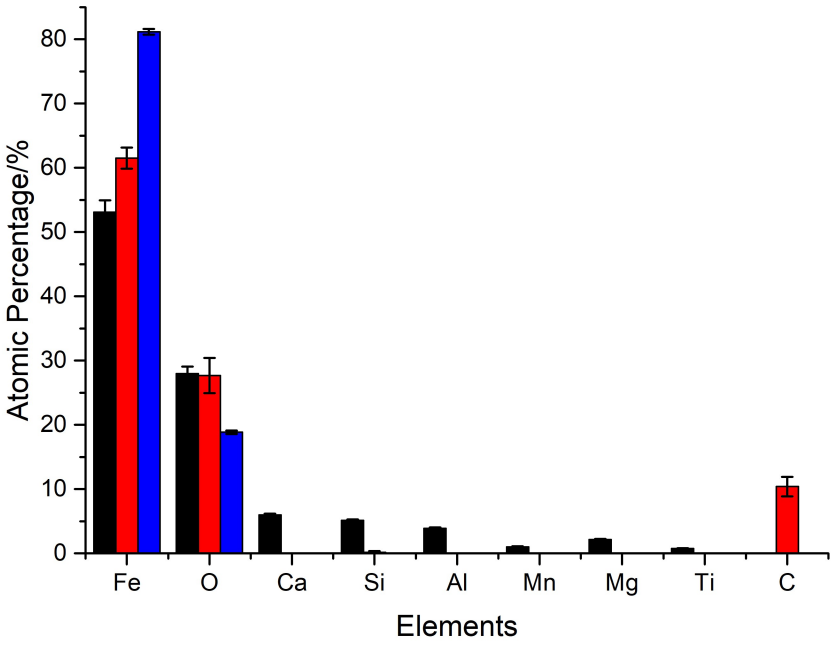

Fig. 5.17: EDX spectra elemental analysis between differently treated S355 steel surfaces. Black: 30 s abrasive blasting. Red: untreated surface with mill scale on top. Blue: polished surface.

on the steel surface.

5.5.2 XPS

The almandine garnet blasted steel surface was analysed with the incident X-ray normal to the sample surface. XPS surveying can tolerate a rough substrate topography which EBSD cannot. The XPS sampling shown in Figure 5.18 shows the abrasive-blasted steel surface to contain several elements (aluminium, silicon, calcium, titanium, and trace magnesium) associated with the garnet abrasive, exclusive to the polished steel. Steel-associated element peaks of iron and manganese have diminished atomic percentages on blast-steel as shown in Figure 5.19. The results indicate significant amount of blasting residue remaining on the post-blasting steel surface, in agreement with EDX data.

The depth profiling experiments give indication of the thickness of the abrasive on the steel surface. In Figure 5.20A, atomic percentages of major elements are displayed. With deeper etching elemental compositions approaches that of bulk steel, indicated by rising iron atomic percentage. Carbon con-

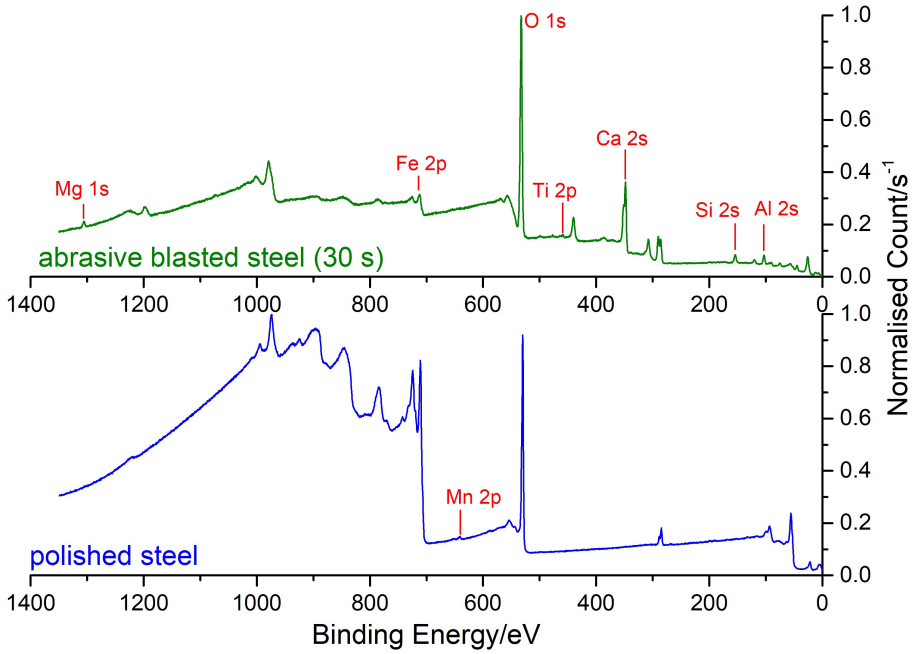

Fig. 5.18: An example XPS surface spectra comparison between a polished and one steel surface that has been abrasive blasted for 30 s. The elements of interest are highlighted in red.

tent drastically decreases at the beginning of etching due to removal of adventitious carbon, however only slowly decreases with further etching. This suggests there may be persistent species within/embedded in the steel. Unlike the depth profiling of polished steel sample in Figure 5.10B in which oxygen atomic percentage rapidly decreased with deeper etching, the oxygen content here remained constant. This suggest species rich in oxygen, such as abrasive materials, are present at a deeper etched level; strongly suggestive of deep abrasive embedding into the steel.

The results above are echoed by those in Figure 5.20B, a depth profile sampling of abrasive associated elements into the blasted steel sample. Despite deeper etching into the sample, garnet-associated elements have essentially maintained their atomic percentages. This result agrees with the results seen in the oxygen atomic percentage profile, as all of the garnet associated elements come in the form of minerals that are rich in oxygen. The trend is likewise indicative of strong abrasive embedment into or accumulation onto the steel surface. The abrasive-associated elemental percentages from XPS is in good agreement with EDX findings.

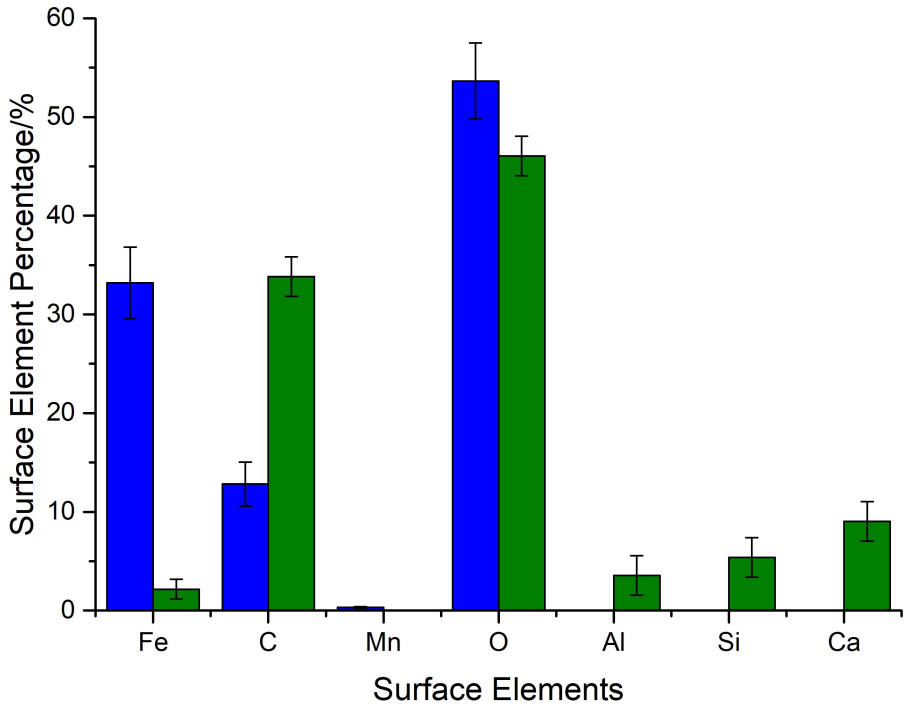

Fig. 5.19: Elemental comparison of XPS elemental analysis between a polished and one steel surface that has been abrasive blasted for 30 s. Blue: polished S355 steel. Green: Abrasive blasted steel.

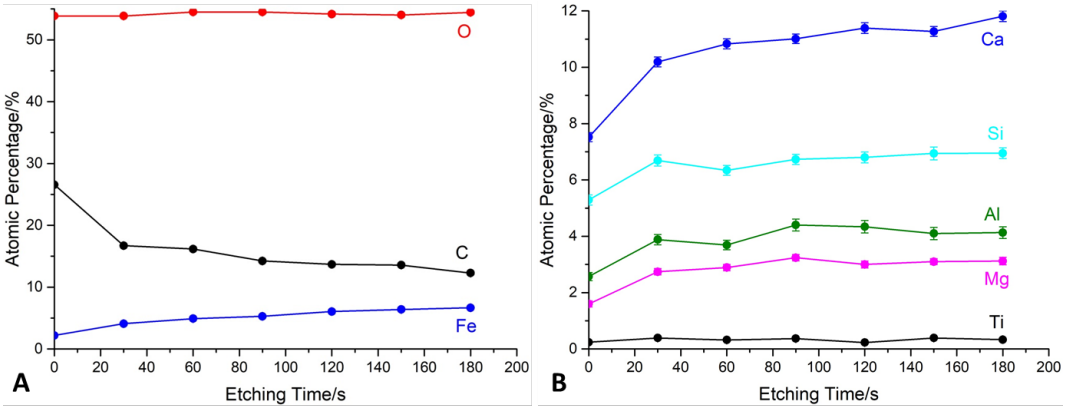

Fig. 5.20: Depth profile of a S355 steel sample abrasive blasted for 30 s, with A) main constituent elements, and B) abrasive associated elements.

5.5.3 TOF-SIMS

TOF-SIMS was performed on two S355 steel samples that had been abrasive blasted by garnet for different durations, to explore the penetration/residue

accumulation effects of blasting time have on the surface.

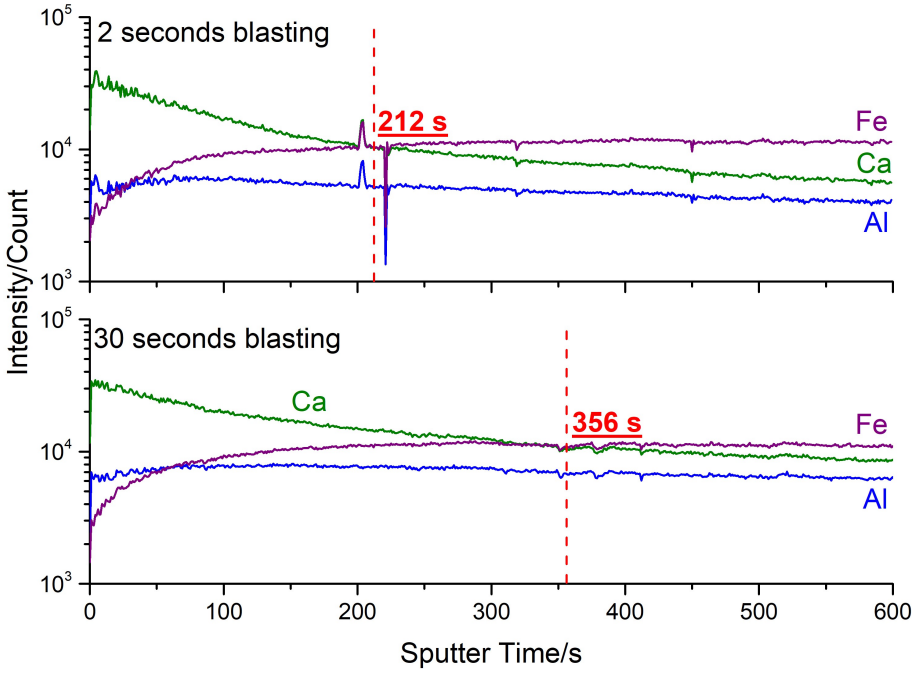

Fig. 5.21: TOF-SIMS depth profile of a S355 steel sample abrasive blasted for 2 s and 30 s, one on top of another for easy comparison. The etch time required for the iron and calcium signal to cross over is highlighted and labelled.

In Figure 5.21, the TOF-SIMS results are shown for a S355 steel surface that has been blasted for 2 seconds and 30 seconds by almandine garnet abrasive. For clarity, the most representative elements of iron, calcium, and aluminium are presented. Both profiles show that garnet-associated aluminium and calcium have a starting signature stronger than iron. With deeper etching, the iron signal increases. This shows that the main contributor to the iron signal is from the steel itself, instead of the iron-containing almandine garnet. The calcium signal is seen to rapidly diminish with respect to deeper sputtering, whereas the aluminium signal appears to be relatively constant.

The differences may be indicative of the different mode-of-adhesion between the two minerals, calcium carbonate and almandine garnet. The calcium carbonate may be spread thinly on the steel surface, hardly penetrating, despite its strong accumulation tendency. The etching easily removes this accumulated spread layer, leading to a more rapid decrease of calcium signal and

an increase of the iron signal; the steel below slowly 'unmasked'. Almandine garnet penetrates into the steel, rather than spreading and accumulating on the surface. Therefore despite deeper etching, the embedded mineral is continuously being etched away, and its secondary ions detected. This leads to the aluminium signal being relatively constant.

The difference in etching-times needed for equal intensity ('signal-parity') between iron (steel) and calcium (calcium carbonate) signals provides a qualitative test of abrasive resiude build-up with respect to blasting duration. A sample abrasive-blasted for 2 seconds has iron-calcium signal-parity at 212 seconds of sputtering/etching. In comparison, the sample blasted for 30 seconds achieves signal-parity in 356 seconds of etching, suggesting abrasive residue accumulation. Therefore there are indications of blasting-time dependence for the accumulation/penetration of the abrasive material on the blasted steel surface.

5.5.4 Elemental Mapping

The differences in elemental composition between garnet minerals and steel provides good contrast through backscattered electrons, enabling EDX elemental mapping to detect microscopic abrasive residues on the steel surface in high spatial resolution. It was therefore used to inspect the surface coverage of the abrasive material on the abrasive-blasted steel.

To simplify the analysis for abrasive residue surface coverage, the initial elemental map shown in Figure 5.22A had the steel-associated iron background removed while maximising the intensities of abrasive-associated elements, and the backscattered image map intensity minimised. The resultant image after processing can be seen in Figure 5.22B. This image is then analysed using the pixel-luminosity histogram generated by image analysis software ImageJ (National Institutes of Health, USA). The surface coverage by abrasive residue is determined using Equation 5.8, with $\%A_{\mathrm{G}}$ being the abrasive residue coverage, and $\%A_{\mathrm{LL}}$ being the percentile area of least luminosity in the histogram, i.e. black background region of exposed steel.

$$\%A_{\mathrm{G}} = 100\% - \%A_{\mathrm{LL}} \tag{5.8}$$

Blasting Duration- and Pressure-Dependence

In industry, there were two variables that can be easily controlled: blasting duration, as suggested by previous TOF-SIMS studies, and the blasting pres-

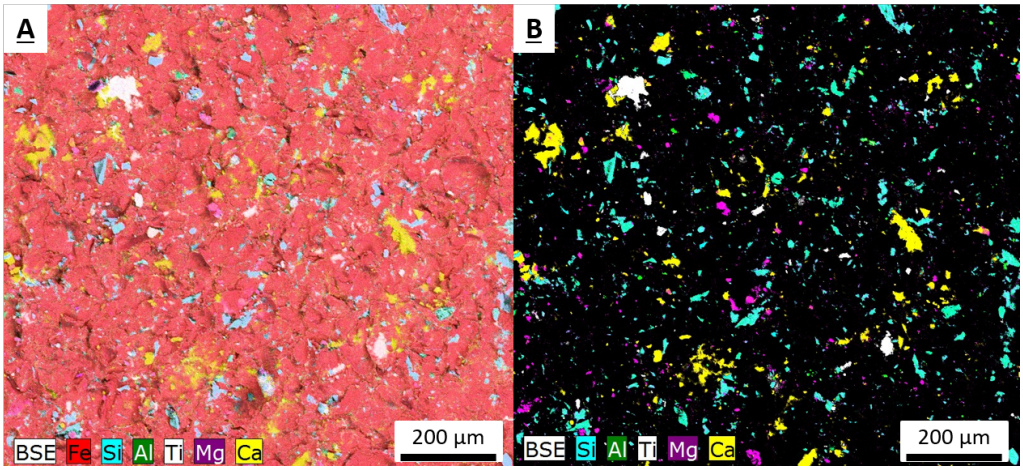

Fig. 5.22: Backscattered Electron (BSE)-EDX mapping of a S355 steel sample abrasive blasted for 10 s, with A) major elements, including the steel surface, represented, and B) garnet abrasive associated elements highlighted. The colours each element is associated with, and the scale, are shown at the bottom of each sub-figure.

sure. The sample is analysed using the elemental map processing to establish a profile between blasting residue surface coverage and the two variables.

Time Dependence

Figure 5.23 summarises the findings of abrasive residue surface coverage time-dependence analysis. There an initial rapid increase of residue surface coverage with respect to blasting duration and then plateaus at around 33% coverage. Therefore despite short blasting times, a significant percentage of the S355 steel surface would be covered with residue.

EDX spectra of steel surfaces blasted for different durations have been analysed. Qualitatively, Figure 5.24A shows that in comparison to the red line that represents a polished sample, garnet associated elements of aluminium, silicon, calcium, magnesium, and titanium appear to 'grow' with respect to longer blasting time. This agrees well with the surface coverage results. In Figure 5.24B, the EDX-determined elemental percentage variation with respect to blasting time is shown. Silicon and aluminium atomic percentages grow rapidly then plateaus, closely resembling surface coverage data in Figure 5.23. Atomic percentage of calcium rapidly rises initially but then falls. This can be attributed to the calcium (carbonate) species depositing only to the surface, with little penetration.

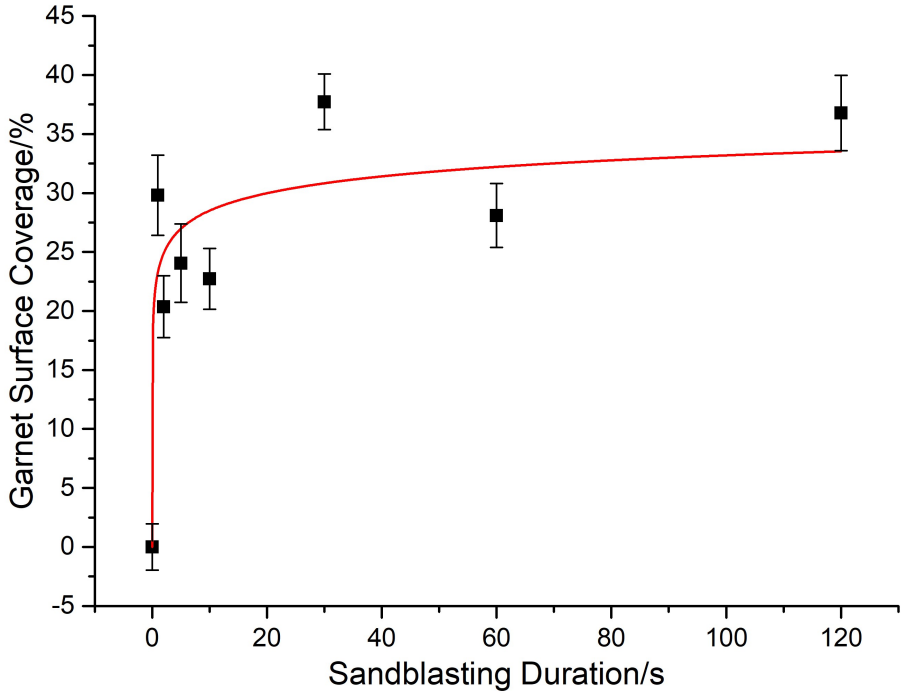

Fig. 5.23: Garnet abrasive residue coverage on S355 steel coupon with respecting to blasting duration, derived from BSE-EDX analysis.

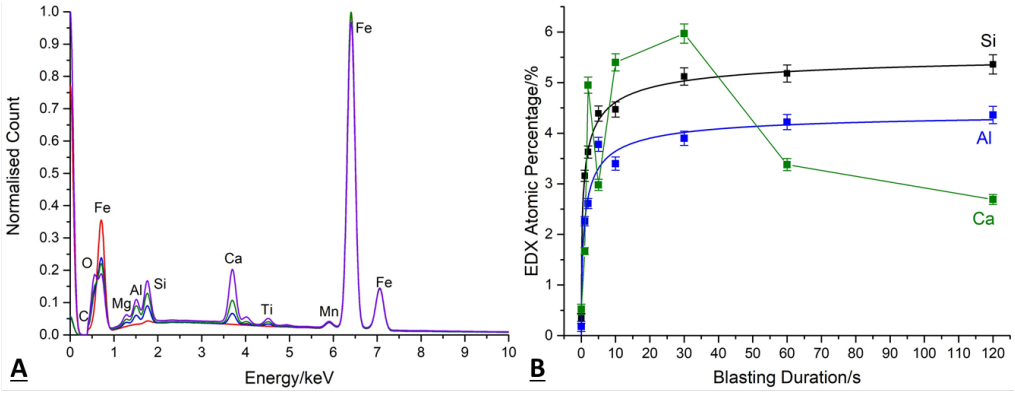

Fig. 5.24: A) EDX spectra compilation of steel surface blasted for different durations with garnet abrasive. Red: polished; blue: 1s blasting; green: 5 s blasting; purple: 30 s blasting. B) EDX determined elemental percentages of almandine garnet associated elements.

XPS analysis results are shown in Figure 5.25. Samples blasted for 1 second and longer are surveyed and the presence of garnet associated elements is established rapidly. The aluminium and silicon content each plateau quickly.

The atomic percentages derived from XPS do not appear to be as high as the EDX survey derived values. Calcium percentage rises rapidly and plateaus at 10%. This is higher than the maximum 6% seen in EDX. The results for the three elements indicate their different modes of surface attachment. The harder almandine garnet embeds into the steel surface readily, therefore the surface-sensitive XPS only partially surveys the residues top-part whereas the more penetrative EDX analysis is able to survey the embedded mineral entirely, with a higher aluminium and silicon percentage. Calcium carbonate conversely is less penetrative, hence much more highly represented in the surface sensitive XPS. This difference of experimental results shows the importance of using multiple techniques to verify surface analyses conclusions.

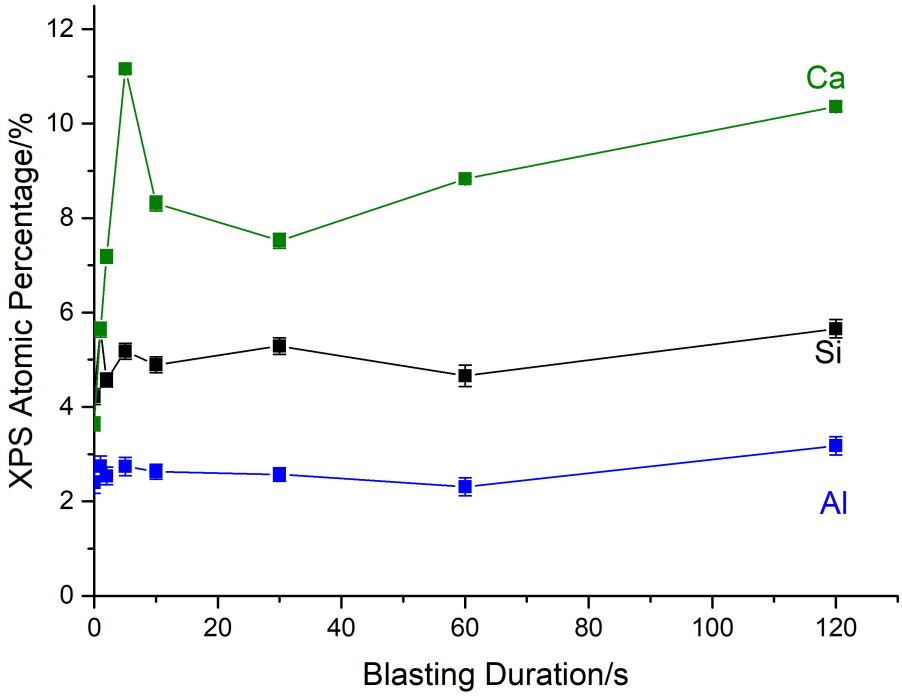

Fig. 5.25: XPS derived atomic percentages of garnet associated elements with respect to abrasive blasting durations.

In Figure 5.26A, EDX and XPS results are compared against each other. All the garnet associated elements on steel are seen to rapidly increase and quickly plateaus with longer blasting times. Though values differ slightly, especially for calcium (whose reasons have already been discussed) both techniques generally agree.

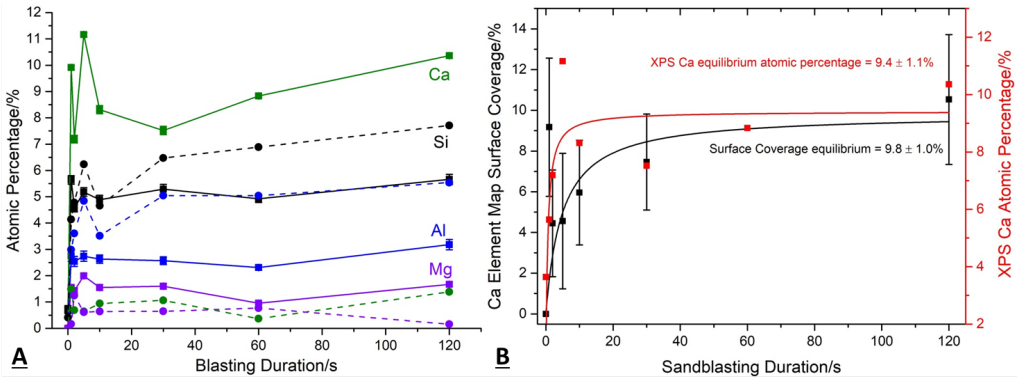

Fig. 5.26: Comparison of results and general trends between surveying techniques, with A) the atomic percentages derived between XPS (square icons, solid lines) and EDX (circle icons, dashed lines), and B) calcium 'coverage' of blasted S355 steel surface between XPS and EDX elemental mapping.

By plotting elemental maps of calcium surface coverage data alongside XPS atomic percentage analysis, as represented in Figure 5.26B, elemental mapping surface coverage results are shown to agree with surface-sensitive XPS data. The techniques therefore show up to 10% of the blasted S355 steel surface is covered by calcium carbonate and up to a third of the surface is covered by abrasive residue (inclusive of calcium carbonate).

Calcium is therefore over-represented in comparison to the quoted bulk composition in abrasive of approximately 1.5%. A model to attempt explaining this phenomenon is proposed below, based on the relative hardness of the substrate and the blasting material. This comparison of results also confirms the high surface sensitivity proposed for the elemental mapping image analysis.

Pressure Dependence

Blasting pressure was varied to 'clean' the steel substrate, under constant blasting time (30 seconds). The blasting residue surface coverage with respect to blasting gun pressure is represented in Figure 5.27. There appears to be no significant variation between blasting pressure and residue coverage. A possible explanation being that at low pressures, the hard almandine garnet particles are sufficiently energetic in removing existing surface materials but not enough to embed into the steel significantly. Whereas at higher pressures, embedment is possible but the frequency of incident abrasive removing existing residues increases, leading to a lack of pressure dependence

in surface coverage.

Nevertheless, the steel surface appears to be visibly 'cleaned' and conforms to industry standards of ISO 8501-2:1994.[129] This means lower pressures down to 20 psi may be suitable for effective cleaning of millscale- or paint-covered surfaces, therefore significantly reducing the amount of power needed.

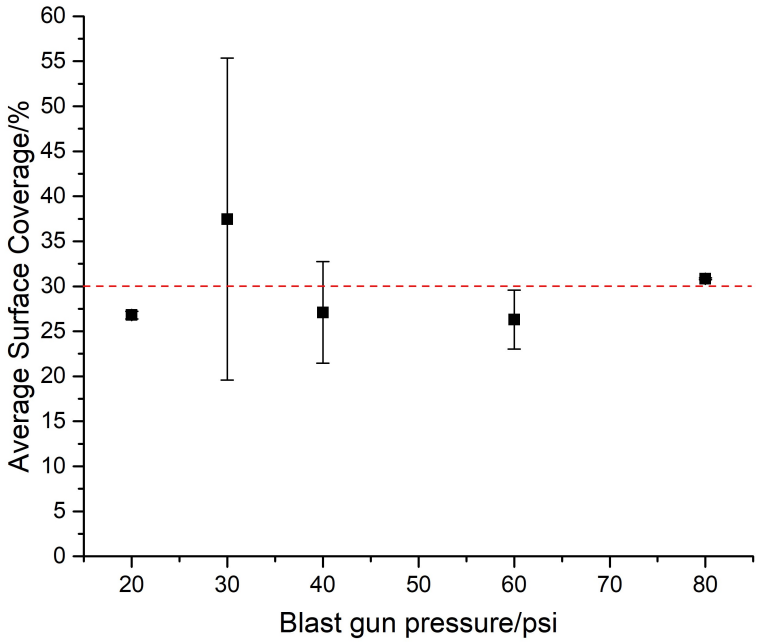

Fig. 5.27: Variation of abrasive residue surface coverage, determined from EDX elemental map image analysis, with respect to blasting gun pressure.

Abrasive-Attachment Model

A model of surface incorporation of abrasive residue is proposed using the relative hardness of the different minerals present in the naturally-derived garnet abrasive. In the Mohs scale of relative hardness, defined and ranked by the ability of a material to scratch the surface of a softer material, hard almandine garnet has a Mohs value of 7.5,[130] softer carbon steel of 4 to 4.5 (iron oxides 5.5),[131] and calcium carbonate of 3.[132] This difference of hardness is proposed to significantly change the behaviour when abrasive materials impact the S355 steel substrate.

When harder almandine garnet collides onto the softer steel substrate, the angular particles impact and rebound off the surface, carrying some of the

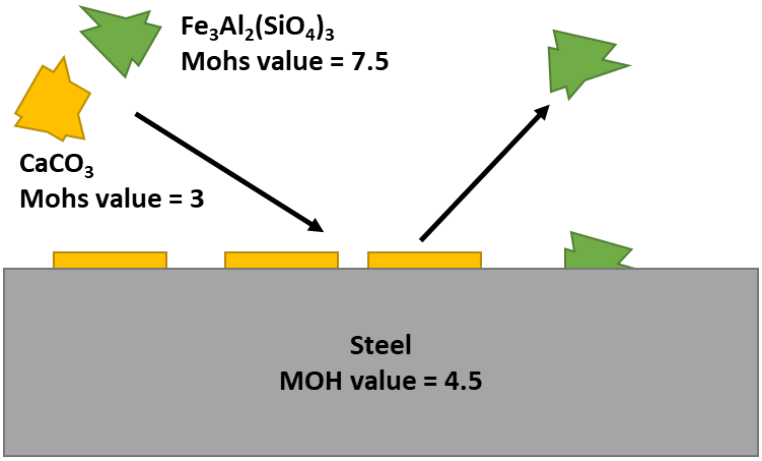

Fig. 5.28: Cartoon of proposed dynamic surface modification of S355 steel by the almandine garnet abrasive blasting.

rust and old paint. Or a portion of particles could collide and embed into the softer steel material. This interpretation is supported by the previously presented XPS, EDX and TOF-SIMS data.

Calcium in the form of calcite is softer than steel. Therefore when impacting the harder steel surface, the mineral deforms and is 'spread' across the steel surface. Incoming calcite either accumulates into slightly thicker layer on the surface, or some calcite is chipped off by subsequent impacting almandine garnet. This dynamic deposition and removal of abrasive residues leads to the equilibrium coverage seen in Figure 5.23. As a result of this 'spreading' deformation, the calcite covers a disproportionally larger surface than its bulk percentage in the abrasive. This is reflected by data obtained from high surface sensitive techniques such as XPS and elemental mapping analyses. The thinly spreading calcite profile is supported by TOF-SIMS data. A schematic of the proposed abrasive action model on the steel surface is summarised by Figure 5.28.

Persistence of Abrasive Material on Surface

It is interesting to see in what manner residue already on the surface may detach. S355 steel samples abrasive blasted for 30 seconds are exposed to various surface cleaning treatments: 120 seconds of nitrogen jet cleaning ('Airjet clean'), 120 seconds soaking in ultrapure water and nitrogen jet blow-dried for 120 seconds ('Rinse'), and 120 seconds sonication in ultrapure water

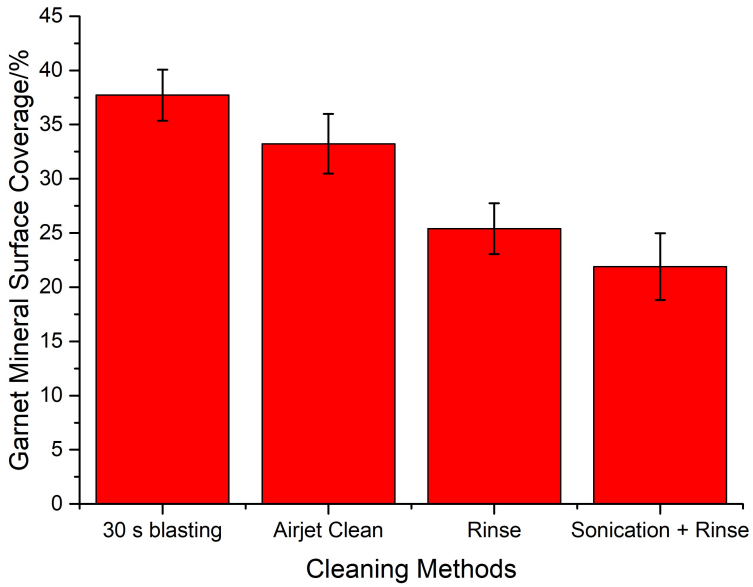

Fig. 5.29: Abrasive residue surface coverage, through elemental map analysis, after different post-blasting surface cleaning methods.

and nitrogen jet blow-dried for 120 seconds ('Sonication + Rinse').

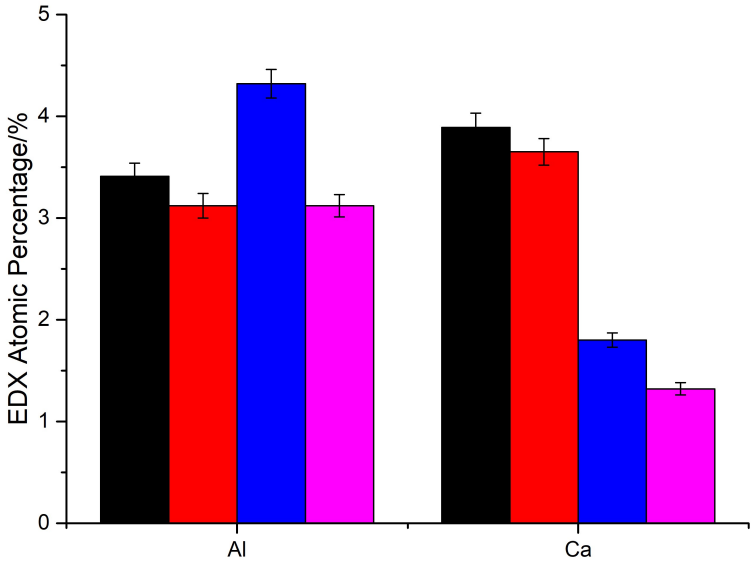

Fig. 5.30: Surface aluminium and calcium content derived by EDX spectra, after different post-blasting surface cleaning methods. Black: 30 s abrasive blasting, Red: 'Airjet Clean', Blue: 'Rinse', Magenta: 'Sonication + Rinse'.

The effectiveness of cleaning methods, compared to a control of 30 seconds abrasive blasted sample, is presented in Figure 5.29. With increasingly 'vigorous' methods of cleaning, the surface coverage by abrasive residue decreases. Nitrogen cleaning alone fails to significantly reduce the residue surface coverage. Soaking in ultrapure water and the extremely aggressive ultrasound sonication cleaning is more effective by comparison. However, despite the forceful cleaning of sonication, approximately 20% of the steel surface remains covered. The results show the blasting material has a strong chemical and/or mechanical attachment to the surface.

EDX spectra analysis reveals the change of elemental content for each cleaning method in removing abrasive residues. In Figure 5.30 results for aluminium, representative of almandine garnet, and calcium, representative of calcium carbonate in the abrasive are shown. The aluminium content remains relatively constant despite the increasing vigour of the cleaning methods. Calcium content is significantly reduced under more forceful cleaning methods with water involved. This result is indicative of either weaker calcium carbonate binding onto the steel surface, or the immersion in water may have led to dissolution of calcium carbonate. In summary, abrasive residue removal from the post-blasting steel surface is extremely difficult.

Industrial Sample Investigation

In additional to the laboratory-based investigation of abrasive-blasted steel samples, it is important to try finding direct evidence of abrasive material presence at the steel-paint interface in industrial samples. Samples provided by Royal Dutch Shell from the Brent oil sites in the North Sea were analysed. The samples were treated with standard industrial procedures of blasting, application of a primer, and a top coat of International Interseal 670HS paint.
To preserve any abrasive remaining at the steel-paint interface, the paint layer was removed gently. The painted samples were immersed in N-methyl pyrrolidone (NMP) for a week to lift the paint layer from the steel without application of external force. The remaining steel substrate and the peeled paint, as seen in Figure 5.31, were then immersed in acetone for a day to aid easy drying in a vacuum desiccator. Both steel and paint surfaces were subsequently analysed using BSE-EDX elemental mapping.

For the steel, elemental maps relevant to garnet abrasive and paint are given in Figure 5.32, showing regions where various elements are concentrated. In the full colour map, zones of red (iron) are seen, associated with the steel

Fig. 5.31: Left: steel substrate with Shell coating gently peeled-off after immersion in N-methyl pyrrolidone. Right: Peeled off paint from the painted steel sample.

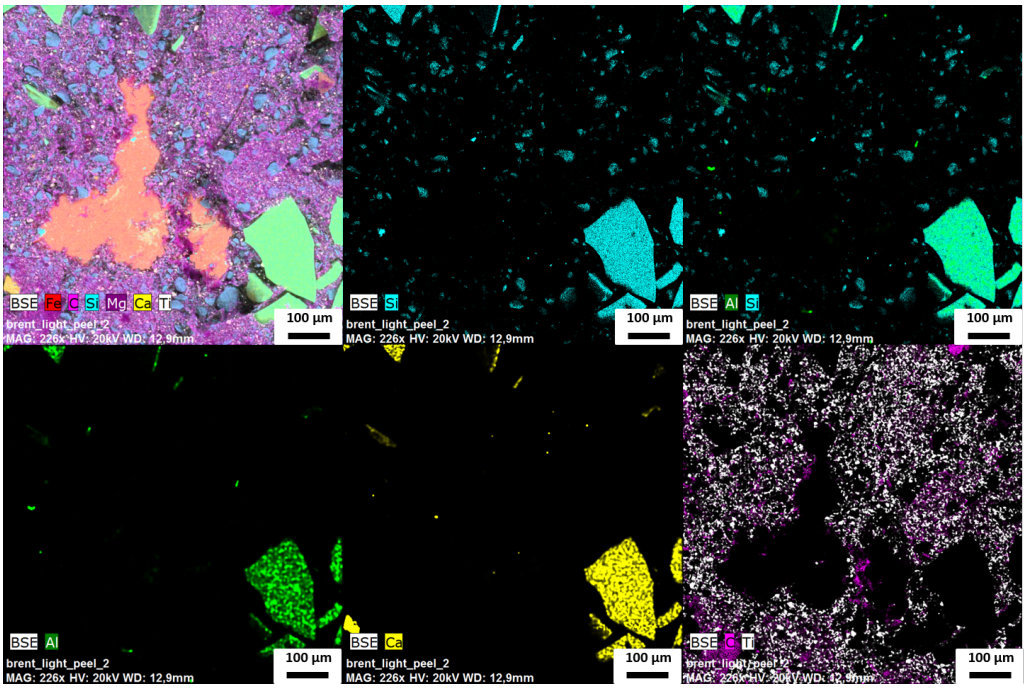

Fig. 5.32: BSE-EDX elemental mapping of the steel. Clockwise from top left: Full colour elemental map with keys to all elements on the bottom left corner, high contrast images of silicon, aluminium & silicon, aluminium, calcium, carbon & titanium maps.

metal. The map shows that through gentle removal of paint, some of the bare metals is exposed. The steel zones are surrounded by pink regions rich

in carbon, associated with paint that has not been peeled off. The carbon regions are heavily associated with much titanium content. Previous analysis of blasted steel shows titanium, from ilmenite, to be a minor component on the surface. Therefore it is unlikely for the titanium to originate from the abrasive blasting. Rather it is some titanium-containing component that has been incorporated into the paint, possibly titanium oxide (TiO_2) common in coating formulations.[133]

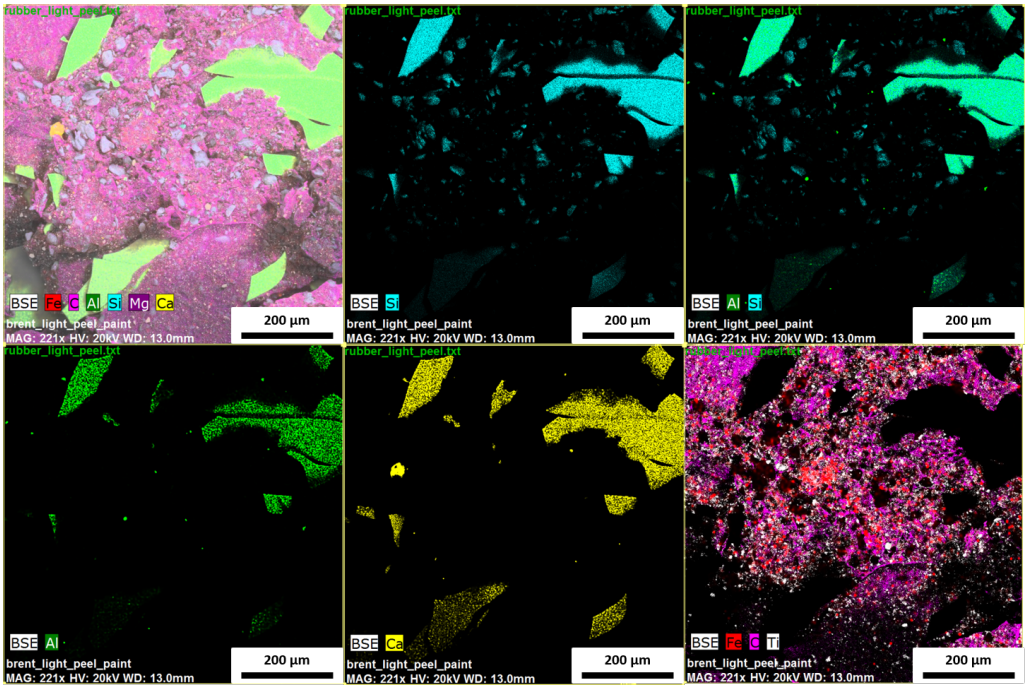

Fig. 5.33: BSE-EDX elemental mapping of the paint. Clockwise from top left: Full colour elemental map with keys to all elements on the bottom left corner, higher gamma images of silicon, aluminium & silicon, aluminium, calcium, carbon & titanium & iron maps.

Abrasive-associated elements are surveyed. Aluminium, silicon, and calcium are associated in discrete regions apart from the steel and paint. These elements are representative of the almandine garnet and calcium carbonate in the abrasive. The localisation of these elements in particular regions, present in both paint- and steel-zones, is strongly indicative of garnet abrasive presence at the steel-paint interface; that the abrasive blasted samples prepared in the lab reflects 'real' industrial samples with significant abrasives residues.

The peeled-off paint is also analysed. The elemental mapping of paint and

garnet abrasive elements are shown in Figure 5.33. The background is dominated by the pink region denoting carbonaceous regions of paint which are associated with titanium. Iron regions are not generally coincidental with silicon and aluminium. Therefore it is unlikely to be from the almandine garnet mineral (also containing iron). Instead it suggests iron oxides native to the steel surface being 'ripped off', revealing a strong affinity between steel surface iron oxides and paint.

In both Figures 5.32 and 5.33, there are no signs of paint residue (i.e. carbon-rich regions) at the garnet associated zones. A possible explanation is the cleavage of garnet being one of the likely routes for paint detachment from the steel, the abrasive forming the weakest link at the steel-paint interface.

5.5.5 Summary of Results

Surface analyses of untreated, polished, and abrasive blasted S355 steel have been outlined. A native surface iron oxide layer on the steel is confirmed. A detailed analysis of this layer has been conducted through XPS and EBSD. A variety of surface iron oxides have been found on the carbon steel which may explain its poor corrosion resistance. Using well-known literature values, the surface chemistry of steel has been inferred, including the average surface group density and oxidation state.

Natural almandine garnet abrasive-blasted steel samples have been analysed. Elemental mapping analysis reveals significant microscopic abrasive residue coverage on the steel surface. Blasting time- and pressure-dependence experiments have been conducted. For blasting time-dependence, it is found that a dynamic equilibrium of residue surface coverage is quickly reached, with approximately a third of the surface covered. No obvious correlation between surface coverage and blasting pressure is seen. Samples provided by industry have been analysed. Garnet abrasive has been found to be present at the steel-paint interface and have formed likely failure points for the coating. The results imply paint adsorption onto *both* the steel and the abrasive must be taken into account.

It is found when compared to its low bulk composition within the abrasive, calcium carbonate is over-represented on the blasted surface. The difference in response in sample depth profiling, and attempted surface 'cleaning' of abrasive residue, between calcium carbonate and almandine garnet has led to a suggested mode-of-attachment for the abrasive minerals. The harder almandine garnet embeds into the softer steel. Whereas the softer calcium

carbonate impacts upon the harder steel and deforms, 'spreading' itself over the blasted surface resulting in a much larger surface coverage footprint than its bulk composition would suggest.

6. CHARACTERISATION OF ALMANDINE GARNET ABRASIVE SURFACE

6.1 Introduction

Naturally-derived almandine garnet abrasive is used to blast the steel surface in order to remove old paint and corrosion products. With the steel surface already characterised, this chapter details the characterisations conducted to better understand the almandine garnet ($[Fe_3Al_2(SiO_4)_3]$) surface, towards determining the adsorption chemistry with other organic or inorganic species.

Almandine garnet mineral exhibits a cubic crystal structure with a space group of $Ia\bar{3}d$. Within the mineral, the iron (II) ions are eightfold coordinated within triangular dodecahedral sites, the aluminium (III) ions are sixfold coordinated within octahedral sites, and the silicon (IV) ions are fourfold coordinated in tetrahedral sites. The coordination sites are illustrated in Figure 6.1, in which iron (II) ions are seen to be in large dodecahedral 'voids' within the aluminosilicate framework. There are no known preferential cleavage planes for the mineral. The almandine garnet surface is to be characterised for the influence of possible iron, aluminium, and silicon surface functionalities due to the absence of any cleavage crystal planes to infer the surface chemistry.

6.2 Experimental

6.2.1 Materials

The original 80 mesh (177 mum) almandine garnet powder supplied by GMA Garnet, Australia, was milled using a Retsch Planetary Ball Mill PM100 to maximise the mineral surface-to-volume ratio for future experiments, in 60 g batches within a 125 mL tungsten carbide jar with seven 20 mm tungsten carbide milling balls. Each batch was done for 20 min at 500 rpm, switching milling direction at 10 minute intervals to prevent compacting the powders making future use difficult.

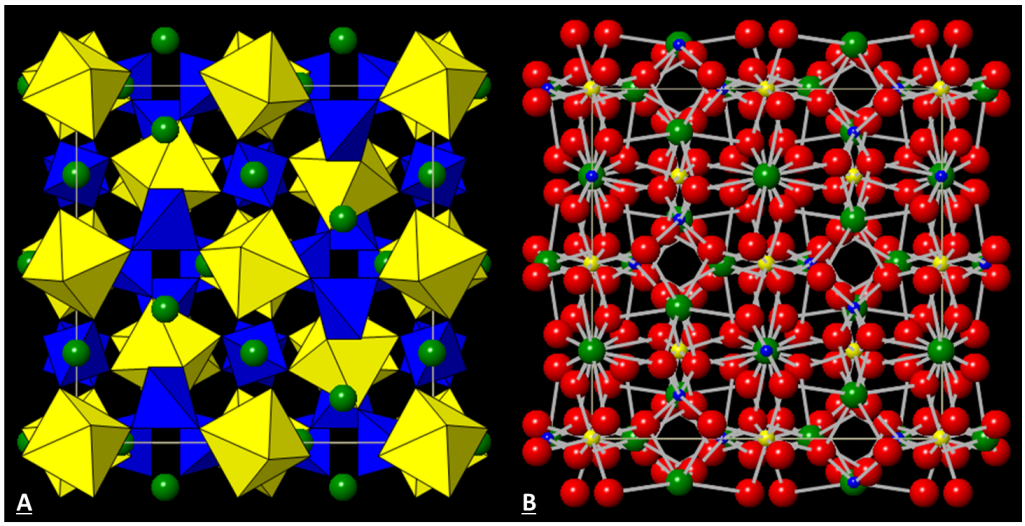

Fig. 6.1: The crystal structure of almandine garnet with A) a polyhedral representation and B) a ball-and-stick representation. Green: iron, Yellow: aluminium, Blue: silicon, Red: oxygen. The yellow octahedrons are AlO_6 units and blue tetrahedrons are SiO_4 units.

The garnet powders were acid-washed using 10%/wt nitric acid solution - 69%/wt nitric acid diluted with ultrapure water. 24 g batches of ball-milled garnet powder was washed with 30 mL of 10%/wt acid and tumbled for 24 hrs, to eliminate possible contamination from other mineral impurities listed in Table 5.2. Initially, evolution of gas, presumably carbon dioxide from calcium carbonate contaminant neutralisation, was observed when acid was added. High weight-percentage acid solutions were chosen to ensure that acid was in excess for complete calcium carbonate neutralisation. This acidic suspension, at pH 1, was then continuously stirred until no visible effervescence was observed, before being left to equilibrate. The suspension was centrifuged using a Thermo Scientific Heraus Multifuge 1 S-R, under a centrifugal force of 15000 g for 30 minutes. The acidic supernatant was discarded and the powder washed five times (50 mL each) with ultrapure water. Each washing step involved the re-suspension of solids, equilibration for 1 hour, and re-centrifugation. Washed solids were then spread on a clean glass petri dish and dried under reduced pressure at 100 °C for 6 hours. The acid-washed garnet has a nitrogen BrunauerEmmettTeller (BET) specific surface area of 5.54 ± 0.03 m^2g^{-1}, a reduction from the 6.38 ± 0.01 m^2g^{-1} when the mineral was first milled, attributed to the loss of finer particles in the acid-washing process.

Almandine garnet surfaces were polished using successively finer diamond paste like those for S355 substrates in Chapter 5, except down to a 100 nm roughness for reflectivity measurements. The washing procedure to remove diamond residues was also similar except the polished garnet substrate was first washed with 2% Decon 90 solution instead of neutracon, as the mineral is not prone to corrosion by Decon 90, unlike carbon steel.

All chemicals are sourced from Sigma-Aldrich unless stated otherwise. Solutions are all made with ultrapure water. (18.2 MΩ cm^{-1} resistivity) High precision pH indicator paper from Sigma-Aldrich is used for pH measurements unless stated otherwise.

6.2.2 Equipment

All experimental instruments were detailed in Chapter 4 unless specifically stated otherwise.

Powdered X-ray Diffraction (PXRD)

PXRD was performed using a D8 Advance Powder Diffractometer, Bruker, using a copper source, with a wavelength of approximately 1.54Å, at the Department of Earth Sciences, University of Cambridge.

6.3 Almandine Powder Characterisation, Surface Treatment, and Dissolution

The natural mineral in the abrasive was analysed through Powder X-Ray Diffraction (PXRD). The results was in good agreement with known almandine garnet spectrum as shown in Figure 6.2.[134,135] Natural garnet abrasive was virtually entirely made out of almandine garnet, with other mineral 'contaminants' (calcium carbonate, ilmenite, silica, Table 5.2). The garnet powders were acid-washed prior to experimentation to remove these impurities. Interestingly, the natural garnet (with other minerals) PXRD spectrum is identical to those of samples which have been 10%-nitric acid-washed garnet powder. Therefore, while PXRD is able to confirm that the major crystal contributor to be almandine garnet, it is insensitive to other very minor crystal mixture components.

The milled garnet powder was characterised with SEM. Particle sizes were reduced from 80 mesh (177μm) to below 20 μm as shown in Figure 6.3 This

significantly increases the mineral surface-to-volume ratio which is useful for adsorption experiments.

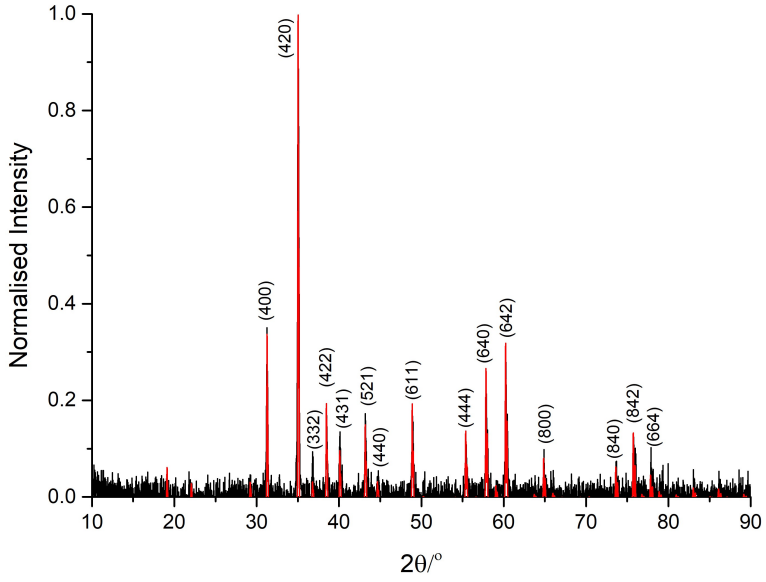

Fig. 6.2: Powder X-ray Diffraction pattern of the garnet powder (black), compared with a database almandine garnet spectrum (red). Miller indices are added for the most prominent peaks for reference.

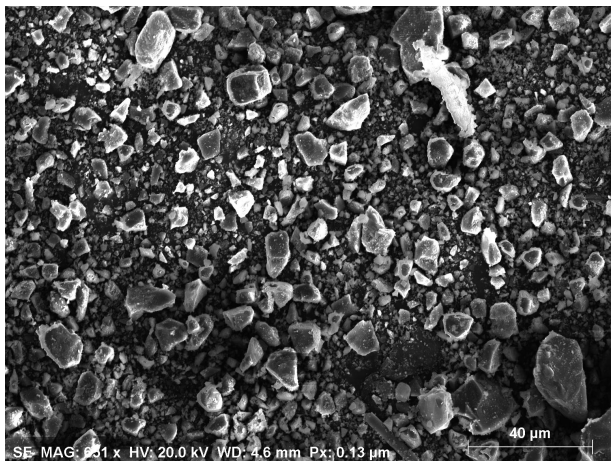

Fig. 6.3: SEM image of ball-milled almandine garnet powder. Powder was sputtered with a thin layer of gold to improve conductivity.

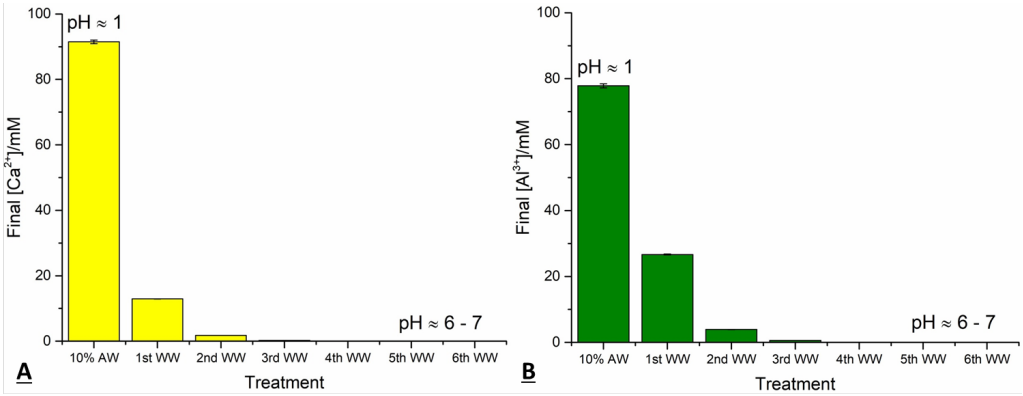

Fig. 6.4: A) Calcium and B) aluminium levels in consecutive washings of 24 g of garnet. AW: 30 mL 10%/wt nitric acid wash, WW: 30 mL ultrapure water wash.

6.3.1 Acid-Washing

The acid-washing process of the milled garnet powder was monitored by measuring the supernatant aluminium and calcium levels using ICP-OES. The results can be seen in Figure 6.4. In the acidic solution (pH 1), calcium and aluminium are detected, indicating calcium carbonate and almandine garnet dissolution into the extremely acidic solution. In further water washings ('WW') the calcium and aluminium solution concentrations decrease. By the sixth water wash, the levels are undetectable by the technique.

EDX analysis reveals that calcium content remains present within the milled-mineral as seen in Figure 6.5. This, in combination with the lack of detectable calcium in final washing solutions, suggests the calcium is contained *within* the particles themselves and cannot be dissolved away. The result means calcium content is unlikely to contaminate any solution that the particles are to be immersed in.

6.3.2 Dissolution Study

Acid-washed almandine garnet powder, with 2.0 g per sample each placed in a centrifuge tube, was mixed with 10 mL 9 mM nitric acid in 100 mM sodium nitrate solution for different durations. The samples were then centrifuged under 15000 g force for 30 min. The supernatant was carefully withdrawn using a pipette. Half of the supernatant was analysed using ICP-OES and the other half had pH tested with a pH probe.

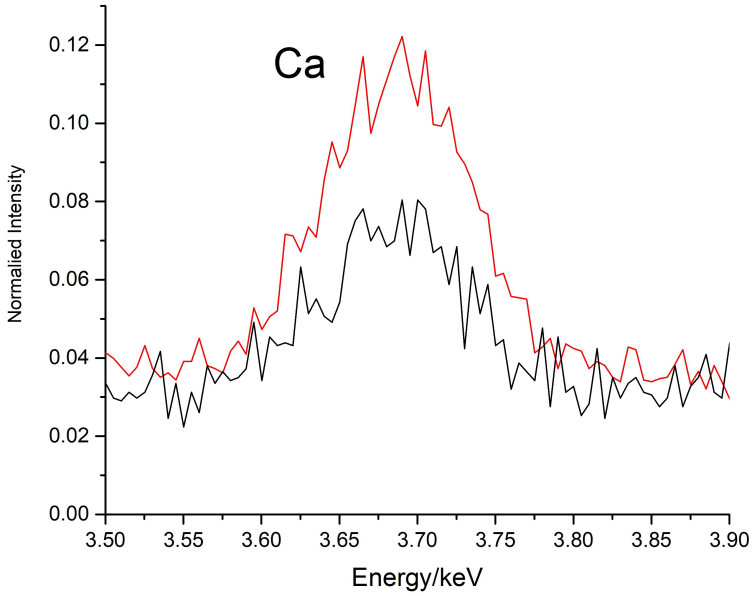

Fig. 6.5: Normalised EDX calcium spectra of unwashed (red) and acid-washed (black) milled almandine garnet.

Using the calcium and aluminium ion concentrations, the mass of mineral dissolved can be calculated with the chemical formulae of almandine garnet ($Fe_3Al_2(SiO_4)_3$) and calcium carbonate ($CaCO_3$). Figure 6.6 shows the progression of mineral dissolution with increasing equilibration time. All samples tested had a pH of 1.98 ± 0.09. The figure shows that almandine garnet does indeed dissolve at very low pH. The dissolution appears to be initially fast then gradually slows down. Up to 0.33 g (out of 2.0 g) of almandine garnet is dissolved in very long timescales (96 hrs). Therefore cautious interpretation of experimental data under long equilibration times should be employed, as the adsorption equilibrium will likely be influenced by the dissolved ions.

In Figure 6.6, there is no evidence of any significant detectable calcium dissolution (green markers) into the acidic solution, even at long equilibration timescales. The result demonstrates the effectiveness of the acid-treatment; even at low pH values calcium dissolution into the solution is unlikely, and in high pH solutions it is even less likely due to lower solubility in basic conditions.[136]

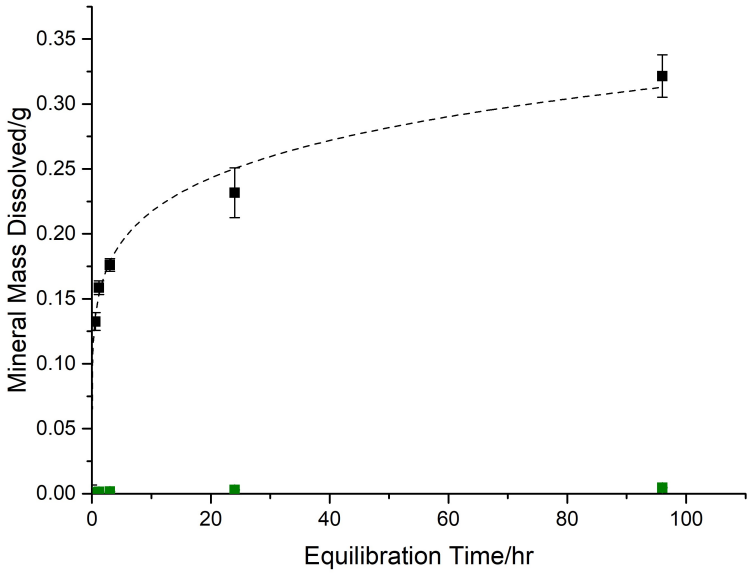

Fig. 6.6: Dissolution of acid-treated garnet powder in 100 mM sodium nitrate solution at pH 2. Black: almandine garnet; green: calcium carbonate.

6.3.3 Summary of Results

The acid-cleaning of the ball-milled almandine garnet powder surface is shown to prevent solution contamination by calcium species. Dissolution study cautions against exposing the substrate to extremely acidic pH if possible.

6.4 Surface Titration

A typical 'titrating up' curve of an acid-washed garnet powder suspension can be seen in Figure 6.7. Inflection points (pK_a = pH, in blue) and points of highest gradient (equivalence points, in red) can be seen. Through multiple measurements, the first (pK_{a1}) and second (pK_{a2}) equilibrium acid constants in different background electrolyte concentrations (10, 50, 100 mM sodium nitrate) are determined to be 4.43 ± 0.26 and 6.13 ± 0.21 respectively for garnet surface groups. The surface group density is calculated to be of 0.95 ± 0.16 sites nm^{-2} (i.e. 110 ± 21 Å site^{-1}, using Equation 4.3 in Chapter 4) in said experimental conditions, should sodium nitrate be an indifferent electrolyte. The pK_a values obtained suggests a 'pristine' point of zero charge (PZC) to be 5.28 ± 0.33,[32] (Equation 4.11) similar to the literature-listed value, around 4.5, for an unbuffered solution.[137]

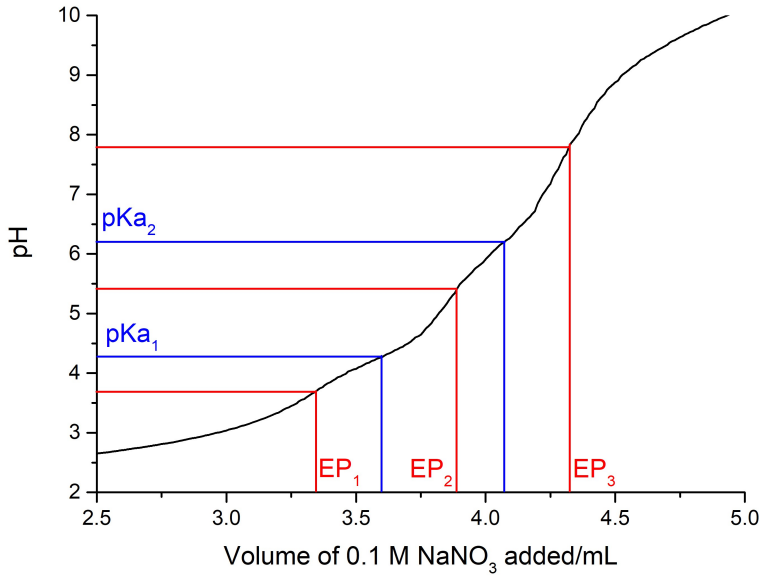

Fig. 6.7: Typical surface titration response of acid-treated garnet, in 100 gL^{-1} suspension in 100 mM sodium nitrate solution. This titration is at a speed of 0.06 mL min^{-1} using 100 mM sodium hydroxide solution. Locations deriving acid constants (blue) and equivalence points (red) are labelled.

The pH responses, with varying acid/base titrant solution concentration (TOTH), under different supporting electrolyte concentrations, can be seen in Figure 6.8. The PZC is the intersection between the solid-less 'blank' and solid-containing titration curves (Equation 4.10). The PZC is determined to be 4.70 ± 0.02, a closer agreement than the 'pK_a-derived' value to the literature PZC titrated by sodium hydroxide (NaOH) and perchloric acid ($HClO_4$).[138] The sodium cation and perchlorate anions are assumed to be inert electrolytes. Inert electrolytes are ions that do *not* specifically adsorb onto the substrate surface.

Considering PZC values of other almandine garnet related-minerals: silicon dioxide have a PZC ranging from 1.6 for quartz to 3.4 for vitreous silica.[139] Aluminium-based oxides have PZCs around 8 to 10.[140,141] Iron oxides have PZCs around 8 to 10, though natural ferrihydrite ($Fe_2O_3 \cdot 0.5\ H_2O$) having PZCs around 5.3 to 7.5.[142] The results listed for aluminium- and iron-oxides are rather higher than the PZC determined in these titration experiments. Hence a novel use of XPS was used to address the surface chemistry, to be outlined later.

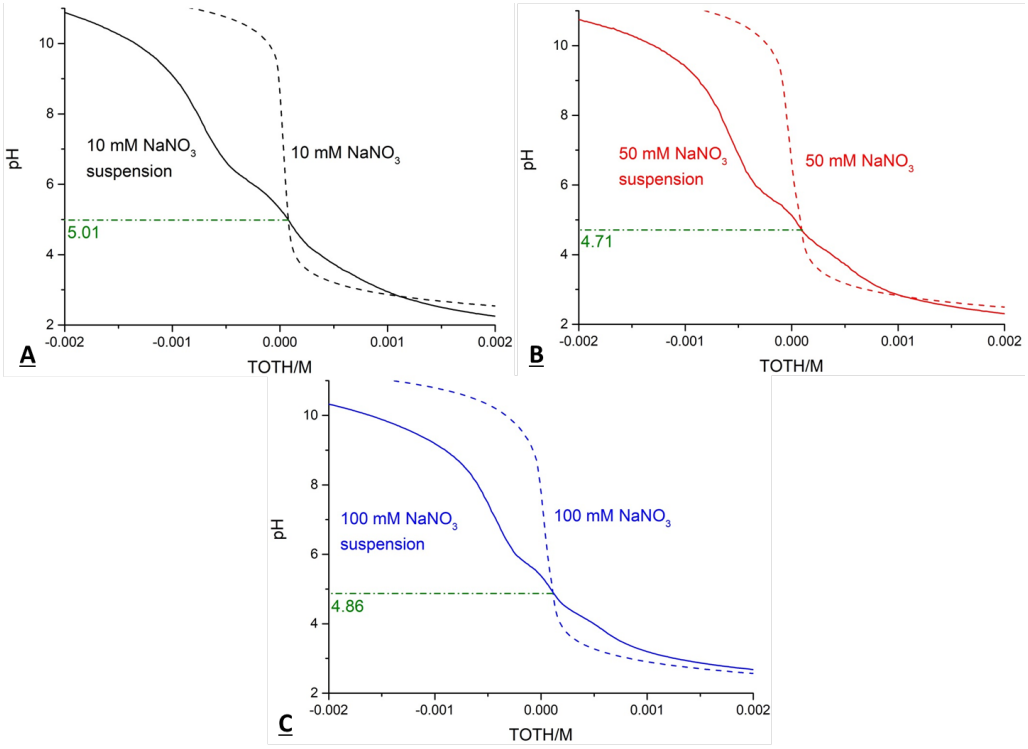

Fig. 6.8: Surface titration for PZC-determination, in 100 gL^{-1} suspension in different concentrations of sodium nitrate supporting electrolyte: A) 10 mM; B) 50 mM; C) 100 mM. Titration speed: 0.6 mL titrant min^{-1}. Dotted line: 'blank' solution without solids; solid line: 100 g L^{-1} acid-washed garnet-suspension

6.5 Zeta-Potential Measurements

Surface titrations are complimented with ζ-potential measurements, electrokinetics experiments that determine Isoelectric Points (IEPs). In inert electrolytes, PZC and IEP values coincide.[143]

ζ-Potential experiments in a range of supporting electrolyte (sodium nitrate and sodium chloride) concentrations are displayed in Figure 6.9. ζ-Potential is seen to be positive at low pH values, in line with literature observations.[126] Almandine garnet surface groups exposed to pH lower than its PZC/IEP are protonated, leading to a net positive surface charge. At higher pH values, above the PZC/IEP, the garnet surface groups are deprotonated and form a negatively-charged surface. This is true for all three background electrolyte concentrations and the two supporting electrolytes tested. The three

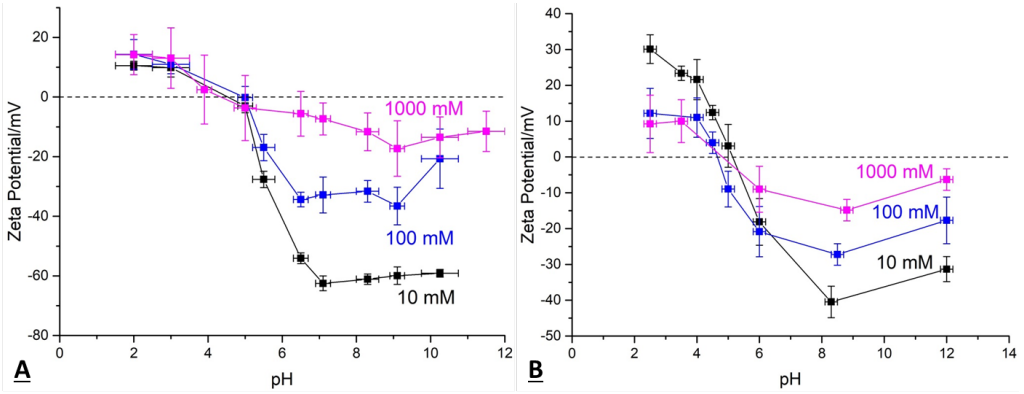

Fig. 6.9: Zeta potential measurements taken for the 1.0 g L^{-1} suspensions of almandine garnet powder in different electrolyte concentrations.

ζ-potential responses are seen to practically intersect at the same pH point, the IEP. The IEP of almandine garnet in sodium nitrate is determined to be 4.64 ± 0.41 (Figure 6.9A), in agreement with surface titration PZC results in sodium nitrate.

In sodium chloride electrolyte, the IEP is around 4.86 ± 0.25 (Figure 6.9B). This is in good agreement with surface titration PZC and sodium nitrate IEP data. The results prove that sodium chloride to be an electrolyte that share similar adsorption behaviour (if any) to sodium nitrate.[144] Further adsorption studies and numerical rationalisations are outlined later in Chapter 11.

6.6 XPS

6.6.1 Depth Profiling

XPS was used to gauge the chemical environment on a polished almandine garnet surface. To compare the composition of the surface to the bulk, depth profiling into the mineral was conducted. The results are shown in Figure 6.10.

The oxygen, silicon, aluminium, magnesium, and calcium content remains constant throughout. The initially higher (then decreasing) iron content near the surface may indicate more contributions to surface groups than in the bulk. Overall, the elemental composition is relatively constant with depth into the sample.

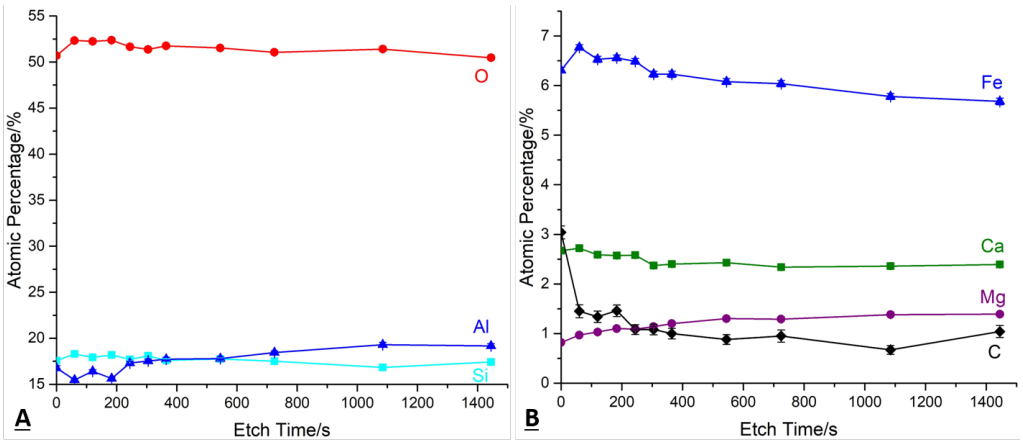

Fig. 6.10: XPS depth profiling elemental survey of polished almandine garnet for A) major and B) minor elements in the spectrum. All sampling was done with the incoming x-ray beam normal to the surface (i.e. 0° stage tilt).

The initial rapid fall of carbon content with etching times indicates a surface layer of adventitious carbon. Further etching into the bulk leads to a plateau at 1% atomic percent, attributed to trapped carbonaceous within the natural garnet mineral. The magnesium content is likely to be due to pyrope, a mineral common in almandine garnet deposits.[145]

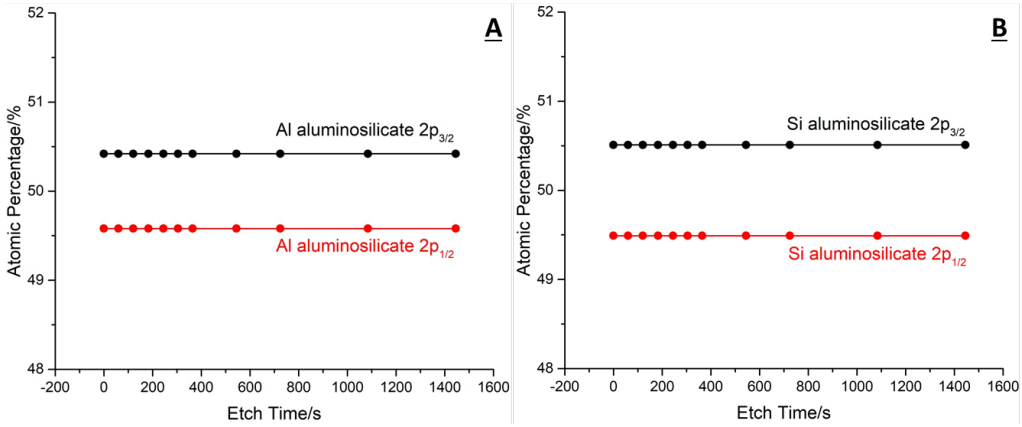

Fig. 6.11: Component fitting results of multiplet peaks for A) Al 2p, B) Si 2p peaks depth profiling, at a sampling angle normal to the surface (0°).

The chemical environments for aluminium, silicon, and iron peaks were analysed to capture any changes to surface chemical environments that would

influence oxygen 1s peak fittings (for 'surface', 'bulk', and adsorbed water species). In Figure 6.11, it can be seen that the chemical environments for aluminium and silicon are constant with increasing depth. Both elements are dominated by its aluminosilicate framework in the bulk.

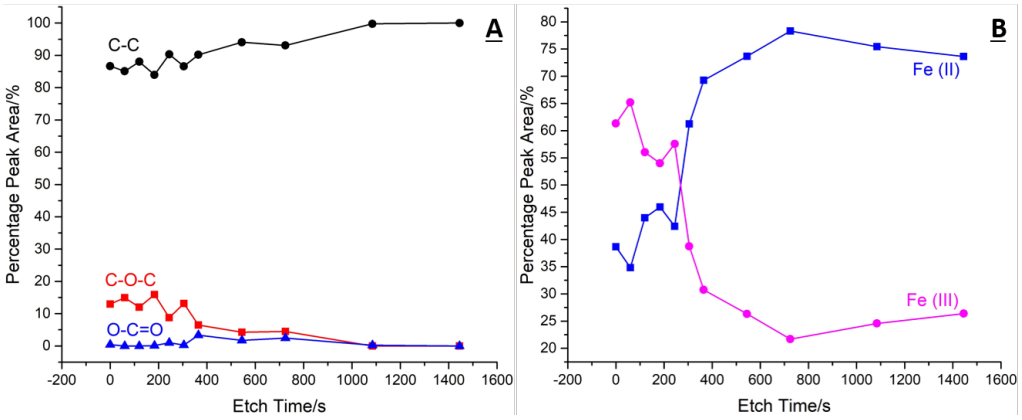

Fig. 6.12: Component fitting results of multiplet peaks for A) C 1s, and B) Fe $2p_{3/2}$ peaks depth profiling, at a sampling angle normal to the surface (0°).

The component peak fittings for carbon are shown in Figure 6.12A. The alkyl bonds (C−C) percentage is seen to increase with deeper profiling. There is a minor and declining oxidised-carbon (C−O−C) and carbonyl (O−C=O) contribution. This shows that although though the adventitious carbon is etched away quickly, as is the more volatile oxidised carbonaceous species. The persistent alkyl signature suggests the possibility of carbon ingrained within the bulk mineral.

Figure 6.12B shows the fitting of the iron 2p regions. The peaks are fitted into two components: iron (II) and iron (III) species. Deeper etching results in an increase of iron (II) and decrease of iron (III) content: at the 'surface', iron (III) is the majority species. This result is perhaps unsurprising: although the bulk composition of almandine garnet indicates only iron (II) content, the surface iron ions are exposed to atmospheric oxygen and can be further oxidised into iron (III). The result suggests that the 'surface' oxygen chemical environment would likely to be influenced by iron (III) species, in addition to aluminium and silicon.

By inspection of the oxygen 1s spectra in surface-normal angle surveying, Figure 6.13, there is little peak asymmetry, suggesting that there are few

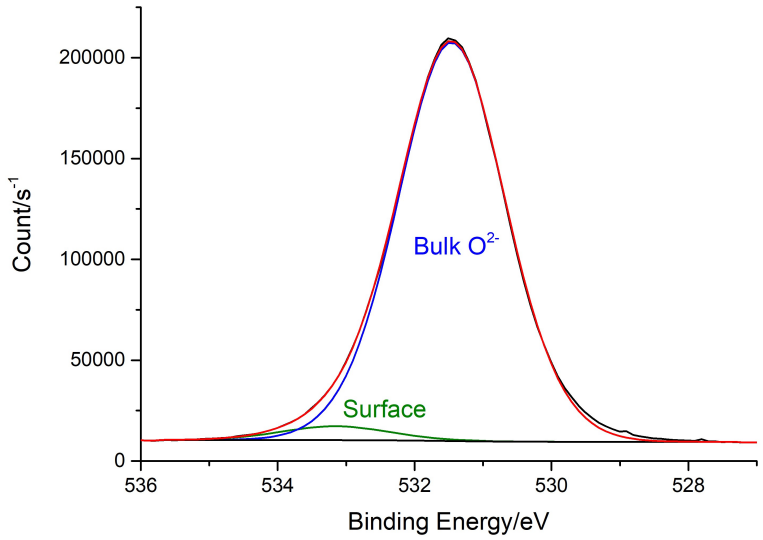

Fig. 6.13: Example peak fitting for an oxygen 1s peak with 0 etching and a sampling normal to the surface (0° stage tilt).

significant contributions of oxygen species other than the bulk. The arrangement is the most surface-sensitive experimental configuration available to conventional XPS without etching. There is little/no chemical information to be gained by peak-fitting these oxygen spectra. Therefore the more surface-sensitive angle-resolved XPS (ARXPS) method is needed, as outlined below.

6.6.2 ARXPS

In ARXPS the higher the tilt angle, the more surface sensitive the measurement, elemental composition with surveying angle is inspected. Figure 6.14A shows the variation of major elements in polished almandine garnet with increasing surface sensitivity: silicon, aluminium, and oxygen atomic percentages remain relatively constant; for carbon, there is a slight increase in atomic contribution. This is as expected as adventitious carbon detection is enhanced, leading to the decrease in oxygen.

The atomic percentage of 'minor' elements, such as iron, calcium, and magnesium, shown in Figure 6.14B, are relatively constant with increasing surface sensitivity. The results indicate no significant changes in chemical composition with increasingly surface sensitive sampling.

Example angle-resolved spectra of aluminium and silicon in almandine garnet

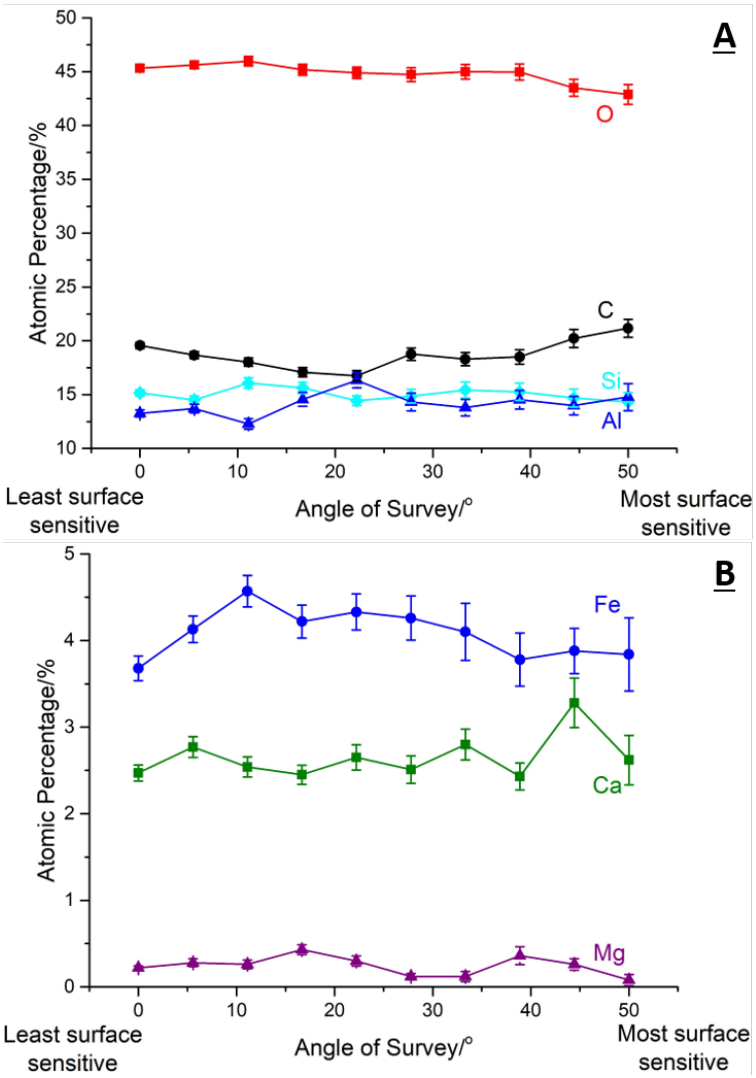

Fig. 6.14: Tilt-angle-resolved XPS survey for A) major and B) minor elements in polished almandine garnet.

are shown in Figure 6.15. At 22.5° (least surface-sensitive) surveying, there is a twin-peak structure seen for both aluminium and silicon 2p spectral regions. Spin-orbit coupling peaks, $2p_{3/2}$ (lower binding energy) and $2p_{1/2}$ (higher binding energy), should have an intensity ratio of 2:1. In Figure 6.15 the intensity ratio is reversed instead, where the lower binding energy shoulder is of lower intensity than the higher binding energy peak. This can only be attributed to multiple aluminium and silicon species, nominally containing 'bulk' and 'surface' peaks.

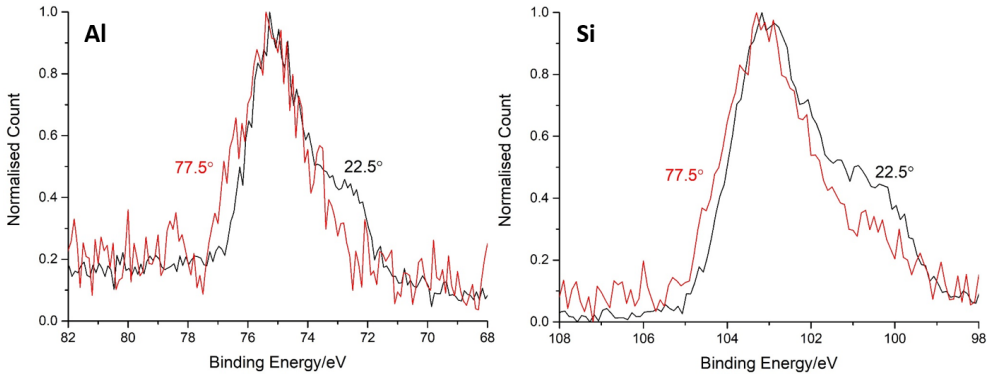

Fig. 6.15: Component fitting of multiplet peaks for aluminium and silicon 2p regions at different surveying angle.

Tab. 6.1: Fitting of the Al 2p XPS peak from polished almandine garnet

Species	**Position/eV**	**FWHM/eV**	**Percentage Area/%**
22.5° Surface $2p_{3/2}$	74.96	1.47	29.4
22.5° Surface $2p_{1/2}$	75.76	1.47	28.9
22.5° Bulk $2p_{3/2}$	72.86	2.36	21.0
22.5° Bulk $2p_{1/2}$	73.66	2.36	20.7
77.5° Surface $2p_{3/2}$	74.96	2.07	41.3
77.5° Surface $2p_{1/2}$	75.76	2.07	40.6
77.5° Bulk $2p_{3/2}$	72.86	1.92	9.1
77.5° Bulk $2p_{1/2}$	73.66	1.92	9.0

'Bulk' species normally have lower binding energies than their 'surface' counterparts.[146] The fitting results are listed in Tables 6.1 and 6.2. For the aluminium 2p region, with increased surveying angle, the bulk 'aluminosilicate framework' peak diminishes and the surface-associated 'alumina' peak dominates. The 'surface' to 'bulk' ratio is around 4.5 at 77.5° survey angle. For the silicon 2p region, the analogous phenomenon is seen. The surface 'silica' to bulk 'aluminosilicate framework' ratio is approximately 3.0 at 77.5° survey angle.

Tab. 6.2: Fitting of the Si 2p XPS peak from polished almandine garnet

Species	Position/eV	FWHM/eV	Percentage Area/%
22.5° Surface $2p_{3/2}$	102.89	1.67	31.4
22.5° Surface $2p_{1/2}$	103.52	1.67	30.7
22.5° Bulk $2p_{3/2}$	100.72	2.23	19.2
22.5° Bulk $2p_{1/2}$	101.35	2.23	18.8
77.5° Surface $2p_{3/2}$	102.89	1.79	37.8
77.5° Surface $2p_{1/2}$	103.52	1.79	37.1
77.5° Bulk $2p_{3/2}$	100.72	2.16	12.7
77.5° Bulk $2p_{1/2}$	101.35	2.16	12.4

'Surface' and 'bulk' peak fits at different surveying angles can be seen in Figure 6.16. The 'surface' contribution is seen to steadily increase with angle of survey, while the 'bulk' contribution becomes smaller. This means aluminium and silicon chemical environments remains influential to the garnet surface group chemistry.

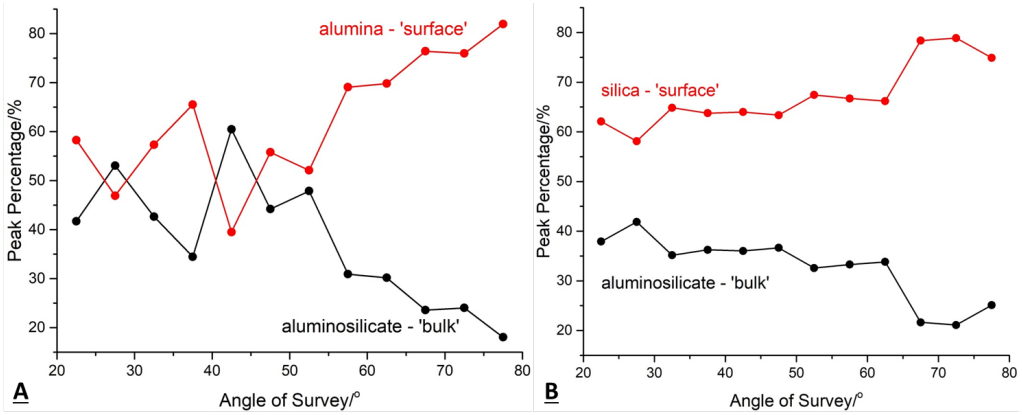

Fig. 6.16: Component fitting results of multiplet peaks for A) Al 2p, B) Si 2p peaks by varying survying angle.

Results of detailed analysis of carbon 1s and iron 2p peaks are shown in Figure 6.17. The increase of surface sensitivity is associated with a modest increase of oxidised-carbon (C−O−C) content, with significant alkyl carbon (C−C) presence. At the least-surface-sensitive surveying angle, the technique indicates a significant amount of ingrained carbon content within the natural mineral. With increased sensitivity, the more volatile/oxidised adventitious carbon species are characterised. Therefore oxygen peak-analysis must include consideration of oxidised-carbon species, though it is difficult to quantitatively account for these issues without a reliable reference material.

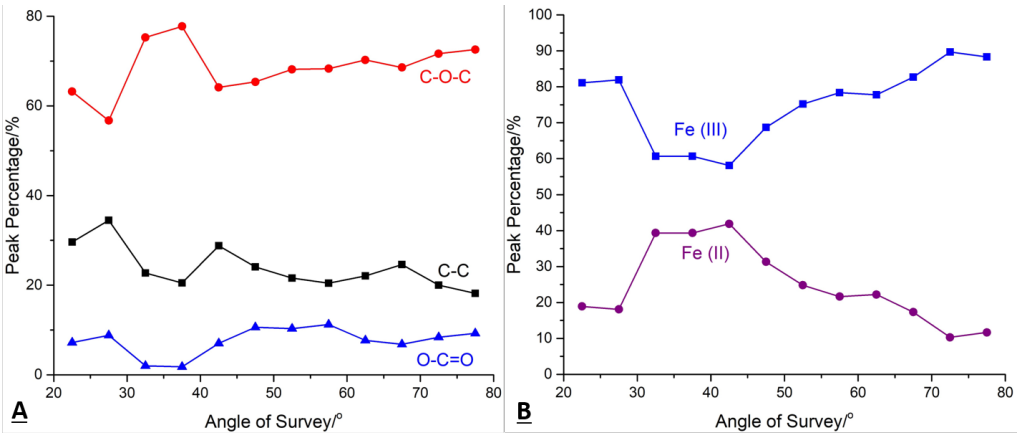

Fig. 6.17: Component fitting results of multiplet peaks for A) C 1s, and B) Fe 2p peaks at varying surveying angles.

With increasing surface sensitivity (surveying angle), the iron (III) content increases very significantly and comes to dominate the surface environment. This is explained by surface iron (II) in the mineral being oxidised into iron (III) by atmospheric oxygen.[147] Therefore the contributions to the oxygen 'surface' peak will likely be from the iron (III) atoms.

The oxygen 1s region was analysed to deduce the chemical nature of surface hydroxyl groups, which are commonly present on metal oxides and silicates.[126,148,149] The optimal conditions to distinguish between the contributions of 'surface' and 'bulk' oxygen species is through the most surface sensitive analysis. Therefore the spectrum measured at 77.5° surveying angle is the focus of the peak-fitting seen in Figure 6.18. The peak has a shoulder, indicative of more than one oxygen chemical environment. Peak-fitting was therefore conducted to identify the different oxygen species.

It is generally considered good practice in peak fitting for component peaks to have similar peak-shapes.[63,150] Fittings are done with the fewest number of peaks to constrain fitting parameters. The percentage area occupied by each fitted component peak is noted, denoting the 'share' of this species within the elemental spectrum. The results are detailed in Table Table 6.3.

The oxygen surface spectra, just like those seen for aluminium and silicon at the same surveying angle, have the surface peak dominating. The ratio between the surface and bulk peak is around 4.2, of similar magnitude to those seen for aluminium (4.5) and silicon (3.0). Similar surface-to-bulk ratio results support the observations from the oxygen ARXPS measurement.

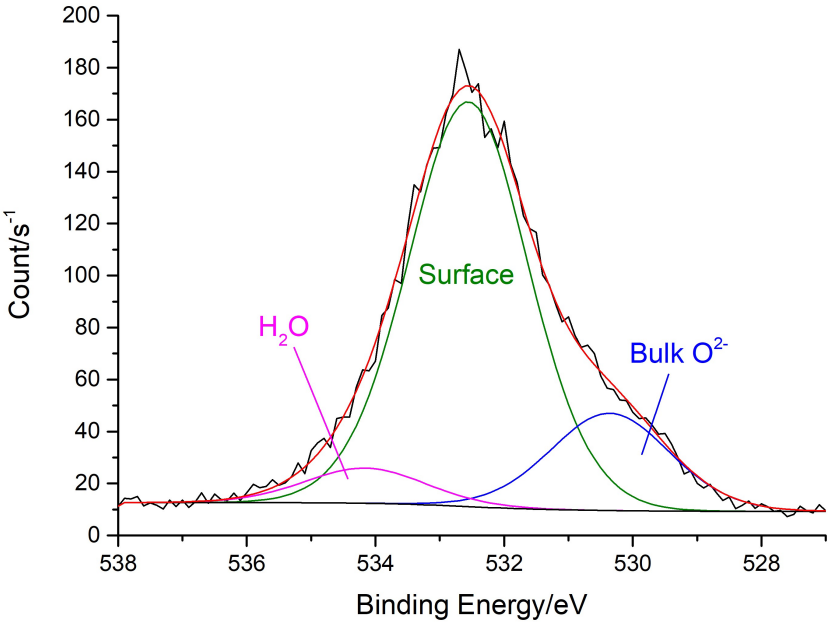

Fig. 6.18: Oxygen 1s peak fitting of various contributing species for a spectrum measured at 77.5° surveying angle, the most surface sensitive available.

Numerous attempts in the literature have been made to use ARXPS data to estimate surface density of oxygen surface groups, by considering a single layer of hydroxyl group or a thicker hydrated oxide region.[148,149] Although many involve assumptions or correction factors that are rather arbitrary. However, it is possible to estimate the thickness of the surface layer based on the surface-to-bulk ratios in the oxygen spectra.

By considering a simple two-layer system consisting of surface and bulk, the ratio of contributions to the overall oxygen 1s XPS peak is given in Equation

Tab. 6.3: Details of component peak fittings for the oxygen 1s region of almandine garnet, surveyed at 77.5° stage tilt

Species	**Position/eV**	**FWHM/eV**	**Percentage Area/%**
Bulk	530.36	2.20	18.1
Surface	532.60	2.20	75.3
Adsorbed Water	534.16	2.20	6.6

6.1, where D_s and D_b are the atomic number densities (atoms per volume) in the surface layer and the bulk layer respectively, t is the thickness of the surface layer, λ is the inelastic mean free path (IMFP) of photoelectrons excited from the oxygen 1s level in the solid, and assumed to be the same value in the surface and bulk garnet layers, and θ is the surveying angle, measured from the surface normal.

$$\frac{I_s}{I_b} = \frac{D_s}{D_b}(\exp(\frac{t}{\lambda \cos\theta}) - 1) \tag{6.1}$$

If it is initially assumed that the surface layer possesses an unreconstructed, bulk-terminated structure, then atomic number densities of both surface and bulk are the same ($D_s = D_b$). Taking the literature value of the IMFP to be 1.1 nm,[149] the surface layer thickness t is estimated at each surveying angle. The calculated results can be seen in Figure 6.19. The averaged values give surface layer thicknesses of 6.3 ± 1.7, 7.3 ± 2.0, and 8.7 ± 2.3 Åfor aluminium 2p, silicon 2p, and oxygen 1s peaks respectively. The general agreement between these values suggests the number densities of the three elements within the surface layer are similar, i.e. the surface layer is not depleted of any particular element relative to the other two.

Corrections to the oxygen 1s photopeaks of native oxide layers on metal surfaces to remove contributions of adsorbed oxygen-containing organic species (O−C=O, C−O−C) have previously been used for the quantitative determination of surface hydroxyl site density.[148] Application of this correction reduces the oxygen-peak-derived surface layer thickness from 8.7 ± 2.3 to 3.4 ± 1.1 Å; no analogous corrections are appropriate for the aluminium and silicon peaks.

The poorer agreements between the 'correction'-included value and the alu-

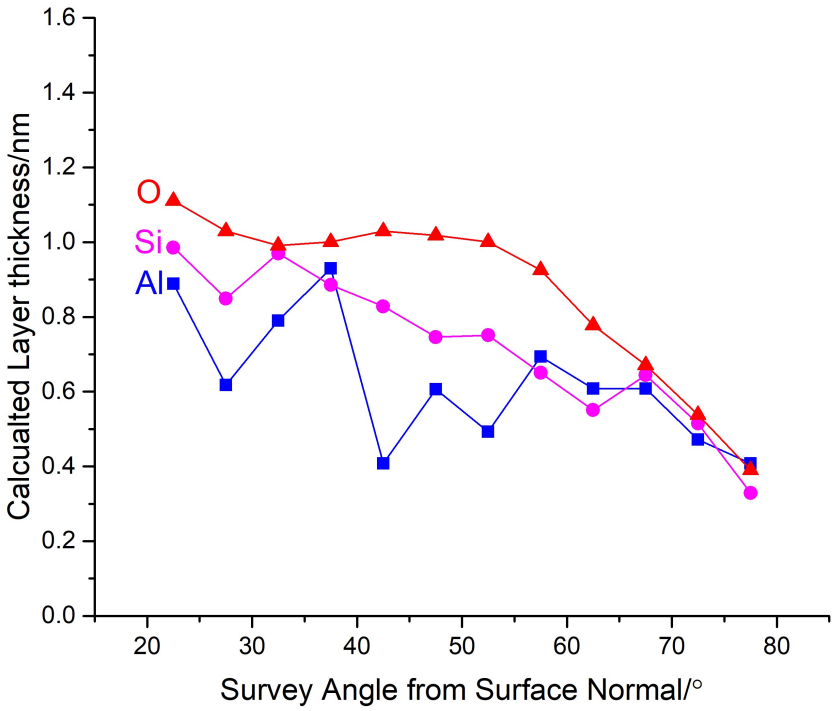

Fig. 6.19: Surface layer thicknesses calculated from ARXPS spectra for Al, Si, O (without any 'correction factor'), at different surveying angles.

minium and silicon results (3.4 vs. 6.3, 7.3 Å, *cf.* 8.7 Åbefore 'correction') suggest that the correction factor significantly overestimates the contribution of adsorbed oxygen-containing species to the oxygen peak in this study. Therefore, the best estimates of the surface-layer thickness is obtained from the agreeing aluminium- and silicon-derived surface layer thickness, 6.8 ± 1.9 Å. In theory a surface site number density can be calculated, but additional evidence of the surface crystal terminations for the natural almandine garnet mineral would be needed.

A literature study has been conducted to see whether any correlation exists between the binding energies of various elemental oxides and their respective surface group acidities. Sparingly soluble oxides were chosen to ensure that surface groups remain when immersed in aqueous solution. Not many have well-characterised surface group acidity values, due to their toxicity or insufficient interest. Iron, aluminium, and silicon oxide data were obtained due to their direct relevance to almandine garnet. Manganese and titanium oxides were included to populate the data set, improving the reliability of any correlations seen.

Tab. 6.4: Details of median binding energies of various sparingly soluble oxides, and their respective acid dissociation constants. Standard deviation are added to the median values to roughly reflect the spread of literature values.

Oxide Element	**Median Binding Energy/eV**	**Median** pK_{a1}**/eV**	**Median** pK_{a2}**/%**
Manganese[151–159]	531.43 ± 0.37	-	6.8 ± 1.6
Iron[32,147,160–162]	531.80 ± 0.34	6.7 ± 1.3	10.1 ± 1.3
Titanium[163–168]	532.40 ± 0.73	4.4 ± 2.5	6.6 ± 1.3
Aluminium[148,169–173]	532.80 ± 0.72	1.5 ± 2.1	9.4 ± 0.7
Silicon[148,174–180]	533.40 ± 0.82	-0.2 ± 0.1	5.8 ± 2.0

The collection of XPS binding energies are exclusively peaks explicitly associated with surface oxygen species. Median values are used due to the wide range of values for both surface oxide binding energies and their corresponding acid dissociation constants. The data is listed in Table 6.4.

The correlation graph is plotted in Figure 6.20. A linear relationship can be seen between median oxide binding energies and the first acid dissociation constant, pK_{a1}. The correlation appears to be less strong for the second acid dissociation constant, pK_{a2}. When the almandine garnet oxygen surface peak binding energy of 532.60 eV is applied, the respective values of first and second acid dissociation constants determined from the correlation plot are 3.41 ± 0.62 and 7.41 ± 0.96. These values are in general agreement with the pK_a values obtained from surface titration, 4.43 ± 0.26 and 6.13 ± 0.21 (in sodium nitrate electrolyte).

The oxygen surface peak in almandine garnet appears to have a chemical environment between iron and aluminium surface groups as shown in Figure 6.20. This is in general agreement with mineralogical evidence seen on the surfaces of weathered almandine garnet, where goethtite (FeO(OH)) and gibbsite ($Al(OH)_3$) precipitation occurs.[180]

Despite no reporting of silicon oxide surface precipitation on almandine garnet, caution must be exercised before any conclusions are drawn about the possible absence of silicon contribution to the surface chemistry. ARXPS sees silicon surface species contribution grows with higher surveying surface

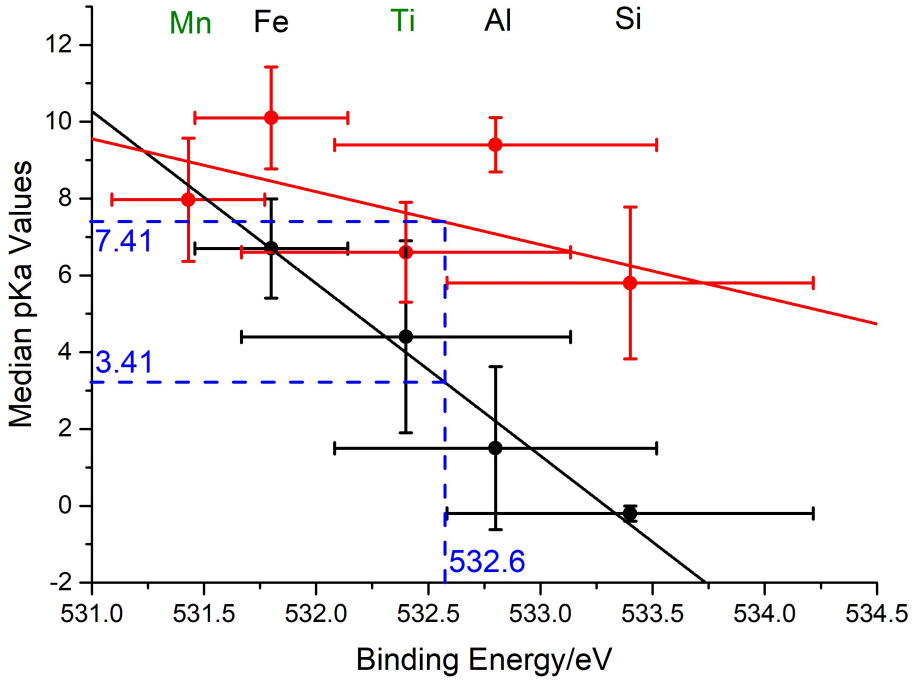

Fig. 6.20: Correlation graph between median shifts of surface oxygen peak against median pK_a values. Black: pK_{a1}; red: pK_{a2}. Blue dashed line represents the interpolation based on the surface hydroxyl peak derived from experimental results at 77.5° survey angle. Green lettered elements are those not present within almandine garnet.

sensitivity. Also in the case of mined garnet powder used for abrasive blasting, selective dissolution and reprecipitation of surface groups is unlikely in contrast to the weathered mineral. Therefore, the surface chemistry is expected to more closely mimic that of bulk-terminated garnet, formed from mineral fractures or cutting. In short, the surface chemical behaviour of almandine garnet remains likely to be an aggregate of iron-, aluminium-, and silicon-hydroxyl groups on the surface.

6.7 Summary of Results

Crystallographic, dissolution kinetics, and surface characterisations have been conducted on almandine garnet. A surface group density of 0.95 ± 0.16 sites nm^{-2}, surface acidity constant of 4.43 ± 0.26 and 6.13 ± 0.21, and PZC/IEP around 4.7 have been collected through surface titrations and ζ-potential measurements in sodium electrolyte-supported solutions. Computational adsorption model rationalisation of this data is to be described in Chapter 11.

The surface oxygen layer of the mineral is proposed to be 6.8 ± 1.9 Åthick. Through a correlation study between the surface oxide binding energy and the acid dissociation constants of elemental oxides, predicted pK_a values for almandine garnet are in general agreement with values from surface titrations conducted. Garnet surface oxygen appears to have a chemical environment similar to a mixture of iron (III)- and aluminium-oxides.

7. ALTERNATIVE BLASTING: DRY ICE-ABRASIVE MIXTURE

7.1 Introduction

In Chapter 5, S355 steel was shown to have significant amount of almandine garnet residue remaining on the post-blasting surface. These present a potential weakness, causing coating deadhesion/failure, and alternative surface cleaning methods that may reduce the residue coverage should be explored. Dry ice blasting is an alternative method that is currently used.[181]

7.2 Experimental

7.2.1 Materials

Dry ice production, blasting machines, and cryogenic storage equipment were provided by Dry Ice Global, Aberdeen, UK. Carbon dixoide pellets were made in cylindrical form, with 5 mm in circular diameter and 10 mm length. Naturally-sourced almandine garnet abrasive used with the dry ice mixture was 30/60 mesh in size, approximately twice the particulate size of the abrasive used in Chapter 5. The default pressure was 7 bar, and the blasting distance 1 m, with garnet abrasive mixed in-stream ('standard' settings).

S355 steel sheets, supplied by Parker Steel, UK, were cut into 50 mm × 50 mm × 8 mm coupons. Some of the coupons were polished down to sub-1 μm roughness using diamond polishing paste from Kemet International Limited. Other samples were used as received, with millscale covering the steel surface.

After blasting, the samples were stored either in vacuum desiccators *in vacuo*, or in desiccators with a petri dish of saturated salt-water mixture of potassium carbonate, sodium bromide, and potassium chloride to control the relative humidity of sample storage. All salts were supplied by Fisher Chemical. The post-blasting temperature of the steel coupon was measured through a Basetech Infrarot-Thermometer IRT-350 Optik infrared laser thermometer.

7.2.2 Equipment

All experimental instruments were detailed in Chapter 4 unless specifically stated otherwise.

7.3 Abrasive Residue Surface Coverage

Time- and blasting pressure-dependence were used to probe any differences in surface coverage induced by these variables. Surface coverages of abrasive residues were determined by the same method outlined in detail in Chapter 5, where EDX elemental maps of the surface were analysed for the area occupied by abrasive-associated elements (aluminium, silicon, calcium, titanium, and magnesium).

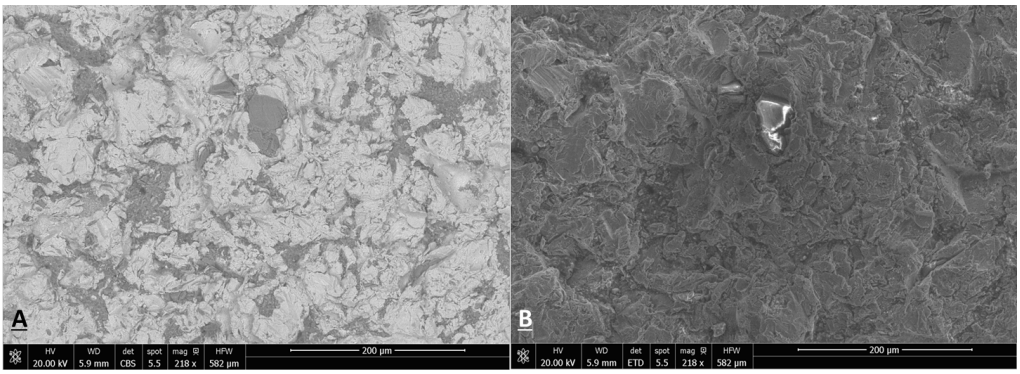

Fig. 7.1: Comparison of micrographs between A) backscattered and B) secondary electrons for a polished steel coupon that has been dry ice-garnet abrasive blasted for 5 seconds at 7 bar.

The BSE micrographs shows contrasting regions on the surface, demonstrated by Figure 7.1A. These are indicative of the presence of abrasive residues on the surface because garnet species have a different contrast to the steel background. The blasting leaves behind a rough surface, as shown in Figure 7.1B. This provides a large 'anchor profile' for enhancing coatings adhesion onto the steel surface, by maximising the surface area of attachment.[182]

7.3.1 Time Dependence

Dry ice-abrasive blasting was conducted for different durations, from a control sample of no blasting to 60 seconds of blasting. Additional experiments

were performed with double the abrasive content in the blast-stream ('more garnet'), hence doubling the abrasive flux.

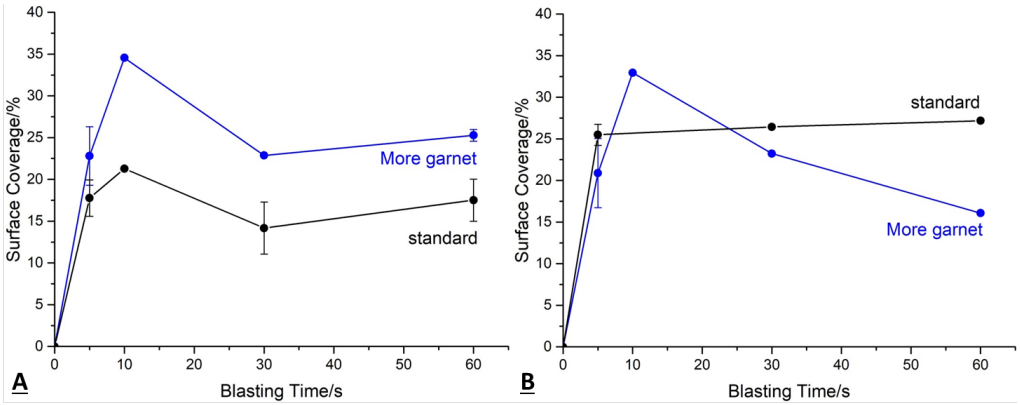

Fig. 7.2: Abrasive residue surface coverages obtained from BSE-EDX elemental map analyses on A) polished, and B) millscale covered S355 steels surfaces with variable blasting time, at 7 bar.

Abrasive residue surface coverage results are shown in Figure 7.2. Similar to abrasive-blasted surfaces with no dry ice included in-stream, the surface coverage rises rapidly in short duration blasting and quickly plateaus.[183] For 'standard' abrasive content, this plateau coverage is around 20% for the polished surface and 25% for a millscale-covered steel surface. With 'more garnet' in the blasting stream, Figure 7.2A shows an increase in surface coverage on polished steel to approximately 27%, while Figure 7.2B shows little change in coverage for the millscale-covered steel, despite additional in-stream abrasive. The reasons behind the fall of surface coverage for the 'more garnet' condition remain unclear.

The origins of the proposed dynamic equilibrium has been detailed in Chapter 5. The harder almandine garnet and softer calcite particles impact on the surface. They respectively embed into, and 'spread' onto the steel. With longer blasting times, the incoming particles either embed in the steel, bounce off while removing surface material, or remove existing residues.

For polished steel samples, increased abrasive content/flux leads to a rise in the abrasive residue surface coverage. The propelled hard abrasive can easily embed in he very thin layer of native harder oxide and soft steel, increasing coverage from 20% to 27%. This is still lower than the 33% coverage seen in blasting experiments with an abrasive-only stream, at a lower pressure of

2.8 bar. These results suggest dry ice-abrasive blasting is able to reduce the residue coverage.

Millscale-covered samples show little difference in surface coverage with the increase of abrasive content in blasting. A possible explanation for this result is the significant amount of work needed to remove the thick, hard millscale. For the 'standard' abrasive-content stream (with higher dry ice percentage), the same pressure carries mostly much lighter particles of soft dry ice (Mohs hardness of 2)[184] that have density of 1.5 g cm^{-3}, with the denser 4.2 g cm^{-3} almandine garnet. It is *postulated* that the garnet particles are likely to be travelling at lower acceleration/velocities than the dry ice, assuming they are of the same grain size as the crushed dry ice exposing them to the same force with the same cross-section.

For the stream with higher garnet content, the higher number of denser garnet particles means the stream travels slower than the 'standard' stream (same force, same cross-section, higher mass, lower acceleration), with the same pressure carrying a larger total mass. The particles therefore impart less kinetic energy upon impact, giving similar cleaning results as the standard abrasive-content stream. The absence of a hard millscale layer for polished steel allows almandine garnet particles to embed into the steel surface, despite lower impact speeds, at higher in-stream abrasive content. This explains the different surface-coverage change with higher abrasive content for polished and millscale-covered samples.

Elemental atomic percentages from EDX spectra of various abrasive-blasted surfaces areas were analysed. Figures 7.3A and 7.3B show respectively the major and minor elements on the blasted polished S355 samples. The oxygen content is seen initially to increase with longer blasting time before plateauing, while the iron content decreases. The results show that the blasting process results in significant oxide on the steel. The initial high iron and low oxygen content demonstrates the polished steel has a very thin film of native iron oxide, whose oxygen signature is later dwarfed by the introduction of abrasive residues.

Figure 7.3B shows the atomic percentages of abrasive-associated elements with increasing blasting duration. All initially increase rapidly, and then reach their respective plateaus. This agrees with the time-dependence surface-coverage results. The most abundant species is almandine garnet ($Fe_3Al_2(SiO_4)_3$), represented by strong signals of silicon and aluminium. Calcium and titanium have much lower atomic percentages, due to their lower content within

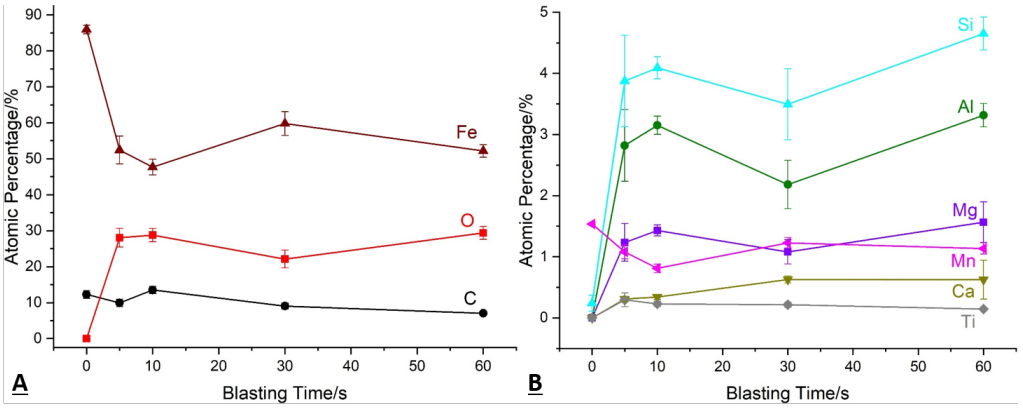

Fig. 7.3: BSE-EDX analysis of A) major and B) minor elements for polished S355 steels surfaces with variable blasting time, at 7 bar, to determine abrasive residue coverages.

the natural mineral respectively as calcite ($CaCO_3$) and ilmenite ($FeTiO_3$) impurities. The manganese content is seen to be independent of blasting time due to it being an alloying element in steel and a possible mineral impurity in the abrasive. The strong magnesium signature may be indicative of pyrope ($Mg_3Al_2(SiO_4)_3$) impurities.

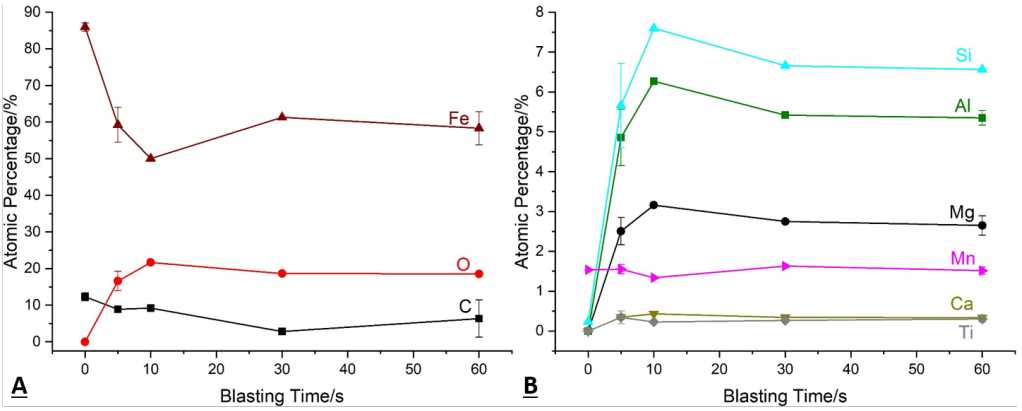

Fig. 7.4: BSE-EDX analysis of A) major and B) minor elements for polished S355 steel surfaces with variable blasting time, with double the 'standard' amount of garnet in-stream, at 7 bar, to determine abrasive residue coverages.

The blasting time-dependence of elemental percentages for surfaces blasted with double the garnet in-stream are plotted in Figure 7.4. The responses

are similar to those, shown in Figure 7.3, at 'standard' abrasive content, except for abrasive-associated elements, whose plateau levels are approximately double those in Figure 7.3B. This agrees with the results suggesting increased surface coverage.

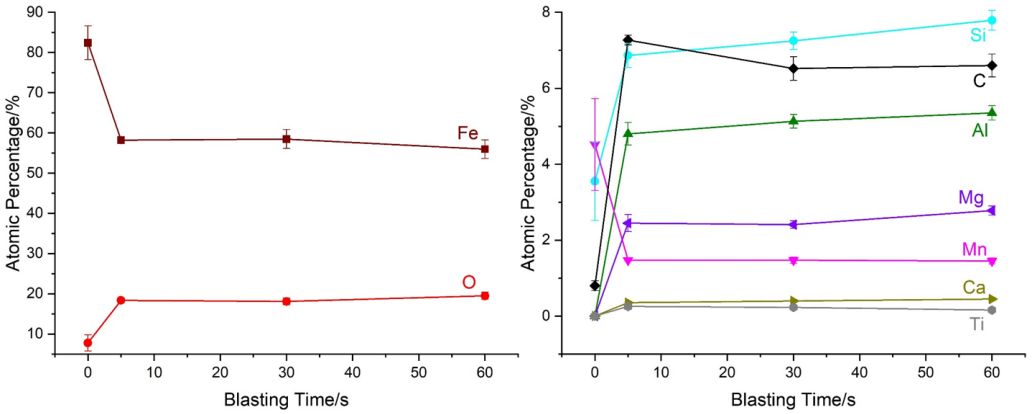

Fig. 7.5: BSE-EDX analysis of A) major and B) minor elements for millscale-covered S355 steel surfaces with variable blasting time, at 7 bar, to determine abrasive residue coverages.

Responses of millscale-covered samples share similar behaviour with or without doubling the abrasive content in the blasting stream, under the same blasting conditions. The major elements reach approximately the same plateaus in Figures 7.5A and 7.6A, with time-dependence behaviour similar to polished steel samples. Minor elements responses for samples that underwent 'standard' and double-garnet abrasive blasting, seen respectively in Figures 7.5B and 7.6B, are also similar. This is in good agreement with coverage data obtained from BSE-EDX map analysis for millscale-covered samples. The rationalisation of data for the millscale-covered samples is exactly the same as that outlined in the discussion of surface coverage.

In summary, the blasting time-dependence study on polished and millscale-covered samples is in agreement with the surface coverage analysis, with abrasive-related elements clearly identified to be remain on the steel surface. Plateau abrasive coverage is achieved rapidly ($\approx$ 10 s). A slight reduction of surface coverage, to around 25% is achieved in standard, 7 bar blasting, in comparison to the 33% coverage after 2.8 bar blasting in a pure-abrasive stream.

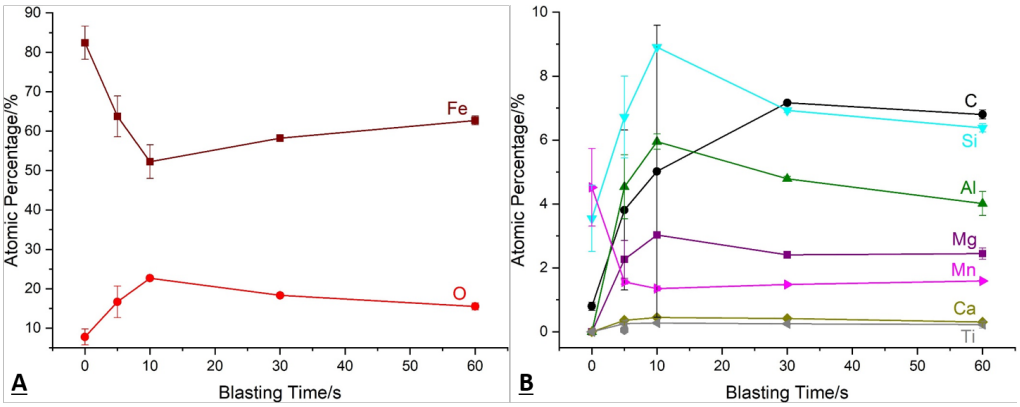

Fig. 7.6: BSE-EDX analysis of A) major and B) minor elements for millscale-covered S355 steel surfaces with variable blasting time, with double the 'standard' amount of garnet in the stream, at 7 bar, to determine abrasive residue coverages.

7.3.2 Pressure Dependence

Under the 'standard' blasting duration of 5 seconds, three different blasting pressures were attempted: 5, 7, and 9 bar. Blasting experiments using double the 'standard' amount of abrasive were also performed.

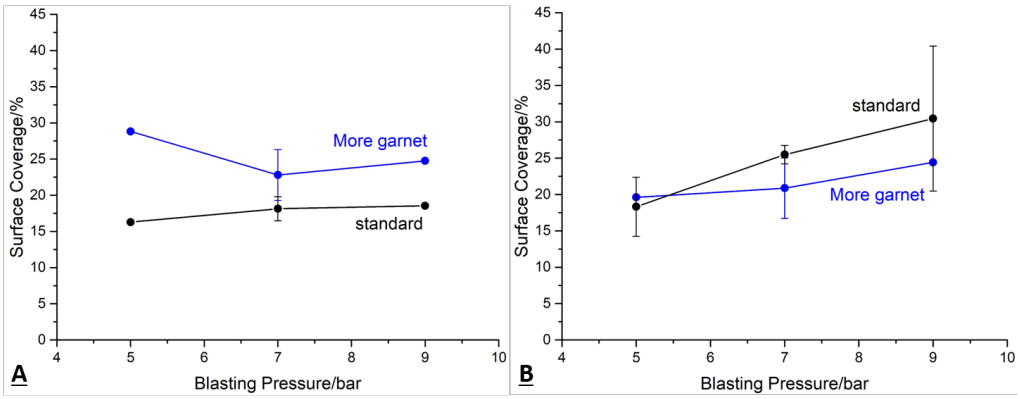

Fig. 7.7: Abrasive residue surface coverages obtained from BSE-EDX elemental map analysis on A) polished, and B) millscale-covered S355 steels surfaces with variable blasting pressure, for 5 s.

The abrasive-blasted polished samples, shown in Figure 7.7A, do not appear to show significant pressure dependence of abrasive residue coverage. Samples blasted with the standard amount of garnet in-steam show approx-

imately 17% of the surface being covered. The samples blasted with double the in-stream abrasive content are found to have around 25% coverage, similar to the plateau/equilibrium coverage for polished samples under time-dependence.

For millscale-covered samples, the average surface coverage on various sites surveyed appears to increase slightly with rising blasting pressure. The results are shown in Figure 7.7B, where an increase of surface coverage from 18% at 5 bar to 30% at 9 bar is seen. Doubling the standard abrasive content leads to a modest rise from 20% at 5 bar to 23% at 9 bar. The coverage error bars in Figure 7.7 are such that the coverages are not necessarily significantly different at different pressures.

The hard millscale is initially removed with great difficulty by the dry ice-abrasive stream. At lower pressures, embedding of almandine garnet may be more difficult, due to the lower abrasive flux and speed. The softer calcite within the abrasive can still 'spread' upon impact and increase surface coverage. At higher pressures, the higher flux of abrasive impacting the steel surface simultaneously embed into the steel and removes previously attached abrasive residues.

By doubling the abrasive content in-stream, resulting in slower moving particles under the same blasting pressures, it prevents significant increases of surface coverage on millscale-covered steel. Increasing blasting pressure may tangibly increase the surface coverage. However with the initial rapid increase of residue footprint, subsequent incoming particles have a higher probability of colliding and removing already-attached residues. Hence no obvious pressure-dependence of surface coverage is observed.

Figures 7.8 and 7.9 show the elemental percentage variation derived from EDX studies of abrasive-blasted surfaces at different blasting pressures for polished S355 samples. Aside from carbon having minor fluctuations due to adventitious carbon (i.e. dust) deposition, all atomic percentages are independent of blasting pressure. The surface blasted with double the amount of garnet in the stream has higher atomic percentages of abrasive-associated elements, as shown in Figure 7.9B. This is in agreement with the time-dependence studies.

Similar observations are seen for millscale-covered steel surfaces. No strong blasting pressure dependence is seen for all elements, as shown in Figures 7.10 and 7.11. Generally, the atomic percentage for abrasive-associated elements

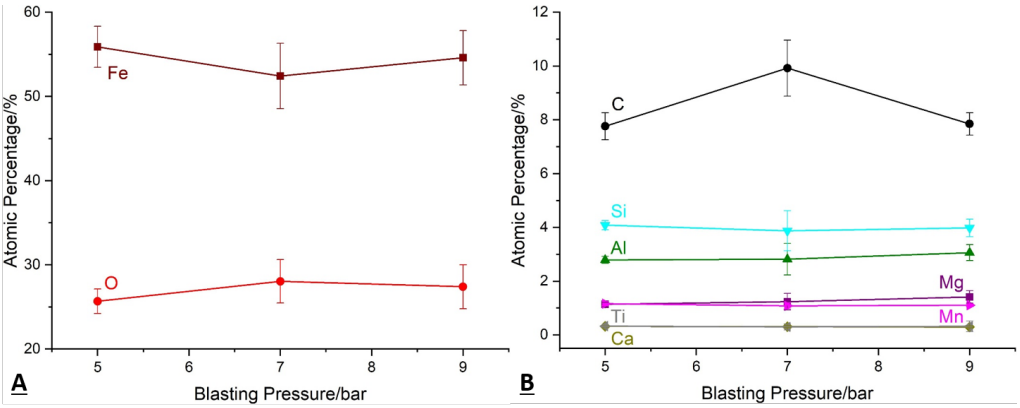

Fig. 7.8: Abrasive residue coverage obtained from BSE-EDX analysis of A) major and B) minor elements for polished S355 steel surfaces with variable blasting pressures, with 'standard' amount of garnet in stream, for 5 s.

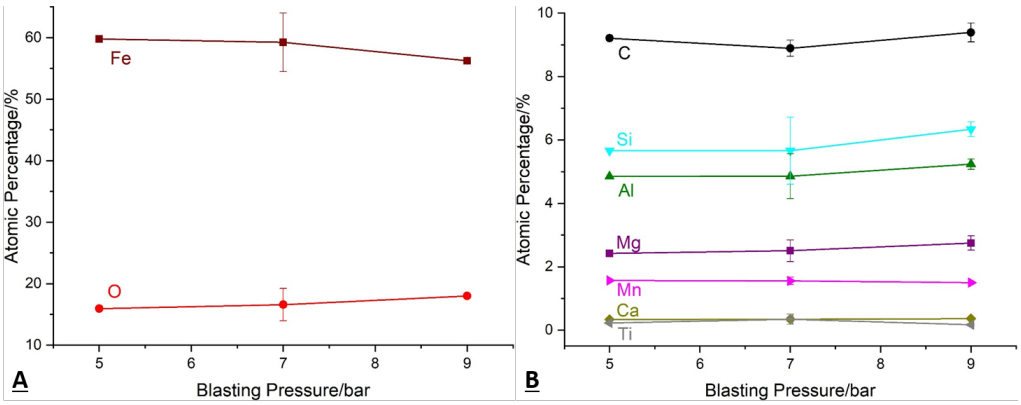

Fig. 7.9: Abrasive residue coverage obtained from BSE-EDX analysis of A) major and B) minor elements for polished S355 steel surfaces with variable blasting pressures, with double the 'standard' amount of garnet in stream, for 5 s.

is slightly higher than on blasted polished steel. For example in Figure 7.10B silicon is seen at 7% whereas it is 4% for polished samples (Figure 7.8B). Few differences in elemental atomic percentages are seen for millscale-covered steel when blasted with doubled the 'standard' abrasive content, as seen in Figures 7.10B and 7.11B.

The lack of pressure dependence for both polished and millscale-covered S355 steel surfaces is in agreement with surface coverage data obtained from BSE-EDX elemental maps as discussed previously. In summary, significant abra-

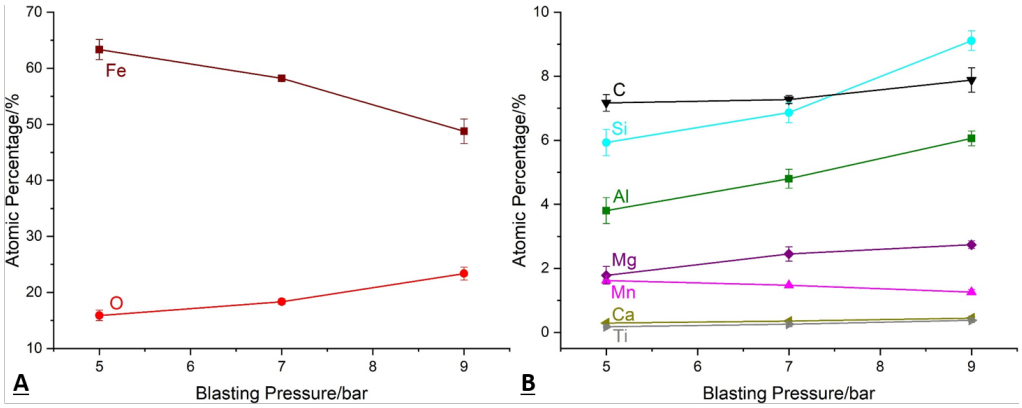

Fig. 7.10: Abrasive residue coverage obtained from BSE-EDX analysis of A) major and B) minor elements for millscale-covered S355 steel surfaces with variable blasting pressures, with 'standard' amount of garnet in stream, for 5 s.

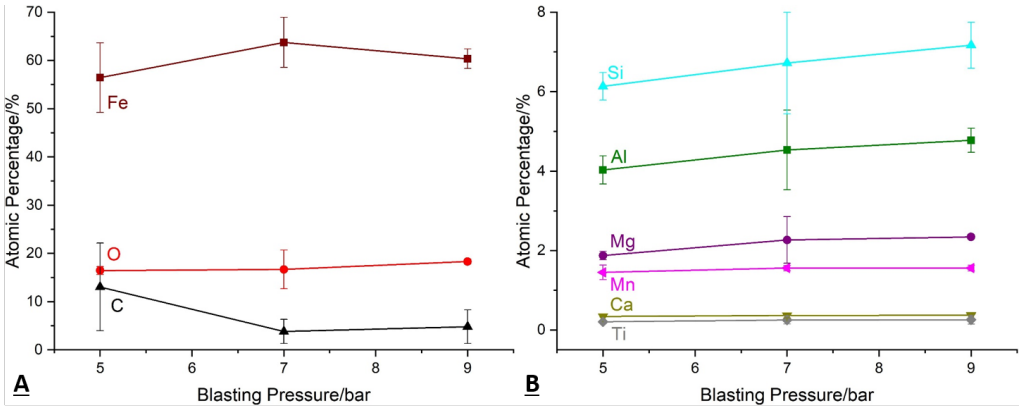

Fig. 7.11: Abrasive residue coverage obtained from BSE-EDX analysis of A) major and B) minor elements for millscale-covered S355 steel surfaces with variable blasting pressures, with double the 'standard' amount of garnet in stream, for 5 s.

sive residues remain on the post-treatment steel surface when cleaned by dry ice-almandine garnet abrasive blasting. For all pressures tested, the surfaces have initial millscales removed by 5 s of blasting. Lower pressure blasting may allow more efficient and safer industrial application.

7.4 Corrosion Spot Analysis

Though a small reduction of abrasive residue coverage is seen by dry ice-abrasive blasting (approximately 20%) when compared to only-abrasive blasting (around 33%), there are apparent cooling effects of dry ice blasting has on the steel. This cooling effect is outlined in Table 7.1: the longer the blasting, the lower the final steel temperature.

Tab. 7.1: Variation of final sample temperature with dry ice-abrasive blasting duration, for both polished and millscale-covered steel samples. Standard deviation values are added to reflect the spread of data values.

Blasting Time/s	**Median Final Temperature/°C**
5	10.2 ± 4.4
10	14.8 ± 2.2
30	2.2 ± 3.7
60	-1.1 ± 7.5

After blasting, samples were left to warm up until any visible front of frost disappears. A final dry ice-only blast was used to 'lap' the sample to remove superficial abrasive dust. Virtually all samples were observed to have a frost layer form immediately after blasting. Longer blasted surfaces had larger initially-frosted areas. This frost leads to surface water condensation and can in turn initiate the corrosion process. Microscopic corrosion sites are seen and their chemical nature is investigated through EDX elemental analysis.

Sites sampled in this study are all from the central regions of the surface, the location that bears the full blasting impact/cooling, to ensure that any corrosion products characterised are induced by sample blasting-cooling.

Corrosion spots were observed in many samples. The corrosion spots are generally seen to be round-edged, oval-shaped, and puckered in the centre. Examples of these corrosion features are seen in Figure 7.12 coloured in pink (A) or red (B). These corrosion features bear a strong resemblance to the round-edged shape of goethite (FeOOH) seen in steel atmospheric corrosion studies.[185]

EDX elemental analysis has been conducted on three different types of sites: blasted 'bare' steel, abrasive-associated regions, and corrosion sites. All are

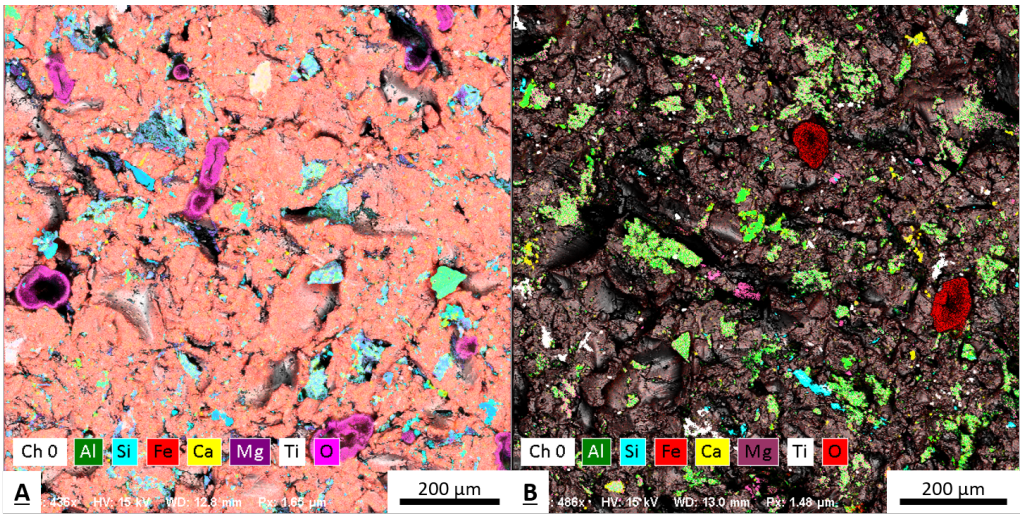

Fig. 7.12: BSE-EDX elemental maps of dry ice-abrasive blasted sites where corrosion is observed: A) millscale-covered steel blasted for 5 s at 5 bar pressure, 6.1 °C final temperature; B) millscale-covered steel blasted for 60 s at 7 bar pressure, -9.2 °C final temperature.

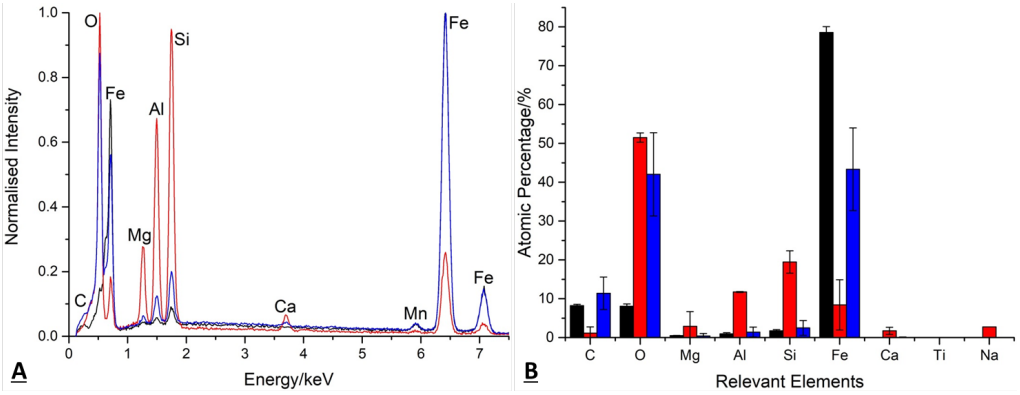

Fig. 7.13: A) EDX spectra of the three site types: steel (black), garnet abrasive residue (red), and corrosion spot (blue) of a sample that has been dry ice-abrasive blasted for 60 s, at 7 bar pressure, with extra garnet. B) elemental analysis compilations of the various steel (black), garnet abrasive (red) and corrosion spot (blue) sites that have been surveyed. Error bars are derived from variations between sites.

identified through elemental maps. A typical spectrum of each site can be seen in Figure 7.13A. For the elemental analysis, data from different sites on different surfaces are compiled for a consistent dataset. The results are shown in Figure 7.13B. For the steel region, small carbon and oxygen signatures

are seen with a strong iron signal, along with a small alloying manganese presence. The garnet regions consist of elements that represent the mineral composition of the natural almandine garnet abrasive used: oxygen (mineral oxides), iron, magnesium, aluminium, silicon, calcium, and a much weaker titanium peaks.

For the corrosion sites, the main elements are oxygen and iron, with a significant contribution of carbon, that is around the same percentage as on the steel region. Trace amount of garnet abrasive associated elements are also found at the corrosion spots. This is unsurprising, as abrasive residue is dispersed across the sampled surfaces, resulting in overlap of corrosion sites and abrasive particulates by corrosion products dissolution and precipitation within condensed water drooplets. The EDX results confirm corrosion spots are iron oxide features.

These corrosion spots are never observed on surfaces blasted only with almandine garnet (without dry ice). The spontaneous corrosion is likely to be caused by water condensation, induced by cooling of the surface due to dry ice blasting.

7.5 Corrosion Spot Density Under Different Relative Humidities

To see whether there was any correlations between storage relative humidity (at 20 °C) and corrosion on post-blasting steel samples, millscale-covered steel were dry ice-abrasive blasted for 5 s and then stored in desiccators maintained at different relative humidity that are common in the North Sea: 40, 60, 90%.[186] The desiccator relative humidity values are controlled through saturated salt solution-salt mixtures.[187] The samples were 'aged' for a month before analysis. Should storage humidity makes significant differences in corrosion spot formation, this longer storage time hopes to makes its effects more apparent.

Corrosion sites are identified by contrasting EDX elemental maps with and without oxygen-associated regions highlighted, as demonstrated in Figure 7.14. The identified corrosion sites are counted for each sampled region. The region area is measured and the corrosion site densities at each storage relative humidity can be then calculated by dividing the number of corrosion spots by the mapped area. The mean and median corrosion spot densities are outlined in Table 7.2. Due to the variability (significant standard deviation)

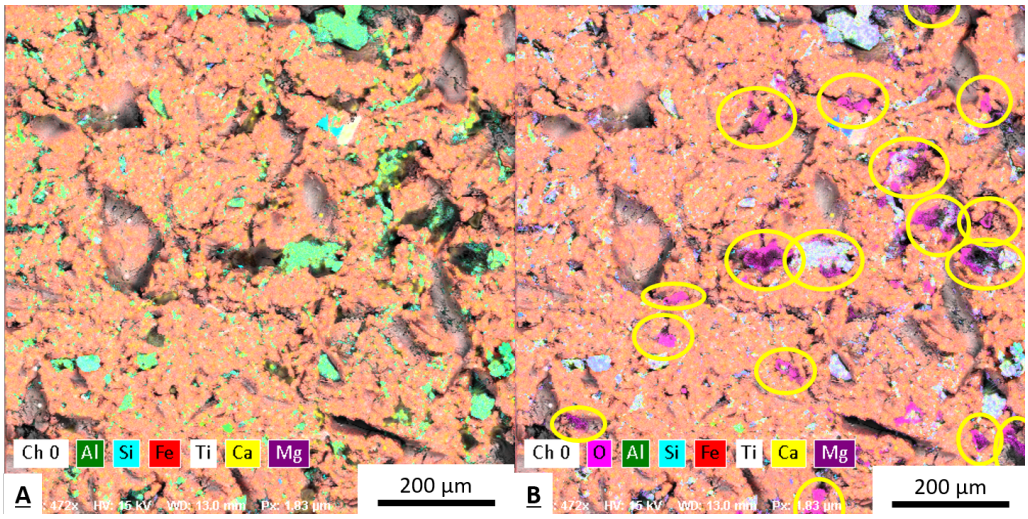

Fig. 7.14: Example of corrosion spot identification, with A) the original elemental map with abrasive-associated elements highlighted, and with B) the oxygen highlighting present. The regions with the most intense oxygen association, that are not closely associated with abrasive residues, are circled in yellow.

Tab. 7.2: Mean and median corrosion spot density on millscale-covered steel samples which have been blasted for 5 seconds, at 7 bar pressure, and stored at different relative humidity in 20 °C.

Relative Humidity/%	**Median Corrosion Spot Density/mm^{-2}**	**Median Corrosion Spot Density/mm^{-2}**	**Spot Density Standard Deviation/mm^{-2}**
40	6.31	7.05	2.46
60	11.82	11.34	3.72
90	9.06	3.54	9.65

of their distribution, the median value is best used to determine the relationship between corrosion site density and humidity. There is no particular trend observable.

It is worth noting that the presence of corrosion spots at low relative humidity (40%), and the lack of relation between corrosion spot density with storage relative humidity, highlights that corrosion may not be simply induced due to a cooled surface leading to water precipitation. Possible inclusion of moisture

from 'wet' compressed air in the cold blasting medium may also be a a factor. The 'universal' value of median corrosion site density is around 7 to 10 sites mm^{-2}. While this is not a particularly large value, corrosion sites in addition to embedded abrasive residue, may form weak points at the steel-paint interface, leading to coatings deadhesion.

7.6 Chapter Summary

A combination of dry ice and almandine garnet abrasive has been used to blast-clean steel coupons, to assess the effectiveness of the cleaning process. Similar to previous garnet abrasive-only blasting, a equilibrium blasting-residue coverage is rapidly reached. This technique reduces abrasive residue coverage from 33% from a pure-abrasive stream to around 20-25%. No pressure dependence of the abrasive residue coverage is seen, though increasing the abrasive content in the stream may increase residue coverage. Future studies should control factors such as abrasive grain sizes, and blasting nozzle diameters, to control the abrasive number density in the stream, in order to determine optimal blasting conditions.

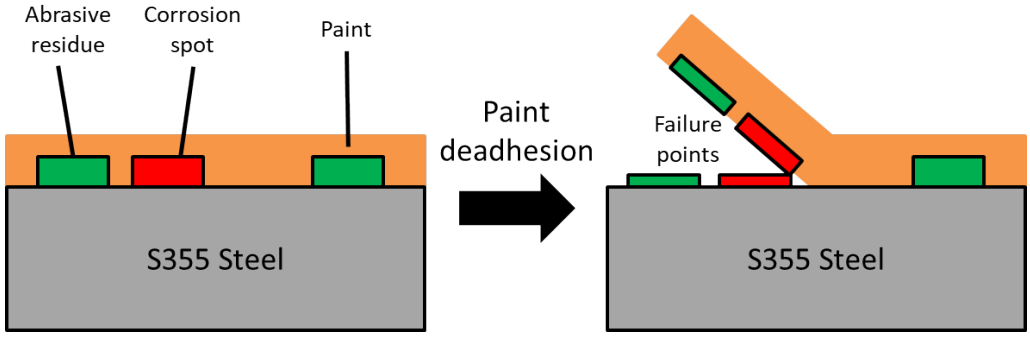

Fig. 7.15: Illustration of the way brittle steel corrosion products and abrasive residue patches may facilitate coatings failure on steel.

The surface cooling induced by the technique leads to iron oxide corrosion spots on the blasted steel. These spots form regardless of the relative humidity and have a median corrosion site density around 7 to 10 sites mm^{-2}. When repainting dry ice-abrasive blasted steel surface, one should be aware of painting over of corrosion spots: brittle corrosion spots and abrasive residues may provide weak points for coating failure, as illustrated in Figure 7.15. The corrosion spots are also a different substrate to steel and abrasive residues

for paints, and they may influence future coating anti-corrosion performance, as iron corrosion products can autocatalyse subsequent corrosion.[188]

8. ADSORPTION AT THE STEEL-LIQUID ORGANICS INTERFACE

8.1 Background

8.1.1 Paint Additives

A number of anti-corrosion treatments and additives have been employed to improve coatings adhesion, in the hope that strongly adsorbing coatings would simultaneously inhibit corrosion. However, literature has suggested that treatments that enhance adhesion of paints onto steel do not necessarily mean improved corrosion resistance.[189]

Surface treatment of steels is often used for metallic components of which the pieces can be totally immersed into a solution to form a cohesive adhesion-promoting or corrosion-resistant film. There are many methods available, including the use of chromate salts to form an acid-resistant chromate passivating layer.[93] Two of the most popular methods are phosphating and silanation. Phosphating involves immersing the steel into dilute phosphoric acid solutions with one or more dissolved alkali metal/heavy metal ions. These solutions contain free phosphoric acid and primary phosphates of the metal ions in the bath. When the steel is immersed into the bath, a reaction, Equation 8.1, rapidly leads to the formation of soluble primary ferrous phosphate. The reaction locally depletes the solution free-acid concentration, causing a rise in pH at the solid-solution interface. The hydrolytic equilibrium between the soluble primary- and the insoluble tertiary-phosphates is upset by this local pH rise, leading to the conversion and deposition of a cohesive, insoluble heavy-metal tertiary phosphates onto the steel that resists corrosion.[190]

$$\mathrm{Fe(s) + 2H_3PO_4(aq) \longrightarrow Fe(H_2PO_4)_2(aq) + H_2(g)} \tag{8.1}$$

Surface silanisation involves using the hydroxyl surface groups, as depicted in Figure 8.1, to hydrolyse alkoxysilanes in order to form X−O−Si−R bonds to the substrate. The strong surface interlinking of silicon-oxygen bonds, as

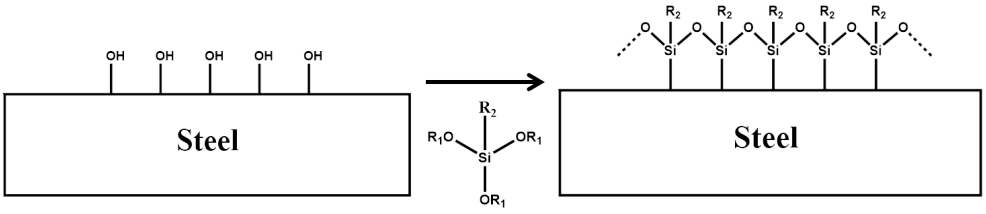

Fig. 8.1: Surface silanisation of steel.

well as the alkyl group linkage that can be cross-linked into the bulk polymer layer, promotes strong adhesion.[191,192]

The immersion procedures often required for these treatments make them rather impractical for large steel structural components used for offshore structures or marine vessels. Additives are often included within paint formulations that aim to promote adhesion and corrosion resistance *in situ* when the paint is applied onto the steel.[193] Many corrosion inhibitors have been proposed. These include amino acids,[194,195] inorganic and organic phosphates,[196–198], carboxylic acids,[79], organic amines,[199] trizaoles,[200] thiols,[201], and other paint-relevant components such as alkyl amines and phenols.[202] Many paint formulations are thinned with volatile organic solvents which are either alkane- or aromatic-based.

In Chapter 5 one-third of the post-abrasive-blasting S355 steel surface was characterised to be covered by abrasive residue. At the steel-paint interface, adsorption of paint organics is to be on both the bare S355 steel and the almandine garnet residues. This chapter and Chapter 9 therefore explore the possible adsorption behaviour of aforementioned chemical functional groups at the steel/almandine garnet-paint interface in organic solvents. Corrosion initiation requires the arrival of corrosive species or water to the steel surface. Therefore potential additives are investigated for their adsorption strengths and geometry on different substrates, to determine which chemical functionalities appear to adsorb strongly for a chemically-rationalised approach to better coatings. Understanding the underlying reasons for strong adsorption allows for coatings design that are *simultaneously* adhesion-promoting and corrosion inhibiting.

8.2 Experimental

8.2.1 Materials

The adsorption isotherms on the S355 steel powder, supplied by Sandvik Osprey, UK were conducted. The S355 powder was characterised with electron microscopy using a JEOL Model JSM 6360LV scanning electron microscope. ImageJ written by the National Institutes of Health, Bathesda, USA was used to size the powder particles. Elemental information was collected through EDX.

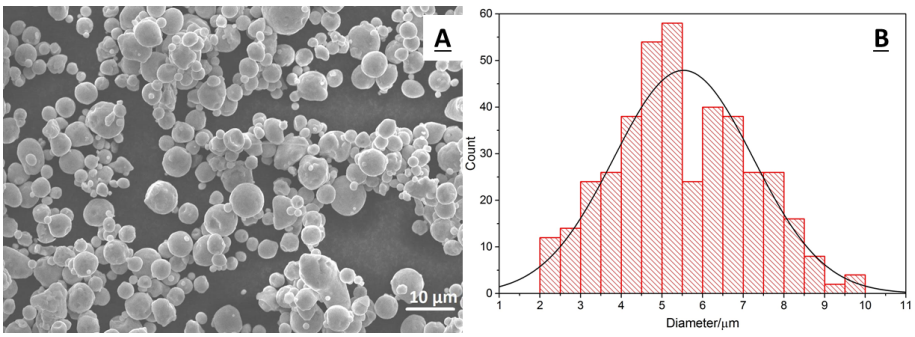

Fig. 8.2: A) Electron micrograph of S355 steel powder collected by the SEM, and subsequent B) sizing of the powder after analysis using ImageJ software. The curve is a Gaussian fit.

In Figure 8.2A the electron micrograph of the powder showed the steel particles to be spherical in shape. Figure 8.2B shows the analysed size distribution of the particles which have an average diameter of 5.53 ± 1.72 μm, leading to a geometrically-derived estimated specific surface area of 0.14 m^2 g^{-1}. This is in broad agreement with BrunauerEmmettTeller (BET) isotherm result of 0.30 ± 0.06 m^2 g^{-1}.

EDX elemental analysis results on the S355 powder are listed in Table 8.1. The S355 powders have a much larger oxygen percentage than polished S355 coupons. This is not surprising as the surface-to-volume ratio of powders was much larger. Therefore, the amount of surface iron oxide present is also much larger. The high surface-to-volume ratio makes the powder ideal for solution depletion adsorption isotherms, to obtain detectable solution concentration differences for reliable measurements.

Polished steel substrates were prepared the same way as described in Chapter 5.

Tab. 8.1: Evaluated elemental composition of S355 powder through EDX.

Element	**Atomic Percentage/%**
Fe	78.0 ± 5.7
O	20.3 ± 5.9
Mn	0.9 ± 0.1
Si	0.4 ± 0.1
C	0.4 ± 0.1

The depletion adsorption isotherm used n-dodecane and toluene as a background solvents. n-dodecane (≥ 99%) was supplied by Merck. Toluene (≥ 99.85%) was supplioed by Fisher Scientific. Organic additives/adsorbates used were 2,4,6-tris (dimethylaminomethyl) phenol (i.e. DMP-30, 95%), 4-mercaptophenol (97%), bis (2-ethylhexyl) phosphate (97%), palmitic acid (≥ 99%), and bisphenol A (≥ 99%). All were supplied by Sigma-Aldrich and were used without any additional purification.

Polished S355 steel substrates for SFG analysis, UV-ozone cleaned for 30 min prior, were immersed in 10 mM additive solutions, blown dry with a dry nitrogen jet, then sampled under a droplet of d_{26}-dodecane (98% deuteration, CK Isotopes Ltd., UK), sometimes containiong the dissolved additive, under a calcium fluoride semi-circular prism. The prism was cleaned using UV-Ozone treatment for 30 min prior to use to remove any organic contaminants. d-dodecane was used to help dissipate excess energy from the lasers and prevent them 'burning' sample surfaces. A schematic of the set-up is shown in Figure 8.3.

8.2.2 Isotherm Sample Preparation

Organic adsorption was conducted at room temperature and pressure using the solution depletion isotherm method. 20 g of S355 steel powder, unless stated otherwise, was placed in 50 mL polypropylene centrifuge tubes (Falcon Brand, Corning Inc.). Solutions of known additive concentrations were added and the final solution was made up to 20 mL. The samples were then tumbled for 24 hrs to equilibrate using a Stuart Scientific Rotator Drive STR4. For samples that used toluene as a solvent, equilibration was conducted in 14 mL glass vials, with all component quantities halved from previously mentioned values to maintain the same ratio between solids and liquids. The solids were separated by centrifugation for 30 min under 15000 g of force using a Thermo

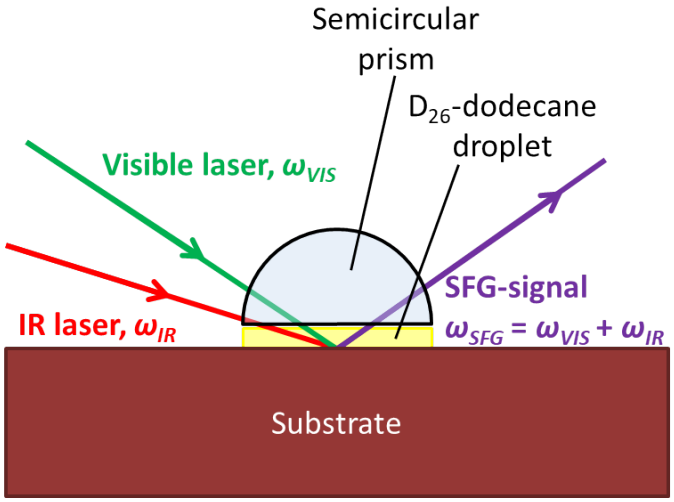

Fig. 8.3: Schematic of the SFG set-up used for assessing organic additive adsorption onto a substrate.

Scientific Heraus Multifuge 1 S-R. The supernatant was withdrawn carefully with a pipette, and the change of concentration was detected using a variety of spectroscopic techniques, depending on the species in question.

8.2.3 Equipment

All experimental instruments were detailed in Chapter 4 unless specifically stated otherwise.

Far-infrared spectroscopy (FIR)

Far-infrared spectroscopy was conducted using a Bruker Vertex 80v spectrometer at the Diamond Light Source, Didcot, Oxfordshire, during off-beam time. The incident radiation was generated by a spectrometer glowing IR source instead of the synchrotron. A shallow incidence of 80° to the surface normal was used, in addtional to a sampling aperture of 20 mm was used to increase incoming beam footprint. Samples were placed within the sample chamber and the chamber was vacuum pumped for 30 min, giving a chamber pressure no higher than 2 mbar. More than 126 scans per sample were made-for high signal-to-noise ratio. The detector was a helium-cooled bolometer. Sample spectra were all referenced to a background spectrum of a smooth gold mirror.

8.3 SFG Sampling of Steel Surface

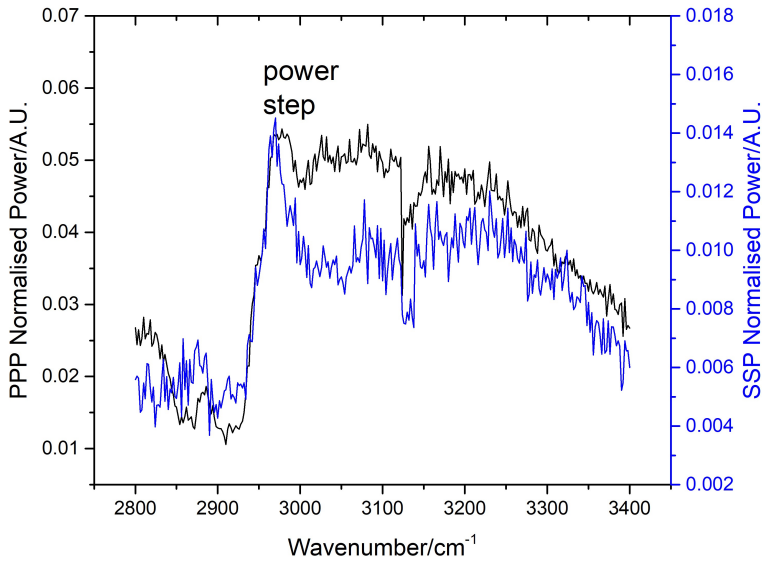

Fig. 8.4: Spectrum of a post-UV-ozone cleaned polished S355 steel substrate.

All steel substrates were UV-Ozone cleaned before exposure to organic solutions. Before immersing the steel sample in an additive solution, a SFG spectrum of steel was taken under a droplet of pure d-dodecane, and is shown in Figure 8.4. There are no above-noise peaks seen in the spectrum, implying no significant adsorbed organic contaminant on the post-UV-ozone S355 surface in the signal-to-noise setting presented in this work. The step observed is a power step from the laser when scanning across the range of frequencies. A similar scan was taken at the phosphate region (1010 to 1700 cm^{-1}) and no peaks were found.

This control experiment was done to ensure that any alkyl and phosphate signals result from organic additive adsorption, rather than possible surface contamination or solvent adsorption onto the steel substrate.

8.4 Adsorption of DMP-30 on Steel

2,4,6-Tris(dimethylaminomethyl)phenol, DMP-30, shown in Figure 8.5 as a compound with three basic tertiary amine groups and a phenol functionality, is commonly used as an epoxy paint component.[202] To understand better how paints adsorb onto S355 steel substrates, it is essential to include adsorption studies of key paint constituents such as this.

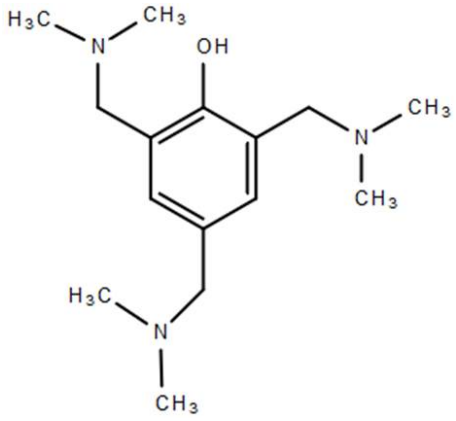

Fig. 8.5: Chemical structure of 2,4,6-Tris(dimethylaminomethyl)phenol

8.4.1 Adsorption Isotherm

Solution depletion isotherms on steel surface is conducted for DMP-30 adsorption onto steel. The phenol group makes it possible to monior DMP-30 concentrations in solutions through UV-Vis spectroscopy . Figure 8.6A shows the spectrum of dissolved DMP-30 in dodecane solvent. There is a prominent peak caused by the analyte located at 285 nm. Hence all quantitative absorbance analysis uses this wavelength.

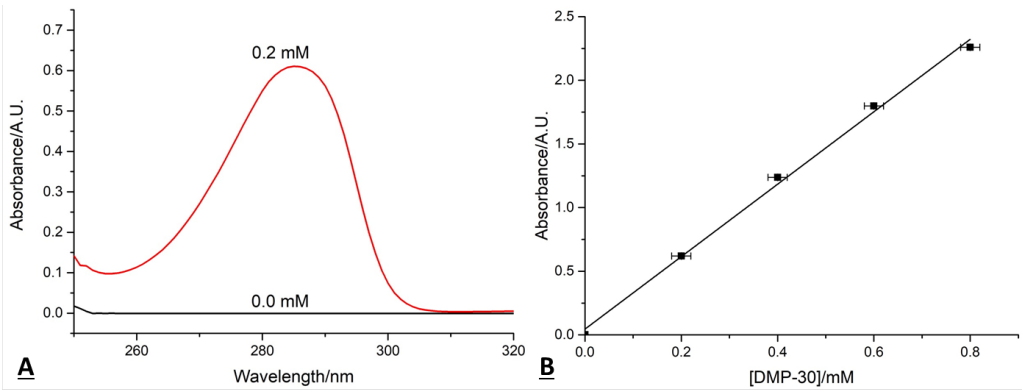

Fig. 8.6: DMP-30 quantitative analysis: with A) the absorption peak sampled for DMP-30 concentrations in dodecane solvent, and B) concentration calibration line.

The concentration determination for the depletion isotherm samples on steel was done by comparing sample absorption at the 285 nm peak to an established calibration line, relating absorbance to known concentrations. A linear

relationship between the two is observed up to 0.8 mM, as shown in Figure 8.6B.

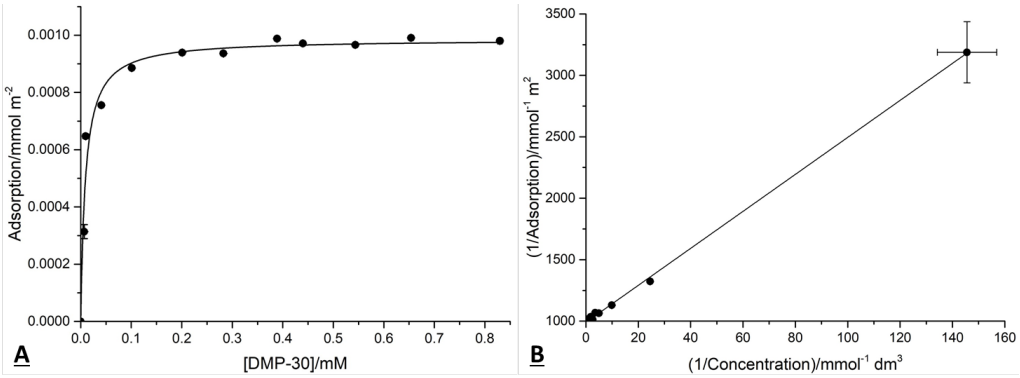

Fig. 8.7: A) DMP-30 adsorption isotherm on S355 steel, conducted in dodecane solvent, including B) linearised Langmuir isotherm representation of isotherm results.

With the DMP-30 equilibrium solution concentrations for different samples determined, the amount adsorbed is calculated using Equation 4.21 in Chapter 4 and plotted with respect to equilibrium solution concentration, as shown in Figure 8.7. Adsorption is seen increasing linearly and rapidly with increasing input DMP-30 concentration then quickly reaches a plateau. This indicates the formation of an adsorbed overlayer of DMP-30 on the steel powder surface and resembles Langmuir-like behaviour. The linearised form of the isotherm results can be used to extract the adsorption constants, K, and overlayer adsorption, Q, through Equation 4.18 in Chapter 4 for different adsorbates.

The Langmuir-like isotherm constant is estimated to be $1.07 \pm 0.19 \times 10^5$ M^{-1}. The amount adsorbed at the plateau is used to infer the area-per-molecule within the adsorbed overlayer on the steel powder, which is approximately 168 $Å^2$. Based on simple geometric arguments this value corresponds to the wide cross-section of the molecule, with each bond length to be approximately 1 Åand the molecule approximated as a flat square (10 bonds across the molecule), inferring DMP-30 molecules to be lying flat on the substrate. The data suggest all three nitrogen atoms, the phenol group, and the aromatic ring are close to/interacting with the surface.

The results agree well with theories of preferential adsorption of heteroatoms (S, O, N etc.) onto steel through their lone pairs, and that the π-electrons

of benzene rings may block the steel surfaces from corrosive media.[203]

8.4.2 SFG

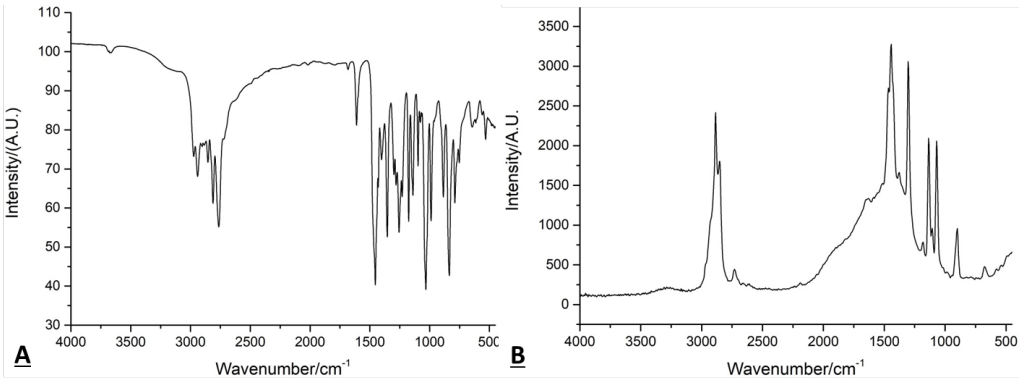

Fig. 8.8: Liquid DMP-30 in A) infrared and B) Raman spectra.

Sum frequency generation was conducted on the DMP-30 modified polished steel coupon. A droplet of 1 mM DMP-30 solution dissolved in d_{26}-dodecane was deposited on the steel surface during SFG-surveying to prevent DMP-30 desorption from the steel surface.

Raman and Infrared spectra of DMP-30, are shown in Figure 8.8. Prominent peaks at shifts just below 3000 cm^{-1} occur in both spectra, attributed to C-H stretches in methylene ($-CH_2-$) and methyl ($-CH_3$) groups. A strong peak at 3060 cm^{-1} is seen in the IR spectrum (weak in Raman) which is typical of C−H stretches in benzene rings.[204] If the modes have dipole change components normal to the substrate, they will be observable according to the surface selection rules.

The SFG spectra for DMP-30 on a polished steel surface can be seen in Figure 8.9, in both PPP and SSP polarisations. The spectra, aside from a power step at 3000 cm^{-1}, show no obvious peaks 8.8 to be identified. This apparent absence of above-noise peaks, in addition to adsorption observed from solution isotherm, shows there are no SFG-observable vibrational modes normal to the surface. This is indicative of DMP-30 molecules lying flat on the surface, in good agreement to isotherm results and is illustrated by Figure 8.10. The wide adsorption-area by DMP-30 makes it a good coating component for strong paint-steel adhesion.

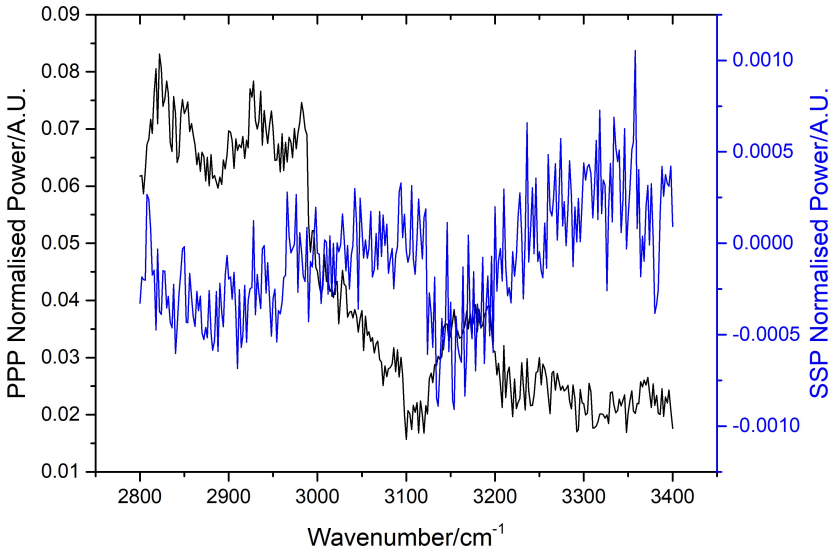

Fig. 8.9: SFG spectra of the steel surface exposed to 10 mM DMP-30 in dodecane, blown dry, and surveyed under 1 mM DMP-30 in d-dodecane.

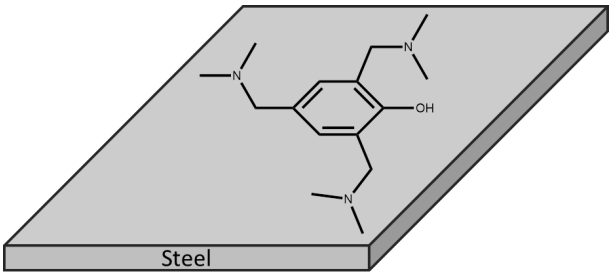

Fig. 8.10: The proposed flat adsorption geometry of DMP-30 on the steel surface.

8.5 Adsorption of Bisphenol A on Steel

Bisphenol A (BPA) is also a common epoxy paint component, whose phenol groups (Figure 8.11) attack epoxides.[202] Although its uses are currently being scaled back due to health concerns, it remains an industrially-relevant. Its adsorption behaviour onto steel is essential to the understanding of epoxy paints performance.

8.5.1 Adsorption Isotherm

Solution depletion isotherms for BPA were conducted in toluene, due its poor solubility in alkane solvents (oils) such as dodecane. Toluene, being a volatile solvent, needs to be handled quickly before evaporation significantly alter-

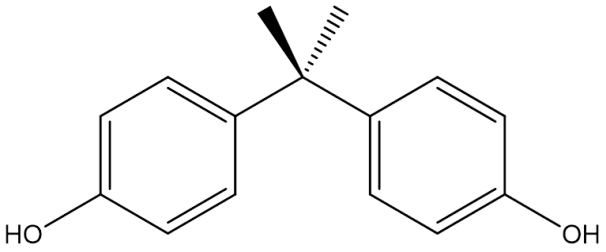

Fig. 8.11: Chemical structure of Bisphenol A

ing solution concentrations. The time of toluene exposure to polypropylene centrifuge tubes was minimised to prevent tube plasticisation and any possible chemical leaching into the supernatant. A toluene background scan was taken before any BPA solution measurements, showing No traces of plasticiser contamination from centrifuge tubes.

UV-Vis spectroscopy was used to analyse the BPA concentration within toluene solution, by monitoring the absorption peak at 287 nm. The absorbance increases with BPA concentration, as seen in Figure 8.12, with a linear relationship up to 0.35 mM. Isotherm samples with higher concentrations were diluted. Dilution errors involved are included with the isotherm data points.

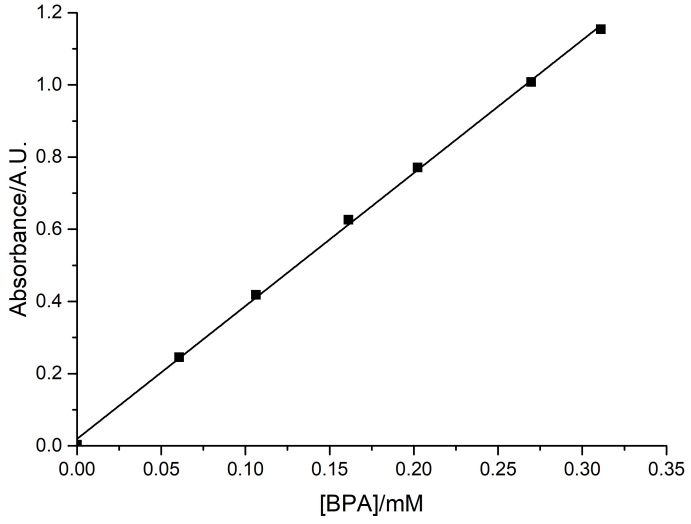

Fig. 8.12: Calibration curve to determine BPA concentration from IV-Vis absorbance.

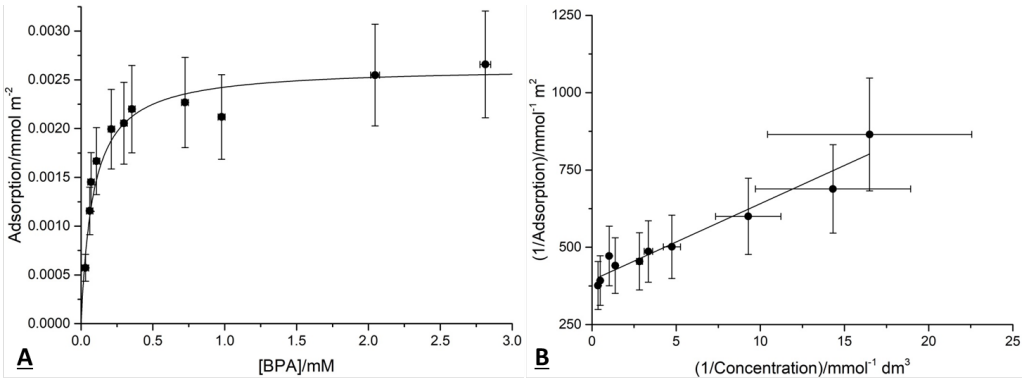

Fig. 8.13: A) BPA adsorption isotherm on S355 steel, conducted in toluene solvent, including B) linearised Langmuir isotherm representation of isotherm results.

The amount adsorbed within each sample suspension is plotted with BPA equilibrium concentrations in Figure 8.13. The data is fitted well with a Langmuir-like isotherm behaviour including the linearised form of the isotherm, with an adsorption constant of 1.18 ± 0.18 $\times 10^4$ M^{-1} (weaker than DMP-30 on steel in dodecane).

Using the plateau adsorption density, the area-per-molecule within the adsorbed overlayer for BPA on steel is calculated to be 63 $Å^2$. Using simple geometric arguments as mentioned previously for DMP-30, each BPA molecule is estimated to have an area of approximately 100 $Å^2$ when laid flat. For comparison, a benzene molecule occupies approximately 40 $Å^2$ when laid flat,[205] and 18 $Å^2$ when vertical.

The isotherm-determined area-per-molecule hints at one of constituent phenol rings of the BPA lying flat on the steel, with the other being relatively upright, constrained by the steric conditions of the two methyl groups at the molecular centre, as demonstrated in Figure 8.14. More precise geometric determination requires other techniques.

8.5.2 SFG

SFG spectroscopy was conducted on polished S355 coupons that were exposed to 10 mM BPA solution in toluene for 24 hrs. To confirm which peaks could be present in the SFG spectrum, the infrared and Raman spectra of BPA were taken and shown in Figure 8.15. Within the region between 2500 to 3500 cm^{-1}, the IR spectrum in Figure 8.15A shows peaks at 2870, 2934,

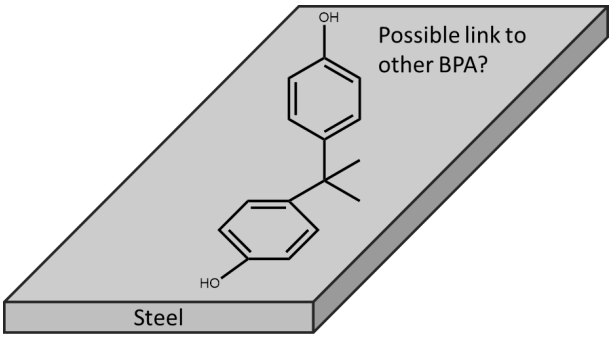

Fig. 8.14: Schematic of proposed adsorption geometry of BPA on steel surface from adsorption isotherm data.

and 2964 cm^{-1}, respectively characteristic of methyl symmetric (r^+), methyl symmetric Fermi resonance peak (r^+_{Fr}), and the antisymmetric methyl (r^-) stretches. There are coincidental peaks in the Raman spectrum in Figure 8.15B. Both spectra have a peak at 3060 cm^{-1} typical of C−H bond stretches from the benzene ring in BPA. The IR spectrum also has a broad peak at around 3300 cm^{-1}, from the hydrogen-bonded phenol hydroxyl groups.

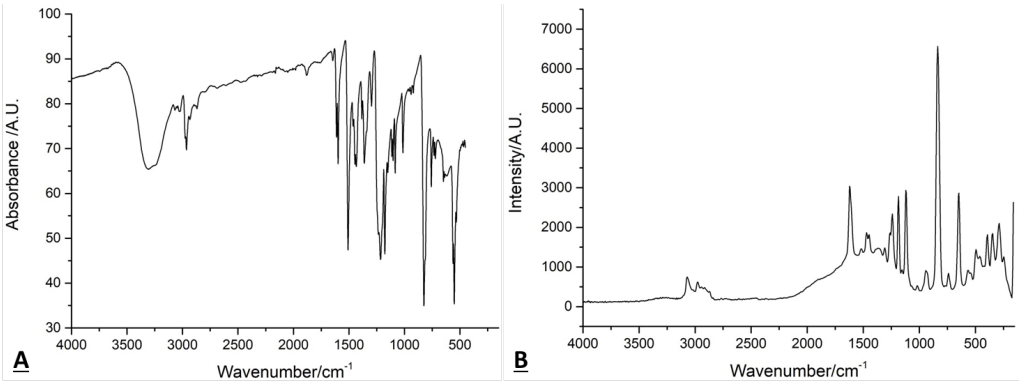

Fig. 8.15: Solid-phase Bisphenol A in A) infrared and B) Raman spectra.

SFG sampling for BPA adsorption on steel is conducted under a droplet of pure d_{26}-dodecane (nothing dissolved within). The sparing solubility of BPA in dodecane makes it unlikely for any BPA desorption to occur from the steel surface into the oil, used to dissipate the energy of incoming lasers.

The SFG spectrum in PPP and SSP polarisations are shown in Figure 8.16. In PPP polarisation, the alkyl stretching peaks at 2870, 2934, 2964 cm^{-1} are

observed. SSP polarisation, which is not particularly sensitive to antisymmetric stretches but is to symmetrical ones, give better defined peaks than those seen in the PPP spectrum. There are no obvious peaks around the 3060 and 3300 cm^{-1} regions in the two spectra.

While there is evidence of BPA adsorption from both isotherm and SFG data, it is unclear how exactly BPA is arranged, so as to give no transitional dipole moment components from the benzene ring C−H and phenol O−H bond vibrational modes normal to the steel surface. Possible explanations include the formation of centrosymmetric multimolecular arrangements, as seen before for carboxylic acid groups dimer formations.[79,199] Centrosymmetric formations are not observable by SFG due to its selection rules (details in Chapter 4). Further high spatial resolution investigation (e.g. neutron reflectometry) into the adsorbed monolayer structure is needed to determine the molecular interactions within.

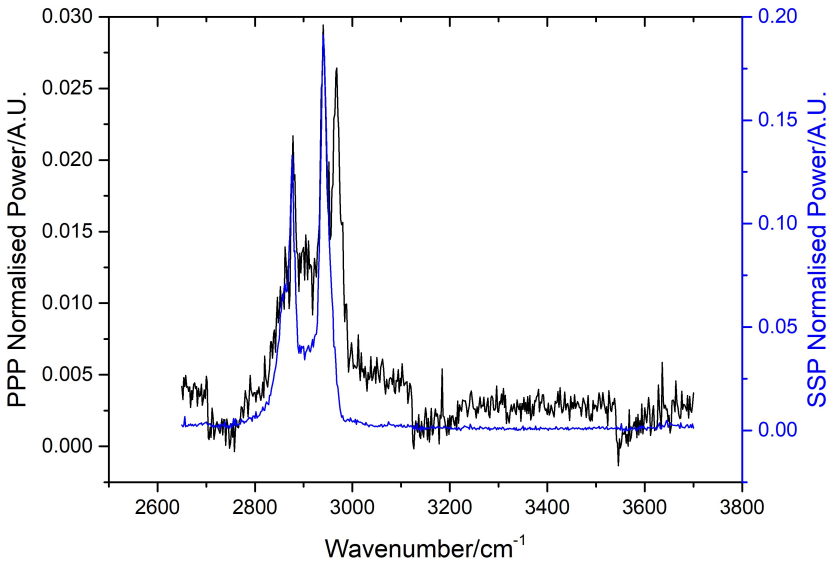

Fig. 8.16: SFG spectra of the polished steel surface exposed to 10 mM BPA in toluene, blown dry, and surveyed under a d-dodecane droplet.

8.6 Adsorption of 4-Mercaptophenol on Steel

Thiol groups have been suggested as effective corrosion inhibitors for steel, especially in aqueous acidic medium.[206–208] The thiol group carries a sulphur 'heteroatom' that has been suggested to strongly bind onto the steel surface.

The benzene ring with its π-electrons possibly retarding corrosive species intruding onto the steel substrate.[203] 4-mercaptophenol (HT), as shown in Figure 8.17, makes a simple yet interesting adsorbate to test whether such strong interactions are present.

Fig. 8.17: 4-Mercaptophenol (HT) molecular structure

8.6.1 Adsorption Isotherm

The adsorption isotherm was conducted in toluene solvent due to the poor solubility of HT in alkane/oil solvents. The benzene ring of HT allows its concentration to be monitored using UV-Vis spectroscopy, as shown in Figure 8.18A, through the absorption peak at 290 nm. The peak appears cut-off at 285 nm due to strong absorption by the cuvette and toluene leading to bad signal-to-noise ratio.

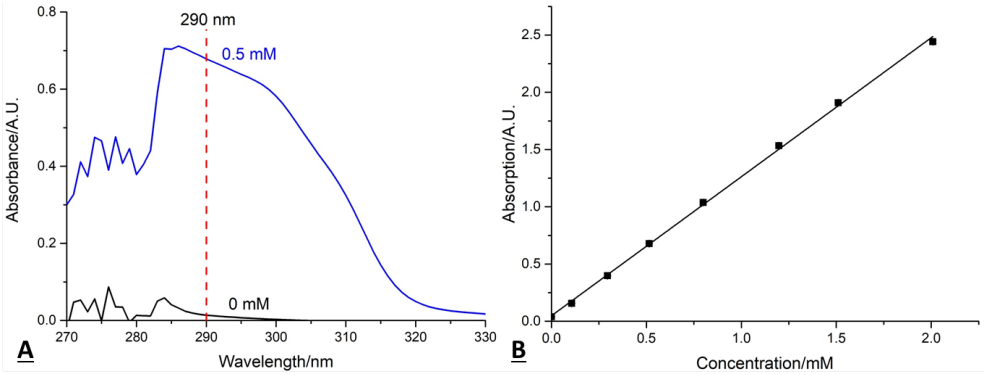

Fig. 8.18: 4-Mercaptophenol (HT) quantitative analysis: A) the UV-Vis spectrum of HT in toluene and B) concentration calibration line.

The calibration line in Figure 8.18B shows the absorbance-to-concentration relationship remains linear up to 2 mM. Samples with higher input concentrations had their supernatant diluted, with dilution errors included. Pure toluene UV-Vis backgrounds were taken to ensure no contaminants are present with the HT analyte.

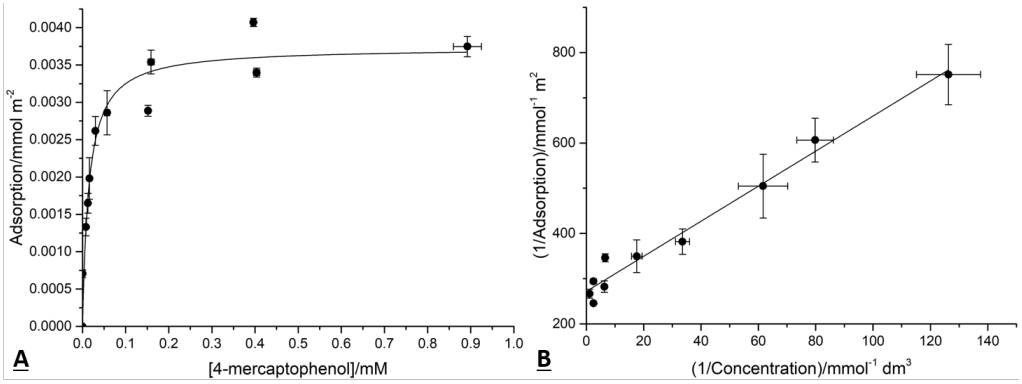

Fig. 8.19: A) HT adsorption isotherm on S355 steel, conducted in toluene, including B) linearised Langmuir isotherm representation of isotherm results.

The solution-depletion adsorption isotherm shows Langmuir-like behaviour, as shown in Figure 8.19. Langmuir-like isotherm adsorption constant is determined to be 6.73 $\pm$ 1.49 $\times 10^4$ M^{-1} through data fitting, indicating adsorption stronger than BPA but weaker than DMP-30. All three molecules share phenol functionalities. Therefore perhaps the sulphur 'heteroatom' of HT with its lone electron pairs may indeed influence the adsorption strength. However, due to the different solvent systems used (dodecane vs. toluene) and their different molecular structures, it is difficult to reach any definitive conlusions on 'heteroatom' attraction effects. Further experiments are needed for such a theory (e.g. far-infrared spectroscopy) to directly observe any metal-heteroatom bonds and their binding strengths.

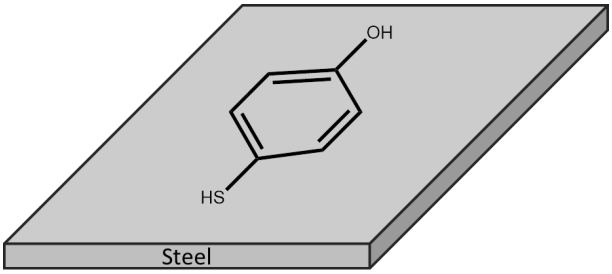

Fig. 8.20: Schematic of proposed adsorption geometry of HT on steel surface.

The adsorption plateau suggests an overlayer area-per-molecule of 44.5 Å^2 for HT. This is similar to the estimated 'flat' molecular area of 40 Å^2, and 18 Å^2 for an 'upright' geometry for a benzene ring.[205] The results are consistent with HT laying flat on the steel surface illustrated in Figure 8.20, to be

confirmed with spectroscopic data.

8.6.2 SFG

SFG spectra in PPP and SSP polarisations were measured. The steel surface was modified by immersing polished S355 steel coupons in 10 mM HT solution in toluene for 24 hrs. The measurement was done under a drop of pure d_{26}-dodecane to dissipate any excess heat generated from the lasers. The very low solubility of HT in dodecane prevented desorption from the steel surface.

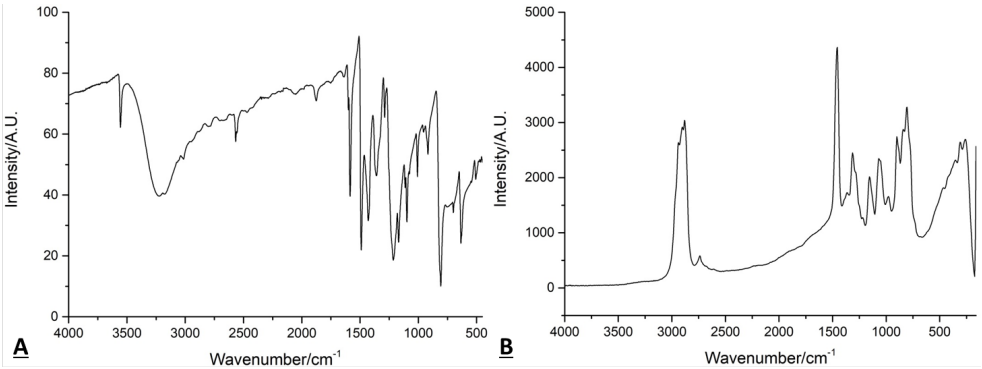

Fig. 8.21: A) Infrared and B) Raman spectroscopy of solid 4-mercaptophenol.

Infrared and Raman spectra were collected for HT, both are shown in Figure 8.21. In the IR spectrum, weak-but-sharp peaks can be been at 2567 and 3556 cm^{-1}, which respectively correspond to free thiol (S−H) and hydroxyl (O−H) stretches. A strong broad peak at around 3300 cm^{-1} suggests hydrogen-bonding between HT molecules through the hydroxyl functionality. The Raman spectrum, Figure 8.21B, shows a strong peak at 2880 cm^{-1} with coincidental absorption in the infrared spectrum. This is possibly a possible C−H peak from the benzene ring.

The SFG spectrum of HT-adsorbed steel is shown in Figure 8.22, with poor signal-to-noise ratio. Under the experimental conditions used, there are no peaks that could be clearly identified. The lack of apparent peaks is consistent with solution depletion isotherm data suggesting the HT molecules to lay flat on the steel, with all the stretches (C−H, C−C, S−H, and O−H) aligning parallel to the surface, rendering them SFG-inactive.

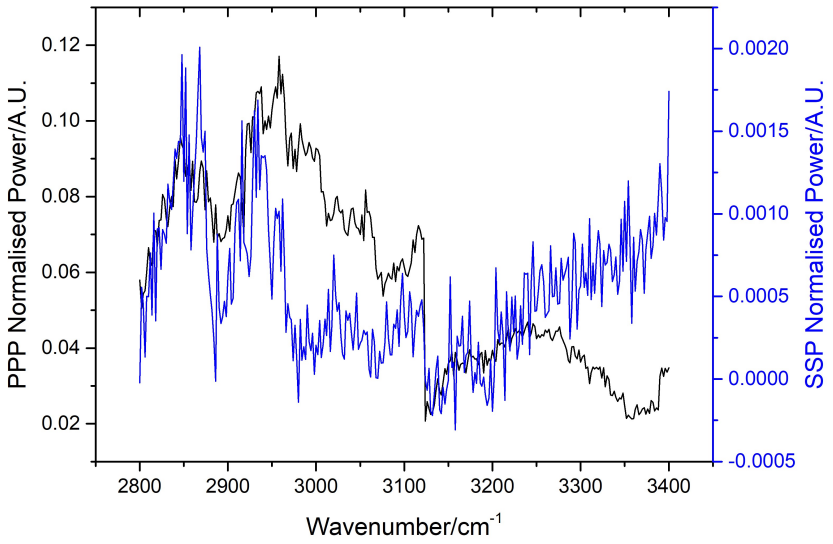

Fig. 8.22: SFG spectra of the steel surface exposed to 10 mM HT in toluene, blown dry, and survey under a d-dodecane droplet.

8.7 Adsorption of Palmitic Acid on Steel

Numerous detailed studies have shown both saturated and unsaturated carboxylic acids have been known to adsorb strongly onto iron oxide surfaces.[78,79,199,209–213] The acid groups have been suggested as a possible corrosion inhibiting functionality. Palmitic acid, shown in Figure 8.23, is a safe, single-chained carboxylic acid that can provide insights into the potential of carboxylic acids as coating-adhesion promoters and corrosion inhibitors on steel.

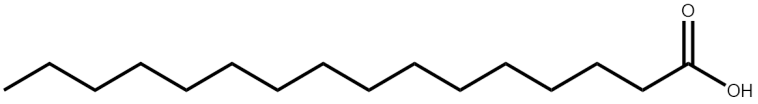

Fig. 8.23: Chemical structure of palmitic acid.

8.7.1 Adsorption Isotherm

A solution depletion isotherm, in dodecane, was used to assess the adsorption behaviour of palmitic acid (PA) on S355 steel. Solution PA concentration was monitored using transmission Fourier-transform infrared spectroscopy (FTIR) due to the strong absorbance by the carboxylic acid. Peaks as seen in Figure 8.24A at 1714 and 1766 cm^{-1} were used, respectively from monomer and dimer species of palmitic acid.[199] The integrated area underneath both

peaks scales linearly with solution concentration up to 3 mM (Figure 8.24B). Any samples with higher solution concentration were diluted, with dilution errors accounted for.

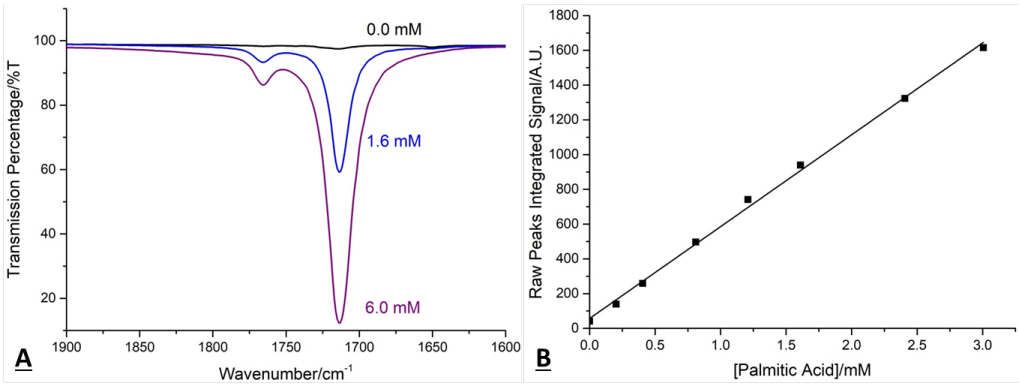

Fig. 8.24: Palmitic acid (PA) quantitative analysis, with A) FTIR peaks of PA monomer (1714 cm^{-1}) and dimer (1766 cm^{-1}), and B) concentration calibration line.

The adsorption behaviour is fitted well with a Langmuir-like isotherm model as shown in Figure 8.25. The equilibrium adsorption constant is 1.82 $\pm$ 0.18 $\times 10^4$ M^{-1} derived using the linearised Langmuir-like model fitting, and the adsorption plateau suggests an area-per-molecule of 36 $Å^2$, much smaller than the area PA lies flat on the steel surface (approximately 100 $Å^2$, each bond to be approximated 1 Ålong, as a rectangle). The small adsorption-area-per-molecule infers an relatively upright adsorption geometry illustrated in Figure 8.26.

The results suggest PA molecules adsorption on S355 to be in line with literature reports of PA adsorption on iron oxides.[79] The monolayer molecular geometry of PA molecules on steel native iron oxide surfaces are well-characterised to have a tilt angle of approximately 45°, hence SFG studies are not conducted.[199,214] The results reinforces the theory of preferential adsorption of electron lone pair-possessing 'heteroatoms' to steel.

The equilibrium adsorption strength is stronger than for Bisphenol A, but weaker than for the 'flat' lying molecules (DMP-30, 4-mercaptophenol). This indicates that the adsorption of carboxylic acids on steel, despite the oxygen 'heteroatom bonding' with the steel surface oxide whose attachment mode remains unclear,[199] may not be as strong as the π-electron-steel interactions

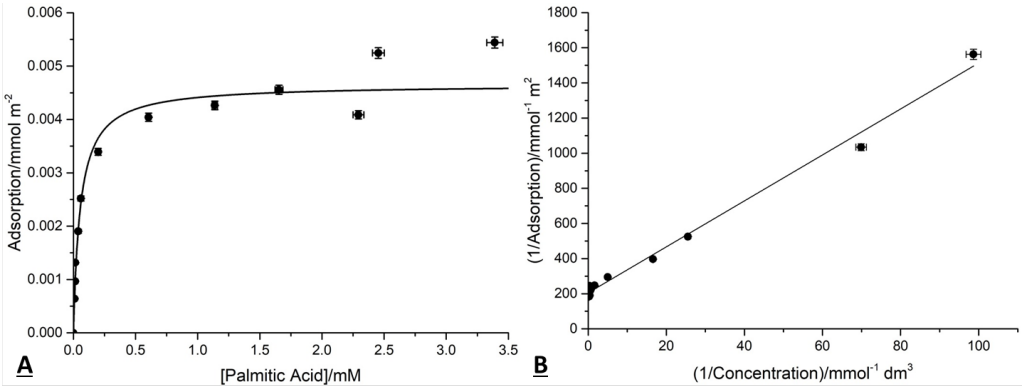

Fig. 8.25: A) PA adsorption isotherm on S355 steel, conducted in dodecane, including B) linearised Langmuir isotherm representation of isotherm results.

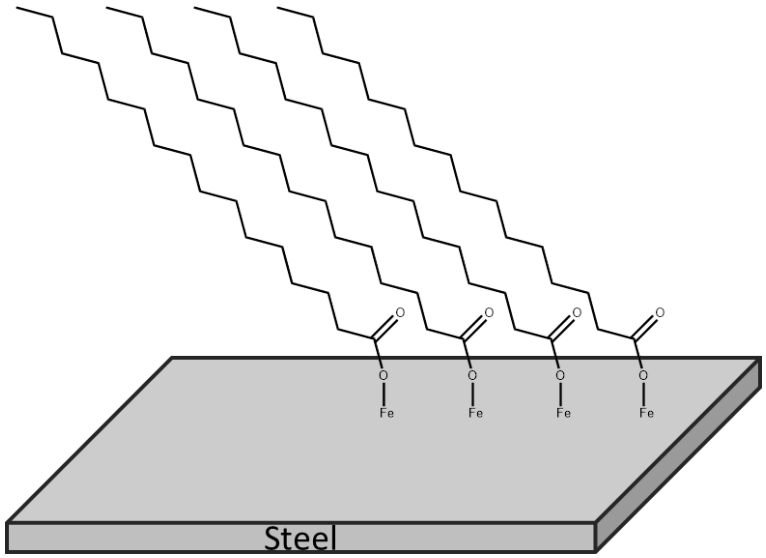

Fig. 8.26: Proposed PA adsorption onto steel, with the attachment model simplistically drawn as unidentate binding though other possible attachment models are also possible.

available to the aromatic species which have their entire molecular cross-section interacting with the substrate. Further experimentation to directly observe possible carboxylic acid-steel chemisorption through far-infrared experiments, would provide useful information on the suitability of PA as a paint additive.

8.8 Adsorption of Bis(2-ethylhexyl) phosphate on Steel

Phosphating of surfaces of carbon steel has been widely used to improve corrosion and wear resistance. The evolution of phosphating technology has included the use of organic phosphate compounds, such as zinc dialkyldithiophosphates (ZDDPs) that exploit tribochemistry to form phosphate glasses and improve wear resistance.[215–217]

In the literature bis(2-ethylhexyl) phosphate (BEHP, Figure 8.27) is often delivered through aqueous or ethanol solvent systems.[196,197] This study determines its adsorption at the dodecane-steel interface, relevant to its possible role as a corrosion inhibitor in alkane-based paints.

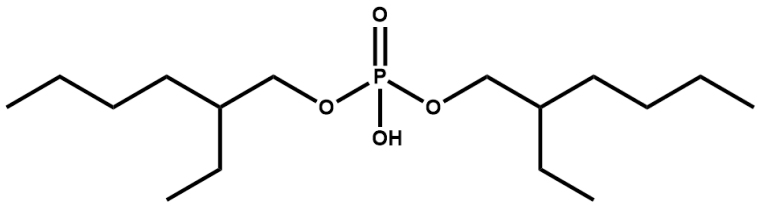

Fig. 8.27: Molecular structure of bis(2-ethylhexyl) phosphate

8.8.1 Adsorption Experiment

The monitoring of BEHP concentration in dodecane was through quantitative nuclear magnetic resonance (qNMR), with dodecane solvent-suppression of its major alkyl chain peaks. In the BEHP-in-dodecane spectrum, peaks coincidental to dodecane spectra are discounted as they either could not be contributed by BEHP, or would be difficult to analyse quantitatively. The BEHP peak of interest is located at 4.0 ppm and is highlighted in Figure 8.28 in green. This peak is attributed to the methylene ($-CH_2-$) hydrogens at the α-position to the phosphate oxygen atoms.

After 24 hrs of equilibration of S355 steel powder and BEHP solutions in different concentrations, colouration in the supernatant is observed as seen in Figure 8.29. Increased BEHP input concentration gives increased colouration, while both dodecane and BEHP stock-solutions are both colourless liquids. A likely explanation is that a reaction between the steel and phosphate yields yellow-coloured product(s), which dissolve well in dodecane.

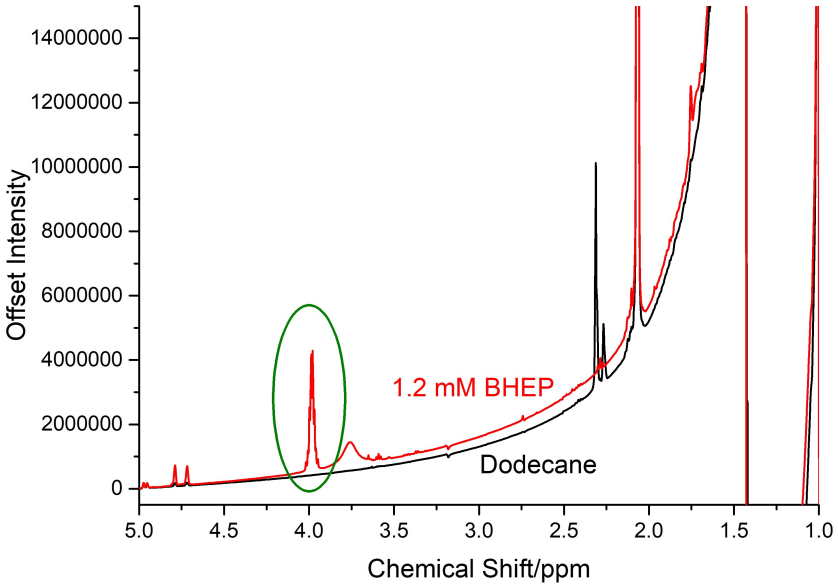

Fig. 8.28: ^{1}H NMR spectra of dodecane and BEHP solution. Signals shifts are referenced under d_6-acetone, and the peak of interest at 4.0 ppm is circled in green.

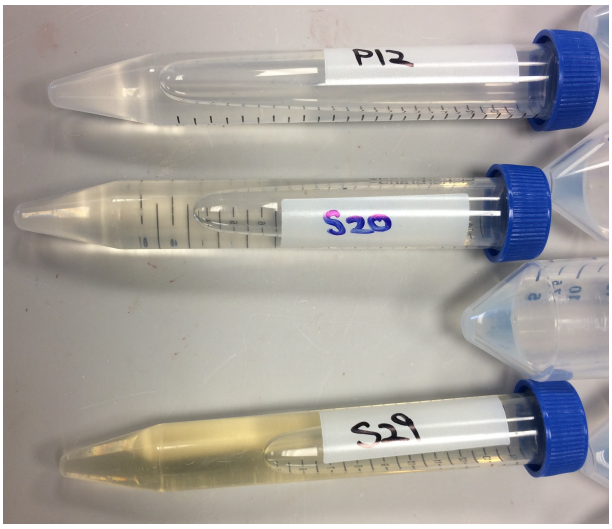

Fig. 8.29: Colouration of dodecane solution after 24 hr equilibration of the steel-BEHP solution. Sample 12: 1.2 mM, Sample 20: 2.0 mM, Sample 29: 20.0 mM BEHP input.

8.8.2 Investigation of Solid- and Liquid-Phase Reaction Products

Both the steel surface and the post-reaction dodecane solution were analysed to determine the reaction products. A polished S355 steel sample was ex-

posed to 10 mM BEHP solution in dodecane for 24 hr. The coupon was then washed with copious amount of n-hexane to remove any excess solution from the surface and analysed.

Solid Phase Products

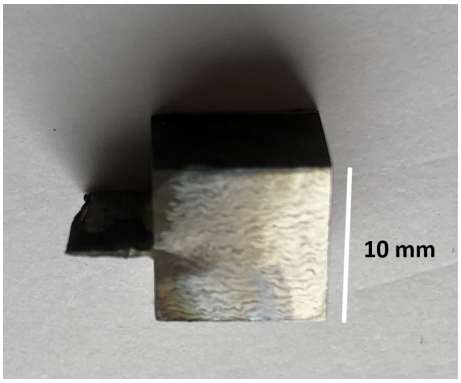

Fig. 8.30: S355 steel coupon post-reaction with 10 mM BEHP in dodecane. The surface has significantly dulled, with 'wave'-like formations.

Visual inspection of the post-reaction polished steel surface shows the previous mirror-finish to be significantly dulled by a black/grey product, as seen in Figure 8.30. This is strong indication that reaction products have been formed/deposited on the substrate, or that the surface topography of the steel has radically changed.

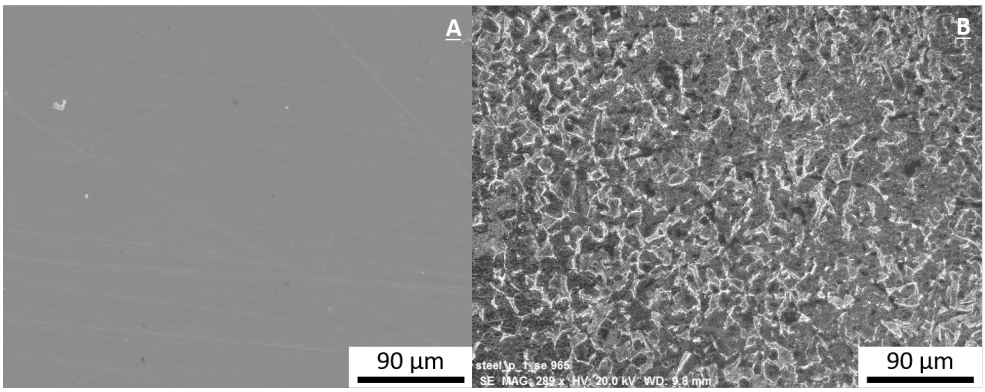

Fig. 8.31: S355 steel surface under SEM secondary electron inspection A) before and B) after exposure to BEHP-dodecane solution.

SEM surveying of the polished steel surface, before and after BEHP exposure, is shown in Figure 8.31. Significant topographical change is seen, with a large increase of surface roughness. EDX area spectra (Figure 8.32) show there is a significant increase in silicon and oxygen signatures, and the addition of a phosphorous signature to the steel surface post-BEHP exposure ('phosphating'). The results suggest phosphorous species, possibly surface phosphates, are formed upon the reaction of steel with BEHP in dodecane/oil.

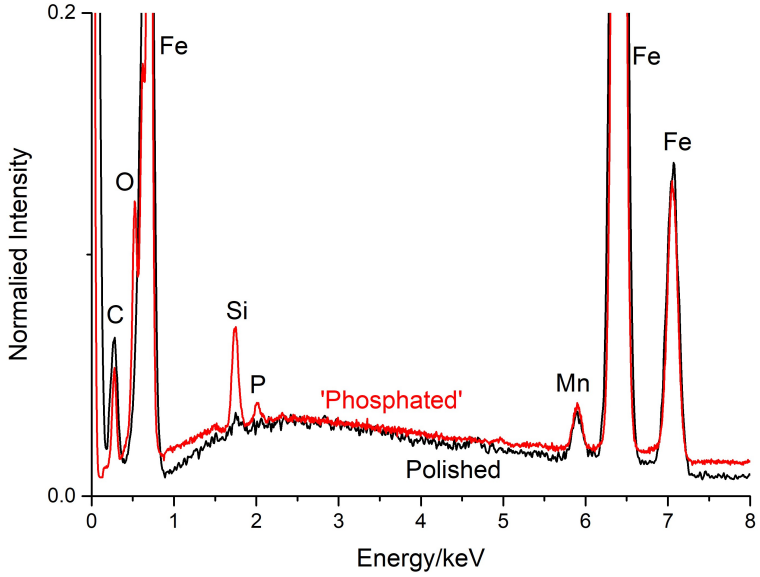

Fig. 8.32: EDX spectra from polished S355 steel before (black) and after (red) the 'phosphating' of the surface.

XPS was used to characterise the solid-state reaction product and to provide surface-sensitive quantitative analysis and chemical environments. Detailed scans were done for iron 2p, carbon 1s, oxygen 1s, and phosphorous 2p peaks, with analogous scans also conducted for polished steel coupons exposed to just dodecane as control samples.

Elemental analysis for both control and 'phosphated' steel surfaces are listed in Table 8.2. The oxygen levels for the two samples are similar, while the 'phosphated' sample has lower iron and carbon atomic percentages than the control. The 'phosphated' surface has a significant 6% phosphorous content, absent in control samples. Therefore the products of the reaction between steel and BEHP contain phosphorous. The similar oxygen atomic percentage for 'phosphated' and control surfaces, despite the diminished share of iron

Tab. 8.2: Elemental atomic percentage survey of control and 'phosphated' steel samples.

Elements	**Control/%**	**'Phosphated'/%**
Fe	11.92 ± 1.35	8.47 ± 0.59
O	46.21 ± 1.10	46.43 ± 0.64
C	41.88 ± 1.19	38.73 ± 0.70
P	-	6.37 ± 0.50

and carbon for the former, is indicative that the reaction products are likely to be oxygen-rich; these 'replace' or coexist with the native iron oxide layer on steel.

Component-peak fitting for each elemental scan was conducted to detail the chemical environments present. The Phosphorous 2p peak is of particular interest, as the only new element introduced by the 'phosphating' process. Figure 8.33 shows the peak-fitted surface phosphorous spectrum, with a spin-orbit coupling gap of 0.87 eV,[218]. Only one phosphorous species is needed to fit the spectral peak; with a binding energy of 133.47 ± 0.25 eV for the $2p_{3/2}$ peak, a FWHM of 1.4 eV. This is in agreement to the binding energy of iron (III) phosphate in the literature.[219]

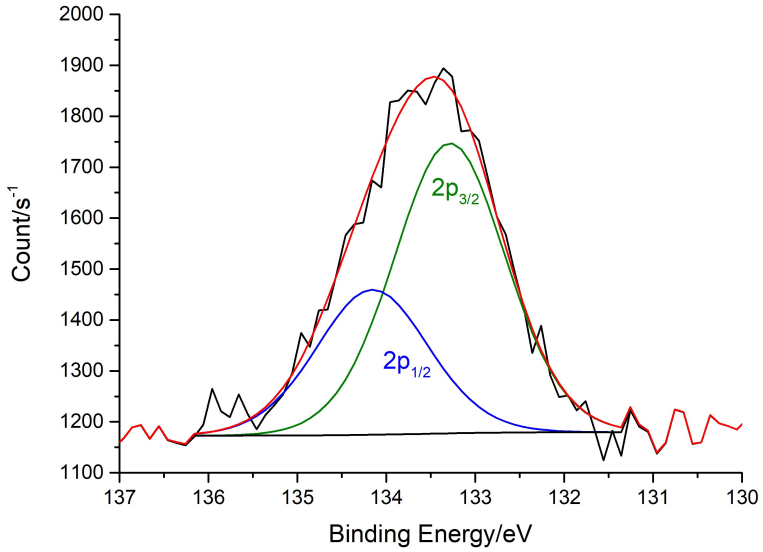

Fig. 8.33: Example XPS spectrum of the phosphorous 2p peak for the S355 steel surface exposed to 10 mM BEHP in dodecane.

Oxygen 1s peak deconvolution is shown in Figure 8.34. Along with identified bulk iron oxide, surface iron hydroxyl (Fe−OH) group, adventitious carbon oxides, and the phosphate species are included. Peaks for surface oxygen species and adventitious oxidised carbon species (based on carbon 1s peak deconvolution) overlap due to lack of literature data to conclusively deconvolute the peak in this region.[148] The phosphate peak is at 533.01 ± 0.31 eV binding energy, with a FWHM of 1.5 eV, in agreement with surface iron (III) phosphate binding energies.[220]

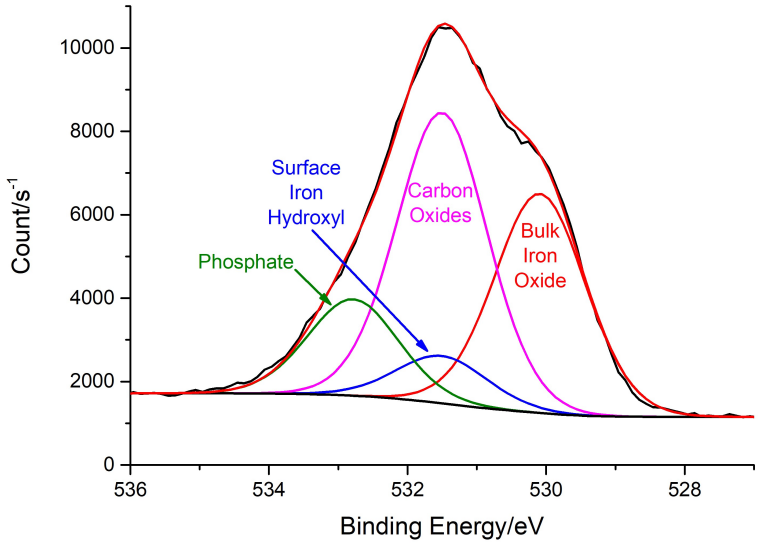

Fig. 8.34: Example XPS spectrum of the oxygen 1s peak for the S355 steel surface exposed to BEHP in dodecane.

EDX and XPS data therefore suggest the product formed on the S355 steel surface is likely to be an iron (III) phosphate. This provides a new oil-based method of phosphating steel surfaces.

Liquid-Phase Products

Analysis of the reaction products in the liquid phase was done through proton (^{1}H) and carbon (^{13}C) NMR spectroscopy. Removal of the background solvent improve detection sensitivity of the reaction product, simplifying the spectra collected, but The low volatility of n-dodecane makes its removal very difficult. Therefore an analogous 'oil' solvent of n-hexane was used instead for the reaction between BEHP and S355 steel powder. After exposing the S355 steel powder to 10 mM BEHP solution in hexane, the supernatant solvent

was removed with a rotary evaporator and the liquid mixture of product(s) and starting material was analysed.

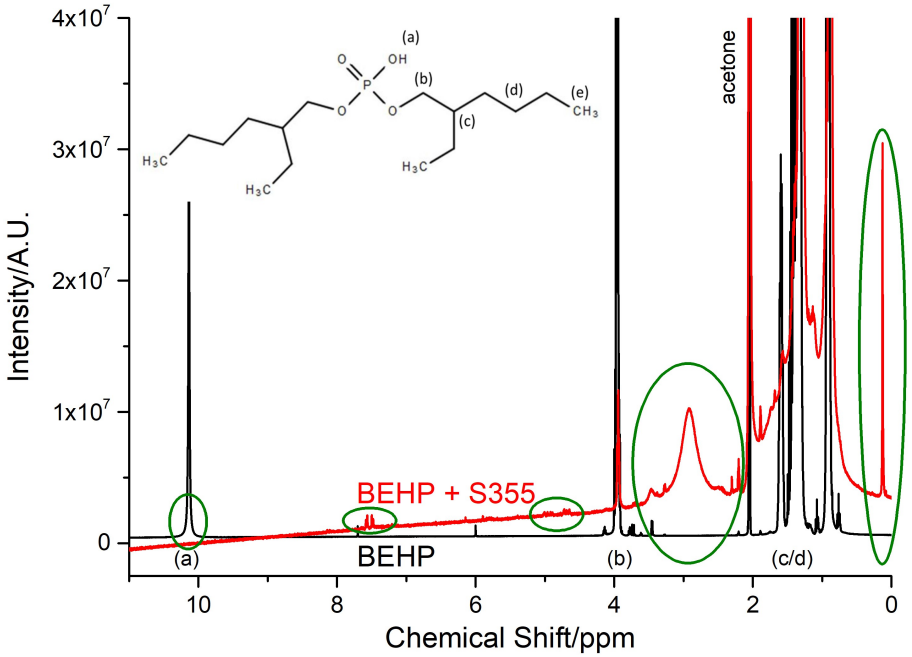

Fig. 8.35: ^{1}H NMR spectra of BEHP, and reaction products of 10 mM BEHP solution in hexane exposed to S355 steel powder for 24 hrs. Both analytes are dissolved in d_6-acetone for NMR analysis. Regions of interest are circled in green.

Figure 8.35 shows the spectral comparison between the 'control' BEHP-only spectrum and the liquid product(s) from the steel-BEHP reaction, with the salient differences circled in green. Of the highlighted peaks, the phosphate-hydroxyl (P−OH) group at 10.2 ppm is no longer present in the reaction product(s). A broad peak at around 3 ppm is seen after the reaction, indicating a possibly fluxional chemical environment. The chemical shift is typical of methylene hydrogens (C−H) situated close to an electron-withdrawing alcohol group (O−H).[221] Unfortunately the widening of the peak obscures any nuclear-spin coupling information that would aid structural determination.

A new peak at 0.1 ppm is also seen in the liquid product(s), suggestive of an aliphatic backbone signal. The peak appears to be a singlet with no splitting. There is insufficient information from the proton NMR spectrum to allow a definitive structural determination.

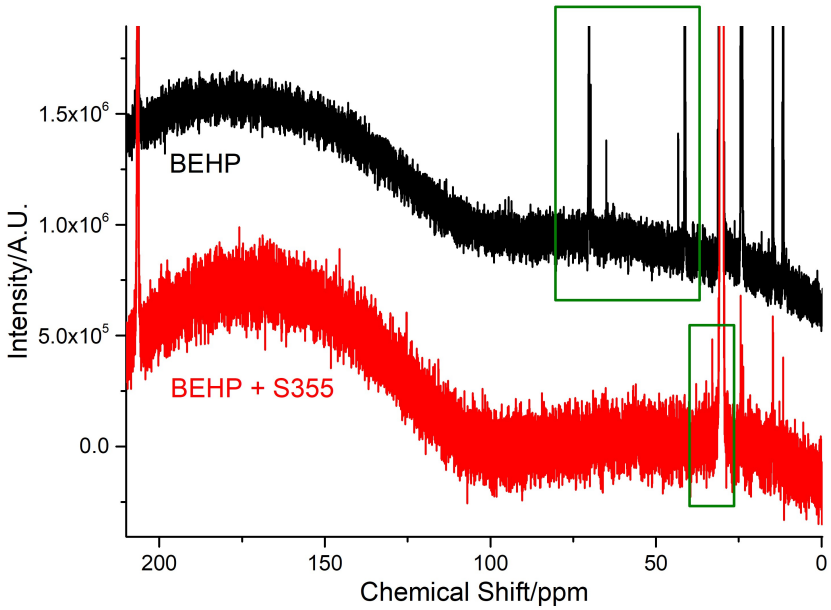

Fig. 8.36: ^{13}C NMR spectra of BEHP, and reaction products of 10 mM BEHP solution in hexane exposed to S355 steel powder for 24 hrs. Both analytes are dissolved in d_6-acetone (30 ppm, septet) for NMR analysis. Regions of interest are in green rectangles.

Carbon-13 spectra, shown in Figure 8.36, were also collected to observe the change of carbon chemical environments. BEHP peaks from 50 to 75 ppm disappear when the phosphate is exposed to S355 steel. The reaction product spectra have few high-shift peaks other than the one at 206 ppm, a peak common with the starting BEHP, whose unknown functionality is not changed significantly by the reaction. This lack of new/previously-existing high-shift peaks and the emergence of new low-shift peaks for the reaction product supports, in conjunction with the proton spectra, the hypothesis of structural changes to the BEHP in its reaction with the steel.

The combined NMR results suggest that while the phosphate head group may have reacted with the steel surface through the phosphorous-hydroxyl group, the oxy-alkyl chains of BEHP may have detached from the head group and dissolved into the similarly hydrophobic dodecane/hexane solvent illustrated in Figure 8.37. This results in a yellow coloured liquid product, possibly with an alcohol functionality instead of a phosphate, which would be in agreement with the solid state phosphorus signature seen on the steel surface *via* XPS.

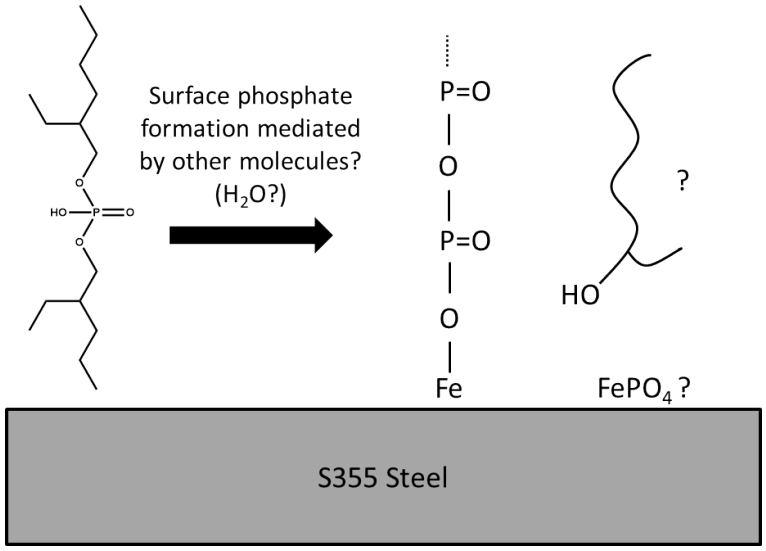

Fig. 8.37: Summary schematic of the proposed BEHP reaction onto S355 steel, showing an iron phosphate polymer product, with the displaced (unknown) aliphatic chain from BEHP in organic solution.

8.8.3 Far-IR and SFG

Far-infrared (FIR) and SFG spectroscopies were used to provide supporting data to XPS and NMR analyses. S355 steel was thermal vapour deposited onto smooth silicon wafers to 100 nm film thickness to create smooth surfaces for maximum reflectance, before being exposed to the 10 mM BEHP solution. The substrate was then washed with n-hexane to remove excess unadsorbed BHEP which are not adsorbed onto the surface for FIR analysis. Background reflectance spectrum was collected using a smooth gold mirror. Polished bulk S355 steel substrates were used for SFG experiments as the intense lasers were able to 'burn' iron film substrates.

FIR spectrum for the BEHP-modified surface is shown in Figure 8.38. No peaks are seen in the black 'blank' sample. The addition of BEHP into the solution introduces new broad peaks at 370 and 600 cm^{-1}, and a possible small peak at 475 cm^{-1}. The peaks at 370 and 600 cm^{-1} can be attributed to the vibrational stretches of the phosphate group.[222] The peak at 475 cm^{-1} may correspond to stretches of the iron-phosphate functionalisation bond (Fe−O−P, broad), expected to be within the 400 to 600 cm^{-1} region.[223] The low intensity of the 475 cm^{-1} peak prevents it to be well-resolved. FIR results therefore support the possibility of phosphate product formation on the iron surface.

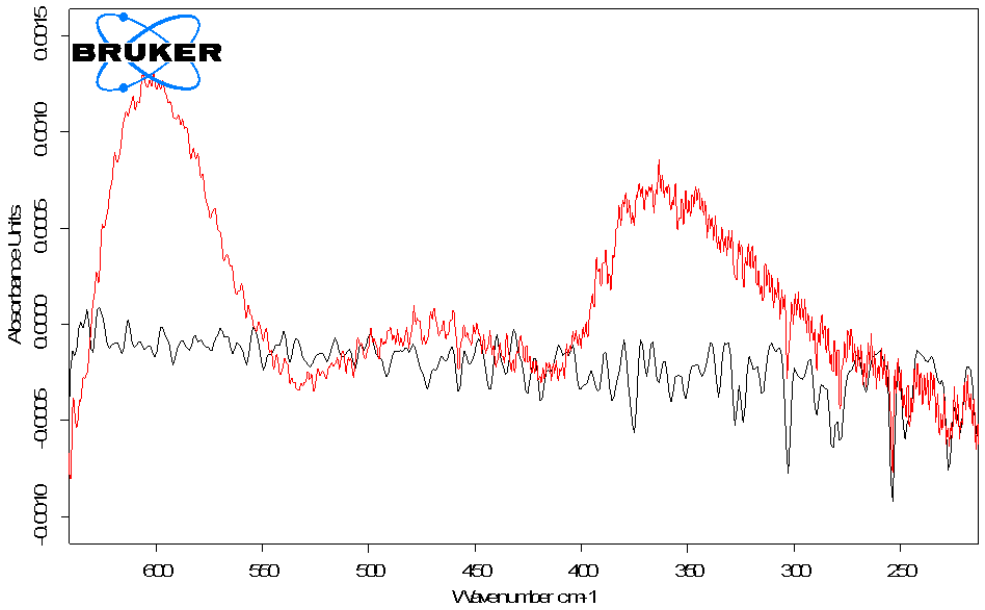

Fig. 8.38: Far IR spectra of a blank steel film sample (black) not exposed to any BEHP but immersed in dodecane, and a steel film exposed to BEHP in dodecane for 24 hrs (red). Both samples were washed with n-hexane as a final step.

In Figure 8.39, Raman and IR spectra of BEHP are shown. Aliphatic peaks around 3000 cm^{-1} and prominent phosphate-associated peaks seen in both IR and Raman spectra from 1000 to 1300 cm^{-1} are of particular interest. SFG surveying of a polished S355 surface exposed to 10 mM BEHP in dodecane solution for 24 hrs was conducted. Alkyl (2800 to 3100 cm^{-1}) and the phosphate-associated region (1000 to 1700 cm^{-1}) spectra were collected, in both PPP and SSP polarisations.

The alkyl region SFG spectrum is shown in Figure 8.40. Clear peaks are seen in both polarisations. Peaks at 2878, 2940, and 2970 cm^{-1} in PPP polarisation can be attributed to stretches by the methyl ($-CH_3$) end group, respectively the symmetric (r^+), symmetric Fermi resonance (r^+_{Fr}), and antisymmetric (r^-) stretches.[76] Similarly the SSP spectral peaks at 2878 and 2940 cm^{-1} correspond to the methyl symmetric and Fermi resonance stretches. The polarisation is insensitive to the antisymmetric vibrational modes.

The phosphate region SSP spectrum in Figure 8.41 shows a peak at 1100 cm^{-1} from the SSP spectrum, but no significant peaks seen in PPP polarisation perhaps due to its lower sensitivity to symmetric stretches in com-

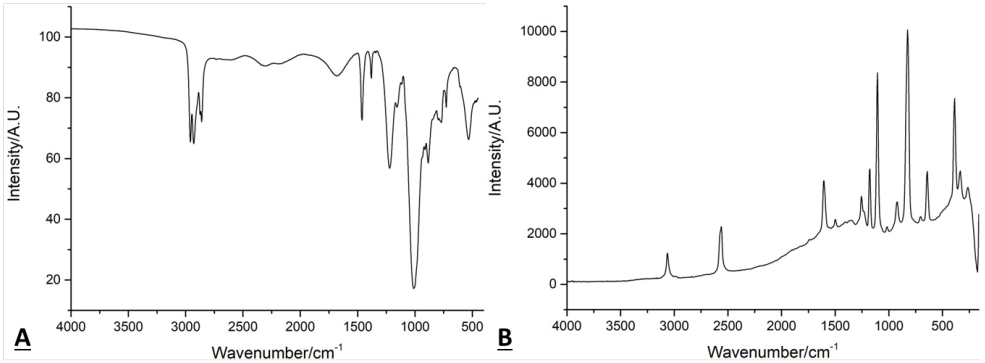

Fig. 8.39: A) infrared and B) Raman spectroscopy spectra of liquid bis(2-ethylhexyl) phosphate.

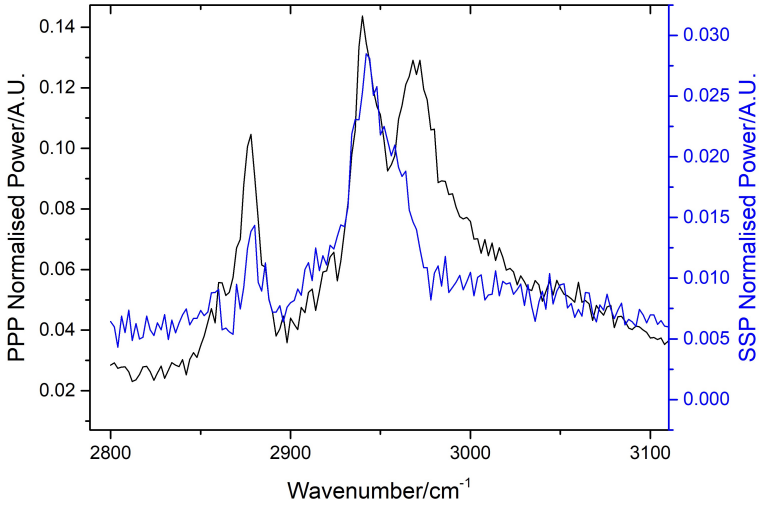

Fig. 8.40: SFG alkyl region spectra of the steel surface exposed to 10 mM BEHP dodecane , blown dry, and surveyed under a droplet of 10mM BEHP in d-dodecane.

parison to SSP polarisation. The signal-to-noise ratio is too low for PPP to clearly determine any peaks present. The peak is attributed to symmetric phosphate stretches (P−O) at the surface.[224] Given the surface-specificity of SFG it therefore confirms the adsorption of alkyl and phosphate species on the S355 steel, although whether these constitute *intact* BEHP molecules remains unclear.

FIR and SFG spectra independently confirm the presence of phosphate species on the S355 steel surface. SFG data suggests alkyl species adsorption on the steel, in addition to the phosphate functionality. The mechanism for phos-

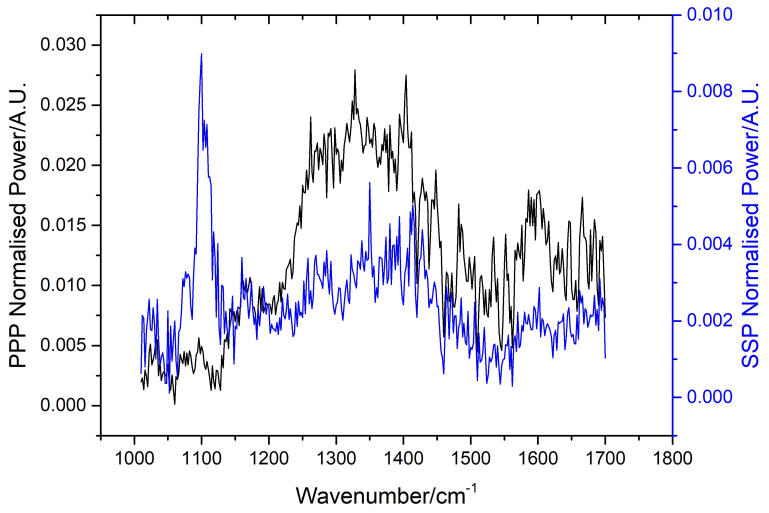

Fig. 8.41: SFG phosphate region spectra of the steel surface exposed to 10 mM BEHP dodecane , blown dry, and surveyed under a droplet of 10mM BEHP in d-dodecane.

phate product formation remains unclear and requires further studies.

Further experiments are needed to measure the effectiveness of the phosphate product in corrosion resistance, for future coating application as suggested in the literature.[225]

8.9 Chapter Summary

Adsorption of organic molecules of various chemical functionalities on the S355 steel surface has been tested. The experiments determine the adsorption strengths of these organic adsorbates and investigate into their adsorption geometries. The results of these investigations are summarised in Table 8.3.

To calculate the 'Molecules per site', surface site density was determined using the XPS and EBSD data in Chapter 5. The ratios between molecules and surface sites are not equal, revealing the adsorbed organic species pack together into overlayers. Different organic species adopt energetically-favourable conformations to pack as closely to each other as possible, rather than each adsorbate bonding to a single surface site, as is commonly seen in adsorbed organic layers.[226,227] Therefore despite the isotherm adsorption behaviour appears to be Langmuir-like, it cannot be considered to be truly Langmuirian.

Tab. 8.3: Summary of adsorption data of various organic molecules on S355 steel.

Adsorbate	**log** $K_{ads}/\mathbf{M}^{-1}$	**Area per molecule/Å^2**	**Molecules per site**
DMP-30	5.03 ± 0.08	168.4	0.1
Bisphenol A	4.07 ± 0.06	63.2	0.3
4-mercaptophenol	4.83 ± 0.10	44.5	0.4
Palmitic acid	4.26 ± 0.04	35.7	0.5
Bis(2-ethylhexyl) phosphate	-	-	-

Bis(2-ethylhexyl) phosphate is observed to react directly with the S355 steel, forming a solid phosphorous-rich product on the surface and yellow coloured product(s) in the dodecane solvent. The sp^3-hybridised phosphate centre should require nucleophilic attack to initialise surface phosphate formation. Trace water in the dodecane solvent or surface iron hydroxyl groups could be said nucleophiles, with 2-ethylhexanol and other aliphatic products as viable lipophilic leaving groups in the dodecane solvent. Future experimentation should test phosphate adsorption under both dried and water-saturated dodecane, to see whether there are any significant differences.

9. ADSORPTION AT THE ALMANDINE GARNET-LIQUID ORGANICS INTERFACE

9.1 Background

Abrasive blasted steel surfaces were seen to have significant almandine garnet abrasive residue covering up to a third of the surface. There is a possibility of competitive adsorption of paint organic additives between almandine garnet and steel at the steel-paint interface. Therefore the adsorption of the same organic additives in Chapter 8 were also tested on almandine garnet in this chapter, to provide the comparative adsorption strengths by each molecule on both steel and garnet substrates.

9.2 Experimental

9.2.1 Materials

Preparation methods of acid-washed almandine garnet powders and polished almandine garnet surfaces were identically to those described in Chapter 6. The surface characterisation of the powders and the polished were also detailed in that chapter. SFG sample preparations used to study the adsorption of different organic additives onto polished almandine garnet surfaces were identical to those used for polished S355 steel surfaces, save for the change of substrate.

9.2.2 Isotherm Sample Preparation

With the exception of using 2.0 g of acid-washed almandine garnet powder instead of 20.0 g of S355 steel powder described in Chapter 8, the experimental protocol for organic solvent isotherm sample preparation and equilibration were identical to those for steel powders.

9.2.3 Equipment

All experimental instruments were detailed in Chapter 4 unless specifically stated otherwise.

9.3 SFG Sampling of Almandine Garnet Surface

SFG spectra of the bare, 30 min UV-ozone cleaned polished almandine garnet surface were collected as a control sample.

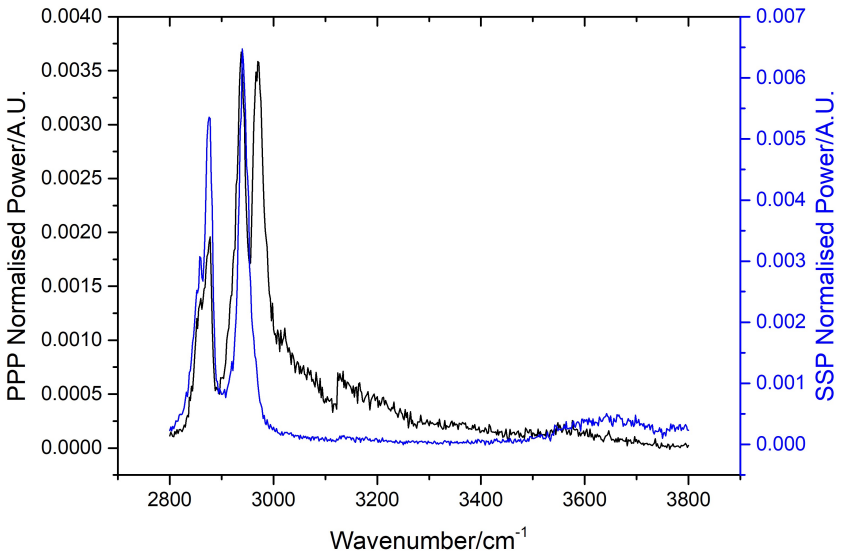

Fig. 9.1: SFG spectra in the alkyl stretching region of the polished, washed, UV-ozone cleaned almandine garnet surface.

The surface spectra were sampled in PPP and SSP polarisations, under a droplet of d_{26}-dodecane with a semi-circular-cylindrical calcium fluoride prism on top of the steel. The results are shown in Figure 9.1. In PPP spectrum, peaks at 2876 with a 2868 shoulder, 2940, and 2970 cm^{-1} are seen. These features correspond respectively of symmetrical methyl (r^+), methylene (d^+), methyl Fermi resonance (r^+_{Fr}), and antisymmetrical methyl (r^-) stretches.[76]

All the aforementioned peaks, except the methyl antisymmetrical stretch, is seen in the SSP spectrum which is not sensitive to antisymmetrical modes. The spectral results show that despite vigorous cleaning, there are residual akyl species, containing both methylene and methyl functionalities, on the

garnet surface. If only said alkyl peaks are seen sample SFG spectra, it is unclear whether any definite conclusions on alykl chain adsorption conformation can be made unless other diagnostic peaks are also present.

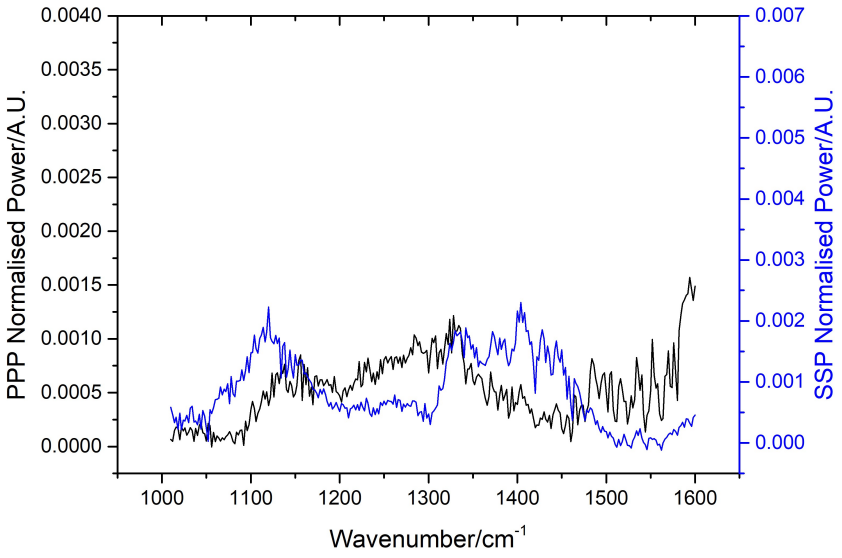

Fig. 9.2: SFG spectra in the phosphate stretching region of the polished, washed, UV-ozone cleaned almandine garnet surface.

Phosphate region spectra is shown in Figure 9.2. There were no obvious above-noise peaks in both PPP and SSP polarisations. Hence no identifiable phosphate-like groups are attached on the polished almandine garnet surface.

To assess the persistence of the alkyl contaminants on/in the almandine garnet surface, polished almandine garnet surfaces were plasma-cleaned for 30 min and re-surveyed. Compared to the washed, UV-ozone cleaned almandine garnet surface, the alkyl signals intensities are weakened as shown in Figure 9.3 for the plasma-cleaned surface. However, they remained present and observable.

SFG surveying of 'control' polished almandine garnet surfaces identified significant alkyl peaks. Organic additive adsorption analyses therefore cannot reply *solely* on alkyl region peak observations, previously used for steel surfaces, but require verification by other experimental results. The surface organic contaminants are persistent, possibly impregnated within the mineral.

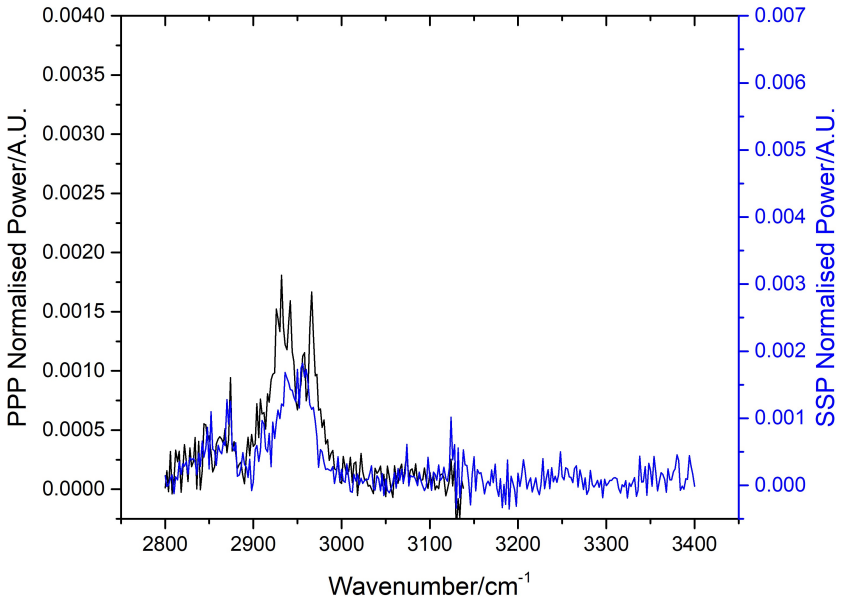

Fig. 9.3: SFG spectra in the alkyl stretching region of the polished, washed, plasma-cleaned cleaned almandine garnet surface.

9.4 Adsorption of DMP-30 on Garnet

9.4.1 Adsorption Isotherm

DMP-30 adsorption onto almandine garnet was monitored through solution depletion isotherm with UV-Vis spectroscopy. The absrobance at 285 nm was used to determine DMP-30 concentration in dodecane after equilibration, using pure dodecane background.

The adsorption response is plotted in Figure 9.4. Adsorption initially rises in a linear fashion, then quickly plateaus when input DMP-30 solution concentration is raised further. A Langmuir-like adsorption model is shown to fit well to the data, shown in a green line with the figure.

Using the linearised Langmuir-like adsorption model (Equation 4.18), the equilibrium adsorption constant on garnet is calculated to be 2.09 $\pm$ 0.36 $\times 10^5$ M^{-1}, stronger than for steel. The area-per-molecule on the surface is 168 $Å^2$. Based on simple geometrical calculations mentioned in Chapter 8, the value is consistent with DMP-30 molecules lying flat on the almandine garnet surface, with all three electron-donating 'heteroatom' nitrogen atoms, the benzene ring, and phenol group contacting the substrate. DMP-30 adsorption on garnet is similar to that seen for S355 steel.

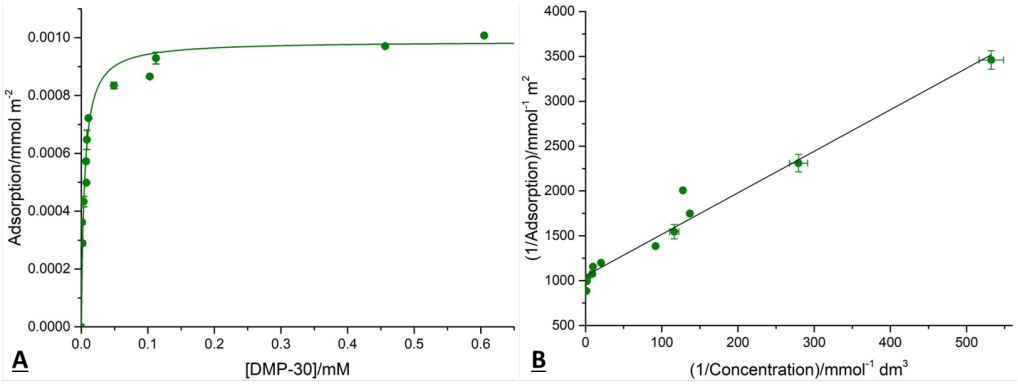

Fig. 9.4: A) DMP-30 adsorption isotherm on acid-washed almandine garnet, conducted in dodecane solvent, including B) linearised Langmuir isotherm representation of isotherm results.

9.4.2 SFG

PPP and SSP polarised spectra were conducted on a polished almandine garnet surface exposed to DMP-30 solution in dodecane. The spectra were collected with a droplet of 1 mM DMP-30 solution in d_{26}-dodecane deposited on top of the surface, to dissipate excess laser energy and to prevent DMP-30 desorption from the surface (Figure 8.3).

Spectra in both polarisations are presented in Figure 9.5. Alkyl peaks of 2852, 2870, and 2940 cm^{-1} can be seen in both polarisation spectra, with an additional peak at 2964 cm^{-1} for PPP polarisation. The first three peaks are respectively associated with symmetrical methylene, methyl, and methyl Fermi resonance stretches. The 2964 cm^{-1} peak is most similar to, but rather low shift (*cf.* 2970 cm^{-1} in literature values),[76] antisymmetrical methyl stretches. The peak is absent in SSP polarisation due to its insensitivity towards antisymmetrical stretches.

The alkyl peaks seen however are coincidental to the peaks seen on the 'control' polished surface without additive modifications. This prevents any definitive conclusions of alkyl species adsorption on almandine garnet. There is also no peak seen at the 3060 cm^{-1} region, typically from the carbon-hydrogen bond (C−H) of a benzene ring. This result is consistent with isotherm adsorption data suggesting DMP-30 to be adsorbed flatly on the garnet substrate as illustrated in Figure 9.6. If any of the benzene ring carbon-hydrogen stretches have dipole change components normal to the surface, they ought to be observable according to the SFG surface selection

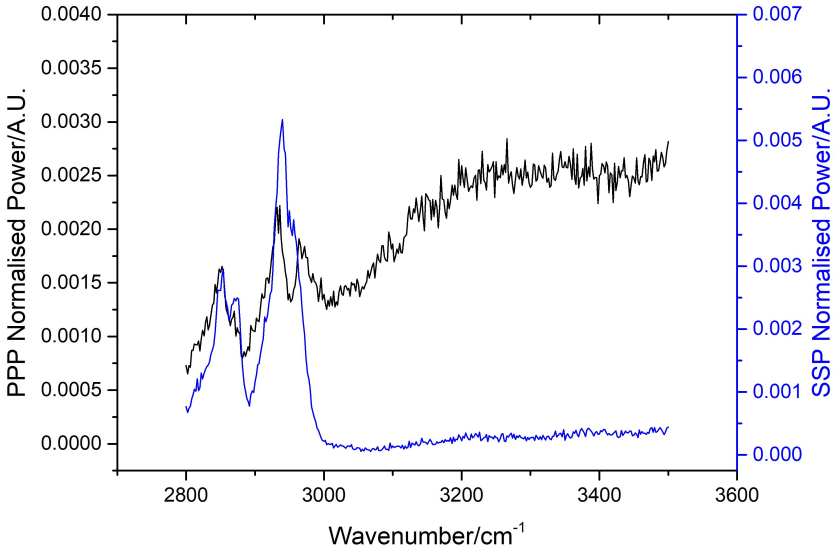

Fig. 9.5: SFG spectra of the polished almandine garnet surface exposed to 10 mM DMP-30 solution in dodecane, blown dried, and surveyed under a 1 mM DMP-30 d-dodecane droplet.

rules.

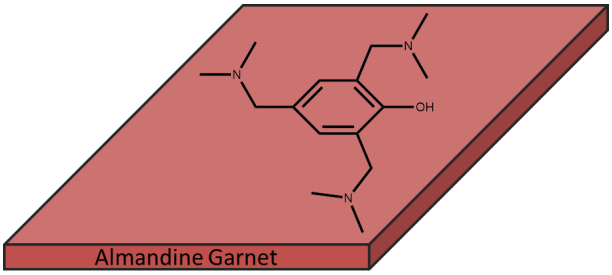

Fig. 9.6: Proposed flat adsorption geometry of DMP-30 on almandine garnet surface.

In Chapter 5, almandine garnet residues at the gently separated steel-paint interface were seen to have no attachment with paint residues. This suggests the cleavage of almandine garnet crystal to be a possible coating failure mechanism, exposing fresh garnet mineral surfaces with no paint on top (illustrated by Figure 7.15 in Chapter 7). The stronger DMP-30 attachment to garnet than steel through isotherm experiments supports this hypothesis.

9.5 Bisphenol A-Garnet Adsorption

9.5.1 Adsorption Isotherm

BPA solution concentrations in toluene were tracked by UV-Vis absorption at 278 nm. Acid-washed almandine powders were mixed with BPA solutions in toluene of known input concentrations to equilibrate. Post-equilibration BPA solution concentration for each sample was used to calculate adsorption of the additive on almandine garnet surface.

The results are shown in Figure 9.7. Adsorption of BPA on almandine garnet initially rises quickly, and then gradually plateaus with raised BPA input concentrations. The data is fitted well with a Langmuir-like isotherm model, shown by the green line within the figure.

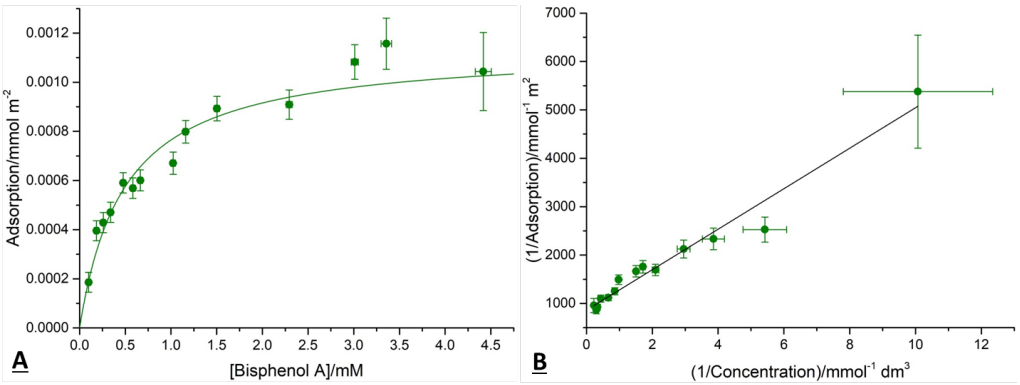

Fig. 9.7: A) BPA adsorption isotherm on acid-washed almandine garnet, conducted in dodecane solvent, including B) linearised Langmuir isotherm representation of isotherm results.

Linearised Langmuir-type model fitting estimates an equilibrium adsorption constant of $2.04 \pm 0.32 \times 10^3$ M^{-1}, almost an order of magnitude weaker than that on steel ($1.18 \pm 0.18 \times 10^4$ M^{-1}). The adsorption plateau signifies formation of a molecular overlayer on the garnet surface, with an area-per-molecule of 146 $Å^2$. Simple geometrical arguments suggests each BPA molecule would occupy an area of approximately 100 $Å^2$ (two benzene rings each occupying 40 $Å^2$ with two steric methyl and two phenol groups). This is consistent with BPA molecules conforming to lie as flatly as possible on the garnet surface and are not very closely packed together, illustrated in Figure 9.8. This inferred distribution is sparser than the adsorption on steel by BPA.

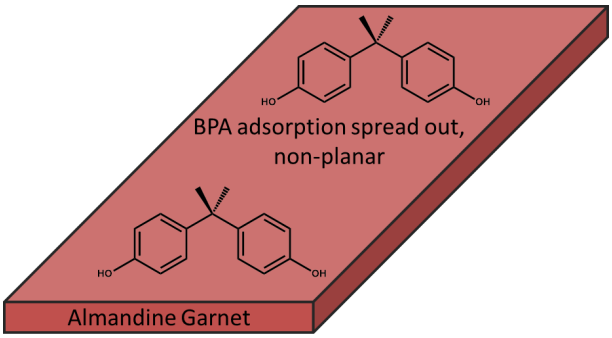

Fig. 9.8: Proposed spaced out, non-planar adsorption geometry of BPA on almandine garnet surface.

9.5.2 SFG

The polished almandine garnet surface was exposed to a 10 mM solution of BPA in toluene for 24 hrs. The surface was surveyed under a droplet of d_{26}-dodecane to dissipate excess energy from the intense incident lasers. The low solubility of BPA in dodecane made desorption unlikely. PPP and SSP polarised spectra of the BPA-adsorbed polished almandine garnet surface were collected.

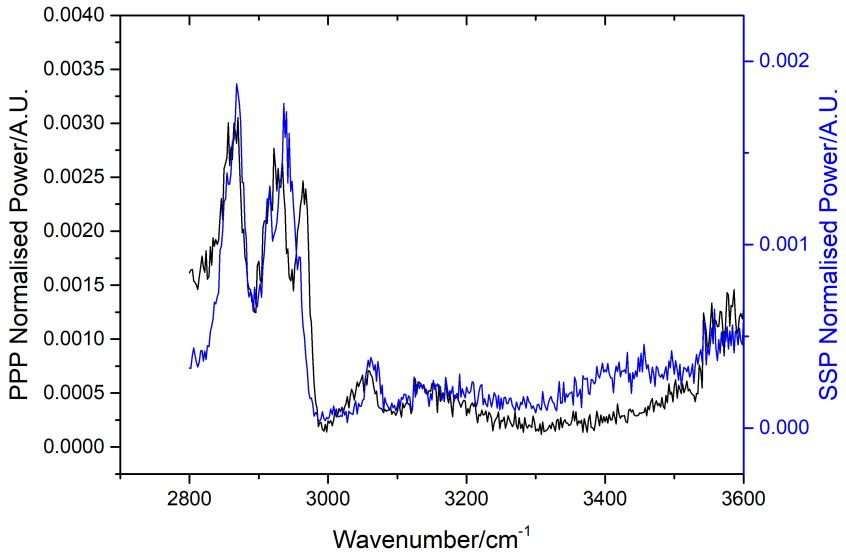

Fig. 9.9: SFG spectra of the polished almandine garnet exposed to 10 mM BPA solution in toluene, blown dry, and sampled under a d-dodecane droplet.

Multiple peaks are seen in the PPP spectrum within Figure 9.9. An asym-

metrical peak at 2868 cm^{-1} is associated with symmetric methyl stretch. A smaller peak at 2940 cm−1 is associated with the Fermi resonance of the symmetrical methyl group stretches. The peak at 2966 cm^{-1} is characteristic of antisymmetric methyl stretches. A weak but distinguishable peak is seen at 3060 cm^{-1}, characteristic of benzene ring carbon-hydrogen (C−H) stretches.

The SSP spectrum also show peaks at 2868, 2940, and 3060 cm^{-1}. A small 'peak' seen at 2916 cm^{-1} is likely due to signal-noise. The existing carbonaceous species on the 'bare' polished garnet surface prevents any definitive conclusions to be made about the alkyl group conformations for the adsorbed BPA.

The presence of the benzene ring carbon-hydrogen stretches at 3060 cm^{-1} however is consistent with BPA adsorption on garnet, in agreement with isotherm findings. This peak suggests not all molecular benzene rings lie parallel to the surface plane, enabling detection according to surface selection rules, despite isotherm data indicating the non-planar BPA molecules to be spread over the surface as widely as possible. Nor are the benzene rings arranged into any centro-symmetric environments that would prevent a SFG detection, previously suggested for BPA-steel adsorption.

The weaker adsorption strength of BPA on almandine garnet than on steel have implications on coating de-adhesion for garnet-abrasive blasted steel surfaces. Coatings are more likely to detach at the abrasive residue regions than at steel. Future work to compare the force required for coating removal from the almandine garnet, against the force necessary to cleave natural almandine garnet would be interesting to determine which link is the weakest.

9.6 Adsorption of 4-Mercaptophenol on Garnet

9.6.1 Adsorption Isotherm

4-mercaptophenol (HT) solution depletion isotherm was conducted in toluene due to its poor solubility in dodecane. HT solution concentration was monitored through UV-Vis spectroscopy, by measuring the absorption at 290 nm. The supernatant was analysed quickly to minimise the effects of evaporation by the volatile toluene in HT equilibrium concentration determination.

Adsorption calculated is presented in Figure 9.10. No observable HT adsorption is seen overall.

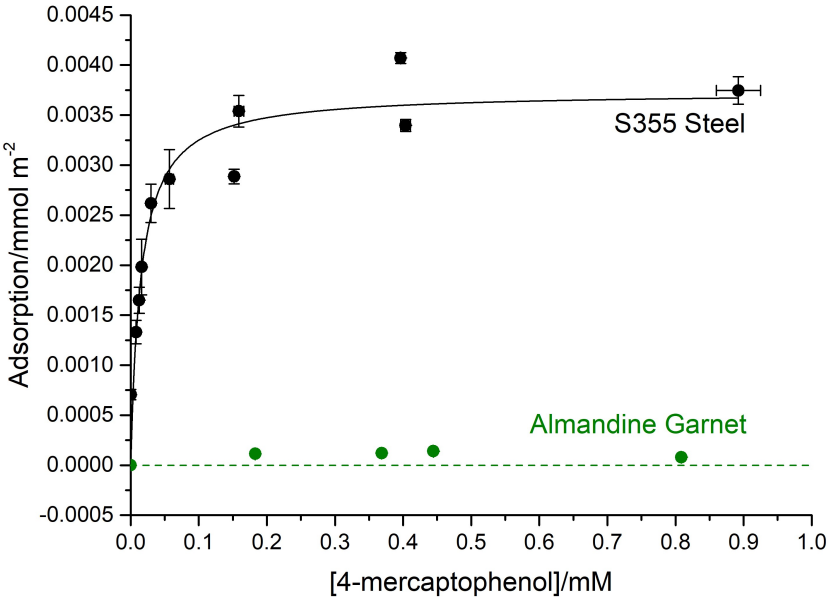

Fig. 9.10: HT adsorption isotherm on acid-washed almandine garnet, conducted in toluene solution. Steel adsorption results are included for comparison.

Previous characterisations of the almandine garnet surface reveal contributions by silicon, aluminium, and iron surface groups. Its surface chemical environment is an intermediate between iron and aluminium oxides. It is therefore surprising that similar adsorption behaviour comparable to surface iron hydroxyl groups on S355 steel for HT is not observed on garnet.

The results suggest adsorption of HT additive in toluene by S355 steel will be the dominant response at the toluene-based paint-garnet blasted steel interface. This presents an opportunity for selective adsorption onto steel for adhesion-promotion purposes to improve coating longevity.

9.7 Adsorption of Palmitic Acid on Garnet

9.7.1 Adsorption Isotherm

Palmitic acid (PA) adsorption on almandine garnet was investigated by solution depletion isotherm experiments in dodecane solvent. PA solution concentration is monitored through transmission infrared (IR) spectroscopy and is found to linearly correlate to the integrated peaks areas at 1714 and 1766 cm^{-1}, respectively from the monomer and dimer species of PA.[199]

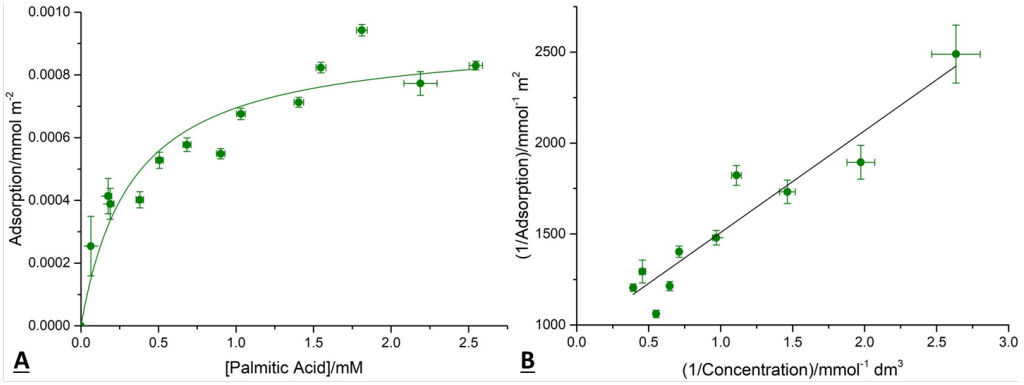

Fig. 9.11: A) PA adsorption isotherm on acid-washed almandine garnet, conducted in dodecane solvent, including B) linearised Langmuir isotherm representation of isotherm results.

The relationship between equilibrium concentration and adsorption of PA onto almandine garnet surface is plotted in Figure 9.11. Langmuir-like isotherm model fit is plotted as a green line and is seen to fit rather well. The adsorption initially increases quickly with PA input concentration then plateaus, indicating the achievement of an adsorbed overlayer.

The linearised Langmuir-type isotherm fitting allows for the estimation of equilibrium adsorption constant and adsorption area-per-molecules, respectively determined to be 3.02 $\pm$ 0.83 $\times 10^3$ M^{-1} and 180 $Å^2$. In contrast to PA adsorption on steel (1.82 $\pm$ 0.18 $\times 10^4$ M^{-1} and 36 $Å^2$), adsorption on almandine garnet is weaker and more sparsely dispersed. The PA molecule probably laid flat on the mineral surface based on simple geometrical arguments (approximately 100 $Å^2$, each bond and terminal atom atomic radius approximated to be 1 Å, simplified as a rectangle), illustrated in Figure 9.12

9.7.2 SFG

Raman and the Infrared (IR) spectra were collected for PA. The spectra are plotted in Figure 9.13. Alkyl stretches are present between 2700 to 3000 cm^{-1}, from the aliphatic backbone. Peak at 1697 cm^{-1} in IR spectrum corresponds to the carbonyl bond stretching which is absent in Raman. Therefore ought not be active in SFG spectra. Many peaks are seen below 1500 cm^{-1} for both spectra which would be SFG-active. For example, a strong peak is seen at 1470 cm^{-1} that is coincidental with IR spectrum, typical of methyl group bending modes.[228]

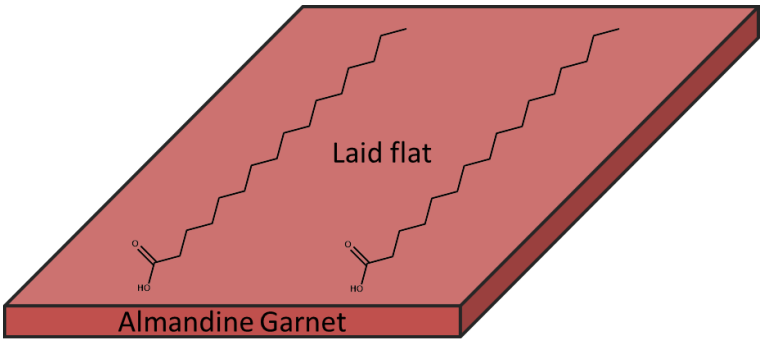

Fig. 9.12: Schematic proposing possible adsorption geometry for the palmitic acid molecules/dimer, based on the results obtained from solution depletion isotherm.

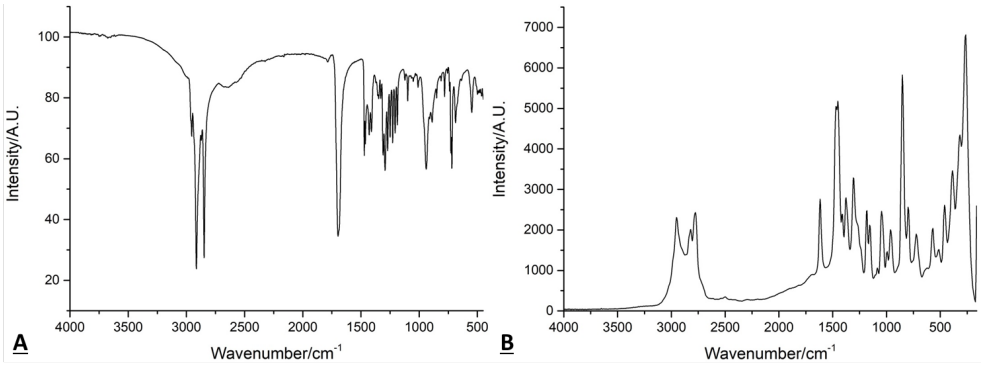

Fig. 9.13: A) Infrared and B) Raman spectra for solid PA.

PPP and SSP polarisation spectra were measured for a polished almandine garnet surface exposed to 5 mM PA solution, sampled under a droplet of 5mM PA solution in d_{26}-dodecane to dissipate excess laser energy and prevent PA desorption.

Alkyl groups associated regions are plotted in Figure 9.14. PPP spectrum has peaks at 2850, 2876, a possible shoulder at 2920, 2940, and 2970 cm^{-1}. These correspond respectively to the methylene symmetrical, methyl symmetrical, methylene antisymmetrical, symmetrical Fermi resonance, and methyl antisymmetrical stretches.[76] These stretches originate from the long alkyl chain of PA. Same peak positions apart from the antisymmetrical stretches are seen in the SSP polarisation. Additional peaks compared to washing-cleaned polished almandine garnet surface (2868, 2876, 2940, 2970 cm^{-1}) tentatively suggest PA adsorption. However due to difficulty in deconvoluting the back-

ground 'control' garnet signal from the additive-modified surface, reliable alkyl chain conformation determination is unfeasible.

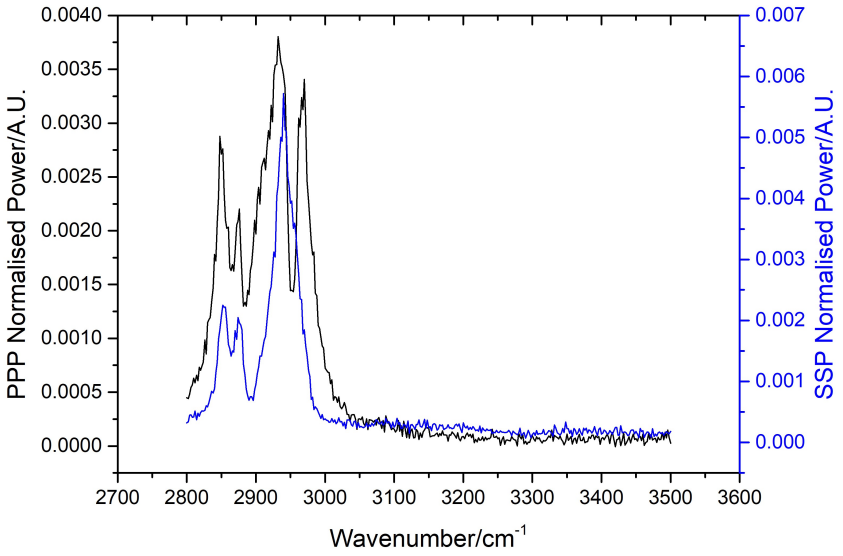

Fig. 9.14: SFG spectra in the alkyl region of the polished almandine garnet surface exposed to 5 mM PA solution in dodecane, blown dry, and surveyed under a 5 mM PA in d-dodecane solution droplet.

The PPP and SSP spectra of the carboxylic acid and phosphate group regions are plotted in Figure 9.15. The carboxylic acid group peak is absent as expected. In SSP polarisation multiple peaks at 1450 to 1490 cm^{-1} are seen, especially the 1470 cm^{-1} peak, with weak or absent peaks in PPP polarisation. These peaks are seen in the IR spectrum and are attributed to surface-adsorbed methylene and methyl group bending dipole moments normal to the surface. The SFG spectra in the carbonyl/phosphate regions confirm PA adsorption onto the mineral, in agreement with isotherm findings, with observable alkyl bending modes. However the data is insufficient to detail the conformation of the adsorbed PA alkyl chain.

The weaker binding of PA onto garnet, in comparison to S355 steel, hints at PA additive preferential adsorbed onto the steel when exposed to an garnet abrasive-blasted steel surface. Further adsorption geometry experiments experiments (e.g. neutron reflectometry) or more aggressive carbonaceous species-removal from the polished garnet surface may be needed to gain further insights into the alkyl group conformation of adsorbed PA on garnet.

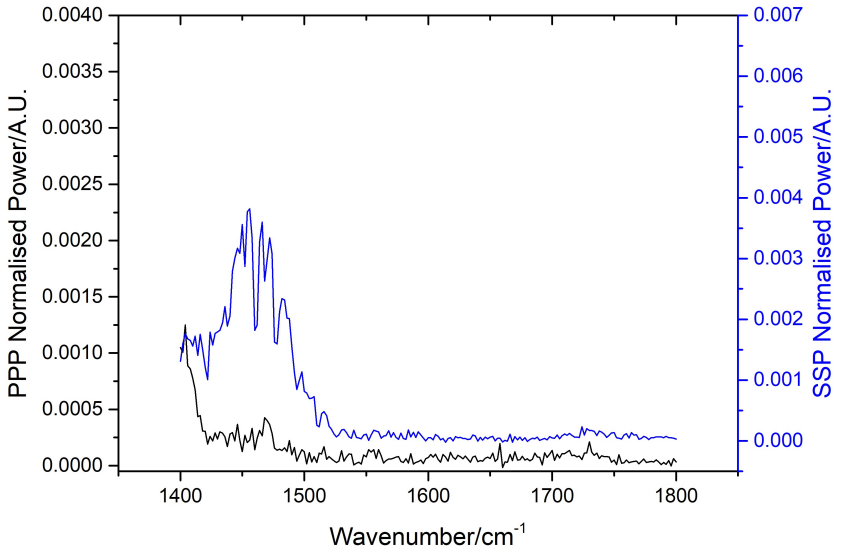

Fig. 9.15: SFG spectra in the phosphate and carboxylic acid-associated region of the polished almandine garnet surface exposed to 5 mM PA solution in dodecane, blown dry, and surveyed under a 5 mM PA in d_{26}-dodecane solution droplet.

9.8 Adsorption of Bis(2-ethylhexyl)phosphate on Garnet

9.8.1 Adsorption Experiment

Bis(2-ethylhexyl) phosphate (BEHP) adsorption on almandine garnet was investigated through solution depletion isotherm. With reference to the ^{1}H NMR spectrum shown in Figure 8.39 in Chapter 8, the peak associated with the methylene hydrogens at α-position to the phosphate oxygens at 4.0 ppm, was used for quantitative additive concentration analysis. The integrated peak areas are found to scale linearly with BEHP concentration in dodecane (Figure 9.16) and are used to determine sample BEHP concentration.

Relationship between equilibrium BEHP solution concentration with adsorption on almandine garnet is plotted in Figure 9.17. A Langmuir-like isotherm model fit is attempted which shows general agreement with the data. Adsorption increases rapidly initially with the rise of BEHP input concentration then quickly plateaus. This is consistent with the formation of an adsorbed BEHP overlayer on the almandine garnet surface.

Using the linearised Langmuir-like isotherm fitting, the equilibrium adsorption constant and area-per-molecule can be calculated. They are respectively

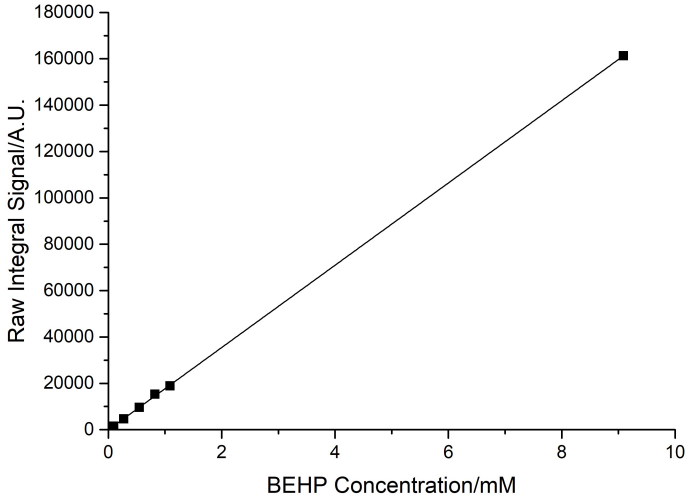

Fig. 9.16: Calibration line relating qNMR spectroscopy integrated area underneath the peak at 4.0 ppm to the concentration of BEHP in solution.

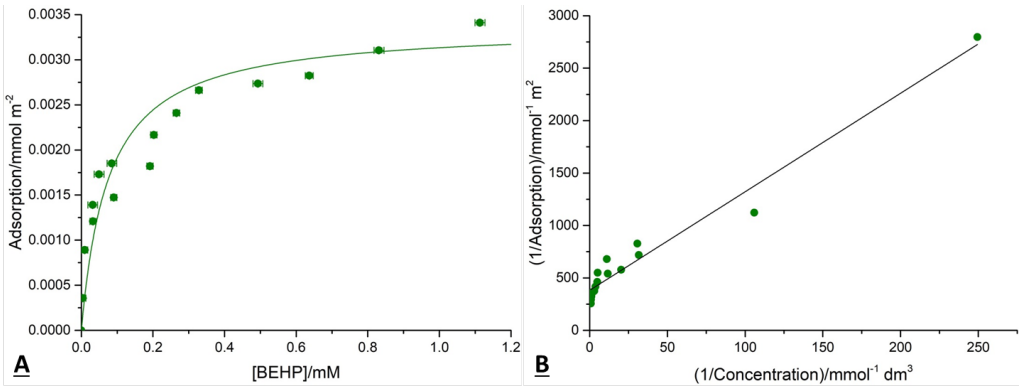

Fig. 9.17: A) BEHP adsorption isotherm on acid-washed almandine garnet, conducted in dodecane solvent, including B) linearised Langmuir isotherm representation of isotherm results.

estimated to be $6.02 \pm 2.94 \times 10^4$ M^{-1} and 49 $Å^2$. This small adsorption area suggests that the molecules are adsorbed vertically on the surface, with the more 'polar' phosphate head group sharing a higher affinity to the likewise 'polar' surface hydroxyl groups on garnet. Using basic geometric calculations, close-packed linear alkyl tails occupy approximately 20 $Å^2$ lengthways (approximating it to be a cylinder). Hence the approximate 50 $Å^2$ for a branched BEHP di-alkyl chain agrees well with an upright adsorption geometry hypothesis. Due to the hydrophobic nature of the dodecane solution phase, it is expected that only a monolayer would form instead of a phosphate

bilayer. In Figure 9.17 it may be possible to argue a bilayer has formed due to tentative indication of two plateaus, one at around 2 μmol m^{-2} (83 Å^2) and the other at 30 μmol m^{-2}. However, this is unlikely as it would indicate a rather diffuse bilayer, with the top layer (166 Å^2) even more diffuse than the bottom (83 Å^2).

9.8.2 SFG

The garnet surface was exposed to a 10 mM BEHP solution in dodecane, blown dry, and subsequently sampled with a drop of 10 mM BEHP solution in d_{26}-dodecane deposited on top, to prevent any phosphate desorption from the surface and help dissipate excess laser energy.

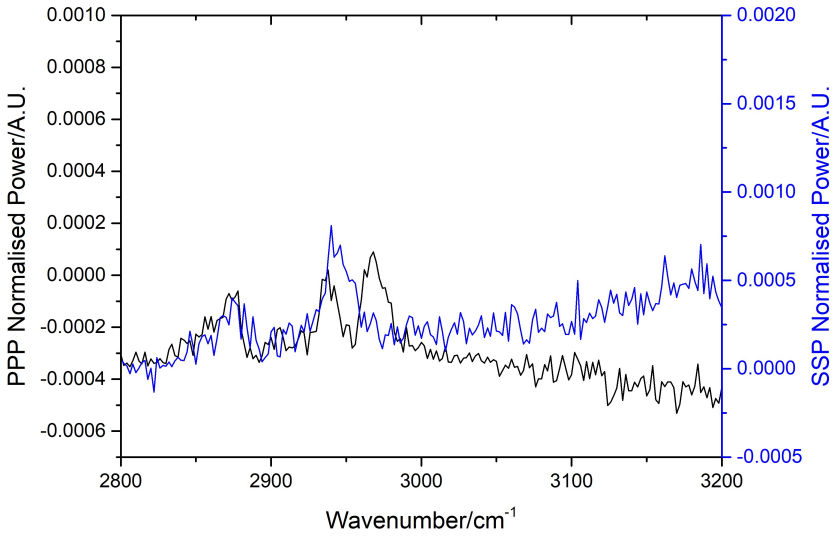

Fig. 9.18: SFG spectra in the alkyl region of the polished almandine garnet surface exposed to 10 mM BEHP solution in dodecane, blown dry, and surveyed under a drop of 10 mM BEHP solution in d-dodecane.

PPP and SSP polarised spectra were collected in the alkyl and phosphate associated regions. The alkyl region spectrum shows weak and noisy peaks, as shown in Figure 9.18. At PPP polarisation, peaks are seen at 2880, 2940, and 2970 cm^{-1}, respectively corresponding to symmetrical, symmetrical Fermi resonance, and antisymmetrical methyl stretches. Same peaks other than 2970 cm^{-1} are seen for the SSP spectra, due to its insensitivity towards antisymmetrical stretching modes. These identified peaks unfortunately are coincidental to those existing alkyl peaks seen on the 'control' polished al-

mandine garnet surface and are unsuitable for verifying BEHP adsorption seen in isotherm results.

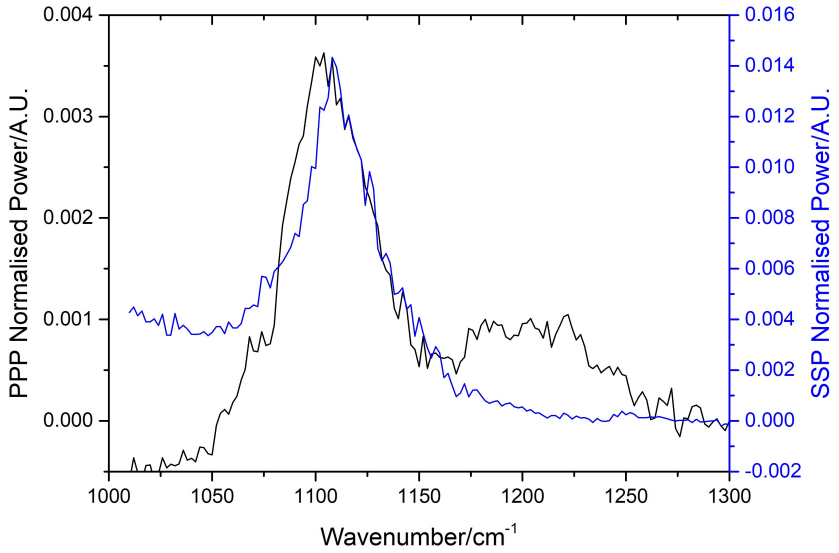

Fig. 9.19: SFG spectra in the phosphate region of the polished almandine garnet surface exposed to 10 mM BEHP solution in dodecane, blown dry, and surveyed under a drop of 10 mM BEHP solution in d-dodecane.

In the phosphate-associated region, a sharp peak can be seen at 1108 cm^{-1} in both PPP and SSP polarisations. There is a possible shoulder peak at 1200 cm^{-1} in the PPP spectrum. The 1108 cm^{-1} peak is associated with the symmetric stretches of the phosphate group, whilst the 1200 cm^{-1} peak is assigned to the phosphate antisymmetric stretches.[224] The strong symmetric stretch signal compared to noise suggests a highly-ordered adsorption arrangement of phosphate groups on the mineral surface. This result is consistent with isotherm-determined upright closely-packed BEHP adsorption geometry, with the phosphate group contacting the surface as illustrated in Figure 9.20.

9.9 Summary of Adsorption at the Garnet Blasted Steel-Organics Interface

In this chapter, the adsorption characteristics on almandine garnet by different organic molecules, that are either paint components or prospective coating additives, are tested. Their adsorption strengths and adsorption

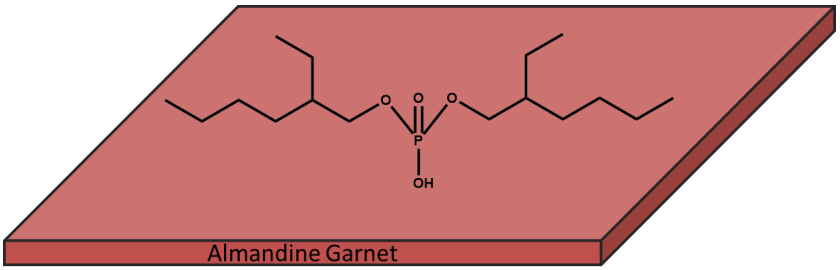

Fig. 9.20: Schematic of the proposed adsorption geometry of BEHP adsorption on almandine garnet, based on adsorption isotherm and SFG data.

conformations on the almandine garnet mineral are investigated and summarised in Table 9.1.

Tab. 9.1: Summary of adsorption data of various organic molecules on almandine garnet and S355 steel.

Adsorbate	**log K_{ads}/M^{-1}**		**Area per molecule/Å^2**	
	Garnet	Steel	Garnet	Steel
DMP-30	5.32	5.03	168	168
Bisphenol A	3.31	4.07	146	63
4-Mercaptophenol	-	4.83	-	45
Palmitic acid	3.48	4.26	178	36
Bis(2-ethylhexyl) phosphate	3.78	-	44	-

The comparison of equilibrium adsorption constants between the steel and garnet substrates show that for the many molecules tested, more tend to adsorb more strongly onto the S355 steel surface than on almandine garnet. This series of experiments explores the options for selective adsorption of molecules on different target substrates. For example, if strong adsorption is wanted solely on steel, but not on the garnet abrasive residue, a thiol-phenol additive such as 4-mercaptophenol is suitable. If stronger adsorption on almandine garnet is desired, coatings with higher molar percentage of DMP-30 or similar compounds should be used.

A comparison of molecules-per-determined-surface site between the garnet and steel substrates is shown in Table 9.2. Like steel, the ratios between molecules adsorbed and surface sites on almandine garnet are not equal.

The data confirms that surface binding densities for the organic molecules are not determined by surface site densities, but by close-packing conformations of the organic overlayer. Hence their adsorption is not truly Langmuirian despite displaying Langmuir-like adsorption behaviour. On the almandine garnet, all but BEHP are adsorbed flatly on the surface, whereas on steel, PA and BPA adsorb non-flatly to the surface. The molecular packing densities seen on garnet are generally lower than those seen on steel.

Tab. 9.2: Summary of molecule per surface site per the adsorbed overlayer data of various organic molecules on almandine garnet and S355 steel.

Adsorbate	**Molecules per site**	
	Garnet	Steel
DMP-30	0.6	0.1
Bisphenol A	0.6	0.3
4-mercaptophenol	-	0.4
Palmitic acid	2.1	-
Bis(2-ethylhexyl) phosphate	0.5	0.5

Binding strengths and molecular adsorption geometries can significant influence the ability of an overlayer in retarding or repelling corrosion species arriving at the steel surface,[199] underpinning the effectiveness of additives to inhibit corrosion and/or promote coating adhesion. Corrosive species may ingress at the garnet-steel interface to initiate corrosion, through the less resistant adsorbed layers on garnet to undermine the coating.

10. STEEL IN MARINE ENVIRONMENTS

10.1 Background

10.1.1 The Marine Environment

The maintenance of steel offshore structures, especially those in the North Sea, is challenging due to frequent exposure to corrosive seawater. An aqueous solution with many dissolved electrolytes, some specifically-adsorb onto the native iron oxides (calcium cation, sulphate, phosphates) on the steel surface.[32] Retarding the intrusion of seawater species is important to corrosion control of steels.[229,230]

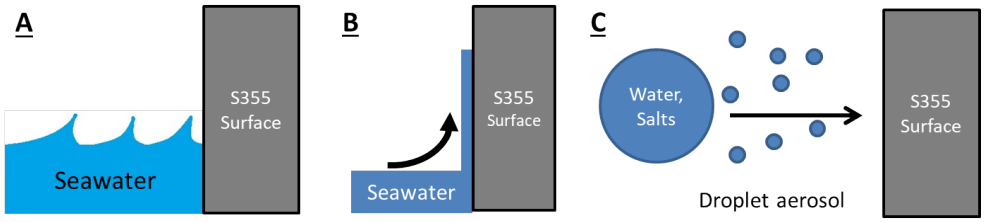

Fig. 10.1: Possible methods of seawater and its dissolved species within for contacting the steel surface for adsorption/corrosion. A) Wave splashing, B) Film migration, and C) Marine aerosol collision.

The mass transport of seawater onto steel is done mainly *via* three methods, all depicted in Figure 10.1. First is direct contact through wave splashing.[231] Second is the migration of thin water films through wetting and capillary action.[232] Third is by marine aerosol impacts. This work focuses on seawater ion adsorption on offshore steel platforms above high tide level, making marine aerosol contact most relevant.[233]

Marine aerosols dominate the atmospheric particle population over remote oceans.[234] There are approximately 100 to 300 marine atmospheric particles cm^{-3}. The size distribution of these aerosols are reported to be trimodal. The smallest mode is the nuclei mode(< 0.1 μm). The accumulation mode

has particle sizes ranging from 0.1 to 0.6 μm. Third and most important is the coarse mode with particles typically larger than 0.6 μm. These coarse mode aerosols carry up to 95% of the total mass of all aerosols despite only comprising up to 10% of the particle population. Therefore these aerosols is the focus of seawater species transfer to the steel surface.[118]

At the marine boundary layer, an atmospheric layer in direct contact or in close proximity to the seawater, coarse mode aerosol concentration is around 5 to 30 particles cm^{-3}. Using atmospheric aerosol concentrations and typical North Sea wind speeds, a very simple estimation of the minimum time needed to achieve full surface coverage of offshore steel structures by aerosol droplets is devised. These estimations inform the urgency required for steel surface repainting during maintenance works.

10.1.2 Investigations Into Marine Corrosion

Many structures close to the coast and offshore are subject to marine corrosion. Many corrosion tests have been conducted focusing on post-corrosion load-bearing abilities,[235–238] often with few details concerning the surface chemistry relevant to subsequent repainting. The studies are usually done in very long timescales, in days,[229] months, if not years,[239–243] on coating-protected surfaces and to steel with different alloying elements.[239,244]

One of the most common tests is the 'flash corrosion' studies at coastal areas, involving daily repeated cycles of surface wetting and drying by marine aerosol impacts.[245] Indirect surface monitoring is done through electrochemical impedance spectroscopy in these studies, using charge-transfer capacitance/resistance as a proxy for corrosion, and Tafel plots to gauge corrosion kinetics instead of studying the surface chemical speciations.[246]

Direct observations of the long-term corrosion interfacial cross-section is often attempted using SEM-EDX analysis to provide elemental atomic percentages,[247] or scraping off the thick corrosion scales for powder crystal diffraction analysis.[229,242] These studies only characterise long-term corrosion products; reportedly made of a mixture of magnetite (Fe_3O_4), lepidocrocite (γ-FeOOH), goethite (α-FeOOH), aragonite ($CaCO_3$), iron carbonate hydroxide ($Fe_6(OH)_{12}CO_3$), and various iron sulphates and sulphides.

While these studies may be relevant to the long-term performance of marine structures, their relevance to the surface chemistry of steel pending immediate repainting is unclear. These steel surfaces are cleaned before application

of coatings, to remove the existing corrosion products and old paints through abrasive blasting.[104] In the very-short timescale of marine aerosol-induced corrosion, in which wet marine aerosols could initiate corrosion upon contact with steel, the corrosion products at the steel-aerosol interface are analysed in this work for their chemical environments and structure in high spatial-resolution, with the aim of informing strategies to arrest corrosion before its long-term propagation.

10.2 Experimental

10.2.1 Materials

The S355 steel sourced in this project were cut into 1 cm x 1 cm x 1 cm 'coupons' and were from Parker Steel, UK. Polished steel coupons were using successively finer diamond pastes, washed and dried as outlined in Chapter 5.

All chemicals listed in this chapter were from Sigma Aldrich, unless stated otherwise. The artificial seawater solutions were made up using 18.2 MΩ cm ultrapure water. The 3.5% salinity artificial seawater recipe followed that of Kester *et al.*,[248] detailed in Table 10.1. Sodium, magnesium, calcium, and sulphate ions were the major electrolyte components in seawater.

Tab. 10.1: Artificial seawater and proposed wet marine aerosol salts table

Salt	**Mass in solution/g L^{-1}**	**Concentration/M**
NaCl	23.85	4.1×10^{-1}
Na_2SO_4	4.01	2.8×10^{-2}
KCl	0.70	9.4×10^{-3}
$NaHCO_3$	0.20	2.4×10^{-3}
$MgCl_2 \cdot 6\ H_2O$	10.83	5.3×10^{-2}
$CaCl_2 \cdot 2\ H_2O$	1.52	1.0×10^{-2}
$SrCl_2 \cdot 6\ H_2O$	0.02	9.0×10^{-5}

Artificial seawater samples of various salinities were prepared from a stock solution of 7% salinity. Their pHs are measured through two methods using an indicator, meta-cresol purple (mCP), and one using an electrochemical pH probe (Unitrode Pt100 connected to a Metrohm 809 Titrando autotitration

unit). For the indicator methods, 3 mL of saline solution has 40 μL of 5 mM mCP solution added to it for measurements.

Three-post copper transmission electron microscopy (TEM) grids for *in situ* lift-out of Focused Ion Beam (FIB) prepared sample were supplied by Agar Scientific.

10.2.2 Salt Drop Experiment

Salt drop corrosion experiments were performed by depositing a 100 μL droplet of artificial seawater onto the centre of a polished S355 steel coupon. The samples were either corroded under varying corrosion time with subsequent identical air exposure time, or under identical corrosion times with varying air exposure times.

The steel coupons were quickly immersed in ultrapure water after corrosion and were gently rinsed five times (50 mL of water each). The sample was then blown dry with a dry nitrogen jet, then exposed to the atmosphere for a designed amount of time. Sample were shielded under plastic petri dishes to minimise the deposition of adventitious carbon on the steel surface during sample preparation. Corroded coupons were stored *in vacuo* in desiccators and were only taken out of vacuum immediately before analysis, to prevent further corrosion.

10.2.3 Equipment

All experimental instruments were detailed in Chapter 4 unless specifically stated otherwise.

Focused Ion Beam in situ Liftout

FIB and sample *in situ* lift were performed using an FEI Helios Nanolab SEM/FIB with an Oxford Instruments Omniprobe attachment, with both ion- and electron-beam capabilities, at the Department of Materials Science and Metallurgy, University of Cambridge. A gallium ion (Ga^+) ion gun was used to for sample milling. Platinum electron- and ion-beams were used to deposit protective platinum layers. Platinum 'welds' between sample and the Omniprobe, and TEM-capable copper grids were conducted through electron-beam deposition. The corroded sample was not completely preserved due to air exposure in transfer, between electron microscopes. The samples were stored in vacuum dessicators to minimise air exposure time.

10.3 Aerosol Flux and Aerosol Salinity Effects on Adsorption

10.3.1 Aerosol Flux

The course mode aerosols make up the majority of the marine aerosol mass transport, with well-defined particle dimensions (≥ 0.6 μm). A simple 'flux'-based calculation is used to estimate the timescales needed to achieve full surface coverage of a unit area by these aerosols.

$$F_A = C_A \times S_w \tag{10.1}$$

$$\frac{1}{t_{min}} = F_A \times A_A \tag{10.2}$$

$$= C_A \times S_w \times A_A \tag{10.3}$$

An approximate atmospheric aerosol concentration, C_A, with variable wind speed, S_w, is used to calculate the incident aerosol flux F_A, outlined in Equation 10.1. This flux allows for the estimation of the time required for total unit surface area coverage by aerosols shown in Equation 10.2, with minimum full-coverage time t_{min} and A_A the geometrically approximated contact area of each marine aerosol droplet.

The landed aerosol droplets on the steel are approximated as spherical-tops, with a top height of h, and part of a proposed sphere of radius r. The base area is calculated from the reported contact angle at the steel-water-air interface of 60.9°.[249] The volume of the spherical top, calculated through Equation 10.4 in reference to Figure 10.2, is equal to the volume of a spherical aerosol particle.

The lower bound radius for course mode aerosols of 0.3 μm (diameter 0.6 μm) is used. This leads to the average deposited aerosol spherical-top base area of 0.72 μm^2. Assuming that the spherical tops are not overlapping in deposition and are close-packed on the surface (with 96.9% packing efficiency), the full coverage time t for a metre-squared surface can be estimated as a function of wind speed through Equation 10.2.

$$V_{top} = \frac{1}{3}\pi h^2(3r - h) \tag{10.4}$$

The lower bound timescale estimates of full aerosol coverage with varying

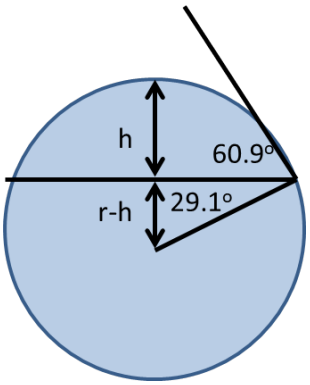

Fig. 10.2: Spherical-top geometry schematic, with spherical top height h.

wind speed, based on the smallest course mode particles, are shown in Figure 10.3. At wind speeds of 7 ms^{-1} or above, typical for low altitudes (*leq* 10 m) above the open sea,[113] full coverage is achieved in fewer than ten hours. In an atmosphere rich in aerosols (30 particles cm^{-3}), full coverage is achieved in less than 2 hrs. Even if full coverage is attained prior to repainting, aerosol impacts on the exposed steel will deposit ions on the steel surface and induce local corrosion.

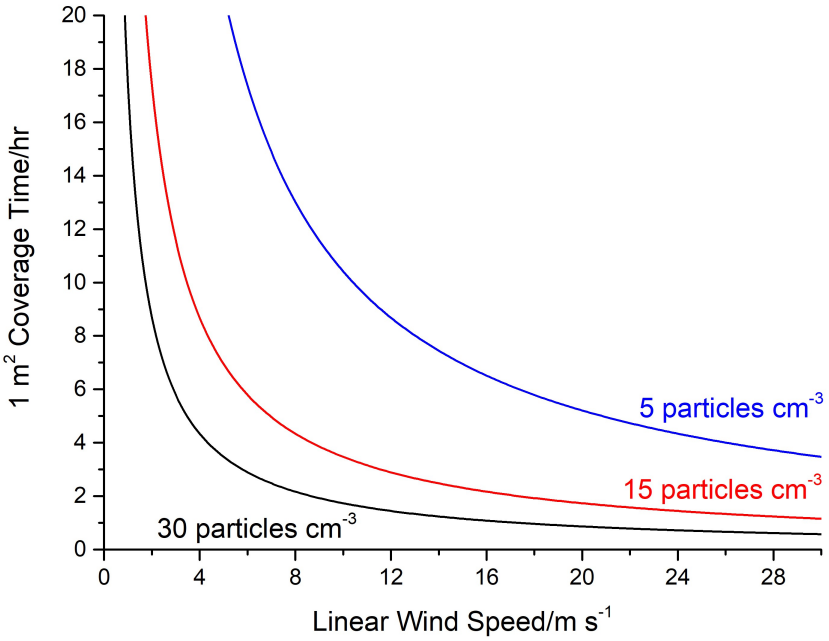

Fig. 10.3: Time required for full marine aerosol coverage for different aerosol concentrations and wind speeds.

An order of magnitude calculation is used to compare the number of seawater ions to the number of surface sites on S355 steel. With an estimated spherical-top base area of 0.72 μm^2 per landed aerosol, the total number of specifically-adsorbing ions such as calcium and magnesium ions are of the same order of magnitude with the surface site number of (10^{-17} mol) which competitive adsorption between ions begins.

When seawater is exposed to a much larger surface area of steel, such as wave splashing or capillary rise, the number of surface sites outnumbers specifically-adsorbing ions, leading to all ions to be adsorbed onto the steel iron oxide surface.

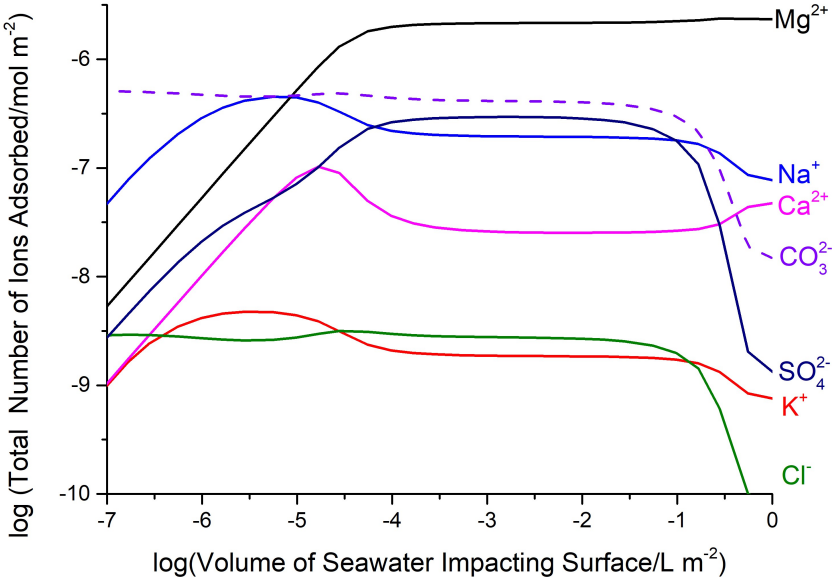

Fig. 10.4: Calculated number of ions adsorbed on the S355 steel surface when impacted by vairable volume of seawater of pH 8. Calculation work done by Dr. David Madden, unpublished.

Figure 10.4 shows the variation of Visual MINTEQ-calculated ion adsorption from artificial seawater at typical seawater pH 8, to volumes of seawater impacting on the steel surface (assumed to have native a hydrous ferric oxide (HFO) layer on top). For an aerosol, the volume of seawater impacting per unit surface area is 10^{-4} L m^{-2}. If the droplet is to splash or slide across the surface, this decreases the seawater volume-to-surface ratio. If multiple aerosol droplets are to land the same surface then the seawater volume-to-surface ratio would increase.

In low seawater volume-to-surface scenarios, surface sites outnumber ions and every ion is adsorbed. The number of ions adsorbed rises linearly with their rising availability, as seen on the left of Figure 10.4. Sodium, except for the carbonate, is the most adsorbed ion on the surface due to its high concentration in the seawater. When carbonates are adsorbed onto the steel/HFO surface, the equilibrium involving carbonate, bicarbonate, carbonic acid, and dissolved atmospheric carbon dioxide shifts towards further production of carbonates in solution. The surface adsorption of carbonate then leads to more gaseous carbon dioxide to dissolve, promoting dominant carbonate adsorption despite its initial low concentration in seawater (Table 10.1).

At the high seawater volume-to-surface regime (aerosols landing, $\geq 10^{-4}$ L m^{-2}), the abundance of ions exceeds the number of surface sites present, leading to competitive adsorption in preference to more strongly binding ions. Using the existing ion adsorption data on hydrous ferric oxides,[32] an approximation to the native oxide layer on steel surfaces at the steel-water interface, magnesium is calculated to be the most adsorbed ion; trumping the calcium cation and the sulphate anion.

Therefore for steel surfaces exposed to seawater aerosols or much seawater, one would expect the specifically-adsorbed magnesium, calcium, and sulphate ions to be present at the corroded steel-paint interfaces, which the corrosion products (analogous to hydrous ferric oxide) bind strongly to.

10.3.2 Aerosol pH

Marine aerosols can have varying salinity due to water evaporation occurring while they are airborne. The further the aerosol is situated from the marine boundary layer (altitude above sea level saturated with water vapour) the higher its salinity, due to decrease of relative humidity with increasing altitude, leading to evaporation, as summarised in Figure 10.5.

At aqueous liquid-solid interfaces, pH plays a significant role in adsorption, as adsorption of charged species/ions onto a substrate is moderated by the surface charge.[32] Positively-charged surfaces at a given pH binds onto anions better and negatively-charged surface bind more readily with cations. The pH of seawater in different salinities is therefore characterised, analogous to water evaporation from the marine aerosol particles, which could subsequently influence ion adsorption on the marine-corroded steel.

Artificial seawater solution of different salinities were made and their pH val-

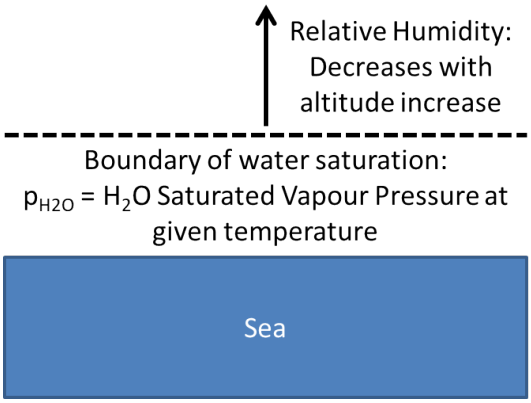

Fig. 10.5: Schematic demonstrating the origins of aerosol water content decrease with increasing altitude above sea level. The higher the altitude the aerosol is located, the lower its water content due to evaporation.

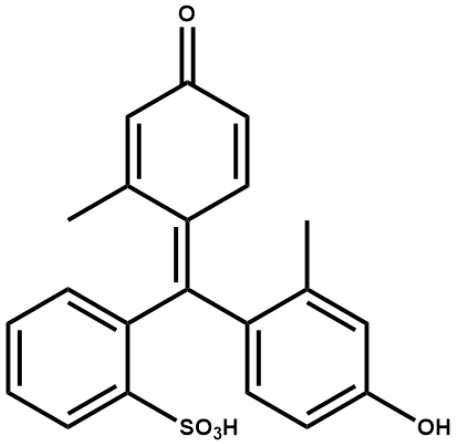

Fig. 10.6: Chemical structure of a m-cresol purple (mCP) molecule.

ues measured. The first pH measurement method used meta-cresol purple (structure in Figure 10.6), following the procedures outlined by Liu *et al.*.[250] The second method also used mCP as a pH indicator. A series of buffer solutions of stable pH were made ranging from pH 7.20 to 8.20 as calibration samples to indicator colour change. UV-Vis spectroscopy monitored the ratios between indicator adsorption peaks at wavelengths 434 and 578 nm. pH of sample solutions in different salinities is determined by comparing their absorption peak ratios to those of the calibration samples. Thirdly the saline solutions pHs were determined using a pH probe.

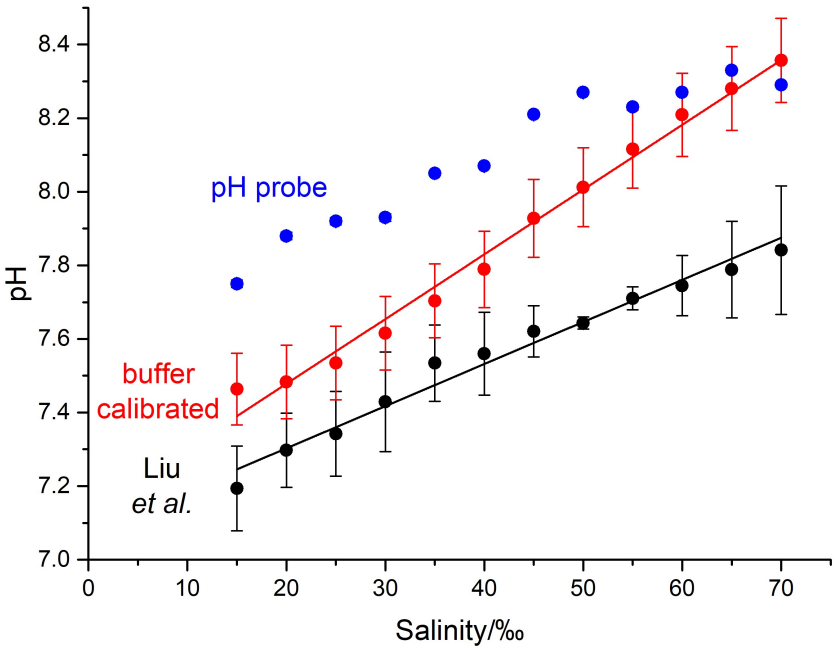

Fig. 10.7: Results of artificial seawater pH measurements through three methods.

The pH measurement results of all three methods are all presented in Figure 10.7. pH values determined for a particular salinity are all within approximately half a pH unit between each method. The agreement is reasonable for a non-buffered solution. The pH prove determined values at higher-than-ocean salinity levels (i.e. $> 35‰$) should be treated with caution due to a number of potential issues, including pH probe reference electrode stability, and electrical potential drift caused by the liquid junction potential due to high solution ionic strength.[251] Nevertheless, the good agreement of values between the three measurements show that marine aerosol pH increases with increasing seawater salinity. Hence more saline aerosols would impact the steel surface with a higher solution pH and should facilitate more preferential cation adsorption.

Naturally occurring seawater has a salinity around 3.5% (35‰). pH measurement results determine the pH of artificial seawater made to be range between 7.5 to 8.1. This is in good agreement with the literature listed range of 7.5 to 8.4.[252] Hence the artificial seawater synthesised is a suitable reagent for future experiments. The observed rise of pH with salinity is supported in the literature.[253] The rise may be attributed to basic anions such as the bicarbonate ($pK_a = 6.35$) and carbonate ($pK_a = 10.33$).[254] The rise in salinity increased the concentration of these ions in solution, leading to a rise in pH.

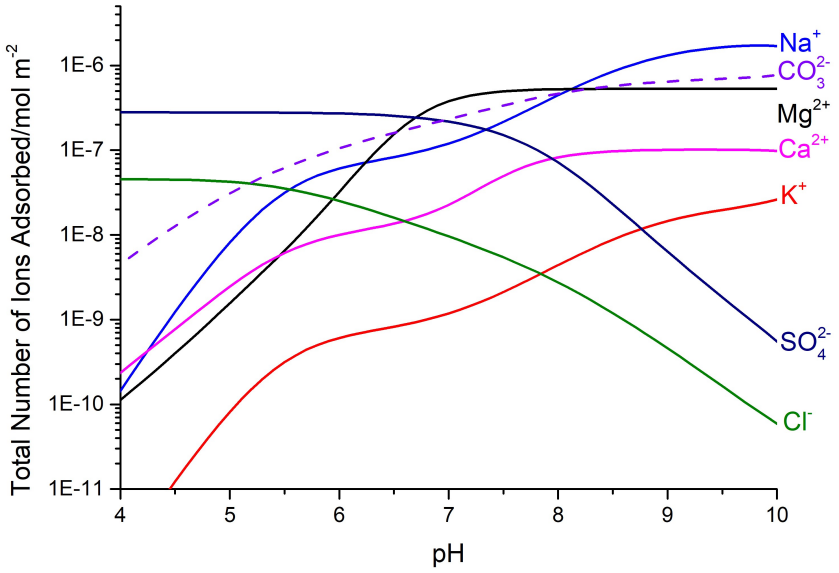

Fig. 10.8: Calculated numbers of ions adsorbed on the surface when impacted with 0.01 mL m^{-2} 3.5% seawater of variable pH values. Calculation work done by Dr. David Madden, unpublished.

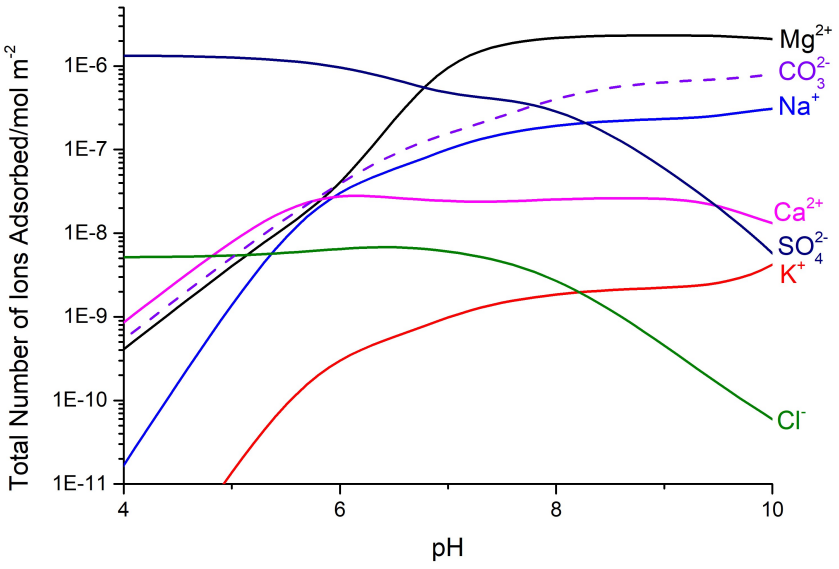

Fig. 10.9: Calculated numbers of ions adsorbed on the surface when impacted with 10 mL m^{-2} 3.5% seawater of variable pH values. Calculation work done by Dr. David Madden, unpublished.

Seawater ion adsorption on steel (hydrous ferric oxides) at different pH values were calculated by Dr. David Madden, and were included for completeness.

Figures 10.8 and 10.9 showcase the adsorption regime, respectively, in low and high seawater volume-to-surface ratios. The adsorption of anions is generally favoured at low pH values and for cations at high pH. Carbonate adsorption increases with the rise of pH due to deprotonation of carbonic acid and bicarbonate species, increasing carbonate anion concentration leading to further adsorption.

In the pH range relevant to marine aerosols, 7.2 to 8.4, low seawater volume-to-surface ratio leads to dominant magnesium, sodium, and carbonate adsorption onto the surface iron oxide. In the high volume regime magnesium adsorption dominates. In a typical salt drop corrosion experiment used in the later section, a 100 μL artificial seawater droplet is deposited on a polished 1 cm^2 steel surface, the volume-to-surface ratio is 1000 mL m^{-2}, within the high volume regime which significant magnesium adsorption is expected.

10.4 Analysis of Corrosion Products in Short Corrosion Timescales

Corrosion studies in the literature are dominated by very long timescales. They are far too long to be relevant to offshore structure cleaning and repainting which occur within hours, or days.[239,242,243,255]

Marine aerosols are postulated to be the main mass transport mechanism of seawater and its salts onto the steel, initiating corrosion immediately upon surface impact. It is therefore important to understand the chemistry and structure of the corrosion products formed on the steel surface in these short timescales (minutes, hours). For they are the topmost substrate which paints would bind onto.

Short timescale marine corrosion were convenient simulated through a 'salt drop experiment' devised by U. R. Evans,[256] where a droplet of artificial seawater was deposited on a polished S355 steel coupon, and the corrosion products on the steel surface analysed.

10.4.1 Anodic and Cathodic Site Microanalyses

The salt drop steel corrosion experiments were conducted using two variables: seawater corrosion time and post-corrosion air exposure time. Corrosion experiments vary one variable and keeping the other constant. When the

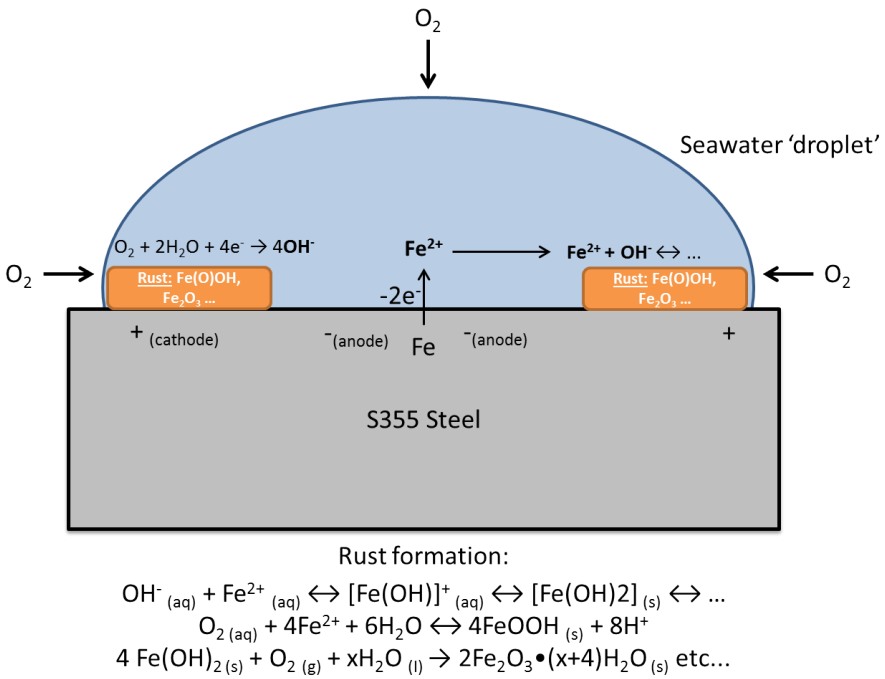

Fig. 10.10: Schematic showing the anatomy and reactions of a salt drop corrosion experiment, noting the localisation of cathode and anode sites.

air exposure time was varied, the seawater exposure time was kept at 2 hrs for all samples. With varying seawater exposure time, a constant of 1 hr air exposure time was kept.

Figure 10.10 shows the schematic of a salt drop experiment. A 'concentration cell' is formed by the oxygen concentration gradient within the droplet. The electrochemical half-cell equations are listed in both Equations 10.5 and 10.6. The regions of higher oxygen concentration, at the outer edges of the droplet, are the cathodic sites and anodic site form at regions of lower oxygen concentrations at the coupon centre.[257]

$$\mathrm{Fe^{2+}(aq) + 2e^- \rightleftharpoons Fe(s)} \tag{10.5}$$

$$\mathrm{O_2(g) + 2H_2O(l) + 4e^- \rightleftharpoons 4OH^-(aq)} \tag{10.6}$$

Differences of surface chemistry at both the anodic and cathodic site surfaces were studied. Figure 10.11 shows the different stages of the corrosion experiment. The mirror-finished polished sample (leftmost) was visibly corroded

by the seawater droplet (rightmost). After the seawater droplet was washed off (top, centre sample), the visibly reflective anodic (inner, yellow cross) and dulled cathodic (outer, red cross) regions were analysed.

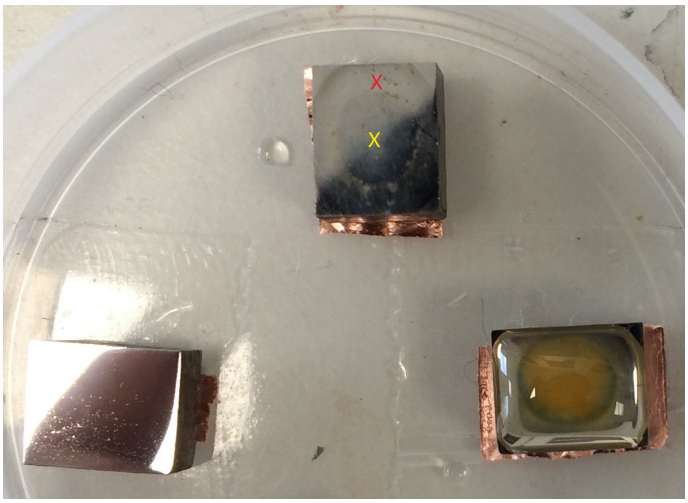

Fig. 10.11: Photograph showing three polished S355 steel surfaces undergoing different stages of the salt drop experiment. Left: steel surface prior to corrosion. Right: steel surface under corrosion by artificial seawater droplet on top for 1 hr. Centre: corroded steel surface with seawater droplet rinsed off and dried with nitrogen jet, with visible anodic (yellow cross) and cathodic (red cross) regions.

Air Exposure Time Dependence

The elemental analyses by EDX and XPS of the anodic region are presented in Figure 10.12. The atomic percentages of all major elements are shown to be relatively constant and independent to air exposure duration. Data variations are likely due to the fluctuations of adventitious carbon content between samples, affecting the carbon atomic percentage.

The deconvoution of major element (carbon, iron, and oxygen) peaks present through component peak fittings is presented in Figure 10.13. The carbon composition remains constant with respect to air exposure time after corrosion, dominated by alkyl (C−C) species commonly associated with adventitious carbon. This is likewise true for the minor oxygen-containing carbon species.

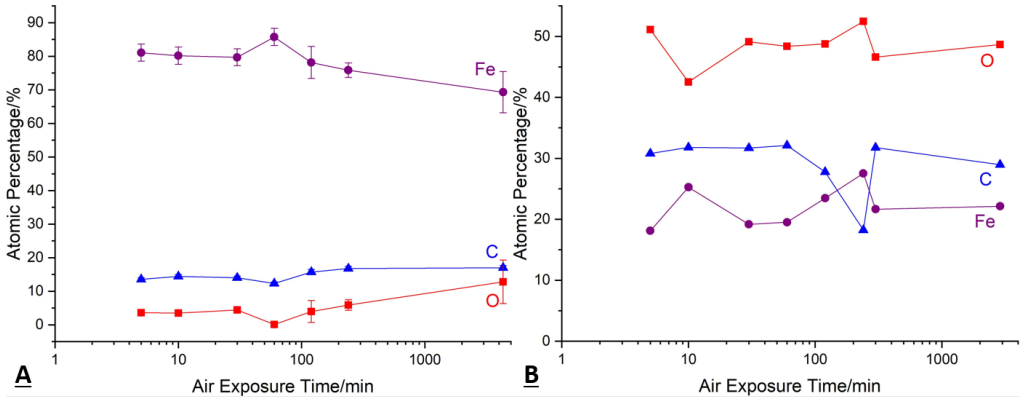

Fig. 10.12: A) EDX and B) XPS elemental analyses at the anodic region on polished steel as a function of air exposure time, after 2 hrs artificial seawater droplet exposure.

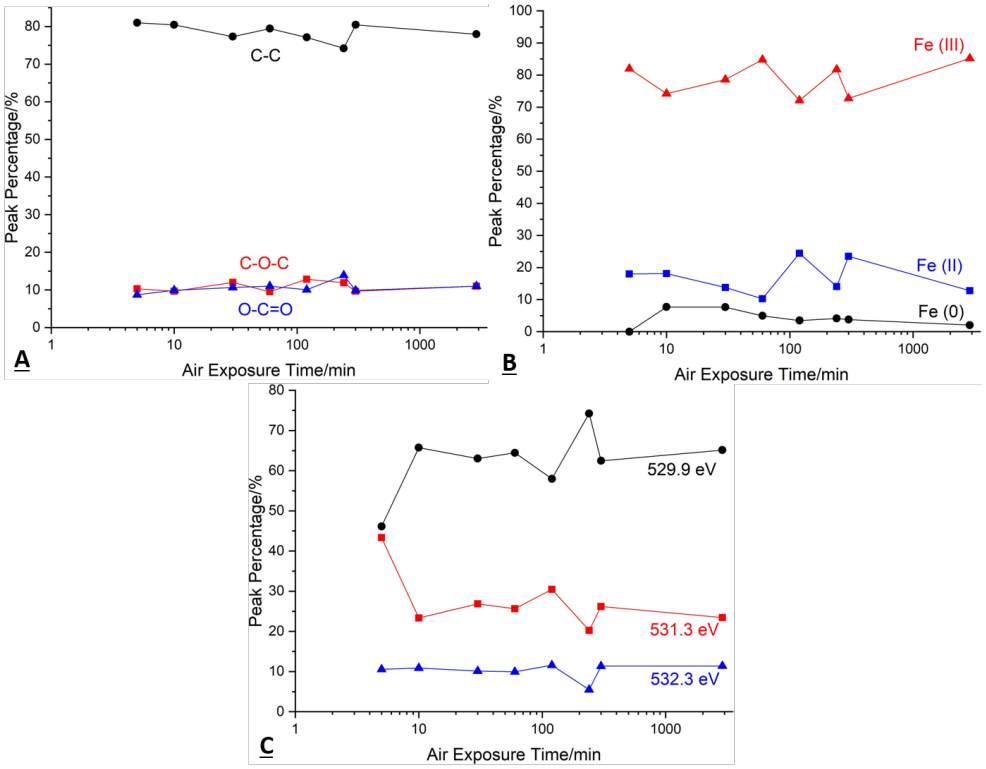

Fig. 10.13: A) Carbon 1s, B) iron 2p, and C) oxygen 1s XPS component peak analyses at the anodic region on polished steel as a function of air exposure time, after 2 hrs artificial seawater droplet exposure.

For the iron 2p peak, iron (III) is seen to be the consistently dominant species. Iron (II) is the second most common, with trace metallic iron (0) detected. There is little variation seen in association with post-corrosion air exposure time. The detection of metallic iron (0) environment is indicative of a thin iron oxide layer formation at the anode, its thickness smaller than the photoelectron escape path ($\approx$ 20 Å) for the chemical environment to be detected. This result also suggests a mixed iron (II) and iron (III) reaction product at the anode.

Oxygen 1s component peak fitting identifies three peaks of different binding energy shifts: 'Bulk oxides' at 529.9 eV, 'surface oxides' at (e.g. X−OH groups) 531.3 eV, and adventitious oxidised carbon and other surface oxides at 532.3 eV.[147,148,160]

The anodic oxygen speciation appears independent to air exposure time, in good agreement with XPS and EDX elemental analyses which oxygen level is constant. This is unsurprising with the anodic site being the location of elemental iron oxidation and dissolution, leading to a the exposure of a 'new' steel surface by corrosion whose composition is insensitive to post-corrosion air exposure times.

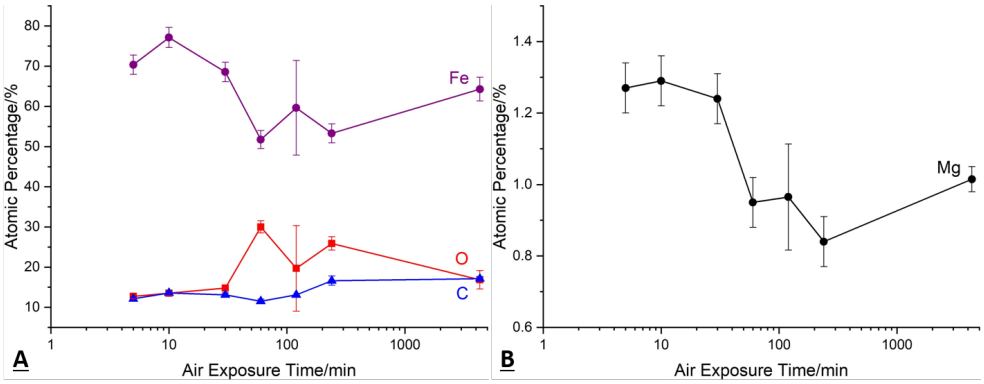

Fig. 10.14: EDX elemental analysis at the outer cathodic region on polished steel as a function of air exposure time, after 2 hrs artificial seawater droplet exposure.

In the cathodic region, corrosion product deposition is clearly visible through dulling of a previously reflective steel surface. Figure 10.14A shows EDX elemental analysis of major elements iron, oxygen, and carbon remaining constant in composition with respect to air exposure time, with perhaps a

tentative decrease of iron content and increase in oxygen atomic percentage. It may be indicative of a maturing/thickening of iron oxide layer at the cathodic site.

EDX analysis for magnesium content shown in Figure 10.14B reveals a small but significant presence on the steel cathodic region at around 1% atomic percentage. This is consistent to theoretical prediction of magnesium specific-adsorption onto the iron oxide corrosion products.

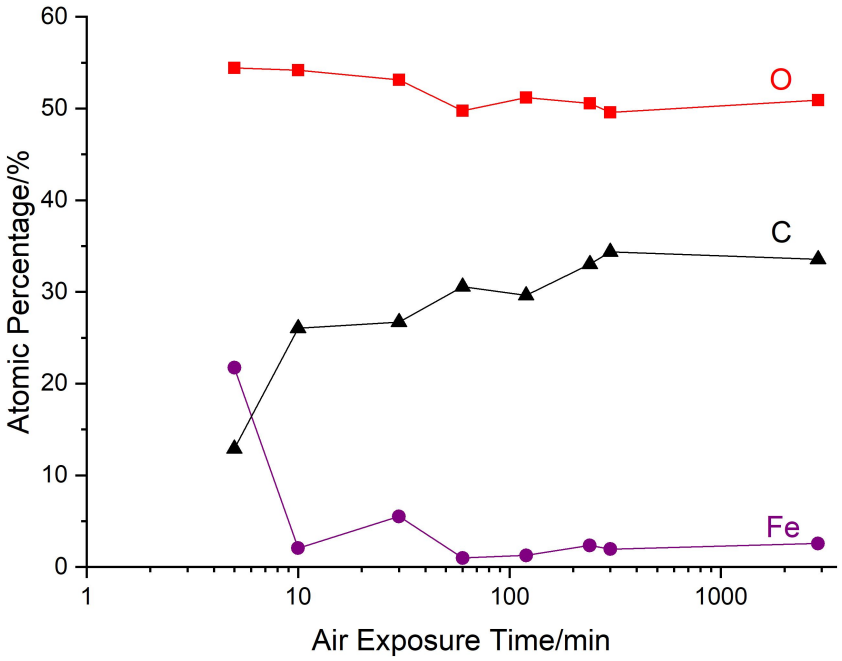

Fig. 10.15: XPS elemental analysis at the outer cathodic region on polished steel for the major elements as a function of air exposure time, after 2 hrs artificial seawater droplet exposure.

XPS results of major and minor elements present on the seawater-corroded S355 steel surfaces are respectively presented in Figures 10.15 and 10.16. The oxygen remains more or less constant with respect to air exposure times, in good agreement with EDX data. The variation of carbon is responsible for the fluctuation in iron percentage. With little variation to oxygen content, it is likely that the longer air exposure times has lead to an increase of oxidised carbon content on the cathode surface, possibly as oxidised adventitious carbon or carbonate formations. The fall of iron content with longer air exposure times makes iron carbonate formation unlikely.

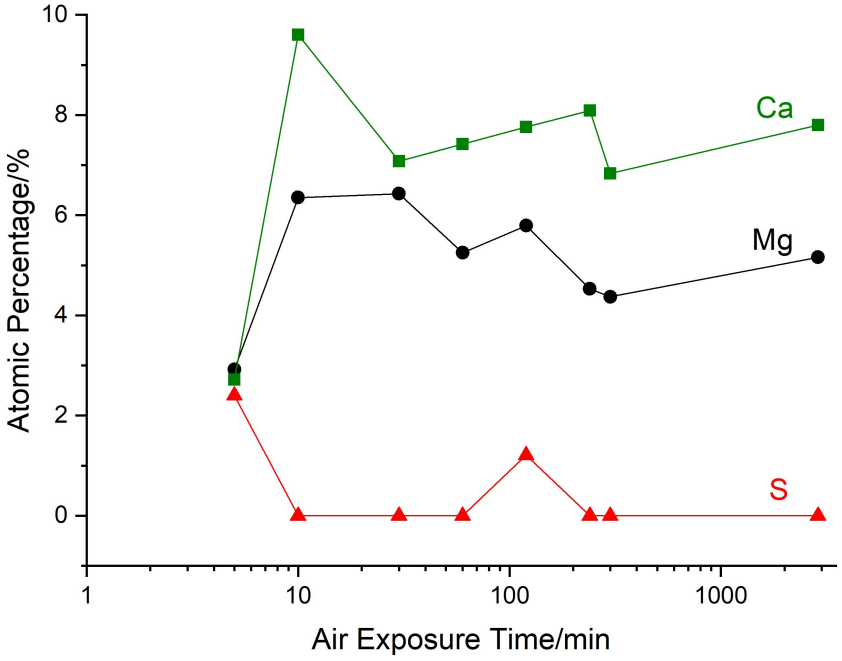

Fig. 10.16: XPS elemental analysis at the centre cathodic region on polished steel for the minor elements as a function of air exposure time, after 2 hrs artificial seawater droplet exposure.

XPS has a shown number of minor seawater-associated elements of magnesium, calcium, and sulphur to be present at the cathodic region. Their atomic percentages remain relatively constant to air exposure times. Calcium and magnesium each have significant elemental signatures up to 7%. This is in good agreement with ion-adsorption modelling on hydrous ferric oxides and EDX data. XPS is able to detect adsorbed minor elements due to its higher surface sensitivity (*cf.* EDX).

The results of component peak analyses of carbon 1s, iron 2p, and oxygen 1s peaks are presented in Figure 10.17. For carbon and iron components peaks, they remain at constant level with respect to air exposure times. Iron (III) species and carboneceous alkyl (C−C) carbon, with significant oxidised carbon content, are seen to dominate the cathodic region surface as it does with anodic regions. The carbon results are consistent with adventitious oxidised carbon as shown previously in XPS elemental analysis.

Marked differences between anodic and cathodic regions are seen for the oxygen peak fitting. The species of associated with 'surface' (e.g. X−OH groups, 531.3 eV) functionalities is seen to dominate the 'bulk' (529.9 eV)

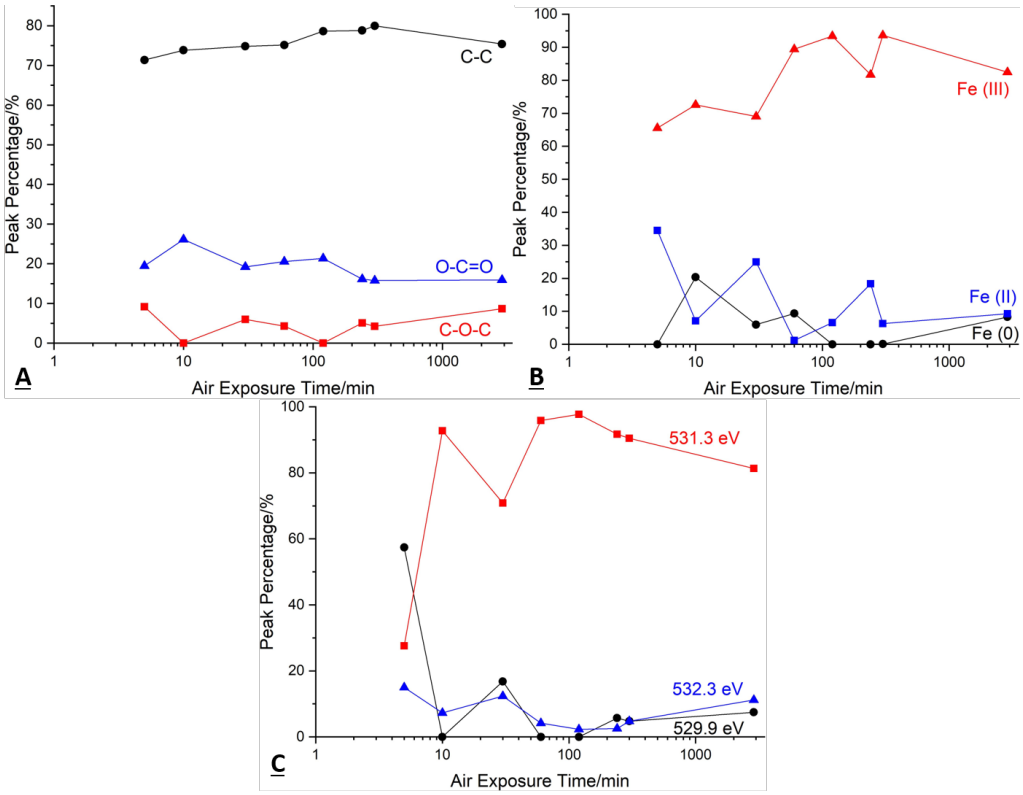

Fig. 10.17: A) Carbon 1s, B) iron 2p, and C) oxygen 1s XPS peak component analyses in the cathodic region on polished steel as a function of air exposure time, after 2 hrs artificial seawater droplet exposure.

and 'oxidised adventitious carbon' (532.3 eV) peaks.[148] This is consistent with an increase of surface contribution by the formation of fine corrosion products. The result suggests the cathodic site chemical environment is more susceptible to adsorption of seawater ions through fine iron oxide corrosion products, in good agreement with XPS elemental analysis of minor elements.

Overall, there are few signs of elemental atomic percentage variation with respect to air exposure time after seawater corrosion, apart from indications of thicker iron oxide formations in a very long air exposure times. This is unsurprising due to the lack of mass transport mechanisms other than atmospheric oxygen reacting with the surface to form more iron oxides and deposit adventitious carbon, once the seawater droplet has been removed. Seawater elements are present at the iron oxide-rich cathodic region, in agreement with numerical model predictions.

Seawater Exposure Time Dependence

Seawater exposure time as a variable was explored, with 1 hr of post-corrosion air exposure time for all samples. Figure 10.18 shows the EDX and XPS elemental analyses at the anodic (coupon centre) region.

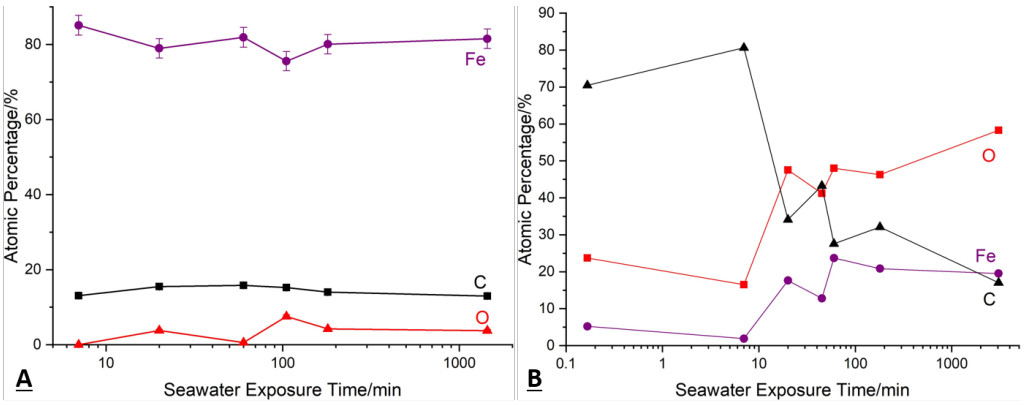

Fig. 10.18: A) EDX and B) XPS elemental analyses at the centre anodic region on polished steel as a function of seawater exposure time, with 1 hr air exposure afterwards.

Elements identified by EDX in Figure 10.18A are seen to have constant atomic percentages with seawater corrosion times. This is within expectation as the anodic region is the site of metallic iron dissolution occurs. The dissolution generates a 'new' steel surface for further corrosion.

XPS elemental analysis results in Figure 10.18B show significant fluctuation in atomic percentages. With longer corrosion times, iron and oxygen content are seen to increase. This is indicative that despite metallic iron dissolution at the anodic site, longer corrosion times still results in a gradual build-up of an iron oxide layer. Both EDX and XPS techniques agree at longer the corrosion times, more iron oxide corrosion products form at the anodic site. Fluctuations in the data are attributed to the variability of adventitious carbon deposition between samples. Apart from data at very short seawater exposure timescale, where there is much adventitious carbon ($\leq 80\%$). When carbon is steady between 30% to 40%, iron enjoys higher atomic percentages at around 20%.

The component peak analysis of the carbon 1s peak is shown in Figure 10.19. For 'short' corrosion timescales ($\leq$ 3 hrs), the carbon species content ap-

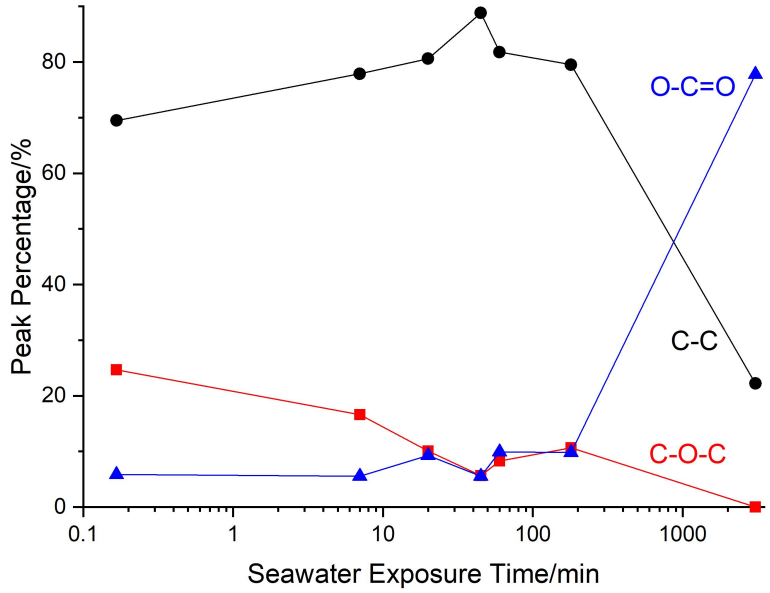

Fig. 10.19: Carbon 1s elemental peak component peak analysis at the anodic site on polished steel as a function of seawater exposure time, followed by atmospheric exposure for 1 hr.

pears to be constant with corrosion duration, with the alkyl adventitious carbon (C−C) species dominant, alongside minor oxidised carbonaceous species (C−O−C and O−C=O).

At longer ($\approx$ 2 days) corrosion times there is a decrease alkyl carbon contribution but a rise in carbonate (O−C=O) surface species. One possible explanation is the development of iron carbonate on the corroded anodic surface. Carbonate adsorption onto iron oxide has been previously identified to be significant in adsorption models (Figure 10.9). Strong carbonate adsorption, with continuous ion generation from atmospheric carbon dioxide, may have led to iron carbonate products formation which would require further experimental verification.

Iron peak fitting results are shown in Figure 10.20. Despite minor variations, the iron (III) content of the samples remain more or less constant with respect to the duration fo seawater exposure. Iron (II) content rises and iron (0) contribution decreases with prolonged corrosion. The results, like previous XPS elemental analysis, are consistent with a thicker layer of native oxide formation at the anodic site with longer corrosion times. The iron (0) photoelectrons become less capable of escaping the sample surface by the

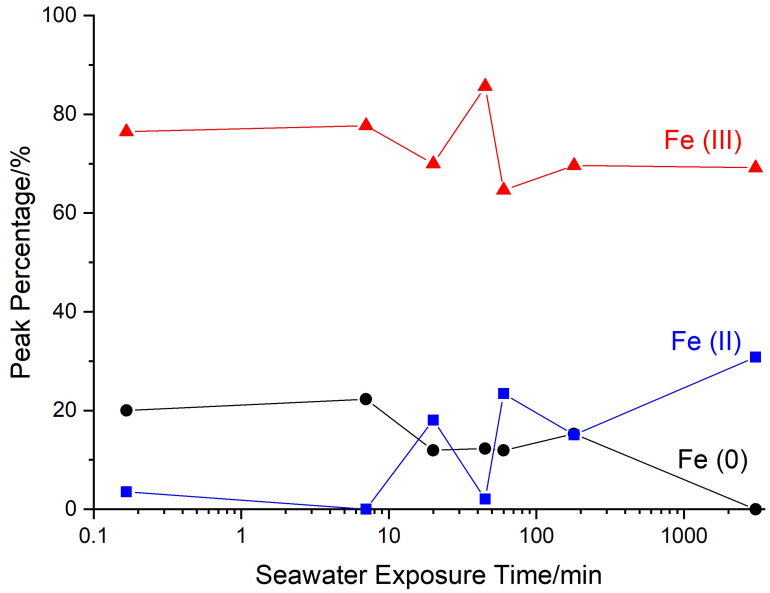

Fig. 10.20: Iron 2p component peak analysis at the anodic site on polished steel surfaces as a function of seawater exposure time, followed by atmospheric exposure for 1 hr.

thickening oxide.

The oxygen component peak analysis is shown in Figure 10.21. Despite significant fluctuations in the data, with the increase of seawater corrosion time, the 'bulk oxide' peak at 529.9 eV remains a significant contribution. The 'surface' (531.3 eV) chemical functionality also remains relatively constant with corrosion duration expect for a fall in contribution at very long corrosion times.[147,160,162,258,259] Oxidised adventitious carbon peaks (532.3 eV) becomes less relevant with longer corrosion times whereas adsorbed water (533.1 eV) peak dominates at long corrosion times, probably due to occlusion of a significant amount of seawater when upon the formation of a thickening iron oxide layer.[148,149]

Visible corrosion product is often seen on cathodic sites. EDX elemental analysis of major elements is shown in Figure 10.22A. Iron content decreases and oxygen contribution increases with increasing seawater exposure times, while carbon content remains constant. The results agree with the increase of iron oxide content at the site.

Figure 10.22B shows that there is a significant presence of magnesium and

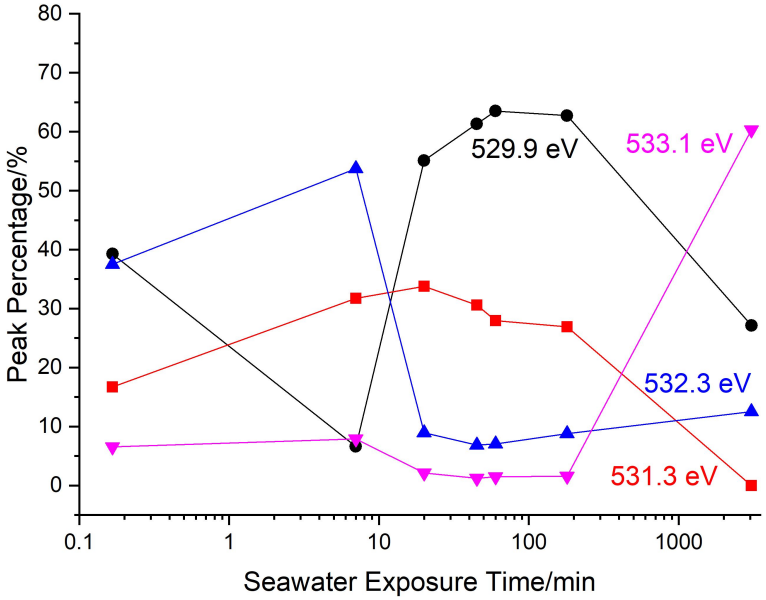

Fig. 10.21: Oxygen 1s component peak analysis at the anodic site on polished steel surfaces as a function of seawater exposure time, followed by atmospheric exposure for 1 hr.

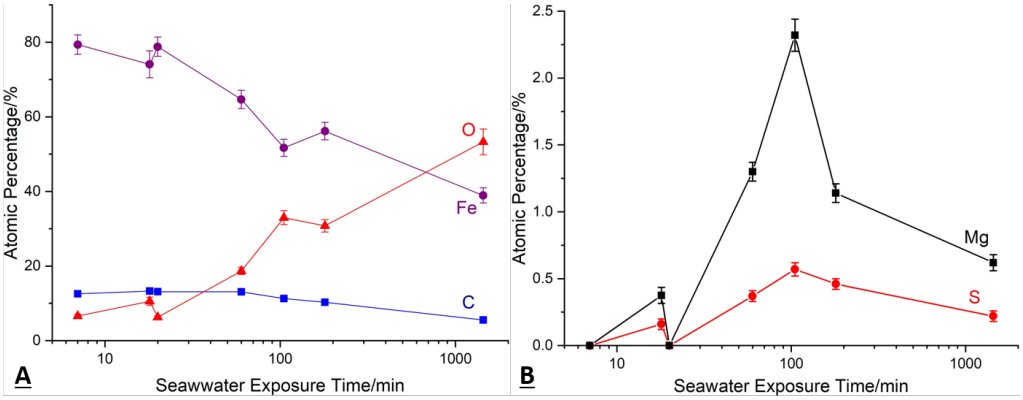

Fig. 10.22: EDX elemental analysis of A) major and B) seawater-relevant minor elements at the cathodic region on polished steel as a function of seawater exposure time, followed by atmospheric exposure for 1 hr.

sulphur at the cathode. The magnesium adsorption rises rapidly with longer seawater exposure time, then steadies at around 1.2% atomic percentage level. A similar trend is seen for sulphur (up to 0.5%). The results are consistent with seawater-ion adsorption/occlusion (magnesium cations and sulphate anions) at the cathodic sites corrosion products.

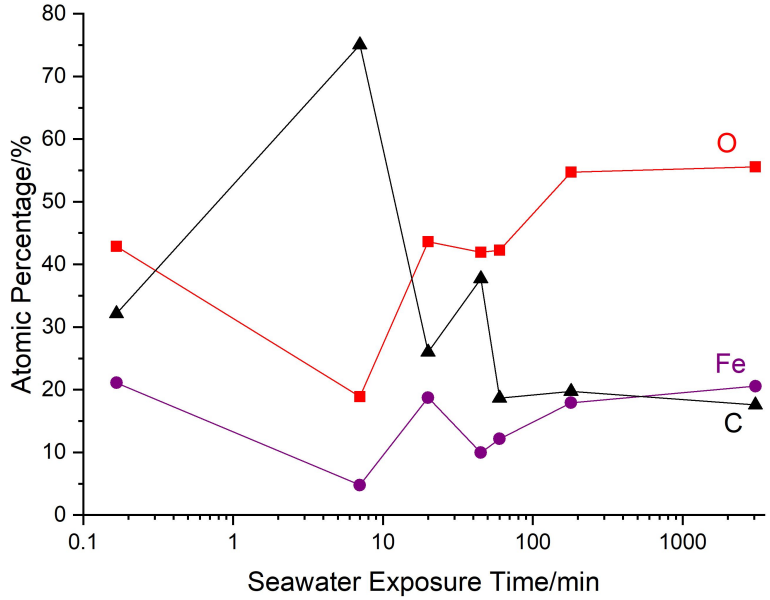

Fig. 10.23: XPS elemental analysis of major elements at the cathodic region on polished steel as a function of seawater exposure time, followed by atmospheric exposure for 1 hr.

XPS cathodic site analysis results for the major elements are shown in Figure 10.23. Significant variation of elemental percentages are seens but are maintained at an approximate constant level. The fluctuation may reflect the potentially complex nature of the corrosion product layer formed.

Figure 10.24 shows the seawater-related elements detected by XPS on the cathodic site surfaces. Despite variations of atomic percentages there is gradual increase for all three elements with seawater exposure times, each reaching around 2.5% in the longer timescale corrosion. Magnesium is the dominant minor element, in good agreement with ion adsorption models on iron oxide. Both XPS and EDX results agree with expected seawater ion adsorption onto the iron oxide corrosion products at the cathodic site. The combined results suppoprt the hypothesis of seawater ion adsorption on the steel corrosion products when corroded by marine aerosols.

Component peak fitting is attempted for all major elements. Figure 10.25 shows the results for the carbon 1s peak. With increasing seawater exposure time, the adventitious alkyl carbon (C−C) is seen to be relatively constant with a slight gradual decrease, while the carbonate (O−C=O) and carbon-oxygen (C−O−C) are minor contributors with marginal increases. This may

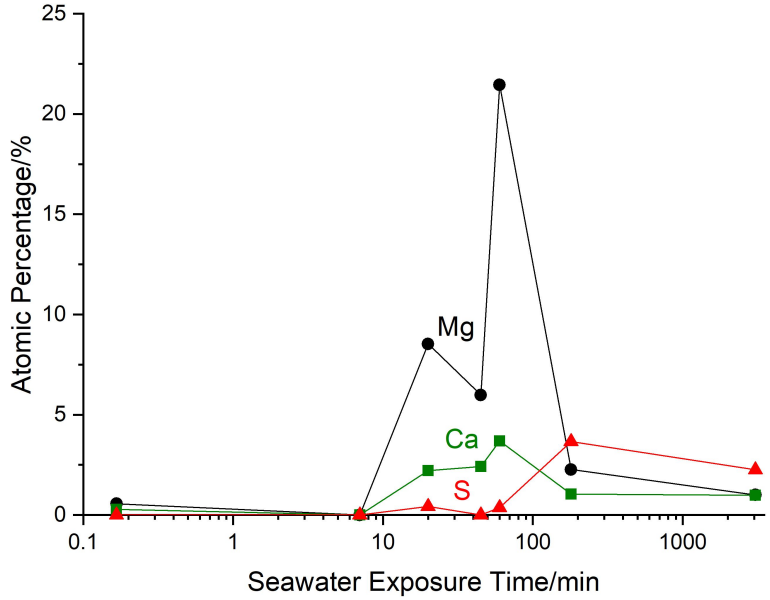

Fig. 10.24: XPS elemental analysis of seawater-relevant minor elements at the cathodic region on polished steel as a function of seawater exposure time, followed by atmospheric exposure for 1 hr.

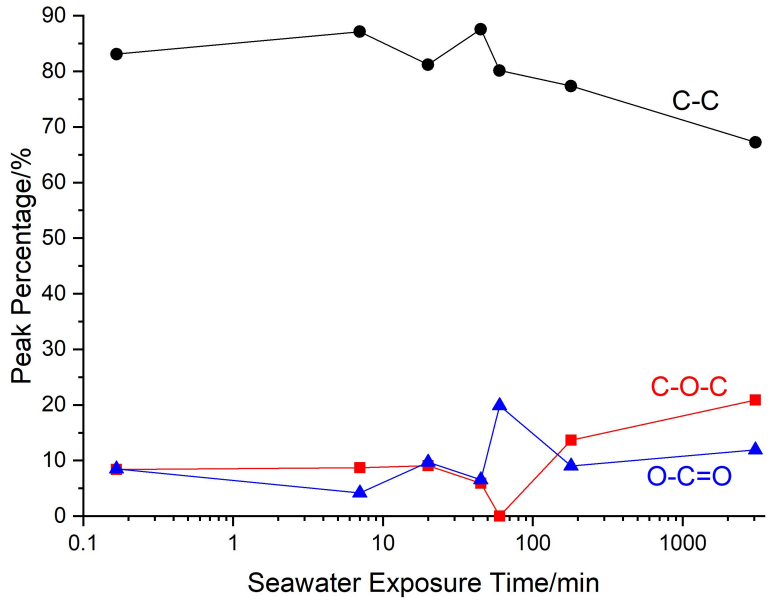

Fig. 10.25: Carbon 1s component peak analysis at the cathodic site on polished steel surfaces as a function of seawater exposure time, followed by atmospheric exposure for 1 hr.

be attributed to the increase of carbonate adsorption at the cathodic region due to prolonged exposure of the seawater droplet in the atmosphere.

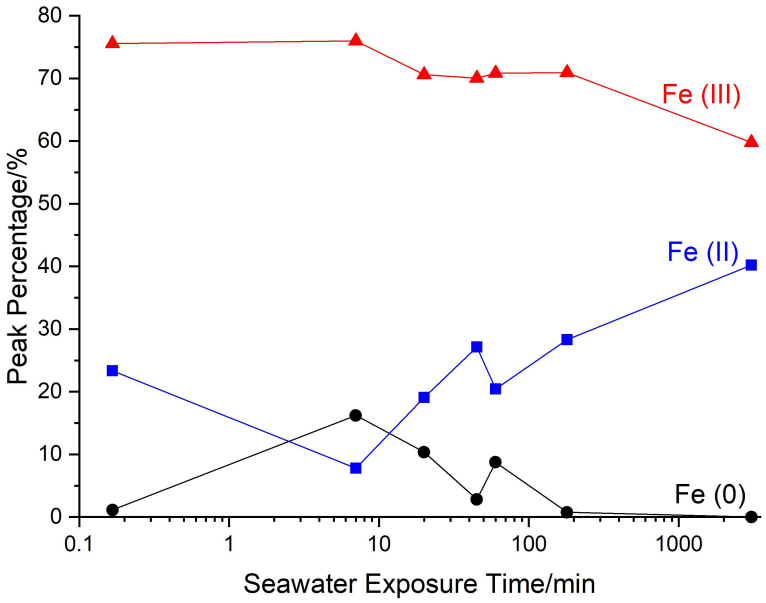

Fig. 10.26: Iron 2p component peak analysis at the cathodic site on polished steel surfaces as a function of seawater exposure time, followed by atmospheric exposure for 1 hr.

The iron 2p peak component analysis is shown in Figure 10.26. It is seen that the iron (III) species continues to dominate the cathodic steel surface. Subtle variations are seen for decreasing metallic iron (0) content, associated with increasing iron (II) contribution. The results may imply that the iron oxide layer at the cathodic region increases in thickness with increased corrosion time. The data fluctuations are attributed to the inhomogeneous nature of corrosion products, with an increased signature of iron (II) oxides.

Oxygen 1s XPS peak component analysis is shown in Figure 10.27. At very short seawater exposure times (below 200 min), the iron oxide 'bulk' (529.9 eV) and 'surface' (e.g. X−OH, 531.3 eV) species are roughly equal, with 'surface' contributions slightly rising and the 'bulk' contribution falling (left-side of figure).[148,149] At longer corrosion times, the 'bulk' contribution is seen to rise again accompanied by the fall of 'surface' species presence. Peak at 532.3 eV is attributed to oxidised species from the adventitious carbon and is seen to decrease rapidly with the rise of seawater exposure time. Adsorbed water (533.1 eV) is seen to play a very minor role throughout.

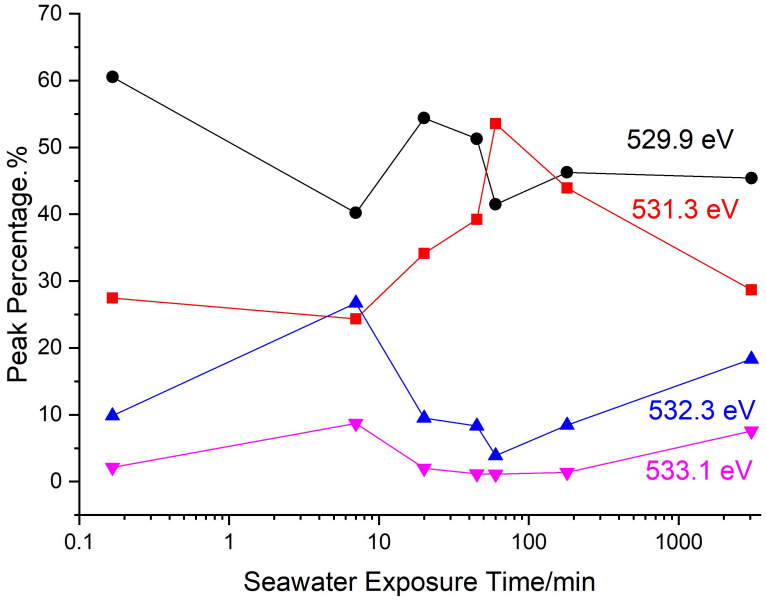

Fig. 10.27: Oxygen 1s component peak analysis at the cathodic site on polished steel surfaces as a function of seawater exposure time, followed by atmospheric exposure for 1 hr.

One explanation of the oxygen signal development is that at short corrosion timescales, deposition of fine iron oxide precipitates at the cathodic site leads to high 'surface' contribution. With further precipitate sedimentation associated with longer corrosion times, it is postulated that they become more compact or combine through aging and/or Oswald ripening. This leads to higher bulk contributions. The presence of adsorbed water (533.1 eV) and its slight increase with seawater exposure time is suggestive of porous sediment iron oxide formations occluding water within.

The increase of seawater exposure time has been shown to increase the thickness of iron oxide layer formation, on both the anodic and cathodic sites of the seawater-droplet corroded steel. The iron oxide layer sees seawater ions adsorbed onto it, in agreement with iron oxide adsorption models.

Through iron and oxygen component peak analysis, it is hypothesised that the structurally-inhomogeneous corrosion product layer formation at the cathodic regions has mostly iron (III) oxides (through further atmospheric oxygen oxidation) at the surface layers but with iron (II) oxide content. Cross-section samples of short corrosion timescales (20 and 105 min) at the cathodic sites are to be analysed for the oxidation states of corrosion products, where

the 'true' iron oxide substrate can be determined in high-spatial resolution.

10.4.2 Anodic Site Formations Analysis

The deposition/formation of corrosion products and associated seawater ion adsorption at the cathodic area makes it interesting.[32] For a more complete study, the anodic region formations was also inspected in detail. Anodic regions of corroded steel have 'lines' that are consistently observed across all samples. An example is shown in Figure 10.28.

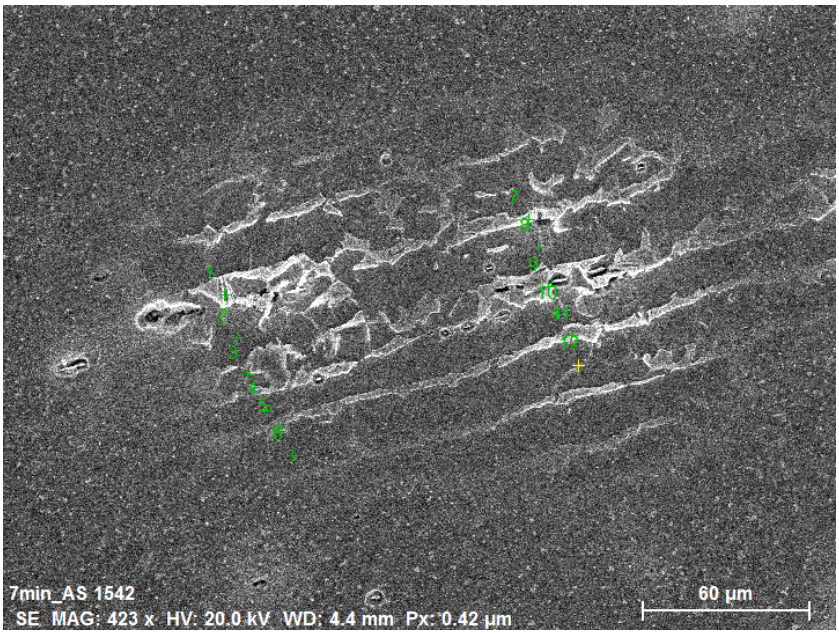

Fig. 10.28: Typical SEM image of anode oxide lines. This sample has a polished steel surface exposed to a seawater droplet for 7 min and exposed to the atmosphere for 1 hr. Sampling points are labelled.

The white lines seen in the SEM images (indicative of electronic charging) are associated with regions of high oxygen content, as shown in Figure 10.29. Whenever there is an oxygen content maximum, an iron content minimum is detected. This is consistent with the formation of iron oxide lines on the anode. Sometimes seawater ions are seen to be associated with these lines but their presence is sporadic.

Image analysis of anodic region oxide lines shows that there are consistent spacings between these anodic oxide lines. In both variable air- and seawater-exposure times samples, the line-to-line spacings are approximately 18 μm

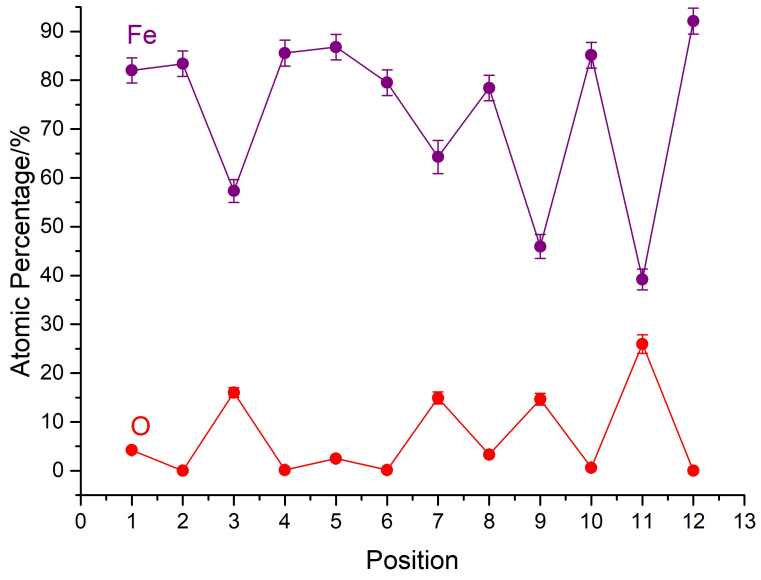

Fig. 10.29: EDX-derived oxygen and iron elemental analysis at different sampling locations listed in Figure 10.28.

wide (Figure 10.30A). Explanations for such a phenomenon include corrosion mechanism artifacts, or possible revealing of the underlying fine structure of the steel, or both.

Figure 10.30B shows anodic lines to be enclosed by corrosion product deposit 'rings' (highlighted in red), which are localised cathodic sites rather than the general region at the outer edges of the seawater droplet. The lines observed are not in parallel to the geometry of said 'rings'. This is contrary to what would be expected should these iron oxide lines be solely the product of corrosion mass transport, which would from a series of concentric oxide rings.

Further investigation is required to determine the oxide line origins, and whether any change of corrosion variables (pH, viscosity, electrolytes etc.) may affect the line spacings.

10.4.3 Cathodic Site Products Cross-Section Analysis

In addition to EDX and XPS surface analyses on the corrosion products-deposited cathode, techniques of higher spatial resolution is needed to gain further details of the surface species present. Surface crystallographic techniques such as Backscattered Electron Diffraction (EBSD) is unsuitable for a corroded steel surface due to the following reasons:

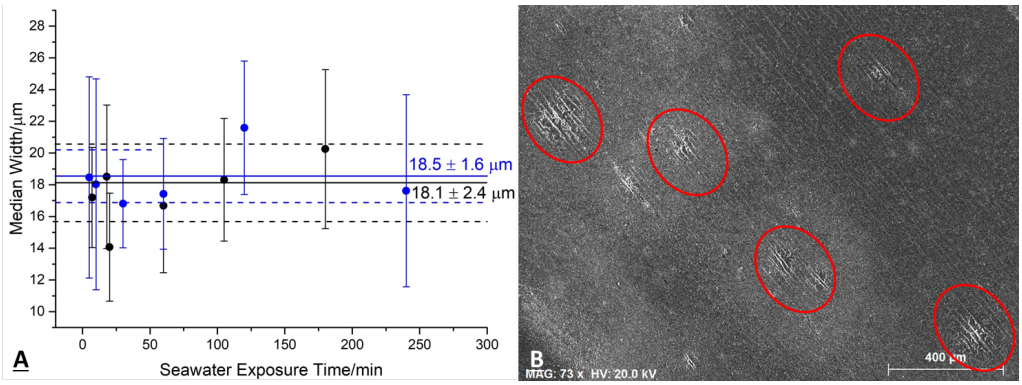

Fig. 10.30: A) Combined results of air-exposure time (blue) and seawater-exposure time (black) anode oxide lines line-to-line widths determined by SEM analysis on corroded polished steel. B) Anodic region of polished steel sample exposed to seawater for 100 min, followed by 1 hr atmospheric exposure. Red circle highlights the anodic corrosion zones.

1. EBSD needs backscattered electrons to leave the sample surface and the diffraction patterns generated by the surface crystals collected by a phosphorous screen. A roughened surface significantly scatters these electrons leading to a weak data acquisition.

2. Insulating nature of iron oxides often lead to signal-drifting during data collection, losing spatial resolution of the technique that made it desirable in the first place.

3. EBSD requires a long data collection time that would prove costly, especially in view of the unreliability of the spatial resolution for electrical insulator surfaces.

Focused Ion Beam coupled (FIB) with Transmission Electron Microscopy (TEM) techniques were used instead to provide a well-resolved cross-sectional view and a simple method for determining the crystallinity of the corrosion products formed.

Samples exposed to seawater for 20 and 105 min, then the atmosphere for 1 hr were selected to give representation of offshore structures exposed to wet marine aerosols in repainting-relevant timescales. Surface cross-sectional wedges were cut from the cathodic regions. The process is outlined in Figure 10.31 to prepare a TEM-suitable 'electron transparent' sample.

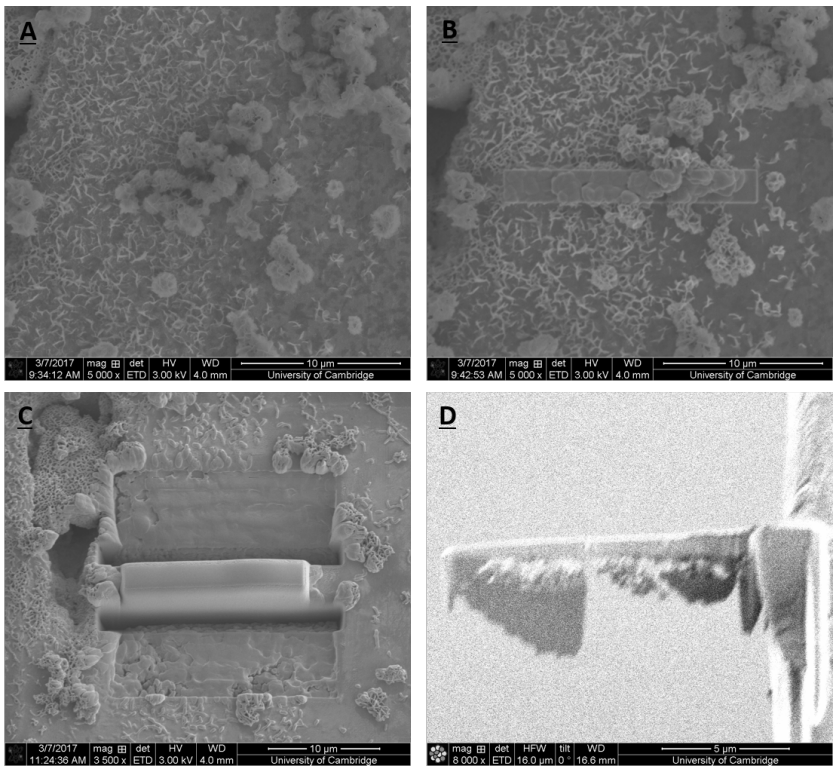

Fig. 10.31: Outline of the FIB sample preparation process for a S355 steel surface exposed to seawater droplet for 105 min, followed by 1 hr atmospheric exposure, at the cathodic site: A) surface iron oxide features are identified; B) a protective layer of platinum is deposited with low-energy electron beam and subsequently with an ion beam; C) trenches around the sample are are milled using a gallium ion beam to facilitate *in situ* sample lift-out; D) the sample lamella is cut and lifted out using an Omniprobe, deposited onto a TEM grid, then thinned using low-energy gallium beam until it is sufficiently 'electron-transparent' for TEM analysis.

In Figure 10.31D, the bottom layer is the protective platinum layers and the top is the bulk steel. The corrosion products formed can be seen between the two layers and are evidently porous. This provides ample surface area of iron oxides for seawater ions to adsorb onto, consistent with EDX and XPS analysis at the cathodic regions.

A TEM microscope with a diffractometer attachment was used to assess the crystallinity of corrosion products formed at the former steel-seawater interface. The TEM micrographs and diffraction patterns are respectively

shown the top and bottom rows of Figure 10.32. In agreement with SEM inspection of the lamella, the corrosion products on the polished steel surface is populated by many voids, indicating the formation of a porous layer at short seawater corrosion times.

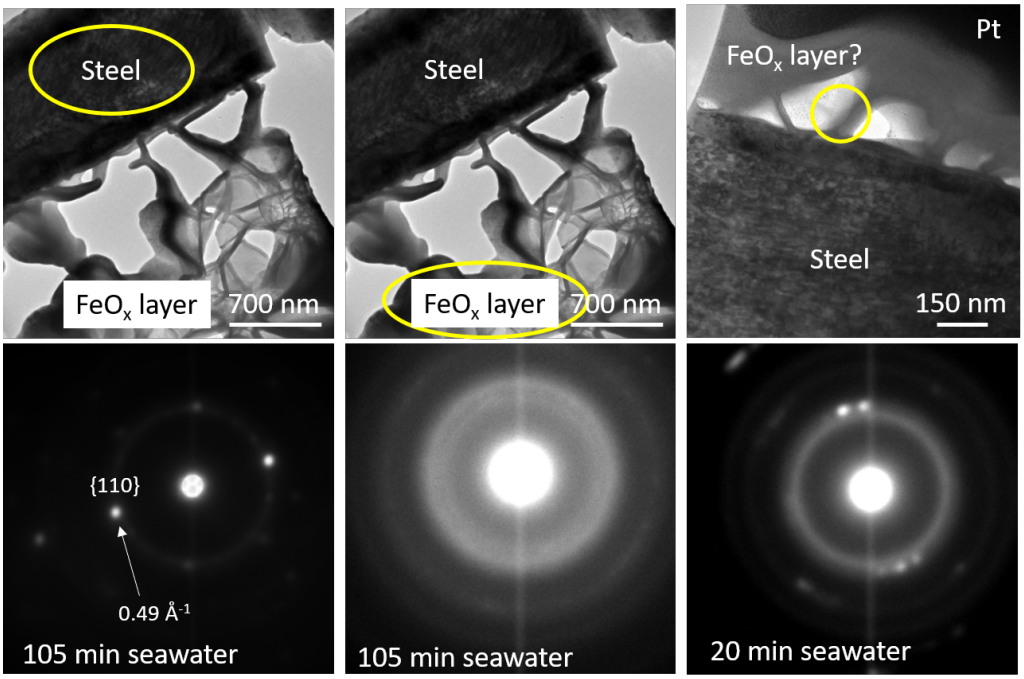

Fig. 10.32: TEM sampling of S355 steel with 20 and 105 min seawater exposure and 1 hr atmospheric exposure. Top row: TEM images of steel-seawater interface corrosion products; Bottom row: TEM electron diffraction patterns taken from the regions indicated by yellow circles in the images above.

In Figure 10.31A, 'nodules' of corrosion products are seen in SEM images. TEM images show no sign of such solid formation in Figure 10.32, whereas 'flake'-like features are seen by both techniques. It is therefore likely that the nodules seen are aggregated formations of the flake iron oxide corrosion products or evolved from them *via* ageing.

The bottom row of Figure 10.32 shows the diffraction patterns at the steel-seawater interface. Electron diffraction was used to assess the crystallinity of the materials. Sharp localised spots originate from small monocrystallites. Powder averaging of of many crystallites give rise to narrow rings. Broad halos around the centre are typical of amorphous materials.

The electron beam collected diffraction spotted pattern of bulk steel for 105 min corroded steel (bottom row, leftmost) is characteristic of ferrite (α-Fe) crystals. Diffraction patterns for the porous corrosion products (centre) at the previously seawater-steel interface show wide circular halos typically seen for amorphous phases. At the rightmost, interface ferrite diffraction patterns are superimposed with broader rings for the thin corrosion product layer for the 20 min corroded steel, indicating the corrosion products to be polymorphous. The combined results suggest that the corrosion products are amorphous/polydomain for short corrosion timescales.

Improved resolution TEM of the corroded polished steel surface cross-sections see the same 'flakes' and 'nodules' features (Figure 10.33). They resemble goethite and lepidocrocite formations on marine corroded steel.[260,261] The corrosion layers are very porous, including the 'nodules' highlighted in yellow circles. Their cross-sections are flower-like aggregates with flake-like corrosion products (present in shorter corrosion times) forming the 'petals'.

The 'maximum' thickness of the layers is observed to rapidly develop at short corrosion times, from 300 nm to 2350 nm for samples respectively corroded for 20 and 105 min. The increase of iron oxide thickness agrees with XPS elemental analysis at the cathodic regions. The evolution of corrosion product morphology is likely due to 'ageing' through continued oxidation, inclusion of other solvated species. The precise mechanism remains complex and is yet unknown.[262]

Overall, marine aerosol corrosion products are identified to be amorphous. Therefore corrosion product surface chemistry cannot be inferred from existing iron oxide crystal data. Longer exposure times for steel in marine conditions results in increased marine corrosion, which in turn leads to thicker corrosion products layers. The surface chemistry, in addition to structure, of short-timescale corroded S355 steel can have significant implications to the paint adhesion strength. The corrosion product layer chemical environments hence are analysed in detail through EDX and EELS.

10.4.4 Chemical Environment Analyses of Cathodic Site Corrosion Product Distribution

Figure 10.34 shows the TEM-EDX elemental mapping for a 20 min seawater corroded steel surface. The top region shows the bulk steel and the bottom formerly seawater/air. After adjusting the contrast the porous iron-containing corrosion product is seen to strongly coincide with oxygen regions,

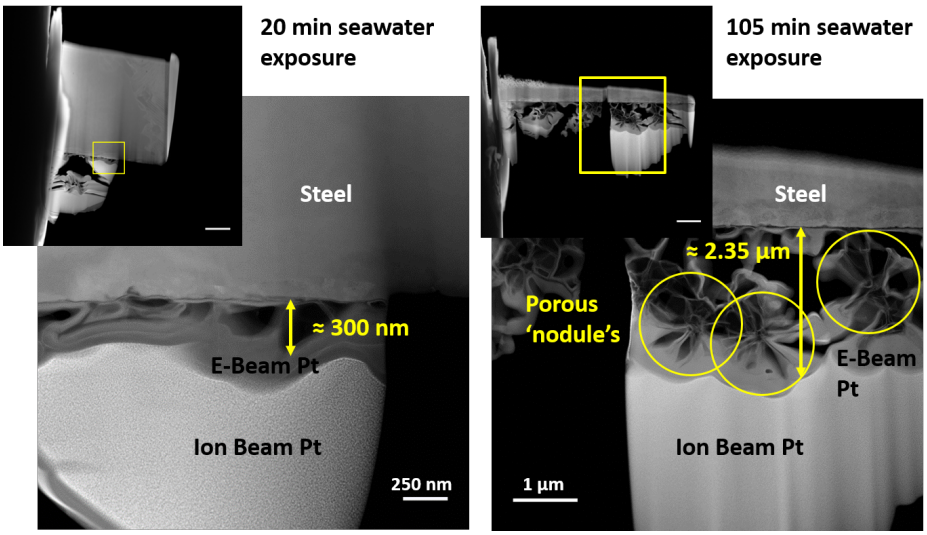

Fig. 10.33: Higher-resolution TEM images of FIB-prepared corroded polished S355 steel surfaces, subjected to different seawater exposure times and 1 hr atmospheric exposure. Inlays: yellow rectangles denote the regions sampled.

as expected from iron oxide corrosion products. Interestingly despite manganese being a significant alloying element in S355 steel, there is no evidence of manganese association with iron other than the uncorroded steel.

The carbon and platinum regions are seen to be coincidental due to the use of FIB platinum precursor, (methylcyclopentadienyl)trimethyl platinum, for protective platinum layer deposition surrounding the corrosion product formations. As a result there is significant carbon residue in the layer.

By comparing the observed raw iron peaks from EELS (between 705 and and 730 eV in binding energy) to standard peak-shapes of iron (0, II) and iron (III) species, the data is unmixed through independence component analysis (ICA) for each oxidation state and is replotted for each environment in Figure 10.35. The ICA separated iron peaks of each oxidation state for samples corroded for 20 (solid lines) and 105 min (dashed lines) are presented.

The iron (0, II) peaks between the two corroded samples are highly similar. The 105 min-corroded sample has a slightly higher main peak shift at 708.26 eV and a visible shoulder at 711.17 eV, in comparison to the main peak shift of 707.96 eV and no clear shoulder for the 20 min exposure sample. These variations may be reflective of incomplete separation of the physical

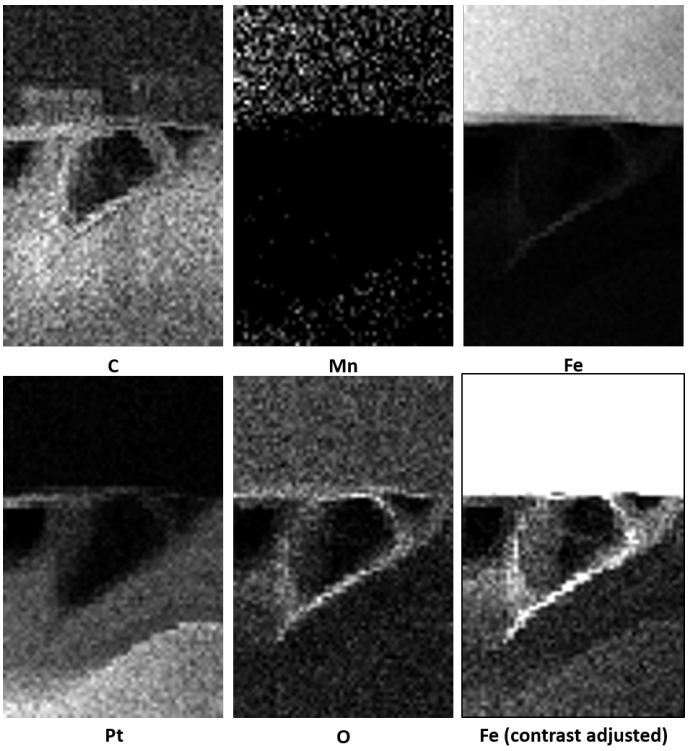

Fig. 10.34: EDX mapping of various elements for a polished S355 steel surface exposed to seawater for 20 min, then in atmosphere for 1 hr.

underlying raw spectra. Therefore a reference spectra based method was used to fit the spectrum images in addition to the quantitative ICA analysis.

From the component spectra analysis presented in Figure 10.36, all iron (III)-associated spectra have distinct oxygen peaks showing strong mutual correlation between the two elements. The lack of a standalone iron (II)-associated oxygen spectrum implies iron (III) oxides to be dominant in the corrosion product layer.

With increased corrosion time to 105 min, an oxygen-associated peak can be seen for the iron (0, II) spectrum previously absent in the 20-min corroded sample. This development is consistent with the generation of iron (II) oxides at longer corrosion times, mixed with iron (III) oxides, in good agreement with XPS iron chemical environment analysis at the cathodic regions. However, due to imperfection in spectra component unmixing by ICA, these spectra comparisons should be treated with caution.

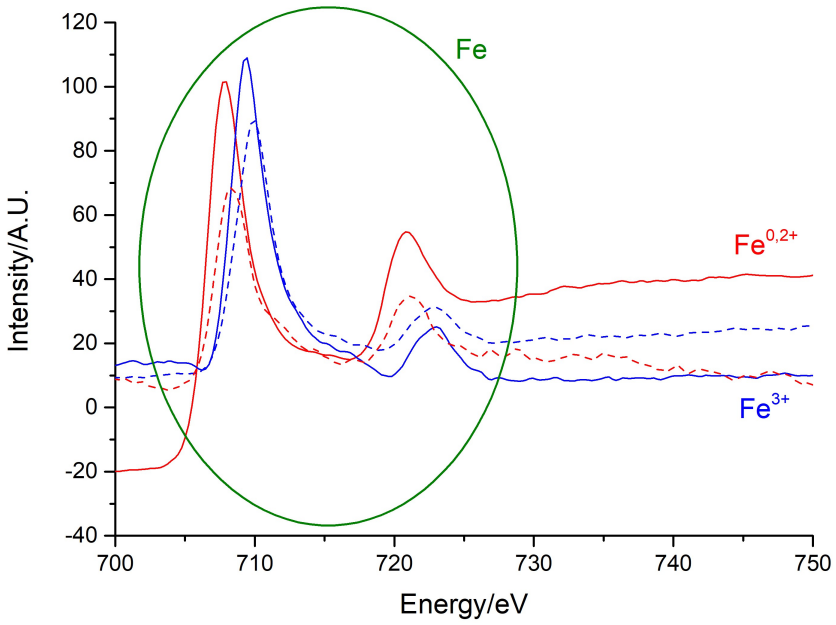

Fig. 10.35: ICA component EELS spectra iron peaks between sample area spectra contributions associated with iron (0, II) and iron (III) environments, at the steel-seawater interface regions for polished S355 steel surfaces exposed to seawater for 20 min (solid lines) and 105 min (dashed lines), then in atmosphere for 1 hr.

Manganese peaks are only associated with iron (0, II) spectra in Figure 10.36, confirming manganese association with the uncorroded bulk steel in agreement with EDX data. There is little or no manganese association with iron oxides.

The location of the different oxidation state iron oxides identified by EELS in good spatial resolution was analysed, obtained through reference spectra line-shape peak fitting of raw iron region EELS data. The resulting amplitude maps reflected the relative proportions of the two iron environments across the EELS spectrum images, away from the iron (0) steel substrate. The reference peak fitting results were used to calculate maps showing the fraction of iron (III) relative to the total iron signal identified. This proportionality enabled the map intensity scale to range from 0 to 1 and removed instability induced by low intensity of any single fitting component (i.e. minimised the effects of signal noise).

Such maps are plotted in Figure 10.38. The figure shows polished steel

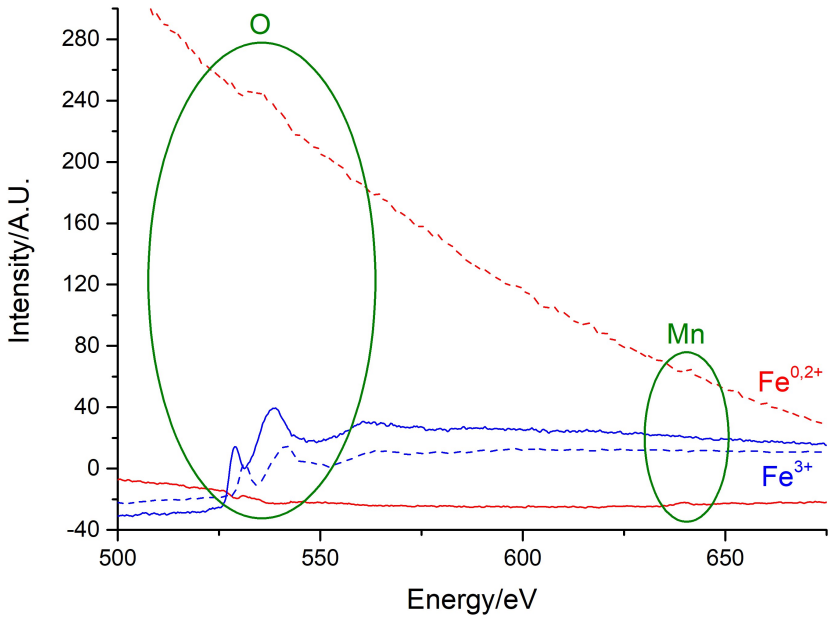

Fig. 10.36: ICA component EELS spectra of associated element peaks between sample area spectra contributions associated with iron (0, II) and iron (III) environments, at the steel-seawater interface regions for polished S355 steel surfaces exposed to seawater for 20 min (solid lines) and 105 min (dashed lines), then in atmosphere for 1 hr.

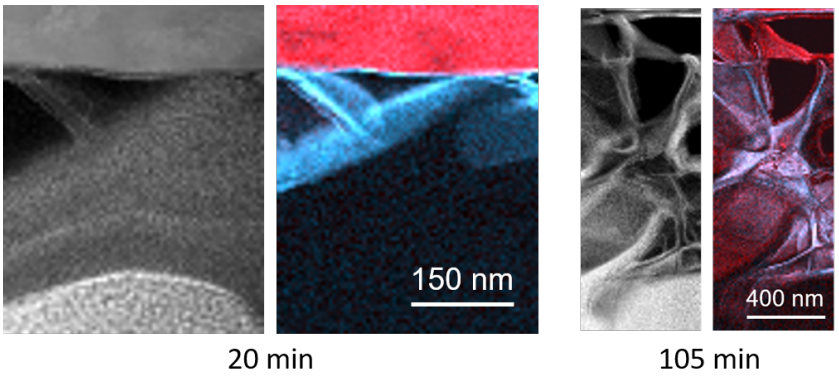

Fig. 10.37: 20 min (0.53 μm × 0.42 μm) and d) 105 min (1.97 μm × 0.71 μm) seawater corroded steel surface layer cross-section TEM micrographs with respective ICA iron oxidation state ($Fe^{0,2+}$: red; Fe^{3+}: blue) component maps of the sites surveyed, at the steel (top)-air (bottom) interface, in relation to EELS spectral ICA analysis in Figure 10.35 and 10.36.

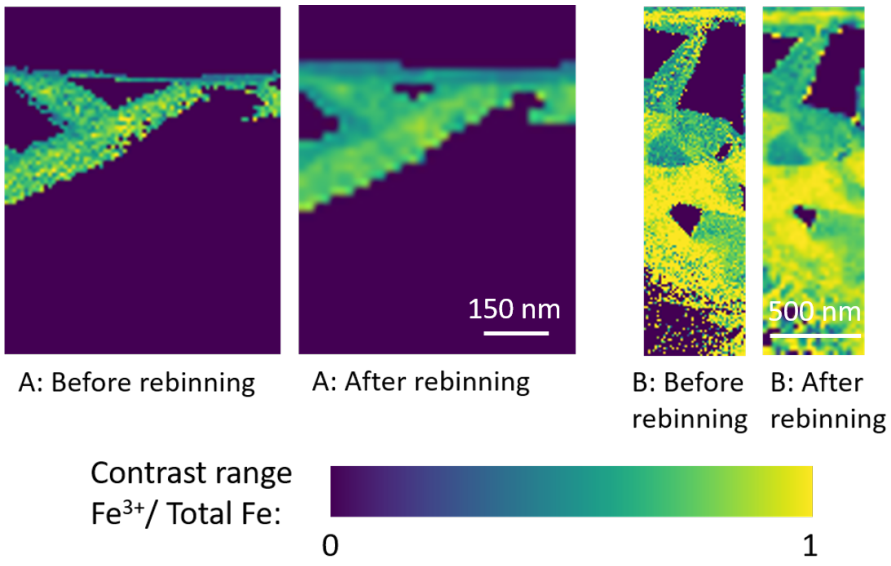

Fig. 10.38: TEM-EELS oxidation state mapping of typical cross-sectional regions at the corroded steel (top)-seawater/air (bottom) interface, before and after rebinning of Fe^{3+}/Total Fe ratio maps, after exposure to seawater for A) 20 min and B) 105 min and 1 hr atmospheric exposure. Widths of individual images: A) 420 nm; B) 555 nm.

samples corroded by seawater for 20 and 105 min. A high (yellow-end) signal indicates dominant presence of iron (III) oxides. The EELS maps are locally averaged ('rebinning') to reduce the effect of noise in the map data. By comparing samples with different lengths of seawater exposure, these maps track the iron oxide oxidation state evolution within corrosion product layers with time.

In Figure 10.38A, the 20 min corroded steel sample is rich in iron (II) oxides close to the steel surface (Fe^{3+}/Total Fe ratio intensity of 0.4). In contrast, the corrosion products close to the former seawater/air phases have an intensity around 0.7, indicating more oxidised iron corrosion products at the exposed boundary.

Figure 10.38B, the 105 min corroded steel sample display a similar trend. However it starts from a pixel intensity of approximately 0.6 close to the uncorroded steel to well above 0.8 at the outer layers of the corrosion product layer. This indicate a much more iron (III) dominated corrosion product layer throughout when compared to the 20 min corroded surface.

The oxidation state maps allows for the conclusions that the corrosion products layers are indeed very inhomogeneous, with iron (II)-rich oxides, sandwiched between iron (III) oxide-rich regions which are exposed to further atmospheric oxygen oxidation at the corrosion product layer-seawater interface when it is first formed as a iron (II) oxide precipitate. This is in strong agreement with XPS chemical environment data analyses.

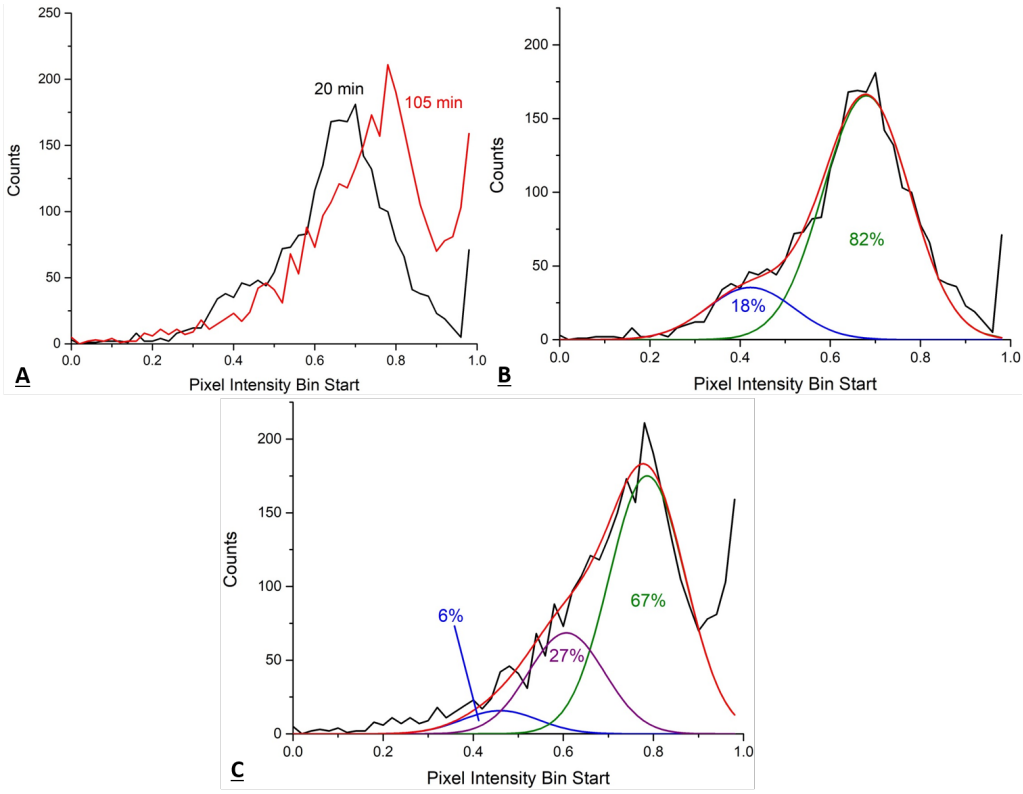

Fig. 10.39: Examples of A) raw histogram and B), C) historgram modal peak fitting of Fe^{3+}/Total Fe pixel intensity maps of S355 steel samples after A) 20 min and B) 105 min seawater exposure and 1 hr atmospheric exposure of all sites surveyed. Sample size, n = B) 353 and C) 1520. Bin width of 0.02 (intensity ratio contrast unit). Red line: sum of fitted Gaussian peaks. All fitted peaks have a FWHM of 0.2.

A semi-quantitative analysis of the iron (III)-out-of-total iron share is considered by using their pixel intensity histograms, as shown in Figure 10.39A. The signal counts of multiple sites surveyed are combined. There is an obvious higher intensity modal peak at 0.79 for the 105 min corroded steel surface than the peak at 0.68 for a 20 min corroded surface. This quantita-

tively demonstrates higher oxidation state products for the longer corroded surfaces.

Histograms are fitted with the simplest, and minimum number of Gaussian peaks each sharing the same full-width-half-maximum (FWHM) values. Example fittings are shown in Figures 10.39B and 10.39C. The 105 min corroded steel surface have higher multi-modal pixel intensities (0.46, 0.61, 0.79) than those found on the 20 min corroded surface (0.42, 0.68). The longer-corroded surface there has more oxidised corrosion product layer in average, confirming the qualitative interpretation offered from the oxidation state ratio maps. A multi-modal distribution of pixel intensities is seen for all corroded samples and it quantitatively highlights the spatial inhomogeniety of the corrosion product layers, possessing a complex mixture of iron oxides with varying oxidation states.

For 20 min of marine corrosion, the relatively thin iron oxide layer has significant iron (II) oxide character, though the outermost region is richer in iron (III) oxides. For the 105 min seawater corroded steel surface, a much thicker oxide is formed dominated by iron (III) oxides and sandwiching iron (II) oxides within the layer. The results are in excellent agreement with XPS results for iron component peak fittings which the iron (III) content is seen to dominate the spectra throughout but with growing iron (II) content with longer corrosion times. The XPS results hinted at a thickening, inhomogeneous corrosion product layer forming and the EELS maps validates this hypothesis.

In summary, surfaces that undergo very-short marine corrosion times can rapidly change in the space of 80 min, rapidly changing the substrate that coatings would bind onto, from a relatively lower (mainly iron (II) mixed with iron (III)) to a much higher oxidation state surface.

10.5 Chapter Summary of Findings and Conclusions

This chapter explores the corrosion behaviour of marine aerosols on freshly-cleaned S355 steel surfaces. Using a simple aerosol number density and flux calculation, marine aerosol are found to fully cover a steel surface in a few hours, even in mild weather conditions. Hence the steel substrate in offshore environments is likely to form microscopic corrosion products that would constitute a new substrate for coatings, in addition to the steel and abrasive residues. Possible mitigating procedures include reduction of the time

between 'surface cleaning' (abrasive blasting) and repainting, and to conduct repainting at low wind speeds to limit paint failure caused by marine corrosion.

Marine aerosols that are transported into higher altitudes with lower relative humidity decrease in water content, leading to higher salinity. Seawater pH is found to increase with salinity. pH has been previously established to be highly influential in seawater ion adsorption. Therefore a lower water content aerosol would result in higher likelihood of positively charged seawater cations being adsorbed onto the steel surface.

An Evans 'salt drop' corrosion experiment has been used to conveniently model marine corrosion of S355 steel over appropriate timescales. Samples using air exposure time as a variable, with same seawater corrosion time for all samples, show few elemental variations at the anodic region. Cathodic regions have visible corrosion products formation, with surface speciation (e.g. X−OH surface functionalities) dominating the oxygen chemical environment due to the presence of fine corrosion products. Seawater relevant ions (calcium, magnesium cations, and sulphate anions) are found to adsorb onto the iron oxide-rich cathodic region, supporting theoretical predictions of ion adsorption.

Samples with seawater exposure times as a variable, under the same subsequent atmospheric exposure time for all samples, have iron oxide corrosion product layer thicknesses increase with corrosion duration, especially at the cathodic regions. Data suggests corrosion product 'ageing' and consolidating in longer corrosion times due to decreasing surface functionality contribution. Seawater ion adsorption at the cathodic region is once again seen, in good agreement with adsorption theoretical predictions. The component peak fitting of the iron 2p peaks suggests the corrosion product layer to be chemically and structurally inhomogeneous.

Microscopy analyses in the anodic region shows iron oxide line formations, with a consistent spacing of around 18 μm. Their orientation appears to be independent to the corrosion region topography and is unlikely to be a feature of corrosion mass transport. Further work is needed to ascertain their formation mechanism.

Transmission microscopy is used to inspect cross-sectional samples taken from the cathodic region of the corroded polished steel surfaces, with varying seawater exposure times. The corrosion product layers are highly porous

and crystallographically amorphous. The thickness of the layers increases rapidly with seawater corrosion time despite the short corrosion timescales. Chemical environment analyses through EDX and EELS suggest corrosion product layers are indeed highly chemically inhomogeneous. Iron (II) oxides are sandwiched between more highly oxidised iron oxides native to the steel surface and the outer layers of oxides further oxidised by atmospheric oxygen into mainly iron (III) oxides. Overall oxidation state of the layers increases with corrosion times.

The results are industrially relevant as it highlights the urgency required for offshore structure repainting. Depending on how quickly the post-abrasive blasted surface is coated, the chemical nature of the iron oxide substrate on the steel is shown to change rapidly (in minutes, hours). Adsorption of seawater ions on the surface, then painted over, can influence the thermodynamics of water ingress below the painted layer at the steel-coatings interface. The surface evolves from an iron (II)-rich substrate in 20 min seawater exposure to a thicker iron (III)-dominated surface in 105 min of corrosion. Understanding the surface chemistry of these substrates contributes towards a more chemically-rationalised approach to improving coating formulations, by targeting and strengthening binding to a particular desired chemical environment.

11. MARINE ION ADSORPTION AT THE ALMANDINE GARNET-AQUEOUS INTERFACE

11.1 Background

The results in Chapter 5 established that after blasting, up to a third of the S355 steel surface is impregnated with abrasive residues. Paint-relevant organics are shown to adsorb onto both steel and abrasive residue surfaces, with a general higher organics affinity to the steel surface than garnet.

For offshore structures, marine aerosols provide transport for seawater inorganic salts onto the post-blasting steel surface. This marine corrosion environment is simulated using a 'salt-drop' corrosion experiment in very short, repainting-relevant timescales, where steel surface corrosion products of iron oxides (porous, of +2, +3 oxidation states) are characterised and show signs of ion adsorption at cathodic corrosion sites. These results are in broad agreement with long timescale corrosion studies in the literature, identifying iron oxides, halite, calcium carbonate deposits, and sulphate deposits within corrosion product layers.[229,242,243]

The adsorption of such ions is shown to influence the conductivity of water ingressing into the interface, and can lead to corrosion delamination of coatings.[263] This chapter therefore investigates the adsorption behaviour of inorganic seawater ions (magnesium, calcium, and sulphate ions)[248] by almandine garnet for its relevance at this steel-paint boundary in marine environment.

11.2 Experimental

11.2.1 Materials

Acid-washed milled almandine garnet powders of a specific area of 5.54 ± 0.03 m^2 g^{-1} were used in this chapter for surface titration, ζ-potential, variable-pH and constant-pH isotherm experiments. The powders had particles sizes below 10 μm. The washing process, surface chemistry, and dissolution behaviours were introduced in Chapter 6. pH of solutions were adjusted using

additions of 100 mM sodium hydroxide or 100 mM nitric acid where appropriate.

Solutions were made by dissolving their respective salts (magnesium, calcium nitrate, and sodium sulphate) in 100 mM sodium nitrate solutions in room temperature. All chemicals were provided by Sigma-Aldrich unless stated otherwise.

11.2.2 Isotherm Sample Preparation

Typically 2.0 g acid-washed garnet powder was placed into 50 mL centrifuge tubes. Each sample was made up to a suspension concentration of 200 g L^{-1}, with the appropriate amount of adsorbate solution (variable-pH isotherms: 0.5 mM magnesium nitrate, calcium nitrate, or sodium sulphate; constant-pH isotherms: varying concentrations of magnesium nitrate or calcium nitrate) in 100 mM sodium nitrate. 100 mM sodium hydroxide or 100 mM nitric acid were added to adjust the pH. Samples were tumbled to equilibrate for 24 hrs at 20 °C, then centrifuged for 30 min under a centrifugal force of 15000 g. Half of the supernatant was carefully removed with a pipette and analysed using ICP-OES to determine the equilibrium adsorbate concentration, while the other half is tested for the equilibrium pH using a Unitrode Pt100 pH probe attached to a Metrohm 809 Titrando.

11.2.3 Equipment

All experimental instruments were detailed in Chapter 4 unless specifically stated otherwise.

11.2.4 Numerical Modelling

Numerical calculations and modelling were performed using Visual MINTEQ, a software written by Jon Petter Gustafsson from the Division of Land and Water Resources Engineering, KTH Royal Institute of Technology, Stockholm, Sweden. Surface characterisations of almandine garnet were obtained by calculated model fittings to experimental data. [**Declaration: All modelling comparisons to experimental data shown in this chapter were done by Dr. David Madden. They were included for contextual and completeness purposes and the details involved were beyond the scope of this thesis. The author claims no credit for their inception.**]

11.3 Zeta-Potential Measurements

Zeta-potential (or ζ-potential) measurements were made with 100 mM solutions of the proposed specifically-adsorbing divalent electrolytes (magnesium, calcium cations, sulphate anions) in 100 mM sodium nitrate electrolyte solution. The experiment was a rough but convenient method to investigate overall surface charge at the 'slip plane'.[34]

In the presence of indifferent electrolytes (electrolytes that do not specifically-adsorb onto the substrate), it is expected the ζ-potential to be positive at pH values below the 'pristine' PZC (PZC without any specifically-adsorbing ions, coincidental to an pristine isoelectric point, IEP) and negative at a higher pH, owing to respective excess protonation and deprotonation of surface groups.

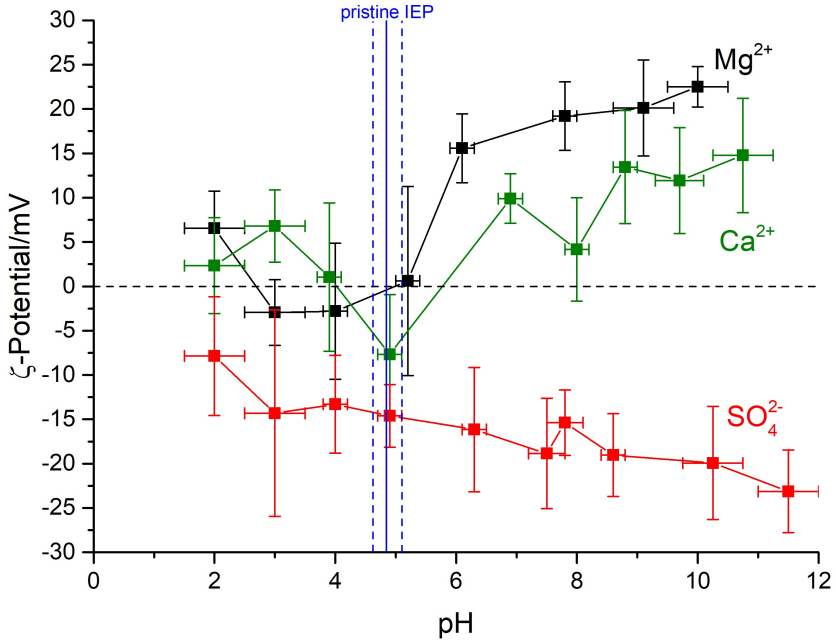

Fig. 11.1: ζ-potential measurements taken for the acid-treated almandine garnet powder in 1.0 gL^{-1} suspensions in 100 mM solutions of different adsorbing electrolytes, in a background solution of 100 mM sodium nitrate. Solid blue line indicates the 'pristine' PZC/IEP, with dotted lines indicating its range within one standard deviation.

The inclusion of adsorbing cations and anions in the diffuse layer, i.e. not necessarily only through specific adsorption, can lead to the ζ-potential to shift respectively positively and negatively according to the charge of ions. ζ-

potential measurements with possible specifically-adsorbing ions in solution are shown in Figure 11.1.

With magnesium and calcium cations addition, low pH has a positively charged surface, with protonated surface groups ($\equiv XOH_2^+$) dominant similar to the results expected for an indifferent electrolyte. The rise of pH sees positive garnet ζ-potentials contrasting the expected negative value for an inert electrolyte. The result is consistent with higher pH encouraging magnesium and calcium ions immobilisation onto the garnet surface, leading to a positive surface charge.

At pH values above the 'pristine' PZC/IEP, the sulphate solution ζ-potential is negative, consistent with the dominant species being the deprotonated surface groups ($\equiv XO^-$). At pH lower than the PZC, however, the ζ-potential remains negative, of opposite sign to what is expected for an inert electrolyte suspension suggesting sulphate ions inclusion within the slip plane.

In summary, ζ-potential measurements supports the inclusion of magnesium and calcium cations, and sulphate anions within the almandine garnet surface slip plane. Though the modes of adsorption, specific or not, requires confirmation through further experiments (e.g. titrations, isotherms) that are to be detailed further in this chapter.

11.4 Surface Titrations

11.4.1 Acid-Base Titrations

Different to indifferent ions, which remain in the diffuse layer and may be included in the slip plane, some ions adsorb much more strongly onto the substrate surface by entering the Stern layer and effect change to the surface potential. They are known as 'potential-determining ions'. These changes are observable through surface titrations, when the experiment is conducted with a significant amount of possible specifically-adsorbing electrolyte present.

The solution pH responses to acid (hydrochloric acid) and base (sodium hydroxide) titration, under different electrolytes in a 100 mM sodium nitrate background, are presented in Figure 11.2. The definitions of TOTH are outlined in Equations 4.4 to 4.8 in Chapter 4, with additional terms from surface charge-contributing species (e.g. $[\equiv XOM^+]$ or $[\equiv XOA^-]$) should specific ion adsorption occurs. In summary, it is the net added acid (positive) or base

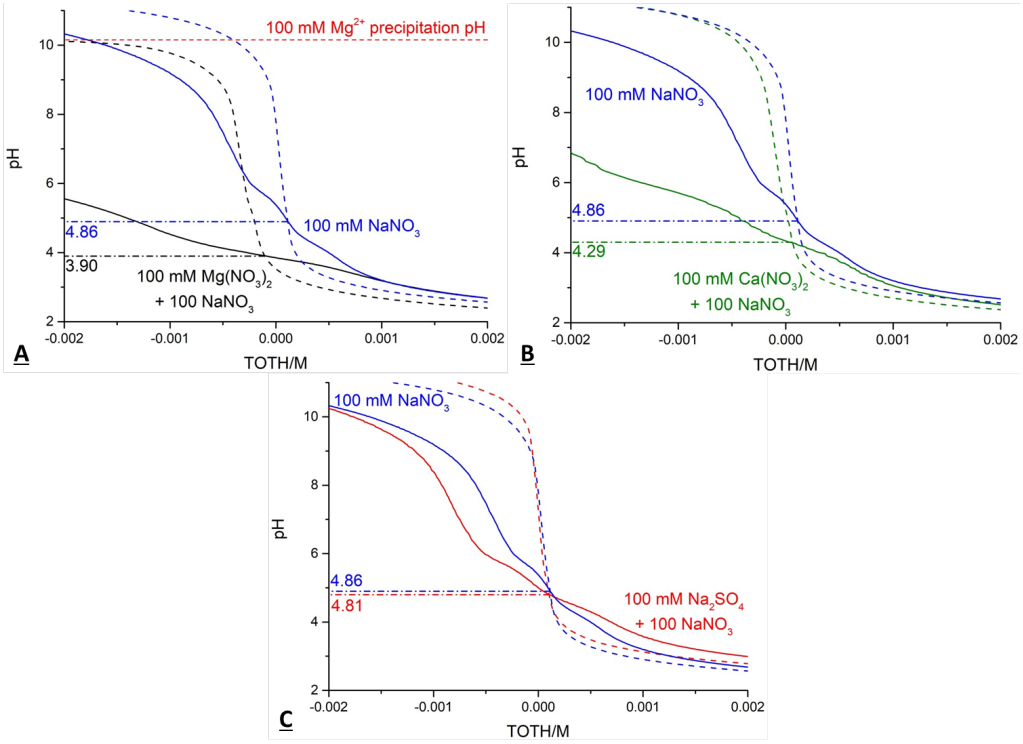

Fig. 11.2: Acid-base titration curves for 50 mL of 100 g L^{-1} acid-treated almandine garnet suspensions in various 100 mM solutions of A) magnesium nitrate, B) calcium nitrate, and C) sodium sulphate in 100 mM sodium nitrate background electrolyte.

(negative) concentrations within the titrated solution. The intercept between the blank (no solids) and suspension (with solids) titration cruves denotes the point when charges surface species equalise each other.

For both magnesium and calcium cations, the increase of electrolyte concentration shifts the cross-over point ('apparent zero charge', $\sigma_{app} = 0$) towards a lower pH and TOTH value compared to suspensions without the ions. This is consistent with the effects of specifically-adsorbing ions.[264]

When cation specific adsorption occurs, there are fewer surface sites on garnet (X−OH) to protonate or deprotonate at a relatively (to inert electrolytes) increased positive surface charge. This makes deprotonation 'easier' at lower cross-over pH values, but quantitatively more base (lower TOTH) is needed to deprotonate the garnet surface groups and equalise the positively charged surface species (e.g. $[\equiv XOH_2^+]$, $[\equiv XOM^+]$ etc.).

The introduction of significant sulphate ions in solution, shown in Figure 11.2C, has not significantly changed the cross-over point when compared to the titrations without. Titration data suggest that sulphate ions do not specifically-adsorb onto the garnet surface under the experimental conditions imposed.

The results therefore support the hypothesis that both calcium and magnesium cations are specifically adsorbing ions on garnet in sodium nitrate supporting electrolyte. Caution should be exercised in deriving any physical values or constants from this data due to the significantly changed ionic strength between suspension titrations. Quantitative data extraction would need numerical modelling work, taking into account the effects of ionic strength changes and different equilibria present on the garnet surface. Therefore such efforts are best started from simple titration systems through salt-solution titrations.

11.4.2 Salt-solution Titrations

Salt solutions with electrolytes that are hypothesised to specifically adsorb onto garnet are used to titrate the almandine garnet surface. The 0.1 M salt solutions (sodium, magnesium, calcium nitrates) were titrated into 50 mL of 100 g L^{-1} garnet suspensions in ultrapure water. All 'blank' titrations by salt solutions into ultrapure water find no pH changes. Therefore any pH changes seen are a result of garnet surface interaction with the dosing ions.

The results of titrating garnet-in-water suspensions with nitrate salt solutions are shown in Figure 11.3. All three nitrate salt titrations similarly start at pH 4.9 and falls when the salts are added, in varying starting gradients and eventually plateaus. This is indicative of proton release when cations are added into solution, suggesting sodium, magnesium, and calcium cations all can specifically adsorb onto the almandine garnet surface. When significant positive surface charge (except sodium) builds up, further cation adsorption is discourages and pH changes reach a plateau.

It is interesting to see sodium specific adsorption onto garnet. Literature data on monovalent salts often suggest them to be indifferent electrolytes based on no apparent PZC/pH changes with increased electrolyte concentrations ($\leq$ 0.1 M) for acid-base titrations for iron oxide, alumina, and silica surfaces.[32,265,266]

[**Modelling work by Dr. Madden**] The pH responses for all three ni-

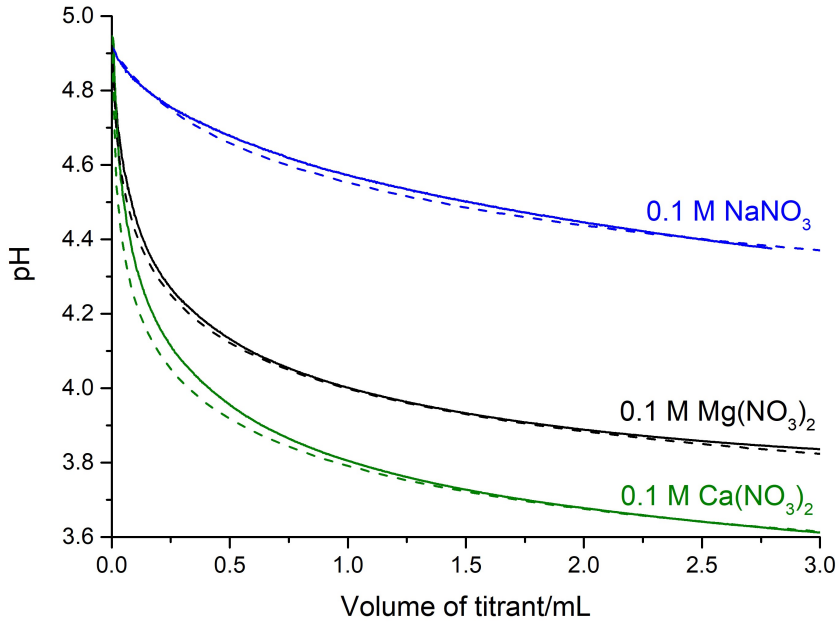

Fig. 11.3: Solution pH changes seen in titration of 50 mL of 100 g L^{-1} acid-washed almandine garnet suspension in ultrapure water, using different 0.1 M solutions of nitrate salts. Dashed lines are numerical modelling using the 'one-proton-released' adsorption model.

trate salts are modelled most consistent with cation specific adsorption that releases one proton per cation adsorption into the solution ('one-proton-released' model, Equation 11.1, with 'instrinsic' equilibrium constant in Equation 11.2). However, no equilibrium constant or surface site density information can be extract from the titrations alone due to their interlinked effects on adsorption, making data insensitive to fitting by either properties. For example, same data can be fitted well with low site densities provided adsorption constant is high, and vice versa. Therefore isotherm experiments were devised to constrain data ditting and derive physical data of the garnet surface groups.

$$\equiv\mathrm{X{-}OH} + \mathrm{M^{n+}} \rightleftharpoons \equiv\mathrm{X{-}OM^{n-1}} + \mathrm{H^{+}} \tag{11.1}$$

$$K^{int}_{\mathrm{M^{n+},2}} = \frac{[\equiv \mathrm{XOM^{n-1}}][\mathrm{H^{+}}]}{[\equiv \mathrm{XOH}][\mathrm{M^{n+}}]} \exp(\frac{+e\psi_s}{kT}) \tag{11.2}$$

11.5 Adsorption Isotherms

11.5.1 Variable-pH Adsorption

Variable-pH experiment probed the adsorption of different ions onto the acid-washed garnet powder surface at different pH values. Each had the same adsorbate ion concentration of 0.5 mM added into a background electrolyte solution of 100 mM sodium nitrate. The adsorbate concentration was chosen to prevent cation precipitation at higher experimental pH values that would lead to false positives in adsorption.

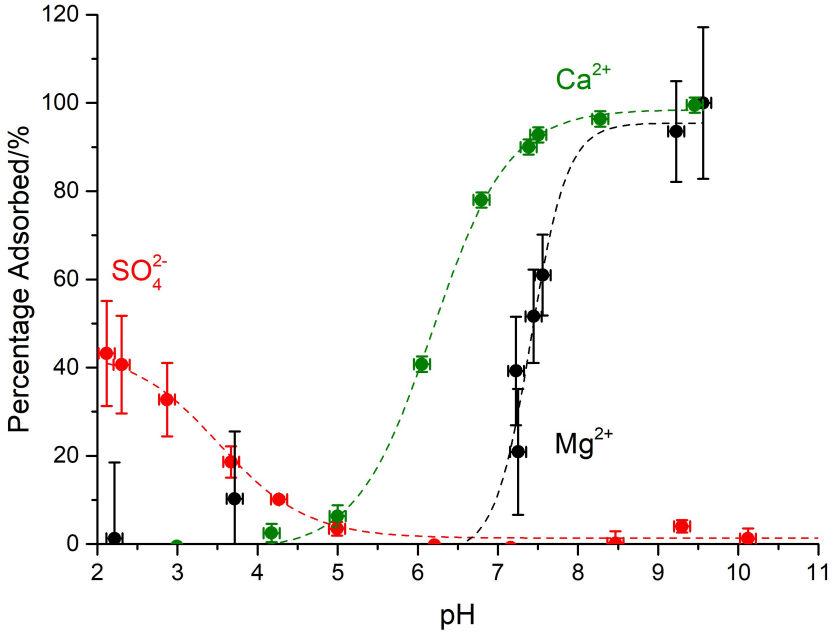

Fig. 11.4: Variable-pH adsorption isotherms for 10 mL of 200 g L^{-1} acid-washed almandine garnet suspended in 100 mM sodium nitrate supporting electrolyte solution, with 0.5 mM solutions of each adsorbate ion added.

The adsorption responses of seawater-related ions are shown in Figure 11.4. Percentage adsorption for magnesium and calcium becomes significant at higher pH values. Equations 11.3 and 11.4 show at higher pH values surface hydroxyl groups favour cation adsorption due to chemical equilibria and electrostatics. The appearance of a 'pH edge', where percentage adsorption of ions increases rapidly with pH, is consistent with cation adsorption data at pH values above a surface 'pristine' PZC/IEP ($\approx$ 5 for almandine garnet).[32,265]

$$\equiv\mathrm{XOH} + \mathrm{M}^{2+} \rightleftharpoons \equiv\mathrm{XOM}^{+} + \mathrm{H}^{+} \tag{11.3}$$

$$\equiv\mathrm{XO}^{-} + \mathrm{M}^{2+} \rightleftharpoons \equiv\mathrm{XOM}^{+} \tag{11.4}$$

Sulphate ion adsorption on garnet is only apparent at low pH. The percentage adsorption is observed to be lower than those seen for cations at high pH values. However, numerical adsorption data extraction in extreme low pH values needs to be treated with caution due to probable garnet dissolution observed in Chapter 6. Dissolution changes the adsorbate surface area and release of potentially specifically-adsorbing electrolytes that would upset the adsorption equilibrium.

The results are in good agreement with the ζ-potential data. Seawater ions are seen to adsorb onto garnet surface in the same pH ranges that ζ-potential results suggest they would, leading to significant surface charge changes when compared to being in indifferent electrolytes. The earlier onset of significant adsorption for calcium cations, compared to magnesium, may be indicative of a stronger adsorption strength. This was investigated through constant-pH solution depletion isotherms.

11.5.2 Constant-pH Adsorption

Constant-pH solution depletion isotherms were used to determine the magnesium and calcium cation adsorption constants on almandine garnet. Sulphate ion adsorption isotherm was not included in this work, due to probable interference in adsorption equilibrium by garnet dissolution at low pH values.

Cations adsorb are seen to adsorb most at high pH values. Cation concentrations are chosen to prevent metal hydroxide precipitation in these high pH solutions, so as to avoid overestimation of cation adsorption during solid-supernatant separation.[267] An suitable pH of 9.35 ± 0.05, is therefore chosen for the cation concentration ranged used in this experiment.

The results of the solution depletion isotherms of both cations are shown in Figure 11.5. Adsorption is seen to initially increase with increasing ion concentration, then begins to plateau when ion concentration is further increased. Both Langmuir and Freundlich model fitting of the data are used.

The Langmuirian model gives adsorption constants of $8.92 \pm 0.23 \times 10^{2}$ M^{-1}

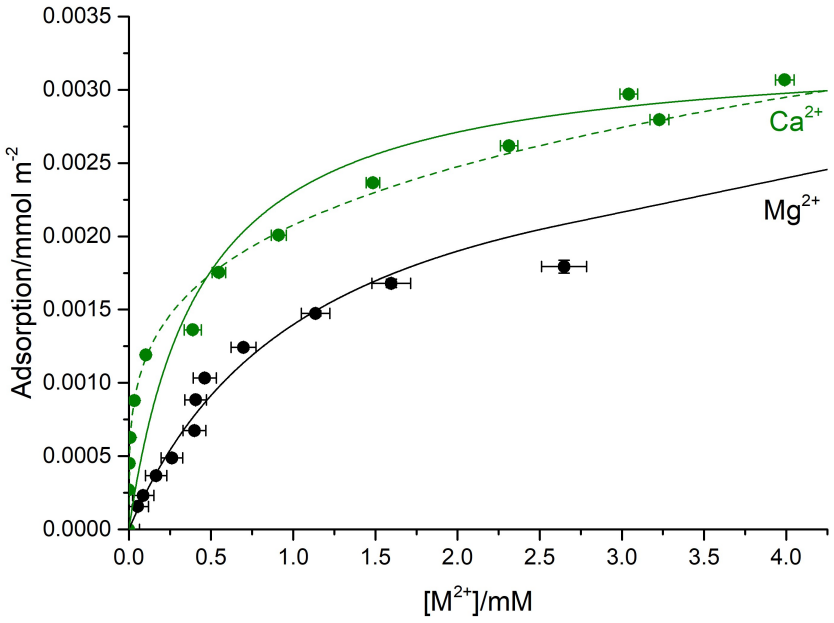

Fig. 11.5: Constant-pH solution depletion isotherms for 200 g L^{-1} acid-washed almandine garnet suspended in 100 mM sodium nitrate supporting electrolyte solution, at pH at 9.35 ± 0.05. Solid lines are Langmuir-like isotherm model fitting. Dashed line is the Freundlich isotherm model fitting.

and $2.30 \pm 0.14 \times 10^3$ M^{-1}, or $\log K_{ads}$ values of 2.95 and 3.36, respectively for magnesium and calcium cations. Both ions have a model monolayer adsorption limit of around 3.5μmol m^{-2}, or approximately 2 sites nm^{-2}.

A Freundlich isotherm fitting has been attempted for the calcium ion only, due to poor fits to magnesium data. The data fit appears to be much better than the Langmuirian fitting. The fitted adsorption constant, K_F, is $6.69 \pm 0.12 \times 10^2$ M^{-1}, with an n value of 3.95 ± 0.09. The Freundlich isotherm is applied as a useful empirical representation of the data, without detailed implications on the physical interactions present.[268]

Despite similarity between Langmuir and Freundlich isotherms fittings, the non-one constant n is consistent with non-ideal ion adsorption where repulsive lateral interactions between adsorption sites are likely present. This leads 'slowed' increase of cation adsorption with respect to increased ion concentrations. One possible explanation would be an increase of electrostatic repulsion on an increasingly positively charged almandine garnet surface dis-

couraging further cation adsorption.

In summary both cations are seen to specifically adsorb onto almandine garnet in high pH conditions, in good agreement with variable-pH and ζ-potential measurements. Calcium cations appear to adsorb more strongly than those of magnesium.

11.6 Theoretical Rationalisation of Marine Ion Adsorption onto Garnet

[**Modelling work by Dr. Madden**] Numerical modelling was used to recogcile the results obtained from salt-solution surface titrations and adsorption isotherms. The fitting of titration results have identified the 'one-proton-released' adsorption model to be most suitable. The adsorption isotherm results contribute to the constraining of surface site density and adsorption equilibrium constant fitting.

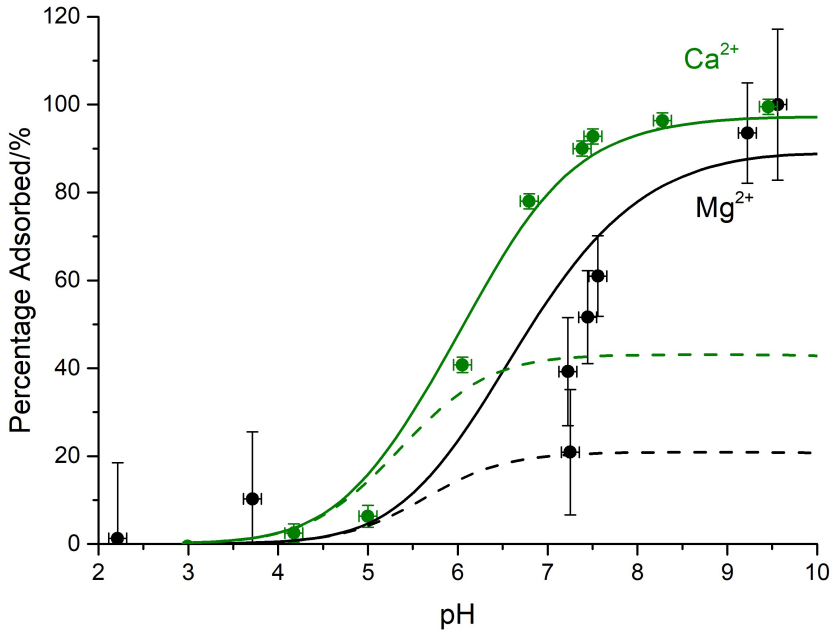

Fig. 11.6: Variable-pH adsorption isotherms for 10 mL of 200 g L^{-1} acid-washed almandine garnet suspended in 100 mM sodium nitrate supporting electrolyte solution, with 0.5 mM solutions of each adsorbate ion added. Modelling results with different adsorption site densities are shown in dashed (1 site nm^{-2}) and solid (40 site nm^{-2}) lines.

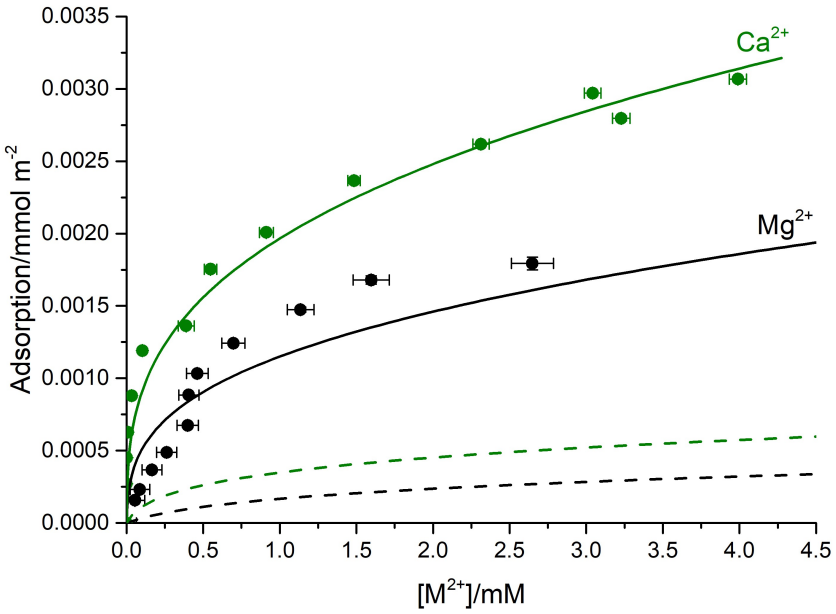

Fig. 11.7: Constant-pH solution depletion isotherms for 200 g L^{-1} acid-washed almandine garnet suspended in 100 mM sodium nitrate supporting electrolyte solution, at pH at 9.35 ± 0.05. Modelling results with different adsorption site densities are shown in dashed (1 site nm^{-2}) and solid (40 site nm^{-2}) lines.

Figures 11.6 and 11.7 show the adsorption of magnesium and calcium adsorption onto almandine garnet surface as predicted by numerical modelling, given the experimental concentrations used and utilising the equilibrium and equilibrium constants (for sodium, magnesium, and calcium adsorption) that provided best fits for salt solution titration results. The higher surface site density clearly fits the experimental data better than lower site density, which severely underestimates the ion adsorption.

Therefore the by reconciling titration and isotherm data through a simple double layer-based, 40 identical surface sites nm^{-2}, and following a 'one-proton-release' model, the equilibrium constants for sodium, magnesium, and calcium cations are respectively $10^{-6.4}$, $10^{-4.7}$, and $10^{-4.0}$. Further work is needed to rationalise the difference in saturation limit surface site density from isotherm model fitting (Langmuir and Freundlich) with numerical model fittings.

11.7 Chapter Summary

In this chapter, seawater ion adsorption on the almandine garnet surface has been characterised through multiple techniques. Some of the seawater ions investigated are shown to specifically adsorb onto the mineral surface and is summarised in Table 11.1.

Tab. 11.1: Summary of seawater-relevant ion binding onto almandine garnet in the aqueous phase.

Ion	**Specific Adsorption?**
Na^+	Yes (Titration data)
Cl^-	No
NO_3^-	No
Mg^{2+}	Yes
Ca^{2+}	Yes
SO_4^{2-}	Maybe

Through numerical modelling of the experimental data from surface titrations and adsorption isotherms, a reasonable constrained fitting of surface site density (40 sites nm^{-2}), mode of cation adsorption (ion displacement of proton from surface group), and adsorption equilibrium constants on the almandine garnet surface is achieved. Relative cation adsorption strengths on the mineral are as follows:

$$K_{ads}^{int}(Na^+) < K_{ads}^{int}(Mg^{2+}) < K_{ads}^{int}(Ca^{2+})$$

The specific adsorption of some ions onto garnet, and occlusion/adsorption onto steel corrosion products of iron oxide as seen in Chapter 10, could have significant implications to the rate of water ingress into the steel-paint interface. This in turn could potentially exacerbate coating deadhesion from the steel surface upon ion arrival. Overall, this body of work has shown that future studies of mineral-ion adsorption *require* a wide data set consisting multiple techniques to ensure the reliability of surface data fitted.

12. FINAL CONCLUSIONS AND FUTURE WORK

In this work, the detailed characterisations of surfaces relevant to offshore structures, the adsorption of species-of-interest onto those surfaces, and the monitoring of corrosion products on steel, had been devised through a diverse range of experimental techniques. The suite of techniques was chosen to provide a mutually-confirmatory approach to ensure validity of conclusions.

A detailed characterisation of abrasive blasting-related surfaces was conducted, starting from as-received millscale-covered S355 steel. The millscale steel was identified to be a thick layer of iron oxide, with minor elements occluded probably by surface contamination. This millscale oxide layer was removed upon polishing. The polished steel was extensively analysed (SEM, TOF-SIMS, XPS, and EBSD) and the techniques verified the presence of a thin native mixed-iron oxide layer on the surface. The success in characterising the surface oxide chemical environments and crystallinity enabled the inferring of surface hydroxyl group density and the average surface iron oxidation state from the literature data. Information that was otherwise difficult to obtain due to the high reactivity of carbon steels in aqueous solutions.

S355 steel was abrasive-blasted with naturally-mined almandine garnet particles. SEM analysis confirmed a very significant amount of abrasive covering the blasted steel surface. This was considered to have very significant effects on coatings performance and related surfaces. Through SEM-EDX elemental maps, abrasive residue surface coverage dependence on blasting time and pressure were studied. The surface coverage rapidly reached a plateau with longer blasting times ($>$ 10 seconds) and covers up to a third of the steel. Interestingly, no pressure dependence was seen for abrasive surface coverage. TOF-SIMS analysis revealed an increased build-up or penetration of abrasive residues associated with longer blasting times. A hypothesised attachment mechanism by the abrasive residues on the steel surface was suggested.

These residues persisted on the steel surface despite very vigorous removal attempts. They were shown to exist at the steel-paint interface. There was therefore important to characterise the mineral surface and its adsorption

behaviour. Garnet adsorption chemistry could significantly influence coating performance when paint is applied on the residue-laden steel.

The surface chemistry of almandine garnet mineral was probed through surface titrations, ζ-potential measurements, and detailed XPS experiments. The aqueous phase data enabled the surface acid constants (pK_a) and the potential of zero charge point (PZC) of almandine garnet to be obtained. The latter data agrees well with the limited literature value available for garnet. The surface chemical environment indicated from XPS reveals the surface groups were intermediate in character between iron and aluminium oxide.

Suggested future work might endeavour to directly observe surface oxygen species from the garnet surface through sensitive surface reflectivity techniques, or transmission spectroscopy of very fine powders to quantify the surface site density. The spectroscopic surveying of milled substrates, however, requires nanometre-scale fineness to maximise surface-to-volume ratio for good surface statistics. This is difficult to achieve mechanically, grinding aids/agents are needed but could contaminate the substrate.[269]

Abrasive residues were identified as potential weak-spots for coatings deadhesion. Therefore dry ice-almandine garnet abrasive blasting was tested as one of the approaches to reduce abrasive residue surface coverage on the steel. While the surface coverage was shown to decrease to around a quarter of the surface (*cf.* a third covered by abrasive-only blasting), significant surface cooling from the blasting led to the formation of iron oxide corrosion spots on the surface. These corrosion spots might provide additional weak links for coating failure, despite the reduction in residue coverage. Future work on steel-coating binding strength, with and without these spots, is needed to confirm the utility of this treatment.

Adsorption of a range of organic species with key chemical functionalities that might be suitable adhesion promoters and/or corrosion inhibitors, onto the steel and garnet in organic solvent systems was surveyed. Solution depletion isotherms derived by a large collection of concentration analysis techniques (IR, UV-Vis, qNMR), estimated equilibrium adsorption constants and approximate adsorption geometries of adsorbates onto the steel and garnet surfaces individually, as useful model component substrates for an abrasive residue-covered S355 steel surface.

Additional molecular adsorption geometrical information was determined

through SFG and far-IR spectroscopies. SFG data independently verified the adsorption of the molecules onto the substrates. Polished almandine garnet surfaces had surprisingly persistent alkyl carbon signatures on the surface even after aggressive plasma cleaning. This significantly obstructed the analytical power of SFG in elucidating the precise adsorption geometry of adsorbates on polished garnet surfaces. Results showed that most paint additives and paint component molecules preferred to bind on steel rather than on almandine garnet. This further supports the hypothesis of abrasive residues at the steel-paint interface may be a weak point for coating failure.

Offshore environments are corrosive to steel surfaces due to the presence of marine aerosols in the atmosphere. Such corrosion may occur rapidly after abrasive blasting but prior to the painting. A simple estimation of the time needed for full coverage of post-blasting steel surface by marine aerosols showed this could occur within a few hours in mild weather. The aerosols increase in pH upon drying with increased height from the sea-level. A 'salt drop' corrosion study was used to identify the surface chemistry of the corrosion products at the clearly identifiable anodic and cathodic sites. For such products would form the topmost substrate for coatings to bind onto.

Detailed analysis of the corrosion products on the S355 steel surface reveal the formation of a porous, highly chemically inhomogeneous iron oxide layers. The adsorption of marine ions by the cathodic site corrosion products was supported by elemental analysis. At short (20 min) corrosion timescales, the corrosion product layer consisted mainly of iron (II) oxides, whereas longer (105 min) corrosion times leads to a dominant iron (III) oxide exterior, encapsulating iron (II) oxides within. The significant changes in corrosion product surface chemistry in the space of 85 min (20 min vs. 105 min corrosion) highlights how rapidly the surface chemical environments changes for offshore steel surfaces, and informs the repainting urgency needed for optimal coating performance.

With proof of significant seawater ion transport onto the abrasive-blasted steel surfaces and their adsorption onto marine corroded steel, experiments were devised to investigate the adsorption of seawater ions onto the almandine garnet abrasive residues. Data consisting ζ-potential measurements, surface titrations, and adsorption isotherms were collected to aid numerical adsorption model fitting on the almandine garnet surface. Using a simple double layer adsorption model, the adsorption equilibria and equilibrium constants of different ions, and the surface site density of the almandine garnet were successfully estimated through well-constrained, co-fitting of the

different sets of experimental values from surface titrations and adsorption isotherms. Surprisingly, the monovalent sodium cation was found to specifically adsorb onto the garnet, albeit at a much weaker adsorption strength than the divalent magnesium and calcium cations that are also prevalent in seawater.

This work showed complicated surface chemistry at the steel-paint interface on offshore platforms, subject to rapid changes. The adsorption behaviour identified could have influence on the binding performance of coatings. The work identified factors useful for future chemically-rationalised anti-corrosion solutions:

1. The suggested mechanism of attachment by blasting abrasive on the steel surface was based on the relative hardness of the materials involved (steel, blasting media, etc.). Future work could exploit other materials of different hardness to prevent corrosion. For example, inclue more soft materials (calcite, metallic zinc) in the blasting medium to achieve full surface coverage by the protective material, that would either provide a better substrate for coating binding, or removing the need for painting altogether.

2. Minimising the time of steel exposure to the marine atmosphere by dosing protective additives, that would bind best on metallic steel, within the blasting medium to arrest corrosion at the earliest opportunity.

Work has already begun on these proposed factors. It is hoped that this work had addressed, and helpfully raised, some of the questions that need further investigating. So that solutions can be found to arrest corrosion on offshore structures.

BIBLIOGRAPHY

[1] J. E. Inglesfield. Surface electronic structure. *Rep. Prog. Phys.*, 45(3): 223–284, 1982.

[2] A. Subramanian and L. D. Marks. Surface crystallography via electron microscopy. *Ultramicroscopy*, 98(24):151–157, 2004.

[3] K. Maisel, L. Ensign, M. Reddy, R. Cone, and J. Hanes. Effect of surface chemistry on nanoparticle interaction with gastrointestinal mucus and distribution in the gastrointestinal tract following oral and rectal administration in the mouse. *J. Controlled Release*, 197:48–57, 2015.

[4] L. Vitos, A. V. Ruban, H. L. Skriver, and J. Kollr. The surface energy of metals. *Surf. Sci.*, 411(12):186–202, 1998.

[5] T. Y. Wong and R. C. Bradt. Microhardness anisotropy of single crystals of calcite, dolomite and magnesite on their cleavage planes. *Mater. Chem. Phys.*, 30(4):261–266, 1992.

[6] V. Barrn and J. Torrent. Surface hydroxyl configuration of various crystal faces of hematite and goethite. *J. Colloid Interface Sci.*, 177 (2):407–410, 1996.

[7] M. J. Madou. *Fundamentals of Microfabrication: The Science of Miniaturization*. CRC Press, Boca Raton, USA, 2nd edition, 2002.

[8] G. Barnes and I. Gentle. *Interfacial Science: An Introduction*. Oxford University Press, Oxford, UK, 2nd edition, 2011.

[9] W. D. Kaplan. Alumina - aluminium interfaces. In A. Bellosi, T. Kosma, and A. P. Tomsia, editors, *Interfacial Science in Ceramic Joining*, volume 58 of *NATO ASI Series*, pages 153–160. Springer Netherlands, Dordrecht, The Netherlands, 1st edition, 1998.

[10] M. Morita, T. Ohmi, E. Hasegawa, M. Kawakami, and M. Ohwada. Growth of native oxide on a silicon surface. *J. Appl. Phys.*, 68(3): 1272–1281, 1990.

[11] H. Over and A. P. Seitsonen. Oxidation of metal surfaces. *Science*, 297 (5589):2003–2005, 2002.

[12] J. J. Frewing. The influence of temperature on boundary lubrication. *Proc. Royal Soc. A*, 181(984):23–42, 1942.

[13] H. L. F. Helmholtz. Ueber einige Gesetze der Vertheilung elektrischer Ströme in körperlichen Leitern mit Anwendung auf die thierisch-elektrischen Versuche. *Ann. Phys.*, 165(6):211–233, 1853.

[14] P. H. Rieger. *Electrochemistry*. Springer Netherlands, Dordrecht, The Netherlands, 2nd edition, 1994.

[15] P. Debye and E. Hckel. The theory of electrolytes. i. lowering of freezing point and related phenomena. *Phys. Z.*, 24:185–206, 1923.

[16] W. Stumm, C. P. Huang, and S. R. Jenkins. Specific chemical interaction affecting the stability of dispersed systems. *Croat. Chem. Acta*, 42:223–245, 1970.

[17] H.-J. Butt, K. Graf, and M. Kappl. *Physics and Chemistry of Interfaces*. Wiley-Blackwell, Weinheim, FRG, 1st edition, Sep 2003.

[18] P. Schindler and H. R. Kamber. Die aciditt von silanolgruppen. vorlufige mitteillung. *Helv. Chim. Acta*, 51(7):1781–1786, 1968.

[19] W. Stumm, R. Kummert, and L. Sigg. A ligand exchange model for the adsorption of inorganic and organic ligands at hydrous oxide interfaces. *Croat. Chem. Acta*, 53:291–312, 1980.

[20] W. Stumm and J. J. Morgan. *Aquatic Chemistry*. Wiley, New York, USA, 3rd edition, 1995.

[21] B. A. Manning, S. E. Fendorf, and S. Goldberg. Surface structures and stability of arsenic(iii) on goethite: spectroscopic evidence for inner-sphere complexes. *Environ. Sci. Technol.*, 32(16):2383–2388, 1998.

[22] J. W. Bowden, M. D. A. Bolland, A. M. Posner, and J. P. Quirk. Generalized model for anion and cation adsorption at oxide surfaces. *Nature-Phys. Sci.*, 245(145):81–83, 1973.

[23] D. E. Yates, S. Levine, and T. W. Healy. Site-binding model of the electrical double layer at the oxide/water interface. *J. Chem. Soc., Faraday Trans. 1*, 70:1807–1818, 1974.

[24] J. A. Davis and J. O. Leckie. Surface ionization and complexation at the oxide/water interface ii. surface properties of amorphous iron oxyhydroxide and adsorption of metal ions. *J. Colloid Interface Sci.*, 67(1):90–107, 1978.

[25] Z. Kolarik. Sorption radioaktiver isotopen an niederschlgen. vi. system eisen(iii)-hydroxyd-strontiumnitratlsung und die allgemeinen gesetzmsigkeiten der sorption am eisen(iii)-hydroxyd. *Collect. Czech. Chem. Commun.*, 27(4):938–950, 1962.

[26] D. S. Smith and F. G. Ferris. Specific surface chemical interactions between hydrous ferric oxide and iron-reducing bacteria determined using pKa spectra. *J. Colloid Interface Sci.*, 266(1):60–67, 2003.

[27] S. Zhu, U. Panne, and K. Rurack. A rapid method for the assessment of the surface group density of carboxylic acid-functionalized polystyrene microparticles. *Analyst*, 138(10):2924, 2013.

[28] H. T. M. Heinrich, P. J. Bremer, C. J. Daughney, and A. J. McQuillan. Acid Base Titrations of Functional Groups on the Surface of the Thermophilic Bacterium Anoxybacillus flavithermus: Comparing a Chemical Equilibrium Model with ATR-IR Spectroscopic Data. *Langmuir*, 23(5):2731–2740, 2007.

[29] M. Szekeres and E. Tombácz. Surface charge characterization of metal oxides by potentiometric acidbase titration, revisited theory and experiment. *Colloids Surf. A Physicochem. Eng. Asp.*, 414:302–313, 2012.

[30] W. Stumm, L. Sigg, and B. Sulzberger. *Chemistry of the solid-water interface : processes at the mineral-water and particle-water interface in natural systems*. Wiley, New York, USA, 1st edition, 1992.

[31] L. M. Schwartz. Uncertainty of a titration equivalence point: a graphical method using spreadsheets to predict values and detect systematic errors. *J. Chem. Educ.*, 69(11):879, 1992.

[32] D. A. Dzombak and F. M. M. Morel. *Surface Complexation Modeling: Hydrous Ferric Oxide*. John Wiley & Sons, Inc., 1st edition, 1990.

[33] J. Lützenkirchen, T. Preočanin, D. Kovačević, V. Tomišić, L. Lövgren, and N. Kallay. Potentiometric titrations as a tool for surface charge determination. *Croat. Chem. Acta*, 85(4):391–417, 2012.

[34] J. Lyklema. *Fundamentals of interface and colloid science. Volume II, Solid-liquid interfaces*. Academic Press, London, UK, 1st edition, 1995.

[35] M. Smoluchowski. Contribution à la théorie de l'endosmose électrique et de quelques phénomènes corrélatifs. *Bull. Int. Acad Sci. Cracovie*, 8:182–199, 1903.

[36] M. Kaszuba, J. Corbett, F. Mcneil Watson, and Andrew Jones. High-concentration zeta potential measurements using light-scattering techniques. *Philos. Trans. Royal Soc. A*, 368(1927):4439–4451, 2010.

[37] H. Y. Erbil. *Surface Chemistry: Of Solid and Liquid Interfaces*. Blackwell Publishing Ltd., Oxford, UK, 1st edition, 2006.

[38] R. I. Masel. *Principles of Adsorption and Reaction on Solid Surfaces*. Wiley, Hoboken, USA, 1st edition, 1996.

[39] M. Jaroniec. Adsorption on heterogeneous surfaces: the exponential equation for the overall adsorption isotherm. *Surf. Sci.*, 50(2):553–564, 1975.

[40] S. Brunauer, P. H. Emmett, and E. Teller. Adsorption of gases in multimolecular layers. *Journal of the American Chemical Society*, 60 (2):309–319, 1938.

[41] K. S. W. Sing. Adsorption methods for the characterization of porous materials. *Adv. Colloid Interface Sci.*, 76-77:3–11, 1998.

[42] I. M. K. Ismail. Cross-sectional areas of adsorbed nitrogen, argon, krypton, and oxygen on carbons and fumed silicas at liquid nitrogen temperature. *Langmuir*, 8(2):360–365, 1992.

[43] L. Jelinek and E. sz. Kovats. True surface areas from nitrogen adsorption experiments. *Langmuir*, 10(11):4225–4231, 1994.

[44] N. Ayawei, A. N. Ebelegi, and D. Wankasi. Modelling and interpretation of adsorption isotherms. *J. Chem.*, 2017:1–11, 2017.

[45] P. Nikitas. A critique of the adsorption isotherms used in electrochemical processes involving the adsorption of organic compounds. *J. Chem. Soc. Faraday Trans. 1*, 81(8):1767–1787, 1985.

[46] D. J. Shaw. *Introduction to colloid and surface chemistry*. Butterworth-Heinemann, Oxford, UK, 4th edition, 1992.

[47] B. He, C. H. Lu, P. J. Han, and X. H. Bai. Short-term electrochemical corrosion behavior of pipeline steel in saline sandy environments. *Eng. Fail Anal.*, 59:410–418, 2016.

[48] Z. Xu, X.-J. Huang, and L.-S. Wan. Techniques for Membrane Surface Characterization. In *Surface Engineering of Polymer Membranes*, pages 5–63. Springer-Verlag Berlin Heidelberg, Heidelberg, FRG, 1st edition, 2009.

[49] T. Maitland and S. Sitzman. Electron Backscatter Diffraction (EBSD) Technique and Materials Characterisation Examples. In W. Zhou and Z. L. Wang, editors, *Scanning Microscopy for Nanotechnology. Techniques and Applications*, chapter 2, pages 41–75. Springer-Verlag Berlin Heidelberg, Berlin, Heidelberg, FRG, 1st edition, 2007.

[50] A. J. Wilkinson and T. B. Britton. Strains , planes , and EBSD in materials science. *Mater. Today*, 15(9):366–376, 2012.

[51] D. B. Williams and C. B. Carter. The Transmission Electron Microscope. In *Transmission Electron Microscopy*, pages 3–22. Springer US, Boston, USA, 2nd edition, 2009.

[52] D. B. Williams and C. B. Carter. Elastic Scattering. In *Transmission Electron Microscopy*, pages 39–51. Springer US, Boston, USA, 2nd edition, 2009.

[53] D. B. Williams and C. B. Carter. Inelastic Scattering and Beam Damage. In *Transmission Electron Microscopy*, pages 53–71. Springer US, Boston, USA, 2nd edition, 2009.

[54] P. Ewels, T. Sikora, V. Serin, C. P. Ewels, and L. Lajaunie. A Complete Overhaul of the Electron Energy-Loss Spectroscopy and X-Ray Absorption Spectroscopy Database: eelsdb.eu. *Microsc. Microanal.*, 22 (03):717–724, 2016.

[55] A. Feldhoff, J. Martynczuk, M. Arnold, M. Myndyk, I. Bergmann, V. Šepelák, W. Gruner, U. Vogt, A. Hähnel, and J. Woltersdorf. Spin-state transition of iron in $(Ba_{0.5}Sr_{0.5})(Fe_{0.8}Zn_{0.2})O_{3-\delta}$ perovskite. *J. Solid State Chem.*, 182(11):2961–2971, 2009.

[56] P. Torruella, R. Arenal, F. de la Peña, Z. Saghi, L. Yedra, A. Eljarrat, L. López-Conesa, M. Estrader, A. López-Ortega, G. Salazar-Alvarez, J. Nogués, C. Ducati, P. A. Midgley, F. Peiró, and S. Estradé. 3D Visualization of the Iron Oxidation State in FeO/Fe_3O_4 CoreShell

Nanocubes from Electron Energy Loss Tomography. *Nano Lett.*, 16(8): 5068–5073, 2016.

[57] T. Koopmans. Über die Zuordnung von Wellenfunktionen und Eigenwerten zu den Einzelnen Elektronen Eines Atoms. *Physica*, 1(1-6): 104–113, 1934.

[58] C. D. Wagner, L. E. Davis, M. V. Zeller, J. A. Taylor, R. H. Raymond, and L. H. Gale. Empirical atomic sensitivity factors for quantitative analysis by electron spectroscopy for chemical analysis. *Surf. Interface Anal.*, 3(5):211–225, 1981.

[59] J. F. Watts and J. Wolstenholme. *An introduction to surface analysis by XPS and AES*. John Wiley & Sons, Inc., 2003.

[60] M. Seah and W Dench. Quantitative Electron Spectroscopy of Surfaces. *Surf. Interface Anal.*, 2(1):1979, 1979.

[61] S. Tanuma, C. J. Powell, and D. R. Penn. Calculation of electron inelastic mean free paths (IMFPs) VII . Reliability of the TPP-2M IMFP predictive equation. *Surf. Interface Anal.*, 35(1):268–275, 2003.

[62] M. A. Newton, S. M. Francis, and M. Bowker. Oxygen adsorption on Cu/Pd[85 : 15]{110}: an angle resolved XPS determination of adsorbate induced reconstruction. *Surf. Sci.*, 269-270:41–48, 1992.

[63] P. M. A. Sherwood. The use and misuse of curve fitting in the analysis of core X-ray photoelectron spectroscopic data. *Surface and Interface Analysis*, 51(6):589–610, 2019. ISSN 10969918.

[64] D. A. Shirley. High-Resolution X-Ray Photoemission Spectrum of the Valence Bands of Gold. *Phys. Rev. B*, 5(12):4709–4714, 1972.

[65] R. Matsumoto, Y. Nishizawa, N. Kataoka, H. Tanaka, H. Yoshikawa, S. Tanuma, and K. Yoshihara. Reproducibility of XPS analysis for film thickness of SiO2/Si by active Shirley method. *J. Electron Spectros. Relat. Phenomena*, 207:55–59, 2016.

[66] S. Tougaard and B. Jørgensen. Absolute background determination in XPS. *Surf. Interface Anal.*, 7(1):17–21, 1985.

[67] S. Doniach and M. Sunjic. Many-electron singularity in X-ray photoemission and X-ray line spectra from metals. *J. Phys. C Solid State Phys.*, 3(2):285–291, 1970.

[68] J. F. Moulder, W. F. Stickle, P. E. Sobol, and K. D. Bomben. *Handbook of X-ray Photoelectron Spectroscopy*. Perkin-Elmer Corporation, Eden Prairie, USA, 1st edition, 1992.

[69] F. Vidal and A. Tadjeddine. Sum-frequency generation spectroscopy of interfaces. *Rep. Prog. Phys.*, 68(5):1095–1127, 2005.

[70] H.-F. Wang, L. Velarde, W. Gan, and L. Fu. Quantitative Sum-Frequency Generation Vibrational Spectroscopy of Molecular Surfaces and Interfaces: Lineshape, Polarization, and Orientation. *Annu. Rev. Phys. Chem.*, 66(1):189–216, 2015.

[71] A. G. Lambert, P. B. Davies, and D. J. Neivandt. Implementing the theory of sum frequency generation vibrational spectroscopy: A tutorial review. *Appl. Spectrosc. Rev.*, 40(2):103–145, 2005.

[72] Y. R. Shen. Basic theory of surface sum-frequency generation. *J. Phys. Chem. C*, 116(29):15505–15509, 2012.

[73] S. Cheon and M. Cho. Difference Frequency Generation Spectroscopy as a Vibrational Optical Activity Measurement Tool. *J. Phys. Chem. A*, 113(11):2438–2445, 2009.

[74] A. I. Lvovsky. Fresnel Equations. In C. Hoffman and R Driggers, editors, *Encyclopedia of Optical and Photonic Engineering*, pages 1–6. CRC Press, Boca Raton. USA, 2nd edition, 2015.

[75] C. D. Bain. Sum-frequency vibrational spectroscopy of the solid/liquid interface. *J. Chem. Soc. Faraday Trans.*, 91(9):1281–1296, 1995.

[76] R. Lu, W. Gan, B. H. Wu, Z. Zhang, Y. Guo, and H. F. Wang. C-H stretching vibrations of methyl, methylene and methine groups at the vapor/Alcohol (n = 1-8) interfaces. *J. .Phys. Chem. B*, 109(29): 14118–14129, 2005.

[77] H. Zhang, C. Romero, and S. Baldelli. Preparation of Alkanethiol Monolayers on Mild Steel Surfaces Studied with Sum Frequency Generation and Electrochemistry. *J. Phys. Chem. B*, 109(32):15520–15530, 2005.

[78] M. H. Wood, R. J. L. Welbourn, T. Charlton, A. Zarbakhsh, M. T. Casford, and S. M Clarke. Hexadecylamine adsorption at the iron oxide-oil interface. *Langmuir*, 29(45):13735–42, 2013.

[79] M. H. Wood, M. T. Casford, R. Steitz, A. Zarbakhsh, R. J. L. Welbourn, and M. Clarke, S. Comparative Adsorption of Saturated and Unsaturated Fatty Acids at the Iron Oxide/Oil Interface. *Langmuir*, 32(2):534–540, 2016.

[80] R. G. Wilson, F. A. Stevie, and C. W. Magee. *Secondary Ion Mass Spectrometry: a practical handbook for depth profiling and bulk impurity analysis*. John Wiley & Sons, Inc., Hoboken, USA, 1st edition, 1989.

[81] A. Montaser and D. W. Golightly, editors. *Inductively coupled plasmas in analytical atomic spectrometry*. Wiley-VCH, Hoboken, USA, 2nd edition, 1992.

[82] E. V. Shunko, D. E. Stevenson, and V. S. Belkin. Inductively Coupling Plasma Reactor With Plasma Electron Energy Controllable in the Range From 6 to 100 eV. *IEEE T. Plasma Sc.*, 42(3):774–785, 2014.

[83] M. Aceto, O. Abollino, M. Bruzzoniti, E. Mentasti, C. Sarzanini, and M. Malandrino. Determination of metals in wine with atomic spectroscopy (flame-AAS, GF-AAS and ICP-AES); a review. *Food Addit. Contam.*, 19(2):126–133, 2002.

[84] L. Benramdane, F. Bressolle, and J. J. Vallon. Arsenic Speciation in Humans and Food Products: A Review. *J. Chromatogr. Sci.*, 37(9): 330–344, 1999.

[85] L. C. Trevizan and J. A. Nóbrega. Inductively coupled plasma optical emission spectrometry with axially viewed configuration: an overview of applications. *J. Braz. Chem. Soc.*, 18(4):678–690, 2007.

[86] T. Lech. Application of ICP-OES to the Determination of Barium in Blood and Urine in Clinical and Forensic Analysis. *J. Anal. Toxicol.*, 37(4):222–226, 2013.

[87] K. Klotz, W. Weistenhöfer, and H. Drexler. Determination of Cadmium in Biological Samples. In Sigel A., Sigel H., and Sigel R., editors, *Cadmium: From Toxicity to Essentiality*, pages 85–98. Springer, Dordrecht, Dordrecht, The Netherlands, 2013.

[88] D. A. Skoog, D. M. West, and F. James Holler. *Fundamentals of analytical chemistry*. Saunders College Publishing, Philadelphia, USA, 7th edition, 1996.

[89] K. E. Heusler, D. Landolt, and S. Trasatti. Electrochemical corrosion nomenclature (Recommendations 1988). *Pure Appl. Chem.*, 61(1):19–22, 1989.

[90] M. D. Durović, Ž. D. Bugarčić, and R. van Eldik. Stability and reactivity of gold compounds From fundamental aspects to applications. *Coord. Chem. Rev.*, 338:186–206, 2017.

[91] A. Michel, M. Otieno, H. Stang, and M. R. Geiker. Propagation of steel corrosion in concrete: Experimental and numerical investigations. *Cement Concrete Comp.*, 70:171–182, 2016.

[92] Z. Ahmad. *Principles of corrosion engineering and corrosion control*. Butterworth-Heinemann, Oxford, UK, 1st edition, 2006.

[93] R. W. Revie and H. H. Uhlig. *Corrosion and corrosion control : an introduction to corrosion science and engineering*. John Wiley & Sons, Inc., 4th edition, 2008.

[94] G. H. Koch, M. P. H. Brongers, N. G. Thompson, Y. P. Virmani, and J. H. Payer. Costs of corrosion and Preventitive stratigies. Technical report, NACE International, Springfield, USA, 2002.

[95] M. C. Moynihan and J. M. Allwood. Utilization of structural steel in buildings. *Proc. Royal Soc. A*, 470(2168):20140170–20140170, 2014.

[96] P. W. Atkins. *Atkins' Physical chemistry*. Oxford University Press, Oxford, UK, 6th edition, 2013.

[97] R. A. Marcus. On the Theory of ElectronTransfer Reactions. VI. Unified Treatment for Homogeneous and Electrode Reactions. *J. Chem. Phys.*, 43(2):679–701, 1965.

[98] R. G. Compton and C. E. Banks. *Understanding Voltammetry*. Imperial College Press, London, UK, 2nd edition, 2011.

[99] A. C. Bastos, M. G. Ferreira, and A. M. Simões. Corrosion inhibition by chromate and phosphate extracts for iron substrates studied by EIS and SVET. *Corros. Sci.*, 48(6):1500–1512, 2006.

[100] W. M. Liu. Beurteilung der Wirkungseffizienz von Korrosionsschutzpigmenten in Beschichtungen. *Mater. Corros.*, 49(8):576–584, 1998.

[101] E. P. M. van Westing, G. M. Ferrari, and J. H. W. de Wit. The determination of coating performance with impedance measurementsIV. Protective mechanisms of anticorrosion pigments. *Corros. Sci.*, 36(8): 1323–1346, 1994.

[102] S. Morsch, S. Lyon, P. Greensmith, S. D. Smith, and S. R. Gibbon. Mapping water uptake in organic coatings using AFM-IR. *Faraday Discuss.*, 180:527–42, 2015.

[103] A. M. P. de Jesus, R. Matos, B. F.C. Fontoura, C. Rebelo, L. Simões da Silva, and M. Veljkovic. A comparison of the fatigue behavior between S355 and S690 steel grades. *J. Constr. Steel Res.*, 79:140–150, 2012.

[104] J. Billingham, J. V. Sharp, J . Spurrier, and P. J. Kilgallon. *Review of the performance of high strength steels used offshore.* HSE Books, Sudbury, UK, 1st edition, 2003.

[105] R. Hudson. Surface Preparation for Coating. Technical report, National Physical Laboratory, Teddington,UK, 2000.

[106] C. C. Shih, C. M. Shih, Y. Y. Su, L. H. J. Su, M. S. Chang, and S. J. Lin. Effect of surface oxide properties on corrosion resistance of 316L stainless steel for biomedical applications. *Corros. Sci.*, 46(2):427–441, 2004.

[107] S. Tardio, M.-L. Abel, R. H. Carr, J. E. Castle, and J. F. Watts. Comparative study of the native oxide on 316L stainless steel by XPS and ToF-SIMS. *J. Vac. Sci. Technol., A*, 33(5):05E122, 2015.

[108] J. Tarabay, V. Peres, and M. Pijolat. Oxidation of stainless steel powder. *Oxid. Met.*, 80(3-4):311–322, 2013.

[109] G. Bhargava, T. A. Ramanarayanan, I. Gouzman, E. Abelev, and S. L. Bemasek. Inhibition of iron corrosion by imidazole: An electrochemical and surface science study. *Corrosion*, 65(5):308–317, 2009.

[110] G. Bhargava, T. A. Ramanarayanan, and S. L. Bernasek. Imidazole-fe interaction in an aqueous chloride medium: effect of cathodic reduction of the native oxide. *Langmuir*, 26(1):215–219, 2010.

[111] S. Ghareba and S. Omanovic. Interaction of 12-aminododecanoic acid with a carbon steel surface: Towards the development of 'green' corrosion inhibitors. *Corros. Sci.*, 52(6):2104–2113, 2010.

[112] P. Jin, G. Bota, W. Robbins, and S. Nesic. Analysis of Oxide Scales Formed in the Naphthenic Acid Corrosion of Carbon Steel. *Energy Fuels*, 30(8):6853–6862, 2016.

[113] W. E. Leithead. Wind energy. *Philos. Trans. Royal Soc. A*, 365(1853): 957–970, 2007.

[114] A. W. Momber. *Blast cleaning technology.* Springer, Heidelberg, FRG, 1st edition, 2010.

[115] E. P. M. van Westing. *Determination of coating performance with impedence measurements.* PhD thesis, Technische Universiteit Delft, 1992.

[116] T. Bos. *Prediction of coating durability: Early detection using electrochemical methods.* PhD thesis, Technische Universiteit Delft, 2008.

[117] A. Forsgren and C. Applegren. Comparison of chloride levels remaining on the steel surface after various pretreatments. *Proc. PCE 2000 Conf. and Exhib.*, pages 271–283, 2000.

[118] J. H. Seinfeld and S. N. Pandis. *Atmospheric Chemistry and Physics: From Air Pollution to Climate Change.* John Wiley & Sons, Inc., Hoboken, USA, 2nd edition, 2006.

[119] N.-M. Barkoula and J. Karger-Kocsis. Review Processes and influencing parameters of the solid particle erosion of polymers and their composites. *J. Mater. Sci.*, 37(18):3807–3820, 2002.

[120] A. V. Levy. Erosion and Erosion-Corrosion of Metals. *Corrosion*, 51 (11):872–883, 1995.

[121] NIST XPS Database, 2012. URL `https://srdata.nist.gov/xps/main_search_menu.aspx`.

[122] U. Schwertmann and R. M. Taylor. The transformation of lepidocrocite to goethite. *Clays and Clay Miner.*, 20(3):151–158, 1972.

[123] J. D. Dana and E. S. Dana. *The System of Mineralogy.* John Wiley & Sons, Ltd., New York, USA, 6th edition, 1892.

[124] N. S. Mancktelow, D. Grujic, and E. L. Johnson. An SEM study of porosity and grain boundary microstructure in quartz mylonites, Simplon Fault Zone, Central Alps. *Contrib. Mineral. Petrol.*, 131(1): 71–85, 1998.

[125] M. Marciuš, M. Ristić, M. Ivanda, and S. Musić. Formation of Iron Oxides by Surface Oxidation of Iron Plate. *Croat. Chem. Acta*, 85(1): 117–124, 2012.

[126] R. M. Cornell and U. Schwertmann. *Surface Chemistry and Colloidal Stability*. Wiley-VCH Verlag GmbH & Co. KGaA, Weinheim, FRG, 2nd edition, 2003.

[127] R. M. Cornell and U. Schwertmann. *Adsorption of ions and molecules*. Wiley-VCH Verlag GmbH & Co. KGaA, Weinheim, FRG, 2003.

[128] A. M. Koziol and S. R. Bohlen. Solution properties of almandine-pyrope garnet as determined by phase equilibrium experiments. *American Mineralogist*, 77(7-8):765–773, 1992.

[129] ISO 8501-2:1994(E). Preparation of steel substrates before application of paints and related products – Visual assessment of surface cleanliness – Part 2: Preparation grades of previously coated steel substrates after localized removal of previous coatings. Standard, International Organization for Standardization, Geneva, CH, 1994.

[130] D. L. Whitney, M. Broz, and R. F. Cook. Hardness, toughness, and modulus of some common metamorphic minerals. *Am. Mineral.*, 92 (2-3):281–288, 2007.

[131] D. Tabor. Mohs's hardness scale - A physical interpretation. *Proc. Phys. Soc. B*, 67(3):249–257, 1954.

[132] M. E. Broz, R. F. Cook, and D. L. Whitney. Microhardness, toughness, and modulus of Mohs scale minerals. *Am. Mineral.*, 91(1):135–142, 2006.

[133] J. H. Braun, A. Baidins, and R. E. Marganski. TiO2 pigment technology: a review. *Prog. Org. Coat.*, 20(2):105–138, 1992.

[134] T. Armbruster, C. A. Geiger, and G. A. Lager. Single-crystal X-ray structure study of synthetic pyrope almandine garnets at 100 and 293 K. *Am. Mineral.*, 77:512–521, 1992.

[135] G. A. Novak and G. V. Gibbs. The crystal chemistry of the silicate garnet. *Am. Mineral.*, 56:791–825, 1971.

[136] J. Sendroy and A. Baird Hastings. Studies of the solubility of calcium salts: III The solubility of calcium carbonate and tertiary calcium phosphate under various conditions. *J. Biol. Chem.*, 71(3):797–846, 1927.

[137] M. Kosmulski. *Surface Charging and Points of Zero Charge*. CRC Press, Boca Raton, USA, 2009.

[138] M. Kosmulski. The Surface Charging at Low Density of Protonatable Surface Sites. *Langmuir*, 21(16):7421–7426, 2005.

[139] J. Persello. *Adsorption on Silica Surfaces*. Marcek Dekker, Inc., New York, USA, 1st edition, 2000.

[140] E. Tombácz. pH-dependent surface charging of metal oxides. *Periodica Polytech., Chem. Eng.*, 532:77–86, 2009.

[141] F. Adekola, M. Fédoroff, H. Geckeis, T. Kupcik, G. Lefèvre, J. Lützenkirchen, M. Plaschke, T. Preocanin, T. Rabung, and D. Schild. Characterization of acidbase properties of two gibbsite samples in the context of literature results. *J. Colloid Interface Sci.*, 354 (1):306–317, 2011.

[142] P. M. Huang, J. Berthelin, J.-M. Bollag, W. B. McGill, and A. L. Page, editors. *Environmental impact of soil component interactions: Metals, Other Inorganics, and Microbial Activities. Volume II*. Lewis Publishers, Boca Raton, USA, 1st edition, 1995.

[143] M. Kosmulski. The pH-dependent surface charging and points of zero charge: V. Update. *J. Colloid Interface Sci.*, 2011.

[144] H. J. Modi and D. W. Fuerstenau. Streaming Potential Studies on Corundum in Aqueous Solutions of Inorganic Electrolytes. *J. Phys. Chem.*, 61(5):640–643, 1957.

[145] G. T. Austin. *Industrial Minerals and Rocks*. Society for Mining, Metallurgy, and Exploration, Inc., Littleton, USA, 6th edition, 1994.

[146] M. J. Dreiling. Quantitative surface measurements of metal oxide powders by x-ray photoelectron spectroscopy (xps). *Surface Science*, 71(2): 231 – 246, 1978.

[147] G. C. Allen, M. T. Curtis, A. J. Hooper, and P. M. Tucker. X-Ray photoelectron spectroscopy of ironoxygen systems. *Journal of Chemical Society, Dalton Transactions*, 0(14):1525–1530, 1974.

[148] E. McCafferty and J. P. Wightman. Determination of the concentration of surface hydroxyl groups on metal oxide films by a quantitative XPS method. *Surf. Interface Anal.*, 26(8):549–564, 1998.

[149] G. W. Simmons and B. C. Beard. Characterization of acid-base properties of the hydrated oxides on iron and titanium metal surfaces. *J. Phys. Chem.*, 91(5):1143–1148, 1987.

[150] D. Briggs and J. T. Grant, editors. *Surface Analysis by Auger and X-ray Photoelectron Spectroscopy*. IM Publications, Chichester, UK, 2nd edition, 2003.

[151] M. Hernandez Ubeda, H.T. Mishima, and B. A. López de Mishima. The electrochemical response of manganese hydroxideoxide films in slightly alkaline solutionsI. The redox couple. *Electrochim. Acta*, 36(5-6):1013–1018, 1991.

[152] R. W. Judd, C. Komodromos, and T. J. Reynolds. Alkali chloride doped manganese oxide catalysts: nature of the active surface. *Catal. Today*, 13(2-3):237–244, 1992.

[153] J. L. Junta and M. F. Hochella. Manganese (II) oxidation at mineral surfaces: A microscopic and spectroscopic study. *Geochim. Cosmochim. Acta*, 58(22):4985–4999, 1994.

[154] M. A. Langell, C. W. Hutchings, G. A. Carson, and M. H. Nassir. High resolution electron energy loss spectroscopy of MnO(100) and oxidized MnO(100). *J. Vac. Sci. Technol A*, 14(3):1656–1661, 1996.

[155] H. W. Nesbitt and D. Banerjee. Interpretation of XPS Mn(2p) spectra of Mn oxyhydroxides and constraints on the mechanism of MnO2precipitation. *Am. Mineral.*, 83(3-4):305–315, 1998.

[156] H. Ohashi, H. Ezoe, Y. Okaue, Y. Kobayashi, S. Matsuo, T. Kurisaki, A. Miyazaki, H. Wakita, and T. Yokoyama. The Effect of UV Irradiation on the Reduction of Au(III) Ions Adsorbed on Manganese Dioxide. *Anal. Sci.*, 21(7):789–793, 2005.

[157] M. I. Zaki, M. A. Hasan, L. Pasupulety, and K. Kumari. Bulk and surface characteristics of pure and alkalized Mn_2O_3: TG, IR, XRD, XPS, specific adsorption and redox catalytic studies. *New J. Chem.*, 22(8):875–882, 1998.

[158] S. Mustafa, M. I. Zaman, and S. Khan. pH effect on phosphate sorption by crystalline MnO_2. *J. Colloid and Interface Sci.*, 301(2):370–375, 2006.

[159] D. Portehault, S. Cassaignon, E. Baudrin, and J.-P. Jolivet. Selective heterogeneous oriented attachment of manganese oxide nanorods in water: toward 3D nanoarchitectures. *J. Mater. Chem.*, 19(42):7947–7954, 2009.

[160] N. S. McIntyre and D. G. Zetaruk. X-ray photoelectron spectroscopic studies of iron oxides. *Anal. Chem.*, 49(11):1521–1529, 1977.

[161] A. Scheidegger, M. Borkovec, and H. Sticher. Coating of silica sand with goethite: preparation and analytical identification. *Geoderma*, 58 (1-2):43–65, 1993.

[162] T. Yamashita and P. Hayes. Analysis of XPS spectra of Fe^{2+} and Fe^{3+} ions in oxide materials. *App. Surf. Sci.*, 254(8):2441–2449, 2008.

[163] K. E. Healy and P. Ducheyne. Hydration and preferential molecular adsorption on titanium in vitro. *Biomaterials*, 13(8):553–561, 1992.

[164] E. McCafferty, J. P. Wightman, and T. F. Cromer. Surface Properties of Hydroxyl Groups in the Air-Formed Oxide Film on Titanium. *J. Electrochem. Soc.*, 146(8):2849, 1999.

[165] T. K. Sham and M. S. Lazarus. X-ray photoelectron spectroscopy (XPS) studies of clean and hydrated TiO_2 (rutile) surfaces. *Chem. Phys. Lett.*, 68(2-3):426–432, 1979.

[166] K. Bourikas, C. Kordulis, and A. Lycourghiotis. Titanium dioxide (Anatase and Rutile): Surface chemistry, liquid-solid interface chemistry, and scientific synthesis of supported catalysts. *Chem. Rev.*, 114 (19):9754–9823, 2014.

[167] J. Cheng and M. Sprik. Acidity of the Aqueous Rutile TiO_2 (110) Surface from Density Functional Theory Based Molecular Dynamics. *J. Chem. Theory Comput.*, 6(3):880–889, 2010.

[168] J. Vörös, M. Wieland, L. Ruiz-Taylor, M. Textor, and D. M. Brunette. *Characterization of Titanium Surfaces*. Springer-Verlag Berlin Heidelberg, New York, USA, 1st edition, 2001.

[169] I. Iatsunskyi, M. Kempiński, M. Jancelewicz, K. Załęski, S. Jurga, and V. Smyntyna. Structural and XPS characterization of ALD Al_2O_3 coated porous silicon. *Vacuum*, 113:52–58, 2015.

[170] I. Olefjord and A. Nylund. Surface analysis of oxidized aluminium. II. Oxidation of aluminium in dry and humid atmosphere studied by ESCA, SEM, SAM and EDX. *Surf. Interface Anal.*, 21(5):290–297, 1994.

[171] B. R. Strohmeier. An ESCA method for determining the oxide thickness on aluminum alloys. *S. Interface Anal.*, 15(1):51–56, 1990.

[172] G. V. Franks and Y. Gan. Charging Behavior at the AluminaWater Interface and Implications for Ceramic Processing. *J. Am. Ceram. Soc.*, 90(11):3373–3388, 2007.

[173] T. Hiemstra, P. Venema, and W. H. van Riemsdijk. Intrinsic Proton Affinity of Reactive Surface Groups of Metal (Hydr)oxides: The Bond Valence Principle. *J. Colloid Interface Sci.*, 184(2):680–692, 1996.

[174] Y. Duval, J. A. Mielczarski, O. S. Pokrovsky, E. Mielczarski, and J. J. Ehrhardt. Evidence of the Existence of Three Types of Species at the QuartzAqueous Solution Interface at pH 0-10: XPS Surface Group Quantification and Surface Complexation Modeling. *J. Phys. Chem. B*, 106(11):2937–2945, 2002.

[175] J. A. Schaefer, J. Anderson, and G. J. Lapeyre. Water adsorption on cleaved silicon surfaces. *J. .Vac. Sci. Technol. A*, 3(3):1443–1447, 1985.

[176] G. W. Simmons, D. L. Angst, and K. Klier. A self-modeling approach to the resolution of XPS spectra into surface and bulk components. *J. Electron. Spectros. Relat. Phenomena*, 105(2-3):197–210, 1999.

[177] L. H. Allen, E. Matijevíc, and L. Meites. Exchange of Na+ for the silanolic protons of silica. *J. Inorg. Nucl. Chem.*, 33(5):1293–1299, 1971.

[178] P. J. Scales, F. Grieser, T. W. Healy, L. R. White, and D. Y. C. Chan. Electrokinetics of the silica-solution interface: a flat plate streaming potential study. *Langmuir*, 8(3):965–974, 1992.

[179] S. Ong, X. Zhao, and K. B. Eisenthal. Polarization of water molecules at a charged interface: second harmonic studies of the silica/water interface. *Chem. Phys. Lett.*, 191(3-4):327–335, 1992.

[180] M. A. Velbel. Natural weathering mechanisms of almandine garnet. *Geology*, 12(10):631, 1984.

[181] A. K. Witte, M. Bobal, R. David, B. Blättler, D. Schoder, and P. Rossmanith. Investigation of the potential of dry ice blasting for cleaning and disinfection in the food production environment. *LWT-Food Sci. Technol.*, 75:735–741, 2017.

[182] F. Elbing, N. Anagreh, L. Dorn, and E. Uhlmann. Dry ice blasting as pretreatment of aluminum surfaces to improve the adhesive strength of aluminum bonding joints. *Int. J. Adhes. Adhes.*, 23(1):69–79, 2003.

[183] J. Poon, D. C. Madden, M. H. Wood, and S. M. Clarke. Characterizing Surfaces of Garnet and Steel, and Adsorption of Organic Additives. *Langmuir*, 34(26):7726–7737, 2018.

[184] E. Uhlmann and R. Hollan. Blasting with Solid Carbon Dioxide Investigation of Thermal and Mechanical Removal Mechanisms. *Procedia CIRP*, 26:544–547, 2015.

[185] K. Xiao, C. F. Dong, X. F. Li, and F. M. Wang. Corrosion Products and Formation Mechanism During Initial Stage of Atmospheric Corrosion of Carbon Steel. *J. Iron Steel Res. Int.*, 15(5):42–48, 2008.

[186] G. de Leeuw. Profiling of aerosol concentrations, particle size distributions and relative humidity in the atmospheric surface layer over the North Sea. *Tellus B*, 42(4):342–354, 1990.

[187] L. Greenspan. Humidity fixed points of binary saturated aqueous solutions. *J. Res. Natl. Bur. Stand. A*, 81A(1):89, 1977.

[188] E. E. Stansbury and R. A. Buchanan. *Fundamentals of electrochemical corrosion*. ASM International, Materials Park, USA, 1st edition, 2000.

[189] J. Marsh, J. D. Scantlebury, and S. B. Lyon. The effect of surface/primer treatments on the performance of alkyd coated steel. *Corros. Sci.*, 43(5):829–852, 2001.

[190] T. S. N. S. Narayanan. Surface pretreatment by phosphate conversion coatings - A review. *Rev. Adv. Mat. Sci.*, 9(2):130–177, 2005.

[191] J. M. Chovelon, L. El. Aarch, M. Charbonnier, and M. Romand. Silanization of Stainless Steel Surfaces: Influence l Application Parameters. *J. Adhes.*, 50(1):43–58, 1995.

[192] C. K. Kang and Y. S. Lee. The surface modification of stainless steel and the correlation between the surface properties and protein adsorption. *J. Mat. Sci. Mat. Med.*, 18(7):1389–1398, 2007.

[193] S. B. Lyon, R. Bingham, and D. J. Mills. Advances in corrosion protection by organic coatings: What we know and what we would like to know. *Prog. Org. Coat.*, 102(A):2–7, 2017.

[194] Yu. I. Kuznetsov, N. P. Andreeva, N. P. Sokolova, and R. A. Bulgakova. Adsorption of the inhibiting anions on passive iron from an aqueous solution. *Prot. Met.*, 37(6):519–524, 2001.

[195] Yu. I. Kuznetsov. Progress in the science of corrosion inhibitors. *Int. J. Corros. Scale Inhib.*, 4(1):015–034, 2015.

[196] R. Yan, X. Gao, D. Lv, and H. Ma. A study on the differences in morphology and corrosion resistance performance between two different bis(2-ethylhexyl) phosphate self-assembled thin films prepared on an iron substrate in water and ethanol solvents. *RSC Adv.*, 6(61):55936–55945, 2016.

[197] W. Guo, S. Chen, Y. Feng, and C. Yang. Investigations of triphenyl phosphate and Bis-(2-ethylhexyl) phosphate self-assembled films on iron surface using electrochemical methods, fourier transform infrared spectroscopy, and molecular simulations. *J. .Phys. Chem. C*, 111(7):3109–3115, 2007.

[198] S. Lata and R. S. Chaudhary. Some triphosphates as corrosion inhibitors for mild steel in 3% NaCl solution. *Indian J. Chem. Technol.*, 15(4):364–374, 2008.

[199] M. H. Wood. *Adsorption at the metal/liquid interface*. Phd thesis, University of Cambridge, 2015.

[200] K. F. Khaled. Molecular simulation, quantum chemical calculations and electrochemical studies for inhibition of mild steel by triazoles. *Electrochim. Acta*, 53:3484–3492, 2008.

[201] A. Srhiri, M. Etman, and F. Dabosi. Thiol compounds as corrosion inhibitors of carbon steel (XC 38) in sodium chloride medium. *Mater. Corros.*, 43(8):406–414, 1992.

[202] J. V. Koleske, R. Springate, and D Brezinski. Additives Reference Guide. *Paint & Coatings Industry*, pages 22–104, 2013.

[203] C. Lai, B. Xie, L. Zou, X. Zheng, X. Ma, and S. Zhu. Adsorption and corrosion inhibition of mild steel in hydrochloric acid solution by S-allyl-O,O-dialkyldithiophosphates. *Results in Physics*, 7:3434–3443, 2017.

[204] M. Govindarajan, S. Periandy, and K. Ganesan. Scaled quantum FT-IR and FT-Raman spectral analysis of 1-methoxynaphthalene. *E-J. Chem.*, 7(2):457–464, 2010.

[205] E. Mack. Average Corss-Sectional Areas of Molecules by Gaseous Diffusion Methods. *J. Am. Chem. Soc.*, 47(10):2468–2482, 1925.

[206] M. Farsak, A. OngunYüce, and G. Karda. Anticorrosion Effect of 4-Amino-5-(4-pyridyl)-4H-1,2,4-triazole-3-thiol for Mild Steel in HCl Solution. *ChemistrySelect*, 2(13):3676–3682, 2017.

[207] V. V. Mehmeti and A. R. Berisha. Corrosion Study of Mild Steel in Aqueous Sulfuric Acid Solution Using 4-Methyl-4H-1,2,4-Triazole-3-Thiol and 2-Mercaptonicotinic AcidAn Experimental and Theoretical Study. *Frontiers in Chem.*, 5:61, 2017.

[208] H. Ouici, M. Tourabi, O. Benali, C. Selles, C. Jama, A. Zarrouk, and F. Bentiss. Adsorption and corrosion inhibition properties of 5-amino 1,3,4-thiadiazole-2-thiol on the mild steel in hydrochloric acid medium: Thermodynamic, surface and electrochemical studies. *J. Electroanal. Chem.*, 803:125–134, 2017.

[209] P. Taheri, J. Wielant, T. Hauffman, J. R. Flores, F. Hannour, J. H. W. de Wit, J. M. C. Mol, and H. Terryn. A comparison of the interfacial bonding properties of carboxylic acid functional groups on zinc and iron substrates. *Electrochim. Acta*, 56(4):1904–1911, 2011.

[210] P. Kern and D. Landolt. Adsorption of an Organic Corrosion Inhibitor on Iron and Gold Studied with a Rotating EQCM. *J. Electrochem. Soc.*, 148(6):B228, 2001.

[211] G. Quartarone, L. Bonaldo, and C. Tortato. Inhibitive action of indole-5-carboxylic acid towards corrosion of mild steel in deaerated 0.5 M sulfuric acid solutions. *App. Surf. Sci.*, 252(23):8251–8257, 2006.

[212] M. Frey, S. G. Harris, J. M. Holmes, D. A. Nation, S. Parsons, P. A. Tasker, and R. E. P. Winpenny. Elucidating the Mode of Action of a Corrosion Inhibitor for Iron. *Chem. Eur. J.*, 6(8):1407–1415, 2000.

[213] P. Agarwal and D. Landolt. Effect of anions on the efficiency of aromatic carboxylic acid corrosion inhibitors in near neutral media: Experimental investigation and theoretical modeling. *Corros. Sci.*, 40 (4-5):673–691, 1998.

[214] M. l. Doig, C. P. Warrens, and P. J. Camp. Structure and Friction of Stearic Acid and Oleic Acid Films Adsorbed on Iron Oxide Surfaces in Squalane. *Langmuir*, 30(1):186–195, 2014.

[215] Z. Yin, M. Kasrai, M. Fuller, G. M.l Bancroft, K. Fyfe, and K. H. Tan. Application of soft X-ray absorption spectroscopy in chemical characterization of antiwear films generated by ZDDP Part I: the effects of physical parameters. *Wear*, 202(2):172–191, 1997.

[216] Z. Yin, M. Kasrai, G. M. Bancroft, K. Fyfe, M. L. Colaianni, and K. H. Tan. Application of soft X-ray absorption spectroscopy in chemical characterization of antiwear films generated by ZDDP Part II: the effect of detergents and dispersants. *Wear*, 202(2):192–201, 1997.

[217] R. J. Bird and G. D. Galvin. The application of photoelectron spectroscopy to the study of E. P. films on lubricated surfaces. *Wear*, 37 (1):143–167, 1976.

[218] XPS Interpretation of Phosphorus. URL `https://xpssimplified.com/elements/phosphorus.php`.

[219] Y. Barbaux, M. Dekiouk, D. Le Maguer, L. Gengembre, D. Huchette, and J. Grimblot. Bulk and surface analysis of a Fe-P-O oxydehydrogenation catalyst. *Appl. Catal., A.*, 90(1):51–60, 1992.

[220] Y. Wang and P. M. A. Sherwood. Iron (III) Phosphate (FePO4) by XPS. *Surf. Sci. Spec.*, 9(1):99–105, 2002.

[221] G. R. Fulmer, A. J. M. Miller, N. H. Sherden, H. E. Gottlieb, A. Nudelman, B. M. Stoltz, J. E. Bercaw, and K. I. Goldberg. NMR chemical shifts of trace impurities: Common laboratory solvents, organics, and gases in deuterated solvents relevant to the organometallic chemist. *Organometallics*, 29(9):2176–2179, 2010.

[222] K. Ding, H. Gu, C. Zheng, L. Liu, L. Liu, X. Yan, and Z. Guo. Octagonal prism shaped lithium iron phosphate composite particles as positive electrode materials for rechargeable lithium-ion battery. *Electrochim. Acta*, 146:585–590, 2014.

[223] A. A. Salah, P. Jozwiak, J. Garbarczyk, K. Benkhouja, K. Zaghib, F. Gendron, and C. M. Julien. Local structure and redox energies of lithium phosphates with olivine- and Nasicon-like structures. *Journal of Power Sources*, 140(2):370–375, 2005.

[224] J. M. Stutman, J. D. Termine, and A. S. Posner. Vibrational Spectra and Structure of the Phosphate Ion in Some Calcium Phosphates. *Trans. N. Y. Acad. Sci.*, 27:669–675, 1965.

[225] M. H. Wood, T. J. Wood, R. J. L. Welbourn, J. Poon, D. C. Madden, and S. M. Clarke. An X-ray and Neutron Reflectometry Study of Iron Corrosion in Seawater. *Langmuir*, 34(21):5990–6002, 2018.

[226] I. F. Lyuksyutov, H. Pfnür, and H.-U Everts. Incommensurate-commensurate transition via domain wall evaporation in an overlayer. *Europhys. Lett.*, 33(9):673–678, 1996.

[227] J. Götzen, D. Käfer, C. Wöll, and G. Witte. Growth and structure of pentacene films on graphite: Weak adhesion as a key for epitaxial film growth. *Phys. Rev. B*, 81(8):085440, 2010.

[228] J. Coates. Interpretation of Infrared Spectra, A Practical Approach. In *Encyclopedia of Analytical Chemistry*, pages 1–23. John Wiley & Sons, Ltd., Chichester, UK, 2006.

[229] H. Möller, E. T. Boshoff, and H. Froneman. The corrosion behaviour of a low carbon steel in natural and synthetic seawaters. *J. South Afr. Inst. Min. Metall.*, 106(August):585–592, 2006.

[230] S. F. Wika. *Pitting and Crevice Corrosion of Stainless Steel under Offshore Conditions*. PhD thesis, Norwegian University of Science and Techology, 2012.

[231] J. G. Liu, Zi. Li, Y. Li, and B. R. Hou. Corrosion process of D32 steel used for offshore oil platform in splash zone. *Anti-Corros. Methods M*, 63(1):56–64, 2016.

[232] G. K. Batchelor. *An Introduction to Fluid Dynamics*. Cambridge University Press, Cambridge, UK, 1st edition, 2000.

[233] F. L. LaQue. Corrosion and Protection of Offshore Drilling Rigs Summary of Discussion. *Corrosion*, 6(5):161–166, 1950.

[234] D. L. Savoie, J. M. Prospero, and E. S. Saltzman. Non-sea-salt sulfate and nitrate in trade wind aerosols at Barbados: Evidence for long-range transport. *J. Geophys. Res.*, 94(D4):5069, 1989.

[235] M. Pauletta, E. Battocchio, and G. Russo. A weathering steel elastomer joint for the connection between new and existing bridges. *Eng. Struct.*, 105:264–276, 2015.

[236] G. Rosenberg and I. Sinaiova. Evaluation of hydrogen induced damage of steels by different test methods. *Mater. Sci. Eng., A*, 682:410–422, 2017.

[237] F. Berto, S. M. J. Razavi, M. R. Ayatollahi, and F. Mutignani. Mechanical behaviour of hot dip galvanized steel connection under cyclic loading. *Procedia Struct. Integrity*, 3:77–84, 2017.

[238] Y. Jin, T. Sheng, W. Kong, R. Zhang, W. Wang, and D. Kong. Effects of strain rate on stress corrosion of S355 steel in 3.5% NaCl solutions. *J. Wuhan Uni. Tech.-Mater. Sci. Ed.*, 31(6):1381–1386, 2016.

[239] R. E. Melchers. Effect of small compositional changes on marine immersion corrosion of low alloy steels. *Corros. Sci.*, 46(7):1669–1691, 2004.

[240] R. Rosliza and W. B. Wan Nik. Improvement of corrosion resistance of AA6061 alloy by tapioca starch in seawater. *Curr. Appl Phys.*, 10 (1):221–229, 2010.

[241] B. Cai, Y Liu, X. Tian, F. Wang, H. Li, and R. Ji. An experimental study of crevice corrosion behaviour of 316L stainless steel in artificial seawater. *Corros. Sci.*, 52(10):3235–3242, 2010.

[242] P. Refait, A. M. Grolleau, M. Jeannin, E. François, and R. Sabot. Localized corrosion of carbon steel in marine media: Galvanic coupling and heterogeneity of the corrosion product layer. *Corros. Sci.*, 111: 583–595, 2016.

[243] H. Möller and P. C. Pistorius. The influence of Mg^{2+} on the formation of calcareous deposits on freely corroding low carbon steel in seawater. *J. South Afr. Inst. Min. Metall.*, 107(3):167–175, 2007.

[244] M. Echeverría, C.M. Abreu, and C.A. Echeverría. Assessing Pretreatment Effect on the Protective Properties of Different Coating Systems Against Marine Corrosion. *Corrosion*, 70(12):1203–1218, 2014.

[245] M. Stratmann. The Atmospheric Corrosion of Iron - A Discussion of the Physico-Chemical Fundamentals of this Omnipresent Corrosion Process Invited Review. *Ber. Bunsenge. Phys. Chem.*, 94(6):626–639, 1990.

[246] Di. Gassama, A. A. Diagne, I. Yade, M. Fall, and S. Faty. Investigations on the corrosion of constructional steels in different aqueous and

simulated atmospheric environments. *Bull. Chem. Soc. Ethiop.*, 29(2): 299–310, 2015.

[247] D. Kong, X. Dong, and J. Wang. Effects of anodic oxidation on corrosion properties of Al coating by arc spraying in seawater. *Surf. Interface Anal.*, 47(9):911–918, 2015.

[248] D. R. Kester, I. W. Duedall, D. N. Connors, and R. M. Pytkowicz. Preparation of artificial seawater. *Limnol. Oceanogr.*, 12(1):176–179, 1967.

[249] J. B. Lee, D. Derome, R. Guyer, and J. Carmeliet. Modeling the Maximum Spreading of Liquid Droplets Impacting Wetting and Nonwetting Surfaces. *Langmuir*, 32(5):1299–1308, 2016.

[250] X. Liu, M. C. Patsavas, and R. H. Byrne. Purification and characterization of meta-cresol purple for spectrophotometric seawater pH measurements. *Environ. Sci. Technol.*, 45(11):4862–4868, 2011.

[251] A. G. Dickson. The measurement of sea water pH. *Mar. Chem.*, 44 (2-4):131–142, 1993.

[252] H. Sverdrup, M. Johnson, and R. Fleming. The Oceans: Their Physics, Chemistry and General Biology. *Oceanography*, page 1104, 1942.

[253] R. Saraswat, M. Kouthanker, S. Kurtarkar, R. Nigam, and V. N. Linshy. Effect of salinity induced pH changes on benthic foraminifera: a laboratory culture experiment. *Biogeosci. Discuss.*, 8(4):8423–8450, 2011.

[254] N. N. Greenwood and A. Earnshaw. *Chemistry of the elements*. Butterworth-Heinemann, Oxford, UK, 2nd edition, 1997.

[255] A. Pardo, M. C. Merino, A. E. Coy, F. Viejo, R. Arrabal, and E. Matykina. Pitting corrosion behaviour of austenitic stainless steels - combining effects of Mn and Mo additions. *Corros. Sc.*, 50(6):1796–1806, 2008.

[256] U. R. Evans. The Ferroxyl Indicator in Corrosion Research, With Special Reference to the Controversy Regarding the Cause of Pitting. *The Metal Industry*, 29:481, 1926.

[257] J. C. Scully. *The fundamentals of corrosion*. Pergamon Press, Oxford, UK, 3rd edition, 1990.

[258] G. Bhargava, I. Gouzman, C. M. Chun, T. A. Ramanarayanan, and S. L. Bernasek. Characterization of the "native" surface thin film on pure polycrystalline iron: A high resolution XPS and TEM study. *App. Surf. Sci.*, 253(9):4322–4329, 2007.

[259] T. C. Lin, G. Seshadri, and J. A. Kelber. A consistent method for quantitative XPS peak analysis of thin oxide films on clean polycrystalline iron surfaces. *App. Surf. Sci.*, 119(1-2):83–92, 1997.

[260] R. A. Antunes, I. Costa, and D. L. A. de Faria. Characterization of corrosion products formed on steels in the first months of atmospheric exposure. *Mat. Res.*, 6(3):403–408, 2003.

[261] J. Alcántara, B. Chico, J. Simancas, I. Díaz, D. de la Fuente, and M. Morcillo. An attempt to classify the morphologies presented by different rust phases formed during the exposure of carbon steel to marine atmospheres. *Mater. Charact.*, 118:65–78, 2016.

[262] M. Kimura, T. Mizoguchi, H. Kihira, and M. Kaneko. Various Scale Analyses to Create Functioning Corrosion Products. In *Characterization of Corrosion Products on Steel Surfaces*, pages 245–272. Springer, Berlin, Heidelberg, Berlin, Heidelberg, FRG, 1st edition, 2006.

[263] R. Posner, O. Ozcan, and G. Grundmeier. Water and Ions at Polymer/Metal Interfaces. In L. F. M. da Silva and C Sato, editors, *Design of Adhesive Joints Under Humid Conditions*, pages 21–52. Springer-Verlag Berlin Heidelberg, Heidelberg, FRG, 1st edition, 2013.

[264] S. Ardizzone, L. Formaro, and J. Lyklema. Adsorption from mixtures containing mono- and bivalent cations on insoluble oxides and a revision of the interpretation of points of zero charge obtained by titration. *J. Electroanal.l Chem.*, 133(1):147–156, 1982.

[265] R. K. Iler. *The chemistry of silica : solubility, polymerization, colloid and surface properties, and biochemistry.* John Wiley & Sons, Inc., 1st edition, 1979.

[266] S. B. Johnson, P. J. Scales, and T. W. Healy. The Binding of Monovalent Electrolyte Ions on α-Alumina. I. Electroacoustic Studies at High Electrolyte Concentrations. *Langmuir*, 15(8):2836–2843, 1999.

[267] P. L. Brown and C. Ekberg. *Hydrolysis of Metal Ions.* Wiley-VCH Verlag GmbH & Co. KGaA, 1st edition, 2016.

[268] M. D. LeVan and T. Vermeulen. Binary Langmuir and Freundlich isotherms for ideal adsorbed solutions. *The Journal of Physical Chemistry*, 85(22):3247–3250, 1981.

[269] C. L. De Castro and B. S. Mitchell. Nanoparticles from Mechanical Attrition. In M-.I. Baraton, editor, *Synthesis, Functionalization and Surface Treatment of Nanoparticles*, chapter 1, pages 1–15. American Scientific Publishers, Valencia, Spain, 1st edition, 2002.